

Diss. ETH No. 23547

# **Time Resolved Flow Field and Droplet Measurements in Wet Steam Turbine Flows**

A thesis submitted to attain the degree of

Doctor of Sciences of ETH Zurich  
(Dr. sc. ETH Zurich)

presented by

**ILIAS BOSDAS**

Dipl. Mech.-Eng., Aristotle University of Thessaloniki  
Born on 29<sup>th</sup> of June 1985  
citizen of Greece

accepted on the recommendation of

Prof. Dr. Reza S. Abhari, examiner  
Dr. Shigeki Senoo, co-examiner  
Dr. Michel Mansour, co-examiner

2016



*ὅτι οὐδὲν οἶδα*  
Σωκράτης (470-399 π.Χ)

*I know one thing: that I know nothing*  
Socrates (470-399 BC)



## Acknowledgments

The present thesis is the outcome of my research work, which I carried out during the five and half years as a research assistant in the Laboratory for Energy Conversion of ETH Zürich. This work would not have been possible without the support and contributions from many people, to whom I am deeply grateful.

I would like to thank Prof. Dr. Reza S. Abhari for having me accepted as part of his research team. His guidance throughout the years was very valuable for my personal career. My skills in management, cost assessment and time optimization have improved throughout the meetings and discussions.

I am very grateful to Dr. Shigeki Senoo for his support in the entire project. His professionalism, patience and kindness helped me through enlightening discussions to expand my knowledge and be a better engineer. In addition, I would like to thank him and the entire MHPS research team in Hitachi, for trusting me and my team in participating in these very unique and expensive measurement campaigns in Japan. I am sure that I will never forget the amazing time that I spent with him during the working hours.

Special thanks to my Professor from Aristotle University of Thessaloniki Anestis I. Kalfas. I would like to especially express my deep gratitude to him for supporting and encouraging me during my entire studies since I met him for the first time in 2006. Είστε ένας πραγματικός δάσκαλος!

My very deep acknowledgements go to Dr. Michel Mansour. He was always there to help and support me not only professionally but also in my personal life's difficulties. He has the talent of being professional and at the same time creating a friendly work environment, which makes the working hours with him to run fast. Thank you for teaching me everything I needed to accomplish this difficult work and thank you for being patient to keep me in the correct path every time that I was getting lost. I hope we will keep in touch in the far future!

In addition, I would like also to thank Flori Alickaj and the workshop team. Without them the development of the probes and not only would not be possible. Flori thanks a lot for staying late in lab with me, away from home, in order to complete the tasks and meet the deadlines!

I would like to thank all my colleagues at the LEC. It was a pleasure to work in such a friendly, multi-cultural working environment. I would like to specially acknowledge the support of Dr. Kai Regina and Rainer Schädler in spending long days with me in the machine hall in order to conduct the measurements in LISA. In addition, I would like to acknowledge Patrick Rebholz and Sebastiano Lazzi Gazzini for our discussions on special issues in fluid mechanics. A special thank goes to Mrs. Marlene Hegner. She has always ensured that all the administrative problems were handled in time.

In addition, I would like to thank Dr. Oran Morris and Dr. Bob Rollinger. I learned many things from both of them and they were always available to

help me with my experiments no matter if they were busy or not. A special thank to Carlo Baumeler for his contribution on the FRAP-OB matlab code and to Ilias Papagiannis for the CFD support. I appreciate a lot the support of Mr. K. Ishibashi and Mr. C. Duan from MHPS research team in Japan. Their contribution during the measurement campaigns was very important to have accurate and reliable results.

Finally, I cannot find any words to appropriately express my deepest gratitude to my family and friends. Σας έχω όλους στην καρδιά μου...Γονείς, Γιαγιά, Λένα, Κατερίνα, Φώτης, Χριστόδουλος, Αλέκος, Θοδωρής, Ηλίας, Λευτέρης, Καλλή, Βαγγέλης, Georgia, Ξάδερφος (Καβάντζας), Σπύρος (Decipher Tone), Φίλιππος, Ζακελίνα, Λεανδράκος, Στέλλα, Βίτωνας, Κώστας, Άννα, Ανθή, Γιώργος, Bruno R, Bruno A, Eva, Denise... Thank you all for supporting me in these difficult times, I hope I will manage to give it back to you because you all deserve it!

Ilias V. Bosdas  
Zurich, May 2016

## Abstract

Today, the largest share of electricity production worldwide still belongs to steam turbines. However, due to the increasing share of renewable energies on the electrical grid, steam turbines require operational flexibility. As a consequence, the machines have to work efficiently under a wide range of operating conditions. In addition, the continuous increase in energy demand necessitates efficient design, as well as power output augmentation. Hence, the area of the last stages of low-pressure (LP) steam turbines is continuously being increased, leading to blade lengths of up to 60 inches. The resulting long rotor blades exhibit higher mechanical vibrations, supersonic relative flow speeds and accelerated rotor leading edge erosion due to droplet impacts generated from condensation. Therefore, the aerodynamic performance and the erosion phenomena in the last stages of LP steam turbines have to be accurately measured and well understood, in order to cope with this challenge and react to the current trend for more efficient power production.

In-depth understanding of the unsteady flow environment is best approached through the development of fast response instrumentation. The first part of the current doctoral thesis describes the development of two novel probes dedicated to wet steam flows – a fast response aerodynamic probe (FRAP-HTH) for unsteady flow field measurements and a fast response optical backscatter probe (FRAP-OB) for coarse water droplet measurements.

The FRAP-HTH probe is comprised of a pair of piezo-resistive pressure sensors that measure the unsteady flow angles, total and static pressure, up to a frequency of 25kHz. A miniature heater cartridge ensures uncontaminated pressure taps from condensed water. The operating principle and calibration procedure of the probe are presented and a detailed uncertainty analysis demonstrates the capability of the novel probe to perform accurate measurements in the wet steam environment.

On the hand, the FRAP-OB probe uses a focused laser light to illuminate water droplets and measures the backscattered light with a fast response photodiode. The novel probe is capable to measure droplet diameters ranging from 40 $\mu\text{m}$  to 110 $\mu\text{m}$  and droplet velocities up to 170m/s. The calibration procedure, uncertainty analysis and the post processing routines are described in addition. The design of the FRAP-OB probe provides the required spatial and temporal resolution suitable for unsteady droplet measurements in the last stages of LP steam turbines.

Both probes proved successful and achieved optimum results. They have demonstrated their ability to perform accurate measurements in several measurement campaigns. For the first time, a unique set of time-resolved wet steam flow field measurements is presented with the aerodynamic probe. Similarly, the optical backscatter probe was used in two different test facilities and has demonstrated its ability to perform unsteady droplet measurements.

The FRAP-OB probe was tested at the stator exit of a one-and-1/2-stage axial gas turbine equipped with a water spray generator. The measurements were performed under two different operating conditions for two different downstream locations. Results have shown, that the maximum concentration of coarse water droplets, over the entire stator pitch, occurs at the trailing edge of the stator. This is due to the water film formation on the stator's pressure side, which sheds from the trailing edge generating water rivulets with coarse droplets. In addition the measurements showed, that the droplet size depends on the local flow field velocity, due to the shear forces between the droplets and the stream flow. Droplet speed measurements revealed, that coarse droplets suffer from a deficit in absolute velocity, thus the increased relative speed results in enhanced rotor leading edge erosion. The time-resolved droplet measurements have shown that the droplet mass rate is modulated by the rotor blade-passing period and the fluctuations are enhanced as the droplets approach the rotor leading edge.

The unsteady measurements performed with the FRAP-HTH probe, at the inlet and exit of the last stage of a LP steam turbine test facility in Hitachi city in Japan, are also presented. Three different operating points, including two part load conditions, were measured. Results have shown, that the secondary flow structures at the tip region are the predominant sources of unsteadiness over the last 30% of the blade span for all operating conditions. In addition, when the mass flow is reduced, the flow is redirected towards the blade tip generating higher pressure fluctuations, due to the strengthening of the secondary flow features. This implies that at low volumetric flow conditions (part load), the blades will be subjected to higher dynamic load fluctuations at the tip region.

The most relevant measurement campaign within the framework of the current thesis was performed at the last stage of a LP steam turbine with supersonic relative flow conditions at the top 15% span of the rotor blade. Time resolved coarse droplet measurements and flow field measurements were conducted at different operating conditions in the same steam turbine test facility in Japan. Results have shown that, coarse droplets were present over the entire stator pitch. One major finding was that the coarse droplets were concentrated at the vicinity of the stator wake's suction side. The coagulation mechanism together with the film break up from the stator's suction surface could be responsible for the droplets' location. Nevertheless, further investigations are needed to fully understand the underlying coarse water droplet formation. The influence of stator rotor interaction on the flow field with the presence of an attached bow shock on the rotor leading edge was also studied. It was demonstrated that the shock wave generates high flow unsteadiness, due to high static pressure gradients across the shock. It was also shown, that the axial gap between the stator trailing edge and rotor leading edge is the



main factor influencing the intensity of the unsteady stator rotor interaction in the presence of the bow shock.



## Zusammenfassung

Heutzutage besitzen Dampfturbinen immer noch den grössten Anteil an der weltweiten Elektrizitätserzeugung. Auf Grund des steigenden Anteils an erneuerbaren Energien im Stromnetz benötigen Dampfturbinen trotzdem Flexibilität in ihrer Betriebsweise. Demzufolge müssen diese Maschinen über einen weiten Bereich von Betriebspunkten effizient arbeiten. Zusätzlich macht der kontinuierlich steigende Energiebedarf ein effizientes Design sowie die Steigerung der Nutzleistung erforderlich. Daher wird die Querschnittfläche der Endstufen von Niederdruck(ND)-Dampfturbinen kontinuierlich erhöht, was zu einer Schaufellänge von bis zu 60 Zoll führt. Diese langen Rotorschaukeln weisen höhere mechanische Schwingungen sowie höhere supersonische Strömungsrelativgeschwindigkeiten und eine beschleunigte Erosion der Rotorvorderkante infolge Kondensations-bedingten Tropfenaufralls auf. Deswegen müssen die aerodynamische Performance und die Erosionsvorgänge in Endstufen von ND-Dampfturbinen präzise gemessen und gut verstanden werden, um dieser Herausforderung gewachsen zu sein und um auf den gegenwärtigen Trend steigender, effizienter Elektrizitätserzeugung zu reagieren.

Für ein detailliertes Verständnis der Verhältnisse in instationären Strömungen kann am besten mit schnellansprechender Instrumentierung herangegangen werden. Der erste Teil der vorliegenden Doktorarbeit beschreibt die Entwicklung von zwei neuartigen Sonden für Nassdampf-Strömungen – eine schnellansprechende aerodynamische Sonde (FRAP-HTH) für die Messung instationärer Strömungsfelder sowie eine schnellansprechende optische Rückstreuungssonde (FRAP-OB) für Messungen von groben Wassertropfen.

Die FRAP-HTH-Sonde besteht aus einem Paar piezo-resistiver Drucksensoren, mit denen die instationären Strömungswinkel sowie der statische und der Totaldruck mit einer Frequenz von 25kHz gemessen werden. Eine miniaturisierte beheizte Hülse gewährleistet, dass die Sondenlöcher frei von Kondenswasser bleiben. Das Funktionsprinzip und die Kalibrationsmethode der Sonde werden vorgestellt und eine detaillierte Analyse der Messunsicherheit zeigen die Tauglichkeit der neuartigen Sonde für präzise Messungen im Nassdampfgebiet.

Demgegenüber wird in der FRAP-OB-Sonde fokussiertes Laserlicht verwendet, um Wassertropfen anzuleuchten und es wird das zurück gestreute Licht mit einer schnellansprechenden Photodiode gemessen. Die neuartige Sonde ist dafür geeignet, Tropfen mit einem Durchmesser im Bereich zwischen  $40\mu\text{m}$  und  $110\mu\text{m}$  und mit Geschwindigkeiten von bis zu  $170\text{m/s}$  zu messen. Es werden zusätzlich die Kalibrationsmethode, die Analyse der Messunsicherheit sowie die Routinen für die Datenverarbeitung und -auswertung beschrieben. Das Design der FRAP-OB-Sonde stellt die erforderliche räumliche und zeitliche Auflösung für die instationäre Tropfenmessung in Endstufen von ND-Dampfturbinen bereit.

Beide Sonden haben sich als erfolgreich erwiesen und erreichten optimale Ergebnisse. In mehreren Messkampagnen haben die Sonden gezeigt, für die Durchführung präziser Messungen geeignet zu sein. Zum ersten Mal wird ein einzigartiger Datensatz an instationären Messungen des Strömungsfeldes im Nassdampf vorgestellt, für den die aerodynamische Sonde angewendet wurde. In entsprechender Weise wurde die optische Rückstreuungssonde in zwei verschiedenen Versuchsständen eingesetzt und es ist gezeigt worden, dass sich diese Sonde für die instationäre Tropfenmessung eignet.

Die FRAP-OB-Sonde wurde am Statoraustritt einer 1½-stufigen Axialturbine getestet, die mit einem Wasserspraygenerator ausgestattet war. Die Messungen wurden unter zwei verschiedenen Betriebspunkten und an zwei in Strömungsrichtung verschiedenen Orten durchgeführt. Ergebnisse haben gezeigt, dass das Konzentrationsmaximum grober Tropfen entlang des Umfangs einer vollständigen Stator-Teilung sich an der Hinterkante der Statorschaufel befindet. Dies liegt daran, dass sich an der Druckseite der Statorschaufel ein Wasserfilm bildet, der von der Hinterkante losgeworfen wird und einen Tropfenstrahl mit groben Wassertropfen erzeugt. Zusätzlich zeigen die Messungen, dass die Tropfengrösse von der örtlichen Geschwindigkeit des Strömungsfeldes abhängt, auf Grund der Scherkräfte zwischen den Tropfen und der Hauptströmung. Messungen der Tropfengeschwindigkeit haben offengelegt, dass grobe Wassertropfen ein Defizit an Absolutgeschwindigkeit aufweisen, womit die erhöhte Relativgeschwindigkeit eine Steigerung der Erosion der Rotorvorderkante mit sich bringt. Die zeit-aufgelösten Tropfenmessungen haben gezeigt, dass der Tropfenmassenstrom am Statoraustritt von der Schaufelpassierperiode des nachgelagerten Rotors moduliert wird, wobei die periodischen Fluktuationen sich intensivieren während die Tropfen sich der Rotorvorderkante nähern.

Ebenso werden die instationären Messungen mit der FRAP-HTH-Sonde vorgestellt, die am Eintritt und am Austritt der Endstufe eines ND-Dampfturbinen-Versuchsstands in Hitachi City in Japan durchgeführt wurden. Dort wurde an drei verschiedenen Betriebspunkten gemessen, inklusive zweier Betriebspunkte mit reduziertem Massenstrom. Ergebnisse haben gezeigt, dass diejenigen Strukturen der Sekundärströmungen stromab der Gegend um die Schaufelspitzen die massgebliche Quelle von Instationaritäten sind. Sie erstrecken sich über die letzten 30% der Schaufelhöhe und sind bei sämtlichen Betriebspunkten vorzufinden. Wird der Massenstrom verringert, so wird die Strömung in Richtung der Schaufelspitze umgelenkt, was zu höheren Druckschwankungen führt, aufgrund der Verstärkung der Sekundärströmungsmerkmale. Dies impliziert, dass die Schaufeln bei geringen Volumenstrom-Bedingungen (Teillast) grösseren dynamischen Lastfluktuationen an der Schaufelspitze ausgesetzt sind.

Die wichtigste Messkampagne im Rahmen der vorliegenden Arbeit wurde in der Endstufe einer ND-Dampfturbine durchgeführt, deren Relativge-

schwindigkeiten an den oberen 15% der Rotorschaufelhöhe supersonisch waren. Zeit-aufgelöste Messungen grober Tropfen sowie des Strömungsfeldes wurden an verschiedenen Betriebspunkten im selben Dampfturbinen-Versuchsstand in Japan gemacht. Ergebnisse haben gezeigt, dass grobe Tropfen entlang des gesamten Umfangs der Stator-Teilung vorzufinden sind. Eine wichtige Erkenntnis war, dass grobe Tropfen in der saugseitigen Nähe des Nachlaufs der Statorschaukel konzentriert waren. Der Koagulationsmechanismus könnte der für diesen Befund verantwortliche Mechanismus sein. Dennoch sind weiterführende Untersuchungen notwendig, um die zu Grunde liegende Entstehung grober Tropfen vollständig zu verstehen. Ebenfalls wurde der Einfluss von der Wechselwirkung zwischen dem Rotor und dem Stator auf das Strömungsfeld für denjenigen Fall untersucht, dass sich ein Verdichtungsstoss vor der Rotorvorderkante befindet. Es wurde nachgewiesen, dass die Verdichtungswelle, wegen der starken Gradienten über den Verdichtungsstoss, eine hohe Instationarität in der Strömung erzeugt. Es wurde ebenfalls gezeigt, dass der Axialspalt zwischen der Hinterkante des Stators und der Vorderkante des Rotors der hauptsächliche Parameter ist, der die Intensität der instationären Wechselwirkung zwischen dem Stator und dem Rotor beeinflusst.



# List of Contents

<b>ACKNOWLEDGMENTS</b> .....	<b>V</b>
<b>ABSTRACT</b> .....	<b>VII</b>
<b>ZUSAMMENFASSUNG</b> .....	<b>XI</b>
<b>LIST OF CONTENTS</b> .....	<b>XV</b>
<b>1 INTRODUCTION</b> .....	<b>1</b>
1.1 Motivation.....	1
1.2 Theoretical background on the operation of low-pressure steam turbines.....	6
1.2.1 Secondary flow field structures.....	6
1.2.2 Inter-blade row interaction at the last stage under sonic and supersonic flow conditions.....	8
1.2.3 Steam turbine operation under low volumetric flow .....	12
1.2.4 Droplets formation mechanisms in steam turbines .....	13
1.3 State-of-the-art in measuring techniques for wet steam flows .....	17
1.3.1 Fast response pressure measurement systems for wet steam environment.....	17
1.3.2 Optical probes for droplet and particle measurements .....	18
1.4 Research objectives .....	22
1.5 Thesis outline.....	24
<b>2 FAST RESPONSE AERODYNAMIC PROBE FOR FLOW FIELD WET   STEAM MEASUREMENTS (FRAP-HTH)</b> .....	<b>26</b>
2.1 Probe development.....	26
2.1.1 The FRAP-HTH probe .....	26
2.1.2 Miniature cartridge heater description .....	28
2.1.3 Pressure sensors calibration.....	31
2.1.4 Virtual 6 sensor mode .....	32
2.1.5 Aerodynamic calibration.....	35
2.1.6 Effect of probe tip overheating on measured flow quantities .....	39
2.1.7 Measurement bandwidth assessment .....	40
2.2 Uncertainty Analysis.....	43
2.3 Specific data reduction algorithm for wet steam flows.....	47
2.3.1 Droplet filtering processing algorithm.....	47
2.4 Summary .....	51
<b>3 FAST RESPONSE OPTICAL BACKSCATTER PROBE FOR COARSE   WATER DROPLET MEASUREMENTS (FRAP-OB)</b> .....	<b>52</b>
3.1 General design requirements and operating principle .....	52
3.2 The FRAP-OB probe .....	53
3.2.1 Optimal light scattering collection angle .....	54

3.2.2	Sample volume .....	55
3.2.3	Photodiode selection .....	58
3.2.4	Dynamic response.....	58
3.2.5	Probe calibration .....	59
3.3	Uncertainty analysis.....	68
3.3.1	Calibration uncertainties.....	68
3.3.2	Measurement uncertainties .....	69
3.4	Single measurement point processing algorithm .....	70
3.5	Phase lock averaging concept for droplet measurements.....	74
3.6	Summary.....	76
<b>4</b>	<b>MEASUREMENTS IN ONE-AND-HALF-STAGE AXIAL TURBINE EQUIPPED WITH A SPRAY GENERATOR.....</b>	<b>77</b>
4.1	Experimental set up .....	77
4.2	Results and discussion.....	80
4.2.1	Results for design and part load conditions at the location of $x/c=2%$ .....	80
4.2.2	Results for part load condition at locations of $x/c=2%$ and $8%$ .....	85
4.2.3	Time resolved results for design and part load condition.....	87
4.3	Summary.....	91
<b>5</b>	<b>MEASUREMENTS IN A 7MW STEAM TURBINE TEST FACILITY ...</b>	<b>92</b>
5.1	Experimental test facility .....	92
5.2	Results and discussion.....	95
5.2.1	Time-averaged measurement comparison between FRAP-HTH and five hole probe .....	95
5.2.2	Steady flow field at rotor exit of L-1 stage .....	97
5.2.3	Time resolved flow field at rotor exit of L-1 stage .....	100
5.2.4	Steady flow field at rotor exit of L-0 stage .....	104
5.2.5	Time resolved flow field at rotor exit of L-0 Stage.....	107
5.3	Summary.....	109
<b>6</b>	<b>MEASUREMENTS IN A 10MW STEAM TURBINE TEST FACILITY WITH SUPERSONIC AIRFOILS NEAR THE BLADE TIP.....</b>	<b>110</b>
6.1	Experimental test facility.....	110
6.2	Results and discussion.....	112
6.2.1	Flow field analysis with FRAP-HTH results.....	112
6.2.2	Flow field analysis at reduced mass flow operation .....	133
6.2.3	Coarse water droplet analysis with FRAP-OB results.....	137
6.3	Summary.....	146
<b>7</b>	<b>CONCLUSIONS AND OUTLOOK .....</b>	<b>148</b>
7.1	Summary.....	148
7.2	Concluding remarks.....	149
7.3	Future work.....	152



<b>APPENDIX .....</b>	<b>155</b>
References .....	156
Nomenclature.....	162
List of Figures.....	166
List of Tables .....	173
List of Publications .....	175
Curriculum Vitae.....	177



# 1 Introduction

## 1.1 Motivation

Energy is a property of objects, which can be transferred to other objects or converted into different forms, but cannot be created or destroyed. One of the most important reasons for humans' technological evolution is energy conversion. Hundred thousands of years ago, humans started using fire to cover nutritional needs and heating. Today, all human activities such as agriculture, health, industry, services, transportation, as well as household activities incorporate energy conversion. It is very obvious how energy is deeply intertwined with aspects of modern life and how strongly is related with human's prosperity. According to the International Energy Agency (IEA), the total world energy demand and economic growth are highly correlated and as a matter of fact, the actual and future needs in energy demand exhibit a positive rate. The last two decades this fact has increased since China and India have extended their energy demand especially in transport and industry. The positive rate of world's energy demand is depicted in Figure 1–1. In this figure, the annual average growth of energy demand and outlook over the period 1990 to 2030 is 1.3%. According to predictions, this corresponds roughly to 16 up to 18 trillion tonnes of oil equivalent worldwide consumption by 2030. Since conventional fuel reserves are not unlimited, a worldwide resource depletion is driven by this high energy consumption [1].

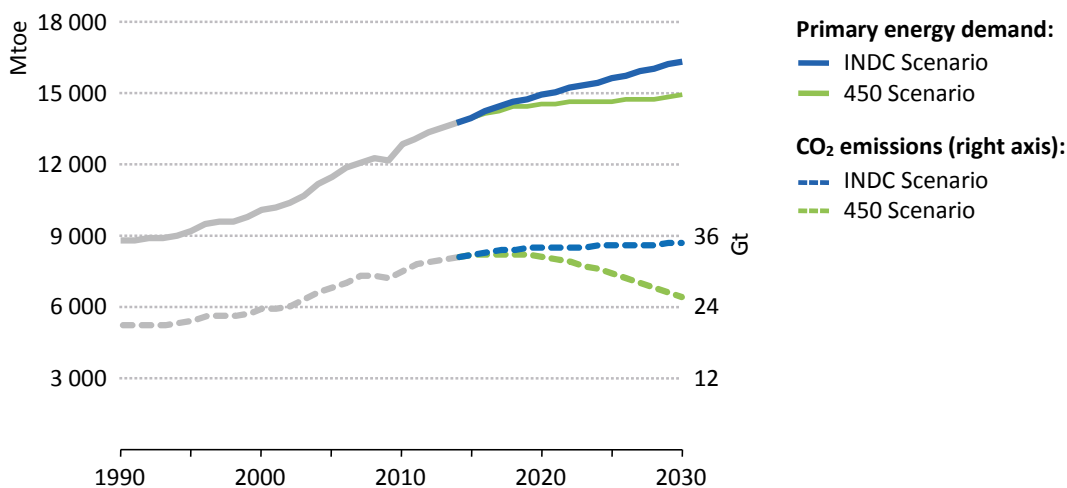


Figure 1–1: World energy demand to 2030 in Mtoe [1]. INDC scenario: Intended Nationally Determined Contributions. 450 scenario: limit concentration of greenhouse gases in the atmosphere to 450ppm of CO<sub>2</sub>.

On the other hand, human activities related to energy conversion are responsible for a continuing rise in global greenhouse-gas emissions and stifling air pollution in many of the world's fast growing cities. It is clear more than

ever the high concerns on global warming since 97-98% [2] of most publishing climate researchers support the findings of the Intergovernmental Panel on Climate Change (IPCC) that “*anthropogenic greenhouse gases have been responsible for most of the unequivocal warming of earth’s average global temperature over the second half of 20<sup>th</sup> century*”. This is as well depicted in Figure 1–1, where it is shown that the CO<sub>2</sub> emissions keep on rising by the year 2030 with the predictions estimating 36Gt of emitted CO<sub>2</sub> gas. Facing this great energy challenge, engineers must react and provide sustainable solutions. The 450 scenario, shown in Figure 1–1, sets out an energy pathway consistent with the goal of limiting the global increase in temperature to 2°C by limiting concentration of greenhouse gases in the atmosphere to around 450ppm of CO<sub>2</sub>. This scenario describes the measures to have around 50% chance of limiting the global increase in average temperature to 2°C in the long term, compared with pre-industrial levels. As a consequence, the energy efficiency has to be improved and the fuel switch to renewables has to be boosted.

As reported in the global status report of 2015 for renewables [3], there is rising awareness worldwide that renewable energy and energy efficiency are critical not only for addressing climate change, but also for creating new economic opportunities, and for providing energy access to billions of people who are still living without modern energy services. In recognition of the importance of renewable energy and energy efficiency for sustainable development, the United Nations General Assembly declared the goal to double the share of renewable energy in the global energy mix from a baseline share of 18% in 2010 to 36% in 2030 [4]. As shown in Figure 1–2, in 2013 renewable energy provided an estimated of 19.1% and conventional fossil fuels of 78.3% of global final energy consumption.

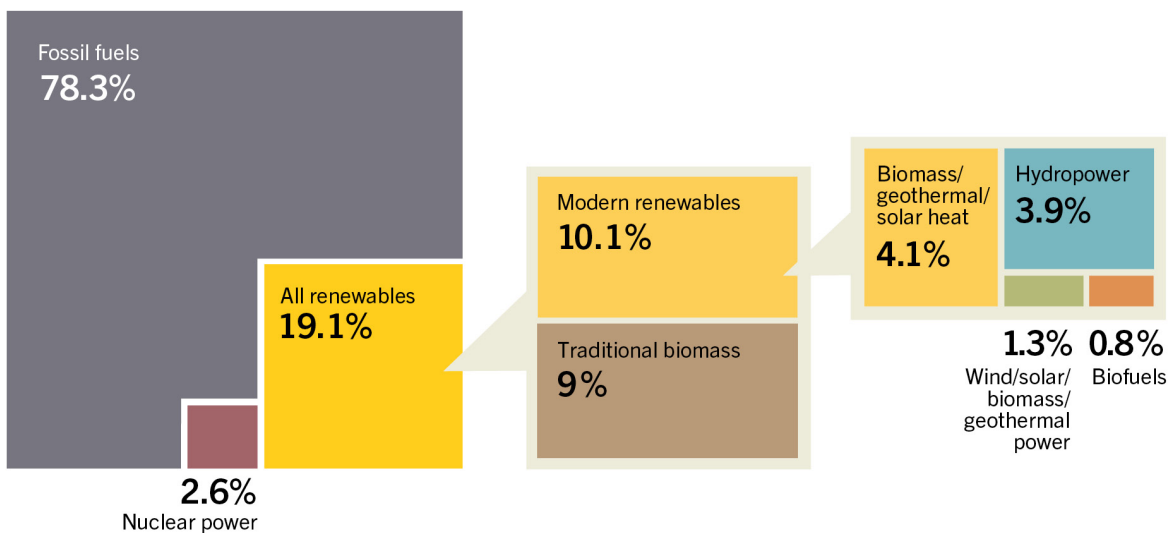


Figure 1–2: Estimated fossil fuel energy share of global final energy consumption in year 2013 [3].

As a result, conventional fossil fuels have still a large part of the total energy consumption worldwide however renewables' share will increase substantially in the following 20 years.

Based on the clear link of the energy challenge with the current work, a description of the total energy demand is studied. The total energy consumption is divided into three main categories, namely industry, transportation and households. Each of these subsectors has a share of approximately 30% of the total global energy demand, according to references [1, 5] and as shown in Figure 1–3, almost 60% of the total power demand is related to power generation (industry) and transportation.

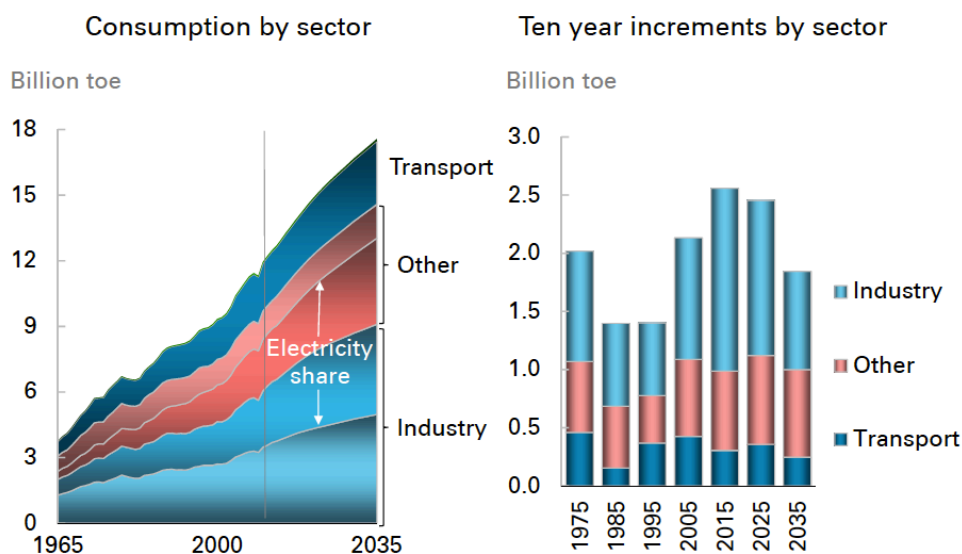


Figure 1–3: World energy demand to 2030 by sector in MBDOE [5].

Turbomachinery is a major player in the crucial fields of industry and transportation. It is used in almost all power production processes (steam turbines, gas turbines, hydroplants, etc.) and its contribution to the transportation sector (aviation & marine) is also considerable. As a consequence, improving the efficiency of the current machines contributes significantly on today's energy challenge.

As described in this chapter, greenhouse gases, in particular CO<sub>2</sub>, have risen to the top of the list of the energy sector's environmental impacts, as being the source of human-made climate change. For more than a decade, the IEA has worked on efficient and effective climate mitigation policies for the energy sector, including efforts ranging from emissions trading to energy end-use efficiency policy and R&D technologies. In order to meet these goals, the share of renewable energies generated using turbomachines has to be increased drastically. Besides the well-known renewable technologies (wind, solar, etc.), geothermal power and Concentrated Solar Power (CSP) are also important. They operate with Rankine cycles as shown in Figure 1–4.

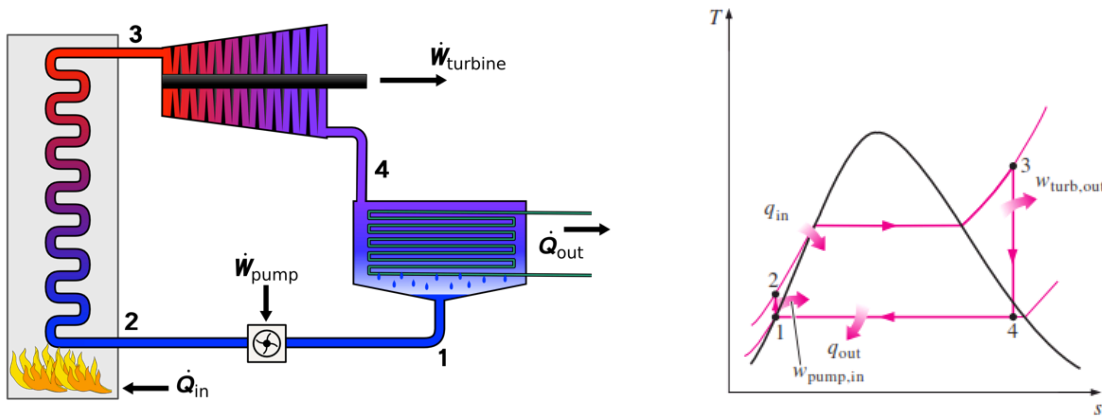


Figure 1–4: Schematic of Rankine cycle (left) with the respective temperature (T)-entropy (s) diagram of a steam turbine (right)[6].

Rankine cycle converts heat into work. Steam is generated in the boiler (2) by providing energy to water, which is then enters the high pressure turbine section (3) and expands generating work on a rotating shaft. As the steam expands in the turbine, it loses energy and changes its phase back to water status in the condenser (4). Steam turbines used in conventional power plants as well as in geothermal power plants operate often with a low inlet temperature of 180°C and condensation phenomena in the last stages produce a dense fog of water droplets with diameter in the order of 0.1 up to 200 $\mu\text{m}$  [7-11]. As shown in Figure 1–5, the presence of these particles results in severe erosion of rotor blades and in generation of aerodynamic disturbances in the main flow. Complicated blade design is required to drain part of the liquid water out of the main flow stream that affects the aerodynamic efficiency of the flow field of the machine. In order to emphasize the erosion concerns, it is worth mentioning that this was always an issue from the early developing stages of steam turbines, as reported by Cook [12] already in 1928!

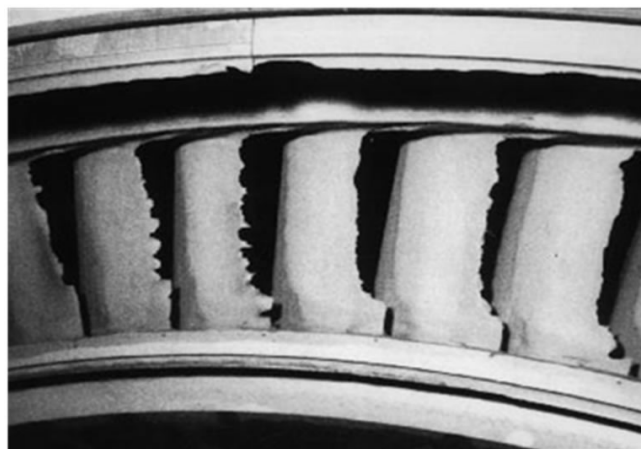


Figure 1–5: Blade erosion in a steam turbine [13].

In addition to particle issues in turbomachines, due to increasing share of renewable power within the existing electrical power network, conventional industrial steam turbines require operational flexibility. They need to be operated efficiently over a wide range of operating conditions at various mass flow rates and different exit vacuum pressures and inlet temperatures. In order to compensate for the machine's reduced performance during part load conditions, taking into account the continuous increase in energy demand, efficient design of steam turbines as well as power output augmentation are required. This implies that the area of the last stages is continuously being increased, leading to blade lengths up to 60 inches [14-16]. The above result in a challenging design with relative supersonic flow speeds at the blade tip region under different wetness mass fractions and droplets sizes that range from few micrometers up to 100 $\mu\text{m}$  in diameter [7, 11] generating high erosion at the rotating blades. In addition, the aerodynamic design of these stages of the machine has a direct impact on their mechanical integrity. This is because the unsteady blade loading leads to high cycle fatigue of the rotating components and it is directly coupled with the evolution of the unsteady three-dimensional flow field. The main drawback is concentrated to the lack of time-resolved experimental data measured in the wet steam environment of the last two stages of LP steam turbines. Five-hole probes equipped with an air purging system are commonly used in the wet steam environment of the last two stages of LP steam turbines. Nevertheless, they are no longer suitable to study and quantify the unsteady blade row interactions affecting the aeromechanical performance of the machines. Early experiments with hot wire anemometers in wet steam have provided the first unsteady flow field information. However, their short operating life, led the researchers to abandon this technology [17]. Consequently, together with water droplet analysis, the investigation of unsteady flow field is essential for improving the efficiency of steam turbines.

Much attention is currently being given to blade and flow passage design using computational flow dynamics (CFD) [18]. In order to obtain accurate results with CFD calculations, experimental data are required to validate the numerical codes. This rule applies for both flow field calculations, as well as particle size and motion calculations. The set of equations that govern fluid flow are the Navier-Stokes equations. Numerical solutions to the Navier-Stokes equations can be obtained with reasonable accuracy using modern, commercially available CFD codes. However, as these codes are intended to predict only the fluid flow field, they are generally not capable of solving transient particle transport kinematic problems. Some CFD codes offer simple single particle transport modules and/or "tracer" visualization techniques but these are essentially just visualization of the flow streamlines or streak lines and do not predict how a multitude of particles would behave as they are carried by a highly unsteady flow. Thus, to analyze particle motion within an unsteady fluid flow, it is necessary to determine the transient flow field (using

CFD codes and validation experiments) and apply time-dependent particle transport equations to model individual particle kinematics within the three-dimensional flow field. As the analysis has to be performed in a complex three-dimensional flow field with very small transient time steps in order to capture the unsteady flow field, the solution to these equations is numerically intensive and difficult. Furthermore, few experimental data are available in the public domain that would allow comparison of predicted results with test data. In particular, advanced CFD models, capable of solving two-phase three-dimensional flows require experimental data for validation [19]. Thus, the need for time-resolved measurements becomes unavoidable. Therefore, in order to improve the design and efficiency of steam turbines, experimental data are mandatory to verify and calibrate the particle and droplet transport models in the complex wet steam environment.

Concluding, modern steam turbines require operational flexibility, due to the increasing share of renewable energies on the electrical grid and this implies that the machines have to work efficiently under a wide range of operating conditions. In addition, the continuous increase in energy demand necessitates efficient design of the machines, as well as power output augmentation. The resulting long turbine rotor blades at the last stages are more prone to mechanical vibrations and accelerated rotor leading edge erosion. In order to cope with the energy challenge and react to the current trends for more efficient power production, the unsteady flow field phenomena in the last stage of LP steam turbines have to be measured and understood. The flow mechanisms that dominate droplets' motion in the gas path of a steam turbine need to be understood and correlated to the main engine's operating flow field. The goals of the engineers have become more challenging and more effort has to be invested towards the direction of:

- Reduce rotor blade high cycle fatigue under part load conditions
- Mitigate the last stage blade erosion due to coarse water droplet impacts
- Reduce the unsteady blade loading and aerodynamic losses caused by the inter-blade row interaction
- Increase engine's lifetime and reduce maintenance costs related to erosion phenomena

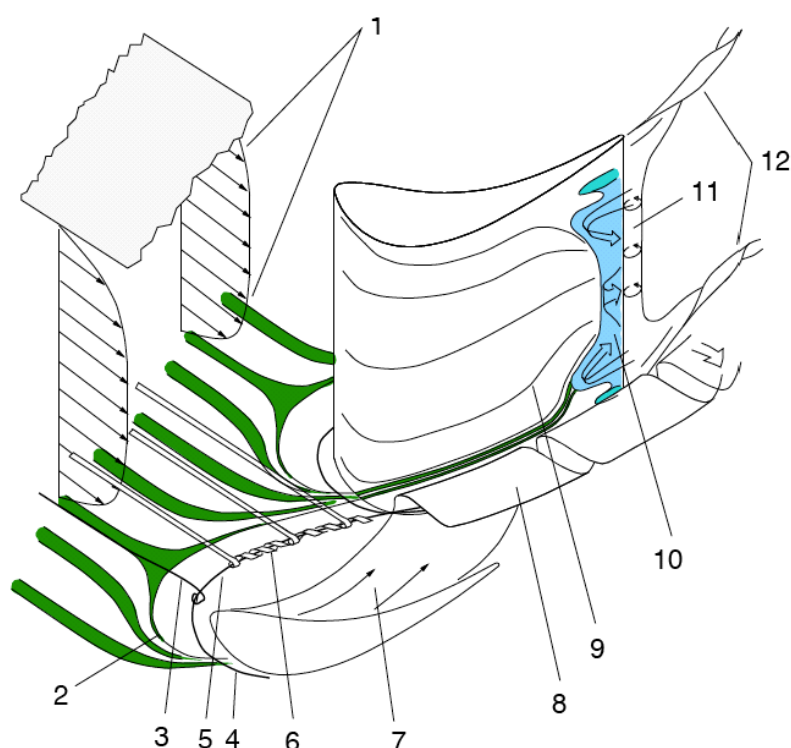
## **1.2 Theoretical background on the operation of low-pressure steam turbines**

### **1.2.1 Secondary flow field structures**

Secondary flows are present in all types of turbomachines. In particular, these three-dimensional flows have been extensively described by Behr [20] for the axial turbine case followed by experimental results focused on the control of the rotor tip leakage by the casing air injection. These secondary flow



structures do not follow the quasi two-dimensional turbine primary flow and they are generated by the redistribution of low momentum fluid within a blade passage. The redistribution occurs, due to the pressure field of a turbine blade region, which causes low momentum fluid to turn on a smaller radius than the main flow also known as flow underturning. The low momentum fluid itself is a result of viscous effects during the development of boundary layers on the endwalls. Although the appearance of the secondary flows depends on the individual design of the turbine profiles some of the features that are typically observed in every turbomachine are summarized in the secondary flow model of Vogt and Zippel [21], as shown in Figure 1–6. Since the work of many research groups has addressed this issue, a short summary is presented in the current thesis. Reviews of these studies are given by Langston in [22].



- |  |  |
|--|--|
| 1: Inlet boundary layer                        | 7: Cross flow in the passage                 |
| 2: Separation line of the inlet boundary layer | 8: Passage vortex                            |
| 3: Horseshoe vortex, inlet flow                | 9: Motion of the suction side boundary layer |
| 4: Horseshoe vortex (suction side leg)         | 10: Separation with backflow                 |
| 5: Horseshoe vortex (pressure side leg)        | 11: Eddying in the wake                      |
| 6: Rolling up of the inlet boundary layer      | 12: Trailing edge vortices                   |

Figure 1–6: Secondary flow model described in [20].

*Passage vortices:* The profiles of a turbine blade row cause a turning of the incoming flow and generate a pressure gradient across the passage. Under the influence of this pressure gradient, the endwall boundary layer of the inlet flow turns on a smaller radius than the main flow, due to its low momentum. As a consequence, within the passage, an endwall cross-passage flow from the

pressure to the suction side of the blade is generated and subsequently rolls up into a passage vortex.

*Horseshoe vortices:* The endwall boundary layer of the incoming flow can be considered to be a layer of tangential vorticity. At the leading edge of a blade profile this boundary layer rolls up into a system of two counter-rotating vortices that pass along each side of the blade leading edge. The pressure side leg of the horseshoe vortex has the same direction of rotation as the passage vortex described previously whereas the suction side leg of the horseshoe vortex has the counter rotation of the passage vortex. In the pressure side, both vortices merge within the passage and appear as one enhanced vortex downstream of the blade. The suction side leg of the horseshoe vortex stays close to the blade and then travels up the suction surface.

*Corner (Counter) Vortices:* A new highly skewed boundary layer is formed on the endwall downstream of the separation line caused by the pressure side leg of the horseshoe vortex. This strong crossflow impinges on the adjacent blade in the suction side corner of the blade profile and forms a new vortex that rotates counter to the passage vortex. The vortex is located right at the endwall suction side corner and its presence reduces the overturning near the endwalls.

The size and strength of the secondary flows depend on the blade turning, the pitch to chord ratio, the aspect ratio and the inlet vorticity. The importance of the secondary flow structures can be seen in their direct negative impact on the performance of a turbine. Endwall vortex flow is responsible for a loss of lift on a profile and increases the aerodynamic losses. According to Sharma and Butler [23], the aerodynamic loss attributed to secondary flows can be as high as 30-50% of the total aerodynamic losses of a certain blade row. The convection of secondary flow with flow angles that deviate substantially from the design may cause additional losses in downstream blade rows as well. The high impact of secondary flows on the loss generation in a turbine has led to three-dimensional blade designs, in order to minimize these flow structures. The principal design approaches are the blade sweep, blade twist and blade lean angles that alter these secondary flows, as well as the blade loading.

### **1.2.2 Inter-blade row interaction at the last stage under sonic and supersonic flow conditions**

Steam turbines are the largest machines among the entire turbomachines. Increasing the annulus area of the last stage in a steam turbine, provides an effective way of increasing the output power as well as the efficiency by expanding the flow and reducing the amount of practically useless kinetic energy at the exit of the machine. However, when the exit area of the last stage is

increased the rotor blades become longer. As a consequence, these machines are characterized by large blade height to hub diameter ratio,  $H/D$ , which is responsible for the large pressure gradient between the hub and tip region. Figure 1–7 shows the typical profiles of static pressure and Mach number at the inlet and exit of the last rotor. In order to satisfy the radial equilibrium, the absolute Mach number at the stator exit increases progressively from tip to hub region. This is indicated in Figure 1–7 with  $Ma_1$ . The Mach number distribution causes supersonic inlet flow conditions expressed with  $Ma_{rel,1}$  at the tip and with  $Ma_1$  at the hub. Therefore, due to the supersonic flow velocities, it is very difficult to avoid shock waves at these two locations within the last stage.

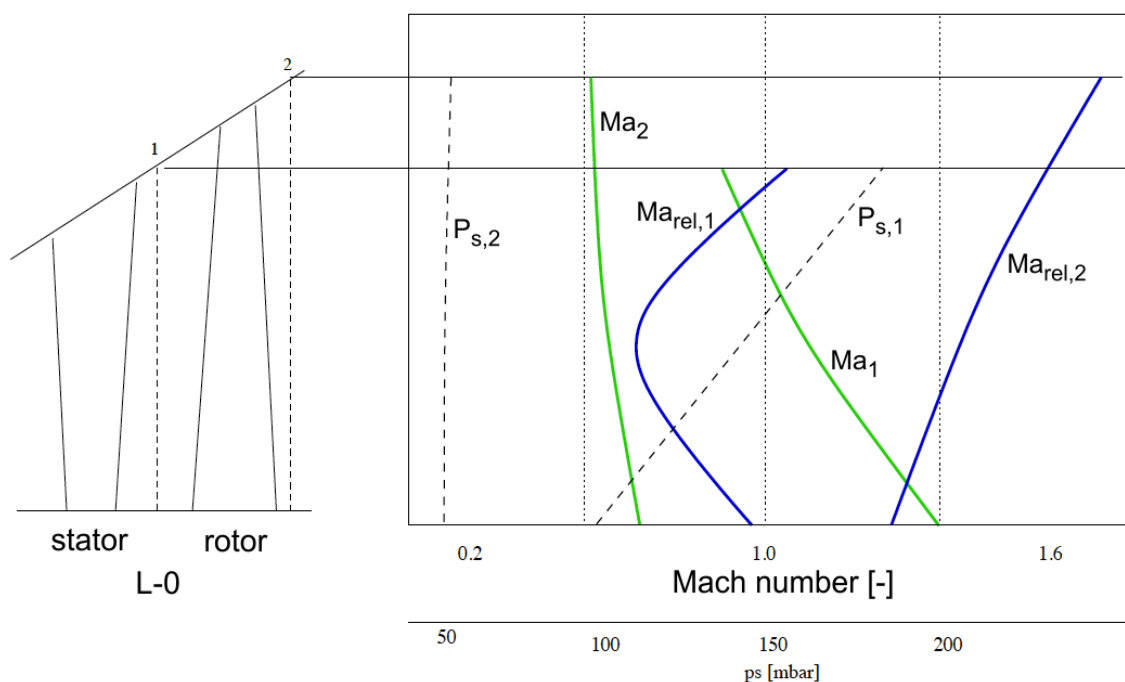
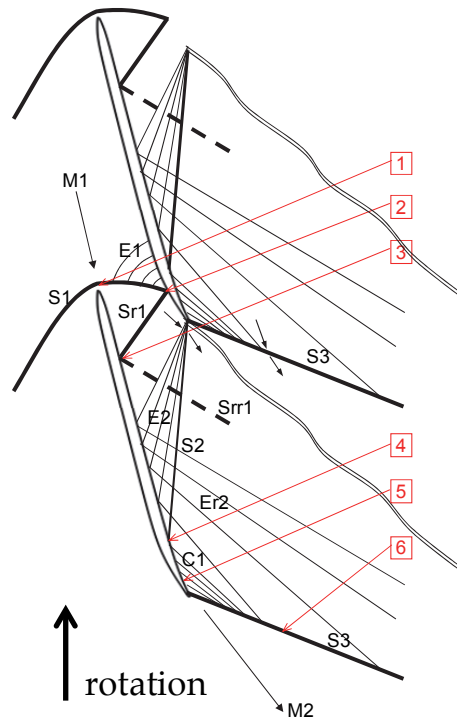


Figure 1–7: Sketch of Mach number and static pressure radial distribution in the last stage of a low-pressure steam turbine [24].

As explained by Havakechian and Denton in [25], the high loading at the hub is associated with a low degree of reaction and negative exit swirl and therefore a very high Mach number resulting in high trailing edge shock losses. On the other hand, at the tip region, the high relative Mach number generates a zone of supersonic flow field at the inlet of the rotor associated to an attached bow shock at the rotor leading edge.

The challenges of designing and operating long turbine blades are mainly focused on achieving low mechanical vibrations and maintaining high aerodynamic efficiency. Depending on the rotational speed of the steam turbine, there is a threshold where the relative inlet and outlet flow to the last rotor blade are both supersonic. Supersonic flows generate shock waves, which are responsible for high aerodynamic loading, as well as high aerodynamic losses [24]. As described by Senoo in [14] and depicted in Figure 1–8, there are six

principal loss mechanisms related to shock waves at the last stage rotor with supersonic relative flow conditions at the inlet.



- 1: Attached bow shock at leading edge ( $S_1$ )
- 2: First shock wave reflection ( $Sr_1$ ) on pressure side
- 3: Second shock wave reflection ( $Srr_1$ ) on suction side
- 4: Trailing edge shock ( $S_2$ ) and reflection on suction side
- 5: Compression waves ( $C_1$ ) due to adverse pressure gradient on the concave suction side
- 6: Trailing edge ( $S_3$ ) shock wave on the suction surface

Figure 1–8: Losses associated to shock waves at the tip region of a supersonic rotor blade profile [14].

The upstream shock wave  $S_1$  appears due to blade blockage and generates total pressure losses. As indicated in Figure 1–8 by number 2, the second loss is caused by the interaction between shock wave  $S_1$  and boundary layer on the pressure side of the neighboring airfoil. The third loss is generated by the reflected shock wave  $Sr_1$  and its interaction with the boundary layer on the suction surface of the blade. Then, the fourth loss, indicated in Figure 1–8 by number 4, is generated by the interaction between the trailing shock wave  $S_2$  and the boundary layer on the suction surface. The fifth loss is caused by the adverse pressure gradient due to the compression waves  $C_1$  originated from the concave suction surface and the last mechanism is the total pressure loss of the trailing edge shock wave  $S_3$ , indicated by number 6 in Figure 1–8, generated by the suction surface flow turning. The largest loss among the six losses is the sixth one, because the Mach number upstream of shock wave  $S_3$  is the highest.

In reality, the flow field is highly unsteady due to the stator rotor interaction, which makes these effects even more complicated and enhances the losses. An experimental investigation on the aerodynamic performance of a supersonic turbine blade was performed by Parvizinia et al. in [26]. In their work, they have studied the interaction of the trailing edge shock (Figure 1–8, number 4) with the boundary layer of the suction side. Various pitch-to-chord ratios were chosen for different exit Mach numbers. In their report, they state that a small pitch to chord ratio exhibits a more steady shock wave, resulting in low aerodynamic losses. Although these experiments were conducted in a cascade test tunnel with stationary blades, the effect of unsteadiness on the aerodynamic losses due to the presence of shock waves was found to be high [26].

A detailed numerical analysis for the design of the last stage with supersonic blade profiles was made by Stüer et al. in [24]. In this work, they have investigated the modulation of the shock wave at the stator trailing edge as well as at the rotor leading edge at the hub and tip regions respectively. CFD results are used to explain the interaction of the shock wave with the boundary layers. Regarding the shock at the trailing edge in the hub region, results have shown extremely high unsteady interactions. The suction side branch of the trailing edge shock meets the suction surface of the rotating blade and multiple reflections interact with both boundary layers, suction and pressure side of the rotor passage, causing peak-to-peak fluctuations in the range of 30% of the mean value. Conversely, their studies on the attached bow shock at the rotor leading edge at the blade tip region, showed reduced levels of unsteadiness. They state that the rotating bow shock is very steady and even weakens to become negligible before it interacts with the upstream stator.

Regarding the last finding, which is also linked to the results of the current thesis, it has to be mentioned that the stator profile is swept forward, as shown in Figure 1–9, in order to increase the axial gap between the stator trailing and the rotor leading edge. It is possible that the weak interaction of the bow shock with the upstream stator is a result of this large axial gap. Since the degree of reaction at the blade tip is high, this form of stacking increases the static pressure, due to improved diffusion and therefore increases the chances of flow separation. This becomes even more pronounced since the flow path distance increases more compared to the physical distance due to the large swirl angle at the blade tip region. The forward blade sweep, which is often followed by the designers, is mainly beneficial from the erosion point of view. Due to the increased flow-path length, coarse water droplets accelerate and their absolute velocity is higher resulting in a reduction in droplet relative speed as well as accelerated droplet break up process. As a consequence, the final droplet impact energy is lower and therefore the erosion rate at the rotating blade is reduced [24, 25, 27].

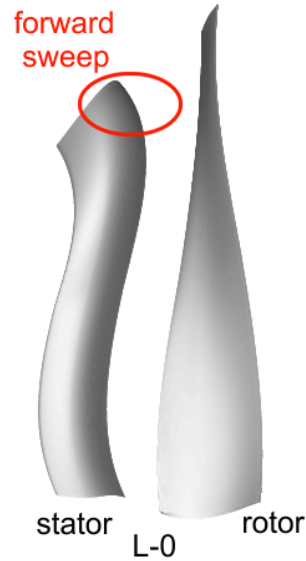


Figure 1–9: Side view of a forward swept stator blade at tip region from the last stage simulated by Stürer et al. [24].

### 1.2.3 Steam turbine operation under low volumetric flow

The variable operating conditions of the steam turbine are of great importance for the last stages of the machine. When the mass flow is reduced, in a part load operation, all flow parameters are affected starting from the low reaction zones (hub) of the last stage rotor blades. In principle, the reduced mass flow generates a highly complex three-dimensional flow field, which can potentially result to a flow inversion in the hub region under very low volumetric flows. This phenomenon is also known as windage or ventilation and has been studied experimentally by many researchers since the 1970's [28, 29]. As shown in Figure 1–10.a and b, when the steam does not pass through the hub region it is redirected towards the blade tip and thus a hub separation region is generated at the exit of the last moving rotor blade.

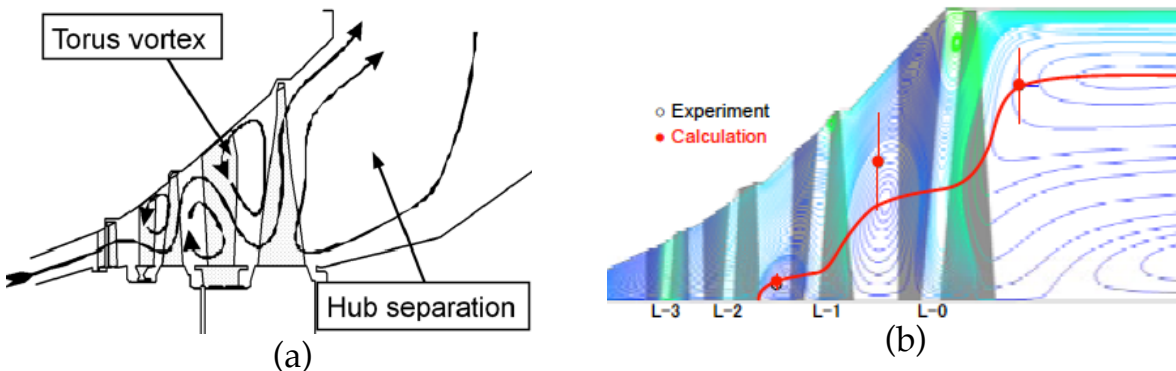


Figure 1–10: Flow field distribution at the last stages of LP steam turbine under ventilation [30] (a) and comparison with experiments from [31] (b).

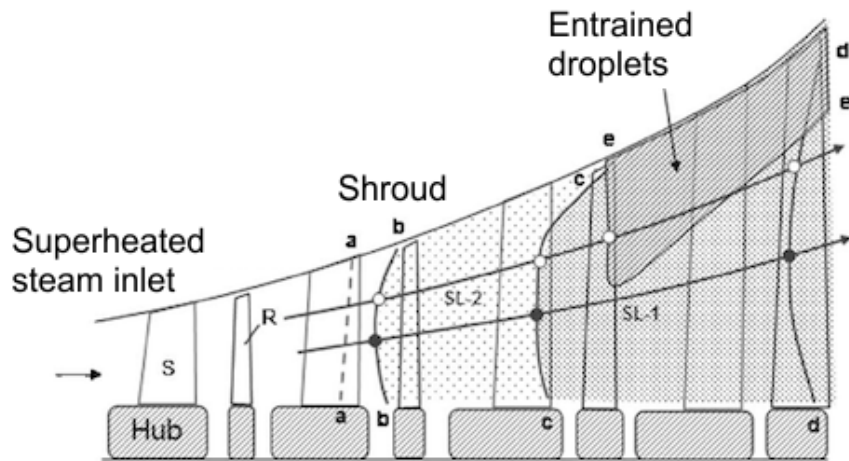
A number of recent publications describes in detail the ventilation process with increased unsteadiness and blade loading, due to flow redirection towards the blade tip [30-34].

It is expected that the increase in flow unsteadiness will generate higher dynamic blade loading and, as a result, higher alternating stresses in the last rotor blade. Intense dynamic stresses are superimposed on the blade centrifugal and gas forces and this can be very critical for the special long and stacked rotor blades of the steam turbine. As described by Megerle et al. [35] there are three principal mechanisms that cause the high alternating stresses under the ventilation condition. These are the unsteady flow field conditions of the reverse flow, the buffeting and the rotating stall. Troyanovskii et al. in [28] have presented the extent of the root flow separation zone as a function of the vacuum level for a typical steam turbine. According to their measurements, a small increase in vacuum, in the range of 10%, will result in a flow reduction from the root zone to the tip region in the last rotor. When the mass flow is reduced to 40% of its nominal value, there is no steam flow over almost 40% of the blade span starting from root region. As the mass flow further is reduced to 30% of its nominal value, the flow separation at the blade root covers up to 50% of the entire blade span. It is worth noting that as the mass flow is reduced, the alternating stresses increase and reach a maximum at around 30% of the rated volumetric flow [28, 35]. The above description of the windage phenomenon provides the general trends since the specific flow field characteristics will depend on the individual turbine design. As presented in chapters 5 and 6 of this thesis, there is a correlation between the high flow unsteadiness measured in the last stage of a LP steam turbine and the reduced mass flow operating condition.

#### **1.2.4 Droplets formation mechanisms in steam turbines**

The droplet formation mechanisms are very complex and the lack of experimental data does not allow a deep and solid analysis of the current topic. Nevertheless, the thermodynamic properties of the steam can provide sufficient information on the status of the generated droplets. There are two types of nucleation related to droplets' formation: heterogeneous and homogeneous nucleation. The difference is on the free energy barrier (Gibbs energy) that is required for the steam to change phase from gaseous to liquid. Homogeneous nucleation occurs in the flow field away from surfaces and thus the energy barrier is high. Heterogeneous nucleation, however, occurs at nucleation sites within the system. It is a faster process because the free energy barrier is smaller, since the nucleus on the blade surface is not spherical due to its contact with the surface. Figure 1-11 provides a simple schematic of the two-phase environment in the steam turbine. The first transition line marked with a-a denotes the saturation line followed by heterogeneous nucleation as indicated with the solid line b-b. However, as stated by Gerber et al. [36], this nucleation occurs due to flow contaminants in the flow that are generally few to

establish an equilibrium. The main primary homogenous nucleation starts at c-c, also called the Wilson line, leading to further secondary homogeneous nucleation along the line d-d. The region e-e is the most interesting one, since it is related to high erosion phenomena at the leading edge of the rotating blades. In particular, small droplets generated from upstream mechanisms coagulate or being collected on the blades resulting in large droplet sizes greater than  $100\mu\text{m}$  in diameter. The fact that fog droplets are the source for the entrainment of large droplets, in e-e region of Figure 1–11, emphasizes the complexity of the two phase flow phenomena in LP steam turbines.



a-a: Saturation line

b-b: Heterogeneous nucleation transition ( $D_d: 0.01\text{-}0.1\mu\text{m}$ )

c-c: Primary homogeneous nucleation transition ( $D_d: 0.001\text{-}0.01\mu\text{m}$ )

d-d: Secondary primary homogeneous nucleation transition

e-e: Secondary droplet region originating from trailing edges of rotating blades ( $D_d: 0.01\text{-}300\mu\text{m}$ )

Figure 1–11: Topology of phase transition in a LP steam turbine presented by Gerber in [36]. Stator and rotor components are labelled with S and R, respectively.

As described in the previous paragraph, the last stages of steam turbines operate always under wet steam conditions, because the steam expands below the saturation line of the Mollier diagram entering the biphasic flow region. The formed water droplets are classified into two main categories: the very fine droplets in the submicron range that create a fog, which follows the stream lines and the coarse water droplets above  $1$  to  $5\mu\text{m}$  in diameter, reaching up to  $300\mu\text{m}$ , that deviate from the main steam flow path, due to high inertia. The fog droplets are not responsible for the rotor blade erosion, since they continue within the blade passage without impacting the moving rotor blades. However, the impact of coarse droplets on the rotor leading edges is one of the main causes of severe erosion rates, as described in [7, 37-39]. One of the formation mechanisms responsible for the growth of large water droplets is presented in Figure 1–12.



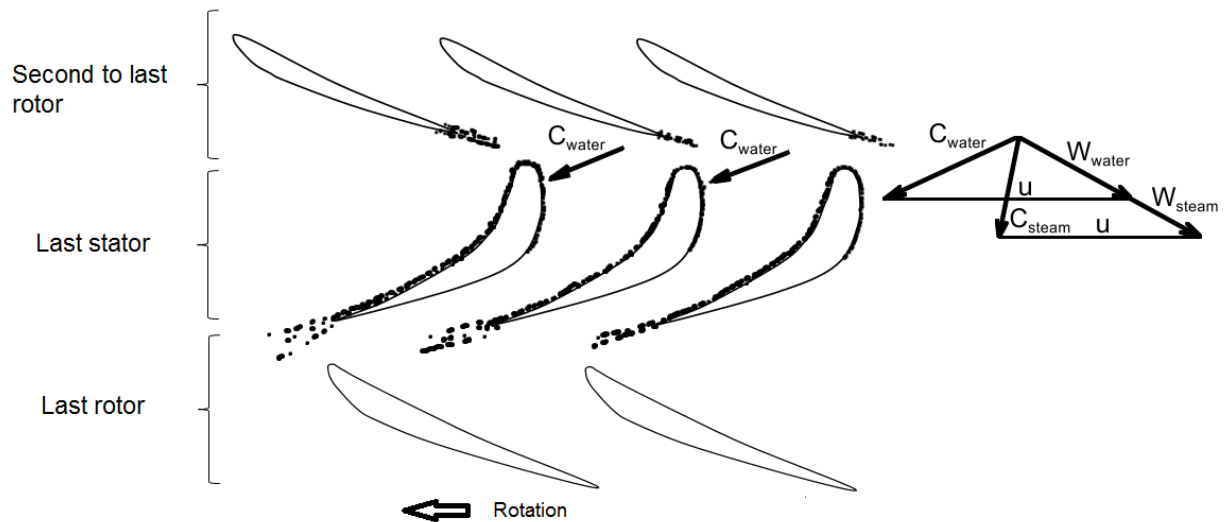


Figure 1–12: Water film formation on last stage stator in a LP steam turbine [7].

Large droplets are generated from the development of a liquid thin film on the stationary blades, involving the deposition of submicron droplets formed by nucleation in the main steam flow. This film is accumulated on the stator's pressure side and has a thickness of the order of 10 to 300 $\mu$ m [40]. The film is driven by shear generated by the high steam velocity and it sheds from the trailing edge of the last stator [41]. The disturbance of the water film and its shedding results in film breakdown and the formulation of the well-known film tearing with the water rivulets, as reported in [7, 9, 41, 42]. This is called primary atomization of large droplets and their size strongly depends on the thickness of the stator's trailing edge. These patterns are non-symmetrical large droplets with equivalent Ferret diameter above 100 $\mu$ m, which are then accelerated due to the drag force of the flow and brake into smaller spherical droplets (secondary atomization) [7]. Moore et al. [7] describe a second mechanism on the formation of a film, on the suction side of the stator, from water droplets that are centrifuged from the second to last row of the moving blades. This is shown as well in Figure 1–12 and is a result of the difference between the absolute velocity of droplets compared to steam.

The rivulet patterns that are torn from the film (either suction or pressure side) have been measured mainly in cascade steam tunnels [9, 11]. Li et al. [9] state that the water film is torn from the pressure side of the stator trailing edge in three different modes: (a) film tearing, (b) spindle tearing, and (c) rivulet tearing, as indicated in Figure 1–13. As the rivulets are accelerated downstream of the stator, due to the drag force, they break into smaller sizes during the secondary atomization. The stability of the droplet then depends on the ratio of the aerodynamic pressure force trying to deform it and the surface tension, which tries to keep its shape spherical. This ratio is expressed by the Weber number in Eq.(1-1).

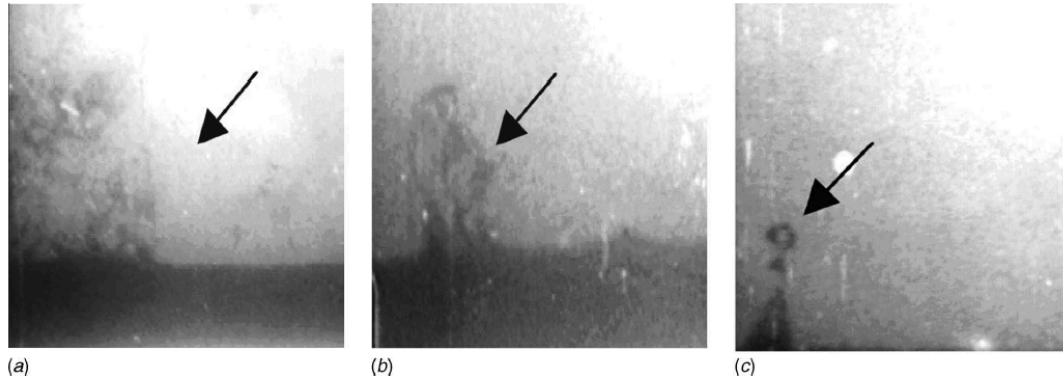


Figure 1–13: Tearing modes of water film according to Li et al. [9]. The three different modes are: (a) film tearing, (b) spindle tearing, and (c) rivulet tearing.

$$We = \frac{D \cdot \rho_f \cdot |\overline{U}_d - \overline{U}_f|^2}{\sigma_d} \quad (1-1)$$

When  $We \ll 20$ , the droplets are spherical and stable in size. As the Weber number increases above the range of 20 to 23, the droplets begin to deform and break up into smaller sizes [17, 43]. Flow field conditions and travel distances affect the final stable droplet size. Thus, short axial gap between stator and rotor blades will not allow the secondary atomization to occur and, as a consequence, the erosion rate will be enhanced. In addition, sharp trailing edges of the stationary blade, generating thin water film are also beneficial. On the other hand, there are only few attempts according to the author's knowledge, to measure the formation of these patterns in the last stages of a steam turbine [37]. The data found in open literature are poor and do not provide solid information to conclude on the growth of the rivulet patterns from real steam turbine measurements.

A more complicated droplet formation mechanism responsible for large droplet sizes is coagulation. Moore and Sieverding in [7] describe this mechanism and support it with experimental data. According to their studies, collision speed, initial diameter, impact angle and static pressure are the main parameters that define the impact efficiency, which results to coalescence. In fact, the collision of two or more droplets obeys statistical laws and therefore probability functions should be implemented to describe this mechanism and improve the understanding.

Independent of the formation mechanism and the resulted droplet size, it should not escape one's attention that the most important parameters for the droplets formation are the static pressure and temperature. Both of these pa-

rameters define the thermodynamic properties of the operating point on the Mollier diagram and therefore the status of the two-phase flow.

### **1.3 State-of-the-art in measuring techniques for wet steam flows**

Turbomachinery flows are highly unsteady, due to interactions between the rotating blades and the stationary stators or vanes. Measurements in this complicated flow field environment require accurate fast response instrumentation to capture the unsteady flow field phenomena. The size of the instruments should be as small as possible to minimize any interaction with the surrounding flow field and the mechanical integrity must be guaranteed for a safe operation. So far, there have been only few attempts to perform time-resolved flow field and droplet measurements in last stages of a LP steam turbine. In the following two paragraphs, a detailed literature review on intrusive probes for measurements in turbomachines is provided.

#### **1.3.1 Fast response pressure measurement systems for wet steam environment**

Pneumatic probes equipped with an air purging system are commonly used in the wet steam environment of the last two stages of LP steam turbines [26, 44-46]. However, they are not suitable to study and quantify the unsteady blade row interactions affecting the aeromechanical performance of the axial-flow turbomachines, due to their low measurement bandwidth [44]. In addition, the purging process, which is required to clean the pressure taps of these probes from the accumulated water, increases significantly the measurement time and therefore the cost of a measurement campaign. Experimental studies of the unsteady aerodynamic excitation of low-pressure steam blades have been conducted in down-scaled air models, as reported in [35]. Nevertheless the literature review in unsteady flow field measurements reveals the lack of instrumentation in aerodynamic probes in the real wet steam environment.

Most of the researchers have performed unsteady pressure measurements with flush mounted pressure sensors on the stator or the outer wall of the flowpath of LP steam turbine. In that regard, Shibukawa et al. [16] investigated the vibration stress behavior and the unsteady pressure under flash back conditions in a subscale steam turbine test model, using fast response pressure sensors mounted on turbine's wall and on rotating blades. Segawa et al. [31] used flush mounted pressure transducers, in order to study the flow field under various operating conditions in a four stage low-pressure steam turbine. The pressure sensors were mounted on the turbine sidewalls and on the stators' surface.

According the current literature survey, only one attempt could be found in the open literature dealing with time-resolved flow field measurements in the flow path of the last two stages of LP steam turbines with probes by Gerschütz et al. [32]. In this work the authors manufactured a fast response total pressure probe for measurements in wet steam. Two different probes

were used in the measurements, as shown in Figure 1–14. Both consist of two pneumatic pressure taps for balancing in flow direction and one total pressure tap equipped with Kulite® sensor for unsteady total pressure measurements. The probes can operate up to 275°C and have a tip diameter of 6mm. However, this type of probe only provides the unsteady total pressure field in areas where the flow field can be considered quasi two-dimensional. A detailed FFT analysis is described in their results at the inlet and exit of the last stage, as well as downstream of the stator in a scaled steam turbine test facility.

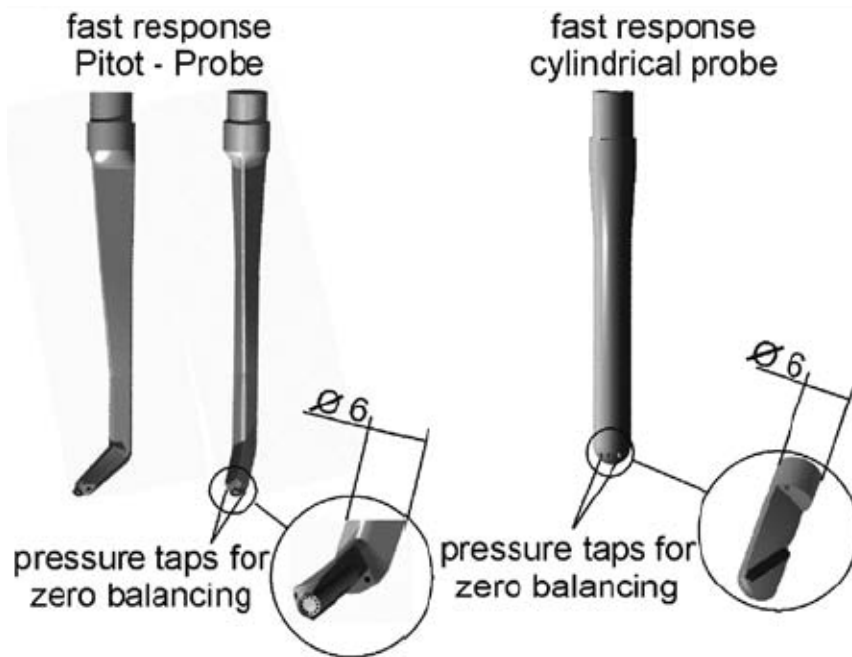


Figure 1–14: Single sensor fast response probe by Gerschütz et al. [32].

### 1.3.2 Optical probes for droplet and particle measurements

Optical techniques are extensively used in droplet and particle measurements in many scientific fields besides turbomachinery [43]. In atmospheric research the first attempts are reported in the 1970's. The researchers present an effort on measuring droplet sizes in the range of 0.1 up 1000 $\mu\text{m}$  and droplet concentrations up 500 $\text{cm}^{-3}$  with optical probes mounted on test flight aircrafts (see Figure 1–15), in order to improve the weather models [47-52]. These probes are utilizing mainly light scattering and imaging techniques but their large size (Casing diameter > 300mm) and specific design geometry are the primary constraints for any type of turbomachinery application. The measurement of droplet size distribution in two-phase flows is of high interest in combustion science, dusty plasma physics and medicine science as well. In order to understand the factors that govern droplet size distribution and motion, different types of instruments have been developed in these fields and presented in [53-55] but never in a compact size of a stem miniature probe type.



Figure 1–15: Optical probes used in atmospheric research mounted on aircraft's fuselage and wing [56].

### 1.3.2.1 Fog water droplet measurements for steam turbine applications

Regarding droplet measurements for turbomachinery applications, there is a significant number of publications dealing with the development of different probes to measure droplets' size and concentration in the stationary frame of the machine. In this area, some of the first attempts were made by Walters et al. [57] and Tatsuno et al. [58]. Tatsuno et al. developed an optical fiber probe to measure water droplets in a steam turbine using the forward scattering method. The probe tip diameter was 20mm and the detectable droplet size range from 0.1 to 5 $\mu\text{m}$ . In measurements performed in a 10MW steam turbine they have reported droplet diameters between 0.2 $\mu\text{m}$  and 1.0 $\mu\text{m}$  at the exit of the last stage. Young et al. [8], measured coarse water flow rates in the last stage of a steam turbine using a custom designed water absorbent probe. Walters [59] describes a light extinction probe, which uses a xenon lamp and spectrophotometer, in order to measure the spectral transmission of wet steam. The probe diameter is 25.4mm and the spectral range of the system is 300 to 1100nm, resolving droplet diameters 0.2 up to 1 $\mu\text{m}$ . The light extinction method is also used in references [46, 60] for particle measurements mainly in steam turbines, in this case for liquid droplets with diameters up to 10 $\mu\text{m}$ . The probe tip diameters are limited to 20mm. A different approach but still for fine droplet sizing ( $d < 10\mu\text{m}$ ) is by Kerckel et al. [61]. The author's developed an optical system using a multiple-line argon laser, in order to measure the size and velocity of water droplets in the last stage of a LP turbine without perturbing the flow. By splitting the laser beam into two through a converging lens, an interference fringe pattern is created forming the probe's measurement sample volume. The observing lenses are collecting light in the backscatter region through a single view port in the machine casing. In their results, the authors report droplet diameters up to 3.6 $\mu\text{m}$  without specifying the exact measurement location in the machine.

A number of recent developments have led to a combination of optical and pneumatic probes within one system for droplet measurements in steam turbines as shown in Figure 1–16. These probes combine a pneumatic part for time-averaged pressure measurements and an optical part for wetness mass fraction measurements in the last stages. Schatz et al. [62] also developed a probe with a diameter of 10mm and wedge geometry for measurements independent of Reynolds number. In addition, this probe incorporates two pressure taps, in order to cover the wide range of pitch angles encountered in the flow through the last stages of LP turbines, due to the high flare angles.

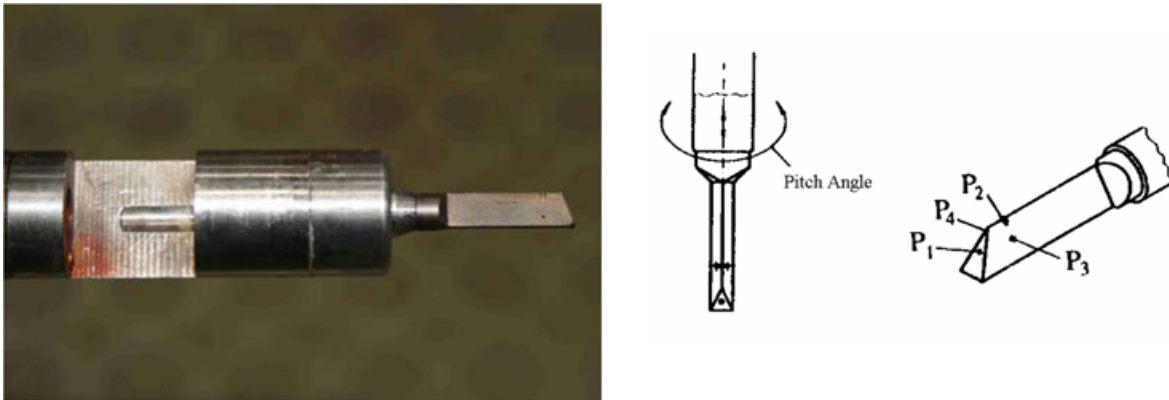


Figure 1–16: The tip from a combined optical and pneumatic probe by Wu et al. [63].

### 1.3.2.2 Coarse water droplet measurements for steam turbine applications

As it has been described so far, the majority of the developed probes for steam turbine applications have a minimum tip diameter of 10mm and a detectable droplet size up to  $10\mu\text{m}$ , mainly implementing time averaging techniques such as light extinction. These probes are suitable for fog droplet measurements and therefore erosion phenomena cannot be fully studied. Cai et al. in [11] have developed an integrated probe system for coarse water droplet measurements up to  $400\mu\text{m}$ . As shown in Figure 1–17, the system consists of a fine droplet measurement subsystem using the light extinction technique and a coarse droplet measurement subsystem using the forward light scattering technique. The probe has a tip diameter of 20mm and it incorporates as well a pneumatic part for the time averaged flow field measurements. In their results at the last stage of a steam turbine, the authors present the droplet trajectories and speeds under various operating conditions. They report that the large and small droplets impact the leading edge at the suction side of the rotor blades, respectively, causing significant erosion. A noteworthy work from the same research group on probe development for coarse droplet measurements with imaging technique is by Xueliang et al. [64]. In this report, the authors present a video-probe system capable to take images of coarse water droplets ( $D_p > 10\mu\text{m}$ ), in order to measure the diameter and velocity. The probe is calibrated using standard monodispersed glass beads up to  $77.2\mu\text{m}$  in diame-

ter, as well as in a spray environment with a known concentration and diameter. The main drawbacks of the last two approaches are the relative big size of the probe tips ( $D_p > 20\text{mm}$ ) and the low measurement bandwidth on the aerodynamic part constraining the measurements to a time averaged flow field analysis.

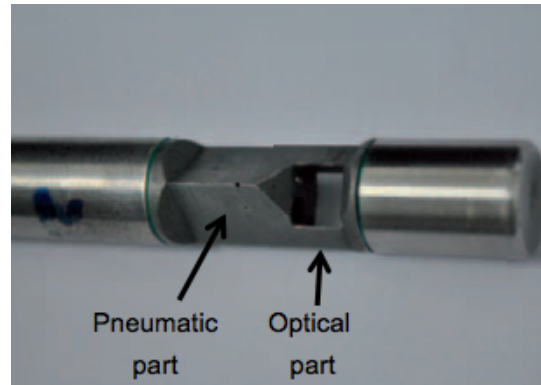


Figure 1–17: Photograph of the combined optical and pneumatic probe by Cai et al. [11].

## 1.4 Research objectives

Turbomachines and in particular steam turbines, are widely used in power production, providing the world with more than 60% of the entire generated electrical power [65]. However, in order to stay competitive in the face of the growing renewable energy market, they require operational flexibility and power output augmentation, due to the continuous increase in energy demand. Considering the complicated steam turbine aerodynamics, with highly three dimensional and unsteady flow field together with water droplets from condensation, the advancements are not trivial. Consequently, in order to improve the current efficiency (~60% in combined cycle) and reliability of these machines, the unsteady flow mechanisms responsible for the aerodynamic losses have to be measured and understood. The correlation to the various engine's operating points is mandatory to investigate the part load conditions. Additionally, coarse water droplet measurements are vital to understand the formation mechanisms, responsible for blade erosion, and improve the mechanical integrity of the last stage long blades.

Until now, the lack of time resolved experimental data makes the analysis hardly feasible. Therefore, understanding the unsteady flow environment is only possible through the development of fast response instrumentation suitable for time resolved measurements in the wet steam conditions. The bi-phasic flow regime of gaseous and wet steam present in the last stages of LP steam turbines generates a very challenging environment with transonic steam flow velocities, water droplets ranging from 0.1 $\mu\text{m}$  up to 100 $\mu\text{m}$  in diameter, as well as absolute static pressure conditions as low as 50mbar. Thus, the crucial features of the probes are the robust design to withstand the harsh conditions, the miniature size to minimize blockage effects and maximize spatial resolution, the high accuracy and finally the high measurement bandwidth due to elevated flow speed (340m/s) and blade passing frequency (8.6kHz).

The above will enable time resolved measurements in the last stages of LP steam turbines and will allow the understanding of the complicated flow phenomena in order to achieve the following research objectives of the current doctoral thesis:

For the flow field measurements,

- Assess the aerodynamic performance at reduced mass flow operation (part load) and quantify flow unsteadiness responsible for high cycle fatigue of the last rotor blades
- Understand the unsteady stator rotor interaction of the top 30% span with rotor inlet supersonic relative flow conditions (~780m/s tip speed), and perform a sensitivity analysis of the aerodynamic losses induced by the presence of the attached bow shock at the last rotor leading edge



For the coarse droplet measurements,

- Investigate the evolution of the water film formation and brake up process on the stator's pressure side for design and part load conditions
- Quantify and analyze the unsteady coarse water droplet size and concentration ( $>10\mu\text{m}$  in diameter) distribution at the stator exit responsible for the rotor blade erosion in the last stage of LP steam turbines

## 1.5 Thesis outline

The chapters of this thesis are structured as follows. The first chapter is the motivation and the following two chapters describe the development of two new instruments suitable for measurements in wet steam conditions. Chapters four, five and six present the measurement campaigns where the probes were tested and chapter seven provides the summary and conclusions of the current research work.

- **Chapter 1** presents the motivation of the thesis and the theoretical background on the flow field phenomena together with the droplet formation mechanisms in the last stages of low-pressure steam turbines. The state of the art in measuring techniques for wet steam conditions is also discussed.
- **Chapter 2** describes the design and development of a fast response aerodynamic probe for unsteady wet steam flow field measurements (FRAP-HTH). The operating principle, calibration procedure and uncertainty analysis are also presented. The final paragraph of this chapter addresses the challenges of processing wet steam data and presents the specific data reduction algorithm developed for wet steam flows.
- **Chapter 3** introduces a newly developed optical backscatter probe (FRAP-OB) for coarse water droplet diameter and speed measurements in turbomachines. The calibration of the novel probe is performed with a droplet generator capable of producing monodispersed water droplets. In addition, the probe is calibrated for droplet speed measurements in the same calibration facility. A detailed uncertainty analysis is presented in the same chapter. Finally, a multi step post-processing algorithm for the droplet detection is described. The effort to improve the signal to noise ratio of the optical backscatter probe in order to increase the accuracy is presented as well in the same paragraph of this chapter.
- **Chapter 4** details measurements performed in a one-and-1/2-stage axial turbine test facility equipped with a spray generator. In this campaign the optical backscatter probe (FRAP-OB) was used. Two different operating conditions were measured at two different axial locations downstream of the first stator's trailing edge. The probe has proven its ability to perform accurate and reliable measurements under real engine conditions.
- **Chapter 5** presents unsteady wet steam flow field measurements with the FRAP-HTH probe in the last stage of a low-pressure steam turbine. The measurements were conducted in a scaled steam turbine test facility in Japan. The test facility and the operating conditions are described in the same chapter. Three different operating points including two reduced massflow conditions, are compared

and a detailed analysis of the unsteady flow structures under various blade loads and wetness mass fractions is presented. The results demonstrate the ability of the newly developed FRAP-HTH probe to provide reliable flow field measurements at the last stages of LP steam turbines under increased wetness mass flow conditions.

- **Chapter 6** presents a unique measurement campaign, that focuses at the top 30% of the stator exit, in the last stage of a LP steam turbine with supersonic airfoils near the blade tip. The measurements were conducted in a scaled steam turbine test facility in Japan. The test facility and the various operating conditions are described in the chapter. Flow field and coarse water droplet measurements were performed with the FRAP-HTH and FRAP-OB probe respectively. The interaction of the rotor leading edge bow shock with the upstream stator is discussed. Time resolved coarse water droplet's measurements are shown for a first time in the wet steam environment of LP steam turbine
- **Chapter 7** summarizes and concludes the outcome of this research work. Suggestions for future work in order to improve the instrumentation, which was developed throughout the current work are provided as well.

## 2 Fast response aerodynamic probe for flow field wet steam measurements (FRAP-HTH)

### 2.1 Probe development

#### 2.1.1 The FRAP-HTH probe

The design and operation of the new fast response probe for wet steam flow field measurements are based on the developments made over the past two decades at the Laboratory for Energy Conversion at ETH Zürich [66-70]. In particular, the new FRAP-HTH probe is an improved version of FRAP-HT probe developed by Lenherr [69, 71] and presented in Figure 2-1.

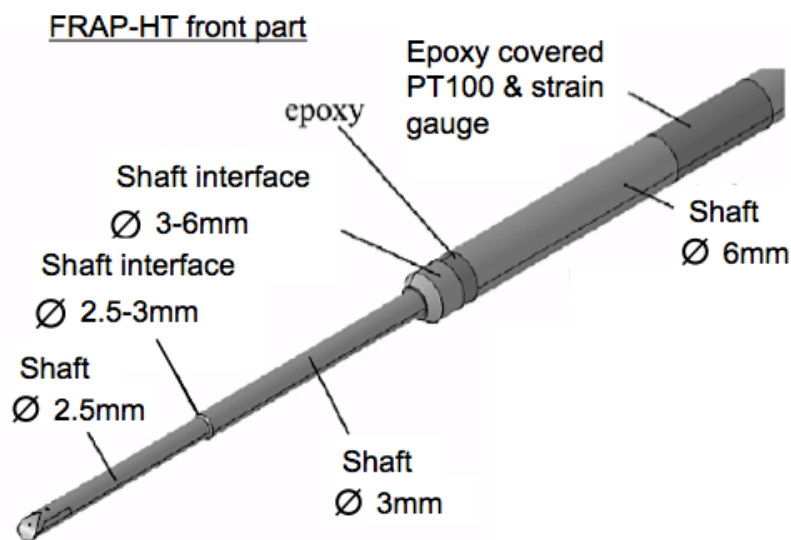


Figure 2-1: Front part and tip schematics of the FRAP-HT probe developed by Lenherr [71].

As indicated in Figure 2-1, the probe consists of two pressure taps one for yaw angle sensitivity (yaw sensor) and one for pitch angle sensitivity (pitch sensor). It has a tip diameter of 2.5mm and overall length of about 0.6m in order to access the flow path inside the machine. The probe utilizes two miniature piezoresistive pressure transducers that are used to measure the flow angles as well as the total and static pressure. The silicon-based piezoresistive pressure sensors operate in a Wheatstone bridge configuration and they are used in a differential pressure mode with a linear pressure range up to 1200mbar. Both sensors are sensitive to pressure and temperature. In order to operate the sensors in a differential mode, the probe tip is pressurized with a reference pressure that is controlled by a high precision pressure controller (PACE 5000). In addition, the two pressure taps are equipped with a shield for protecting the miniature piezoresistive sensors from direct particle impacts. The probe material is stainless steel and it is manufactured with the electro discharge machining (EDM) process.

The standard probe technology requires specific redesign in order to perform time resolved measurements in wet steam flows. The two main challenges are: the water droplets that could possibly clog the probe pressure taps and the high flare angle on the LP steam turbine which induces a large flow pitch angle component. In order to operate the probe with unclogged pressure taps and prevent any water contamination when operated in steam, the tip of the probe is heated few degrees (5 to 10°C) above the flow saturation temperature  $T_{sat}$  according to Eq. (2-1).

$$T_{tip} = T_{sat} + \Delta T \quad (2-1)$$

This is shown as well in Figure 2-2, where the probe tip temperature allows a clean environment locally (pressure taps region) and therefore the fast piezoresistive sensors are functional. In addition, this allows the pressure cavity between the probe surface and the sensor's membrane to remain clean from water avoiding any signal corruption.

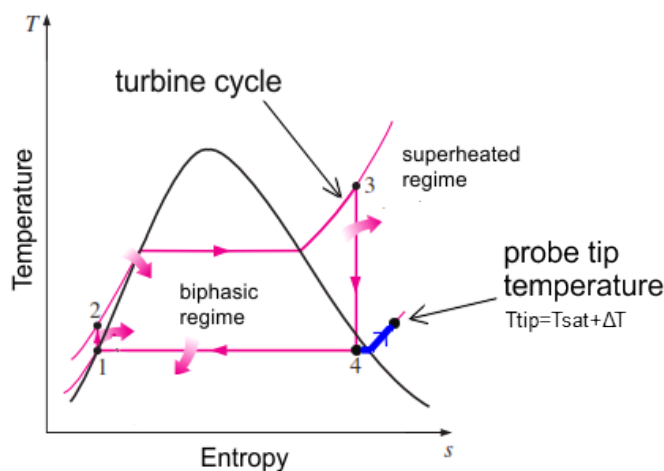


Figure 2-2: Temperature-entropy diagram for a steam turbine operating cycle and the respective probe tip operating temperature.

The FRAP-HTH probe tip as it was used in all measurement campaigns of this thesis is presented in Figure 2-3. A high power density heater (B), which is described in the following paragraphs, is installed at the probe tip (A) on the 2.5mm shaft,  $4.5 \times D_p$  away for the yaw pressure tap. The tip is heated through the miniature heater, which is fed with current at constant voltage. In addition, the probe tip temperature is controlled using a closed-loop PID regulator as depicted in Figure 2-4. The tuning of the PID controller was performed through the empirical method of Ziegler-Nichols [72] in wet steam for various spanwise locations, to cope with the variation of convective heat transfer coefficient induced across the flow path. The target temperature ( $T_{tip\ set}$ ) at the probe tip is achieved by varying the heating power duty cycle based on the actual temperature ( $T_{tip\ measured}$ ), which is measured with the piezoresistive pressure sensors located inside the tip.

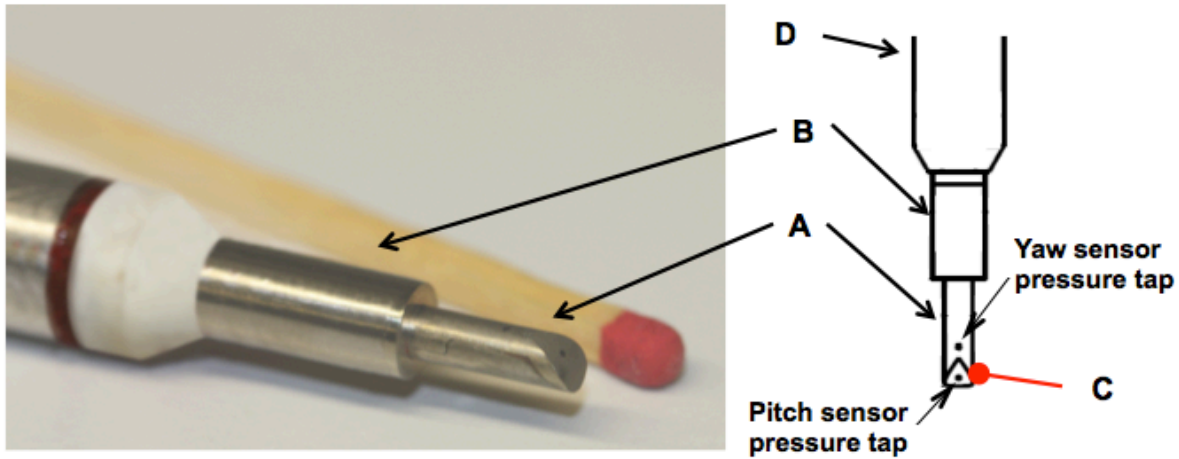


Figure 2-3: FRAP-HTH probe tip schematic. A: Probe tip ( $D_p=2.5\text{mm}$ ), B: Heating elements ( $D_{\text{Heating-Spot}}=4.7\text{mm}$ ), C: Tip temperature monitoring ( $T_{\text{tip}}$ ), D: 8mm shaft.

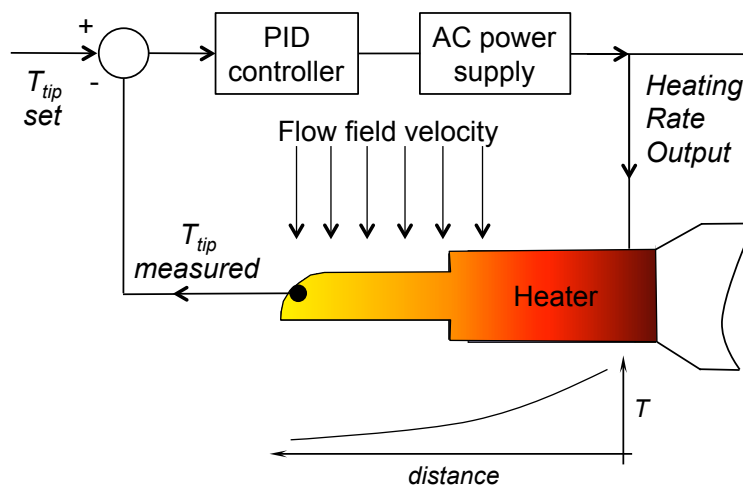


Figure 2-4: PID block diagram for FRAP-HTH's miniature heater control.

### 2.1.2 Miniature cartridge heater description

The performance of the miniature cartridge heater is linked to the temperature overheating achieved at the proximity of the two pressure taps as they are indicated in Figure 2-1. The heater consists of a small heating wire with high specific resistance. The heating wire is installed in a double helix spiral and fed with an AC current at constant voltage. The double helix installation reduces the noise levels of the FRAP-HTH signal since the two running currents of the coil cancel each other. The high thermal conductivity of the ceramic substrate enhances the conduction to the probe shaft. A ceramic low conductivity insulates electrically the heating wire from the surrounding steam and reduces the heat transfer losses due to convection. Finally a stainless steel cylinder is installed on top of the overall assembly to ensure the ro-

bustness of the overall structure. With this miniature configuration an overall installed power of 61W/cm<sup>2</sup> was achieved. The heater has an outer diameter of 4.7mm and an inner diameter of 2.5mm. It is integrated to the probe tip with tight tolerances in order to improve the heat transfer conductivity to the probe's pressure taps. Two thermocouples are installed as well to monitor the actual temperature of the heater.

Initial performance tests were conducted with air in Freejet facility (see Figure 2-11) under representative heat transfer conditions from the last stages of a LP steam turbine. The calculated Nusselt number for the steam environment was based on the Churchill & Bernstein relationship, Eq.(2-2).

$$\overline{Nu}_D = 0.3 + \frac{0.62 Re^{1/2} Pr^{1/3}}{\left[1 + \frac{0.4^{2/3}}{Pr}\right]^{1/4}} \left[1 + \frac{Re^{5/8}}{282'000}\right]^{4/5} \quad (2-2)$$

The resulting average Nusselt number for the flow conditions at exit of the last stage was calculated to  $\overline{Nu}_D = 50$ . With the Nusselt number analogy the representative flow velocity in air was calculated to be Ma=0.17. Nevertheless this is an average value since the turbulence intensity of the flow as well as the wetness mass fraction will affect significantly the actual value of the Nusselt number. In addition, all calculations were performed for zero degrees flow pitch angle, which implies that the velocity vector is perpendicular to the probe axis. When the flow has a pitch component relative to the probe, the convective heat transfer coefficient alters and as a consequence the thermal gradients around the probe will change.

#### 2.1.2.1 Experimental quantification of heating power loss across the probe tip

Two different configurations were tested, in order to study the effect of the heater's axial location on the achieved probe tip temperature. In the first design, annotated with A in Figure 2-5, the heater (green dot) is installed 10 probe diameters from the pressure taps. In the second design, annotated with B, the heater is installed 4.5 probe diameters from the probe tip. Figure 2-5 shows the temperature overhead ( $\Delta T$  from the ambient temperature) of the probe tip as a function of the temperature overhead at the heating spot where the miniature heater was installed. It should be mentioned that the main constrain is the limit of 250°C at the heating spot. This is the maximum temperature limit of the epoxy glue that is used in the probe assembly under which a continuous operation is guaranteed and thus the mechanical integrity of the probe. In all cases there is excess in the installed heating power and the heater is fed continuously with current until the temperature at the heating spot reaches 180°C. The rear part of the probe is thermally insulated with an interface from the front part and a copper rod is installed inside the probe shaft to enhance the conduction from the heating spot (green dot) to the pressure taps

(red dot) for both cases. A margin of 70°C from the actual limit of 250°C is kept in all measurements as a safety factor. As presented in Figure 2–5, the temperature overheat at the probe tip location (red dot) is 35°C and 125°C for case A and B respectively when  $\Delta T_{\text{Heating-Spot}}=180^\circ\text{C}$  for  $\text{Ma}=0.17$  ( $\text{Nu}_D=50$ ).

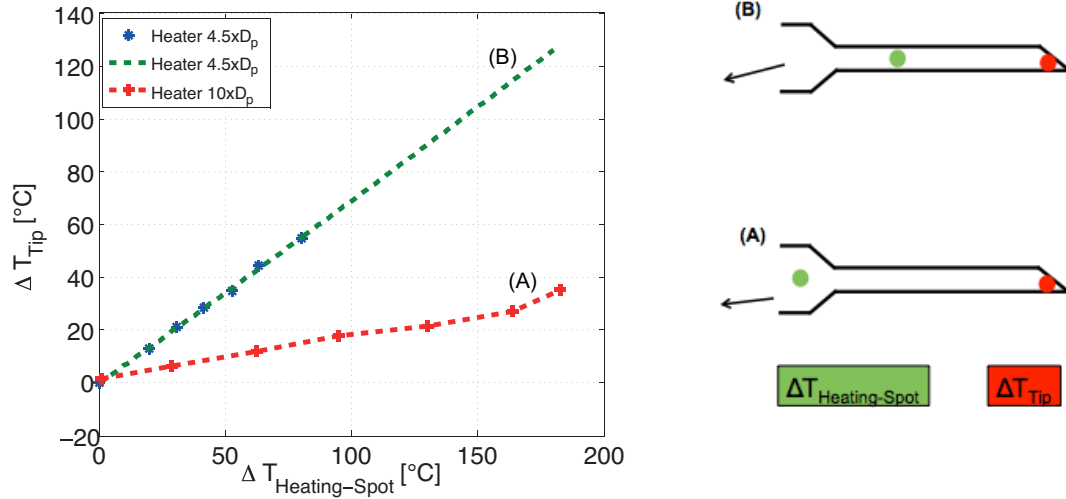


Figure 2–5: Tip temperature overheat for two different heater locations. Case A: 10xD<sub>p</sub> from the pressure taps, Case B: 4.5xD<sub>p</sub> from the pressure taps.

Since the material of the probe and the boundary conditions are the same for both cases, one can see the magnitude of heat losses along the probe shaft with respect to the heater location. The miniature geometry of the probe tip ( $D_p=2.5\text{mm}$ ) in combination with the probe's low thermal conductivity result in high heat losses due to convective heat transfer from the surrounding flow with  $\text{Ma}=0.17$ . An overall heat balance analysis in the axial and radial direction is described in [73] for the B case of Figure 2–5. Results have shown, that 48% of the total heat losses are due to convective heat transfer to the flow, 22% of the losses are due to conduction to the rear part of the probe shaft and only 30% of the total heating power is provided to the probe tip through conduction.

### 2.1.2.2 *In situ validation of heater's performance*

In order to improve the heating performance of the FRAP-HTH probe two major modifications were made. The probe tip material of the 2.5mm shaft (see Figure 2–1) was replaced by an alloy with high thermal conductivity and a hydrophobic coating was applied on the heater part as well as on the 2.5mm shaft in order to reduce the residence time of the condensed water on the probe's surface. The final version of the probe was tested in a low-pressure steam turbine. The facility is described in paragraph 5.1 and the tested condition was operating point three, OP-3 (see Table 9, §5.1). Downstream of the last rotor, the average wetness mass fraction is 8% and the absolute Mach number 0.5. The vacuum conditions generate a static pressure field, which is roughly 8% of the ambient condition.



The temperature results from the pressure sensors as well as from the heater's thermocouple are shown in Figure 2–6.a. In the same plot the measured flow saturation temperature is plotted with blue color. During these measurements the probe demonstrated its ability to overheat the yaw and pitch sensors above the flow saturation temperature (see Figure 2–2) for the entire blade span as presented in Figure 2–6.a. Results have shown that the actual temperature of the heater is on an average 80°C with the maximum value of 110°C at 35% span. The actual heating rate in this case is roughly 20% of the maximum installed power. As shown in Figure 2–6.b below 60% span the temperature of the sensors drops by 4°C and 9°C for the yaw and pitch sensor respectively. The actual temperature of the heater increases from 75°C to its maximum at 110°C. This performance is most probably related to high turbulence intensity in combination with high wetness mass fraction resulting to greater convective heat losses. Nevertheless both sensors remain above the flow saturation temperature considering the uncertainty of  $\pm 0.8^\circ\text{C}$  at  $\text{Ma}=0.5$ .

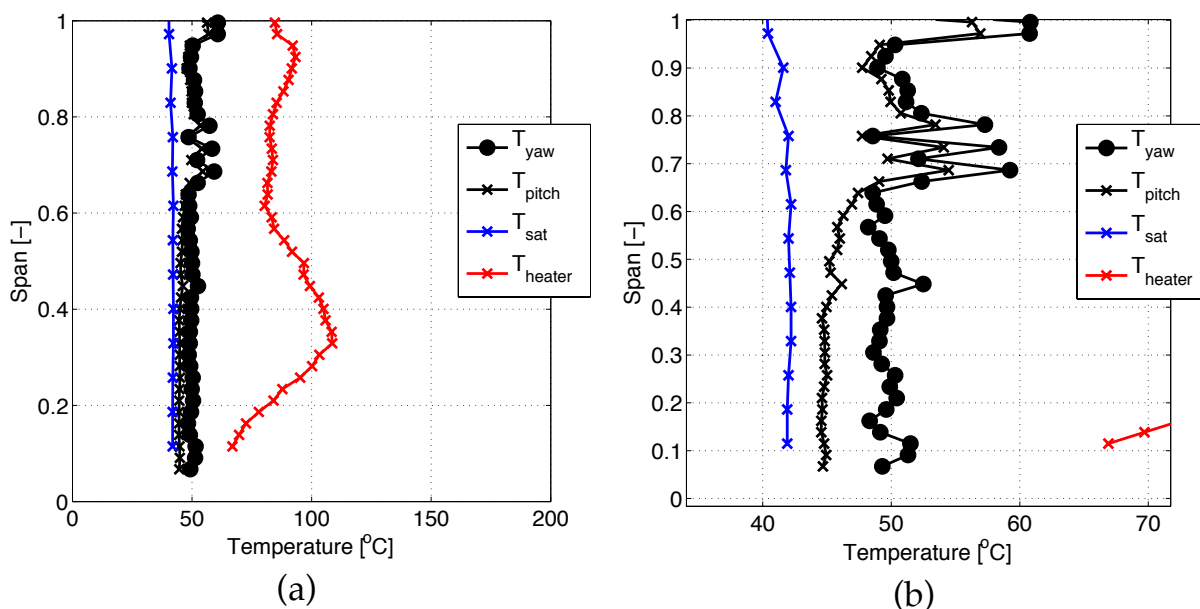


Figure 2–6: Actual temperature of yaw and pitch sensors as well as heater temperature along the blade span for the exit of the last stage of 7MW LP steam turbine with an average wetness mass fraction of 8% for the final version of FRAP-HTH (a). Same results zoomed in for 30 to 72°C (b).

### 2.1.3 Pressure sensors calibration

The working principle of the pressure sensors is a Wheatstone bridge, which is fed with a constant current source of 1mA. As shown in Figure 2–7.a, the excitation voltage,  $U_e$  depends primarily on the membrane temperature and the signal output voltage,  $U$  is primarily proportional to the differential pressure across the membrane. The signal-conditioning unit placed on the rear

part of the probe shaft amplifies the pressure voltage signal by a factor of 100 to enable a high signal-to-noise ratio.

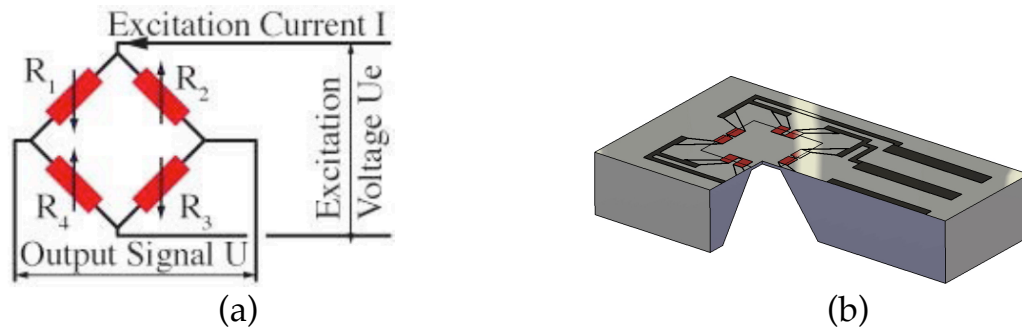


Figure 2-7: Wheatstone bridge schematic (a) and silicon pressure transducer with a cross-section at the diaphragm region(b).

The calibration procedure described by Kupferschmied et al. in [74] is applied to derive a sensor calibration model and to obtain the relationship between the output voltage, pressure and temperature. For the current work, the probe was calibrated within a relative pressure range of 0 to 1050mbar and temperature range from 20 to 120°C. Both ranges define a calibration matrix with corresponding voltage  $U(P,T)$  and  $U_e(P,T)$  as a function of pressure  $P$  and temperature  $T$ . Figure 2-8 shows the sensor calibration results of the FRAP-HTH, where the  $U(P)$  and  $U_e(T)$  are plotted as a function of pressure and temperature for the yaw pressure sensor. The pitch sensor calibration has the same curves with a small difference in sensitivity <1%. This results in a mean pressure sensitivity of 3.8mV/mbar for both sensors and a mean temperature sensitivity of 2.8mV/°C. Nevertheless, during the measurements with the probe each sensor has its own calibration protocol in order to increase the accuracy of the results to the maximum.

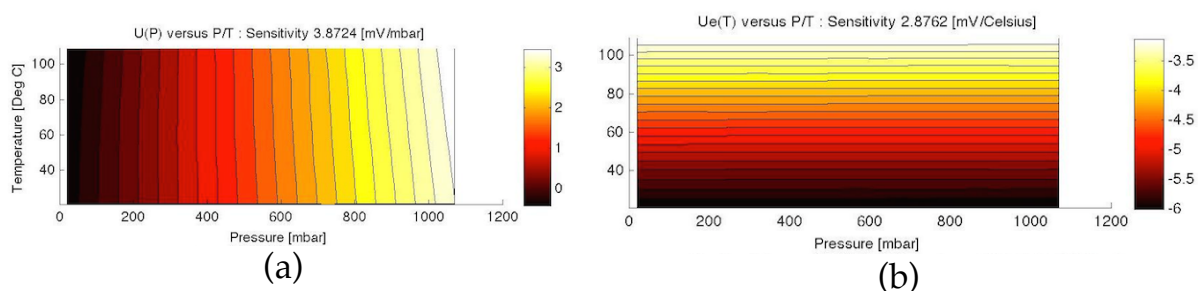


Figure 2-8: Calibration curve in volts for yaw sensor, (a) is the  $U$  output and (b) is the  $U_e$  output.

#### 2.1.4 Virtual 6 sensor mode

The large flare angles present at the last stages of LP steam turbines require a special operation of the new FRAP-HTH probe. Typical tip wall flare angles range from 30° to 40°. Additionally, the probe is inserted 5° to 10° from its vertical axis since the stator trailing edges at the last stages varying along

the span (see Figure 6–1.b). Thus, the relative flow pitch angle to the probe is even larger, due to the insertion angle. As shown in Figure 2–9, in order to enable measurements in such high flow pitch angles relative to the probe, the probe is operated in a virtual six-sensor mode. This measurement concept is an extension of the virtual 4-sensor measurement concept as described in [67, 69], which only allows flow field measurements up to approximately  $35^\circ$  of pitch angle, due to the separation of the flow on the leeward side of the probe.

The schematic in Figure 2–9 shows the virtual 6-sensor mode measurement concept using the current probe that is equipped with two sensors, the yaw pressure sensor and pitch pressure sensor as indicated in Figure 2–3. The yaw pressure sensor is used to measure the actual tap pressures ( $p_1, p_2, p_3$ ) in three consecutive steps. This is achieved by rotating the probe along its axis at three different set angles  $0^\circ, -42^\circ, +42^\circ$  respectively. The pitch pressure sensor is used to measure the actual tap pressures  $p_4, p_5$  and  $p_6$ . The pressure  $p_4$  is recorded when the roll set angle is equal to  $0^\circ$ , whereas  $p_5$  and  $p_6$  pressures are measured at  $-42^\circ$  and  $+42^\circ$  roll angles respectively. Out of this procedure a set of 6 independent pressures from  $p_1$  to  $p_6$  is obtained. These pressure values are then used for the definition of the aerodynamic flow coefficients for flow yaw and pitch angles, static and total pressure as well as the absolute Mach number of the flow, as shown in Table 1.

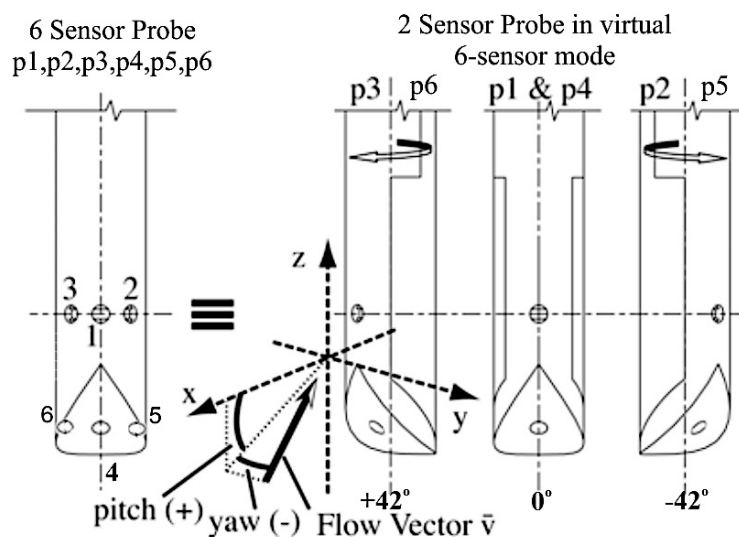


Figure 2–9: Virtual 6-Hole measurement concept with a 2-Hole Probe.

As presented in Table 1, two sets of aerodynamic calibration coefficients are defined according to the actual value of the flow pitch angle relative to the probe tip. The respective flow angle validity range of the two sets of aerodynamic calibration coefficient is plotted in Figure 2–10 for  $Ma=0.7$ . When the measured pressure value of the yaw sensor ( $p_1$ ) is larger than the pressure value of the pitch sensor ( $p_4$ ), the probe is operated using the calibration coefficients defined for sector 1. For this case the aerodynamic coefficients are

standard as described by [67, 69] and summarized in Table 1. However when the measured value of the actual pressure  $p_4$  is larger than the actual pressure  $p_1$ , the probe is operated using the second set of calibration coefficients defined for sector 2. As shown in Figure 2–10, for the new FRAP-HTH probe shape geometry, this condition is fulfilled when the flow pitch angle is equal to  $42^\circ$  for the yaw incidence angle of  $0^\circ$  relative to the probe. The change of the calibration coefficients at the edges of the yaw angle calibration range occurs at  $40^\circ$  pitch.

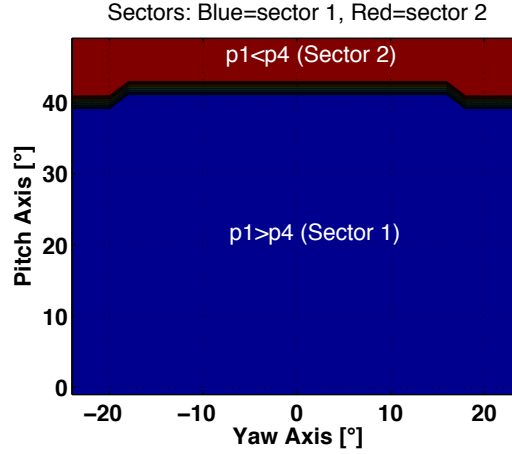


Figure 2–10: FRAP-HTH extended calibration section's schematic for  $Ma=0.7$ .

In the post-processing code each measurement is checked independently. The first set of aerodynamic coefficients is used when  $P_1 \geq P_4$  (sector 1) is fulfilled in order to derive the yaw, pitch, total and static pressures and the second set of aerodynamic coefficients is used when  $P_1 < P_4$  (sector 2).

Table 1: Extended aerodynamic calibration coefficients for FRAP-HTH probe.

Sector 1 when $P_1 \geq P_4$ (Blue sector)	Sector 2 when $P_4 > P_1$ (Red sector)
$K_\phi = \frac{P_2 - P_3}{P_1 - \frac{(P_2 + P_3)}{2}}$	$K_\phi = \frac{P_5 - P_6}{P_4 - \frac{(P_5 + P_6)}{2}}$
$K_\gamma = \frac{P_1 - P_4}{P_1 - \frac{(P_2 + P_3)}{2}}$	$K_\gamma = \frac{P_4 - P_1}{P_4 - \frac{(P_5 + P_6)}{2}}$
$K_t = \frac{P_t - P_1}{P_1 - \frac{(P_2 + P_3)}{2}}$	$K_t = \frac{P_t - P_4}{P_4 - \frac{(P_5 + P_6)}{2}}$
$K_s = \frac{P_t - P_s}{P_1 - \frac{(P_2 + P_3)}{2}}$	$K_s = \frac{P_t - P_s}{P_4 - \frac{(P_5 + P_6)}{2}}$

### 2.1.5 Aerodynamic calibration

The FRAP-HTH probe is calibrated in freejet calibration facility of the Laboratory for Energy Conversion at ETH Zurich. The calibration facility is shown in Figure 2–11 with the probe installed on a three axis-traversing unit with linear motors. The facility allows all six degrees of freedom between the probe and the airflow. The jet exits from a convergent nozzle of 100mm diameter and the probe tip is located 100mm roughly downstream. The head of the probe is translated relative to the fixed jet by tilting and yawing the probe shaft. The flow temperature of the jet is kept stable at 303K ( $\pm 0.3$ K) via a heat exchanger located at the exit of the compressor. All flow quantities from the freejet facility are known and used for the relation of the pressures with the flow angles, total and static pressures, Mach number and flow temperature.

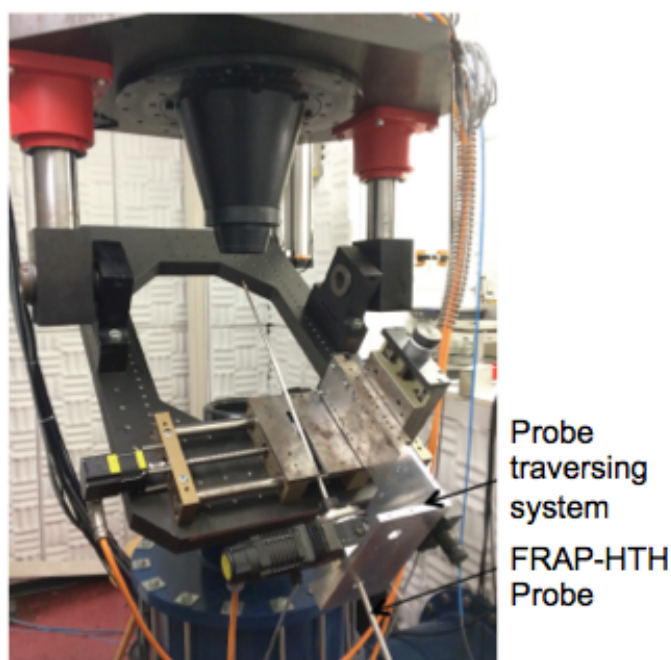


Figure 2–11: Extended aerodynamic probe calibration at Freejet facility.

As described in section 2.1.4, the probe is calibrated in a virtual 6-sensor mode using the 2 sets of aerodynamic calibration coefficients listed in Table 1, where  $K_\phi$ ,  $K_\gamma$ ,  $K_t$  and  $K_s$  are respectively the flow yaw angle ( $\phi$ ), flow pitch angle ( $\gamma$ ) and total and static pressures ( $P_t$  and  $P_s$ ) aerocalibration coefficients. As presented in Table 1, the first or the second set of coefficients is chosen according to the highest-pressure value measured between the yaw pressure sensor in p1 position and the pitch pressure sensor in p4 position. The polynomial curve-fit method of Gallington [75] is applied to the aerodynamic calibration data. In particular, the aerodynamic calibration model is based on a parametric approach and the flow yaw ( $\phi$ ) and pitch ( $\gamma$ ) angles are derived from  $K_\phi$ ,  $K_\gamma$  by an inverse calculation of the Eq.(2-3) and Eq.(2-4) as suggested in [76].

$$\phi = \sum_{i=0}^n \sum_{j=0}^m a_{ij\phi} K_{\phi}^i K_{\gamma}^j \quad (2-3)$$

$$\gamma = \sum_{i=0}^n \sum_{j=0}^m a_{ij\gamma} K_{\phi}^i K_{\gamma}^j \quad (2-4)$$

During the calibration procedure the flow yaw and pitch angles ( $\phi$ ,  $\gamma$ ) as well as the calibration coefficients  $K_{\phi}$ ,  $K_{\gamma}$  are known and the polynomial coefficients  $a_{ij\phi}$  and  $a_{ij\gamma}$  are derived for the solution of this set of linear equations using a least square approximation. The same approach is followed for the total and static pressures' polynomial coefficients using Eq.(2-5) and Eq.(2-6). Since the coefficients  $K_{\phi}$ ,  $K_{\gamma}$  and the flow angles  $\phi$  and  $\gamma$  are known, the polynomial coefficients  $a_{ijt}$  and  $a_{ijs}$  are derived from the solution of these two linear equations,

$$K_t = \sum_{i=0}^n \sum_{j=0}^m a_{ijt} \phi^i \gamma^j \quad (2-5)$$

$$K_s = \sum_{i=0}^n \sum_{j=0}^m a_{ijs} \phi^i \gamma^j \quad (2-6)$$

In an unknown flow field the derived calibration polynomial coefficient vectors are used for the evaluation of the unknown flow quantities from the measured set of the six pressures from p1 to p6 at a given probe measurement location.

For the current work the FRAP-HTH probe was calibrated for several Mach numbers from 0.2 up to 0.8 with a step of 0.1. For compactness of the thesis, only the calibration results for Ma=0.7 are presented and analyzed in the current section. Figure 2–12 and Figure 2–13 show the resulting spatial distribution of the calibration coefficients for the first (sector 1) and second sector (sector 2) respectively, covering an overall range of  $\pm 24^\circ$  in yaw angle and of  $-1^\circ$  to  $+49^\circ$  in pitch angle. Each figure set shows the four independent calibration coefficients as listed in Table 1 and described in that paragraph of the thesis. It can be seen that for both sectors the calibration surface for the yaw angle coefficient  $K_{\phi}$  is primarily a function of the yaw angle  $\phi$  and is decoupled from the pitch flow angle  $\gamma$ . The same characteristic is observed for the pitch angle coefficient  $K_{\gamma}$ , which is fairly well decoupled from yaw flow angle  $\phi$ . In the ideal case, the surfaces for the total and static pressure coefficients are symmetric with respect to  $0^\circ$  yaw axes. An insignificant asymmetry is observed which is related to the surface finishing of the probe tip during the manufacturing process. Additionally, in comparison to previously published

FRAP-HT probes aerodynamic calibration data [67, 69], the surface pressure distribution around the probe tip of the new FRAP-HTH probe has changed due to the potential field effect of the heater (B) located close to the tip as shown in Figure 2–3. It mainly affects the total pressure and stagnation pressure coefficient distribution in sector 1. The stagnation condition is now obtained at 25° pitch angle whereas for the standard FRAP-HT the stagnation pressure is achieved at 10° pitch angle for Ma=0.7. In addition, the presence of the heater has the benefit to delay the separation of the boundary layer for positive pitch angle incidence, enabling a larger measurement range in positive pitch flow angles compared to the standard FRAP-HT probe.

The accuracies of the calibration models obtained from the polynomial interpolation are provided in Table 2 for Ma=0.7. The best calibration curve fit is obtained with a polynomial order of 6 and 4 for the yaw and pitch flow angle respectively and for a polynomial order of 8 and 6 for the total and static pressure coefficients as defined in Eq.(2-5) to Eq.(2-6). For both sectors the models deviations remain below  $\pm 0.25^\circ$  and  $\pm 3\text{mbar}$  in flow angles and pressures respectively. It is worth mentioning that the relatively high error of this particular Mach number for the total pressure in sector 1 is due to the three-dimensional shape of the calibration coefficient  $K_t$ , as presented in Figure 2–12.

Table 2: FRAP-HTH calibration model accuracy for Ma=0.7 and calibration range of  $\pm 24^\circ$  in Yaw and  $-1^\circ < \text{pitch} < 49^\circ$  in pitch.

Parameter:	accuracy	
	Sector 1	Sector 2
$\phi$	$\pm 0.15^\circ$	$\pm 0.12^\circ$
$\gamma$	$\pm 0.24^\circ$	$\pm 0.06^\circ$
$P_t$	$\pm 490 \text{ Pa (1.3\% } P_{\text{dyn}})$	$\pm 95 \text{ Pa (0.25\% } P_{\text{dyn}})$
$P_s$	$\pm 287 \text{ Pa (0.77\% } P_{\text{dyn}})$	$\pm 244 \text{ Pa (0.65\% } P_{\text{dyn}})$

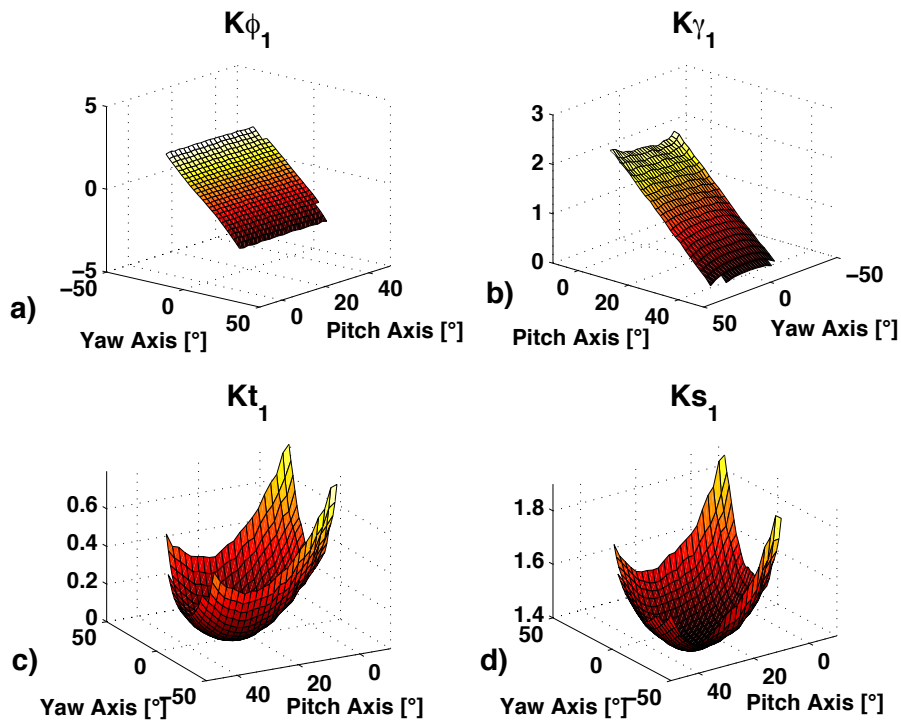


Figure 2–12: Aerodynamic calibration coefficients for sector 1, (a) yaw angle, (b) pitch angle, (c) total pressure, (d) static pressure.

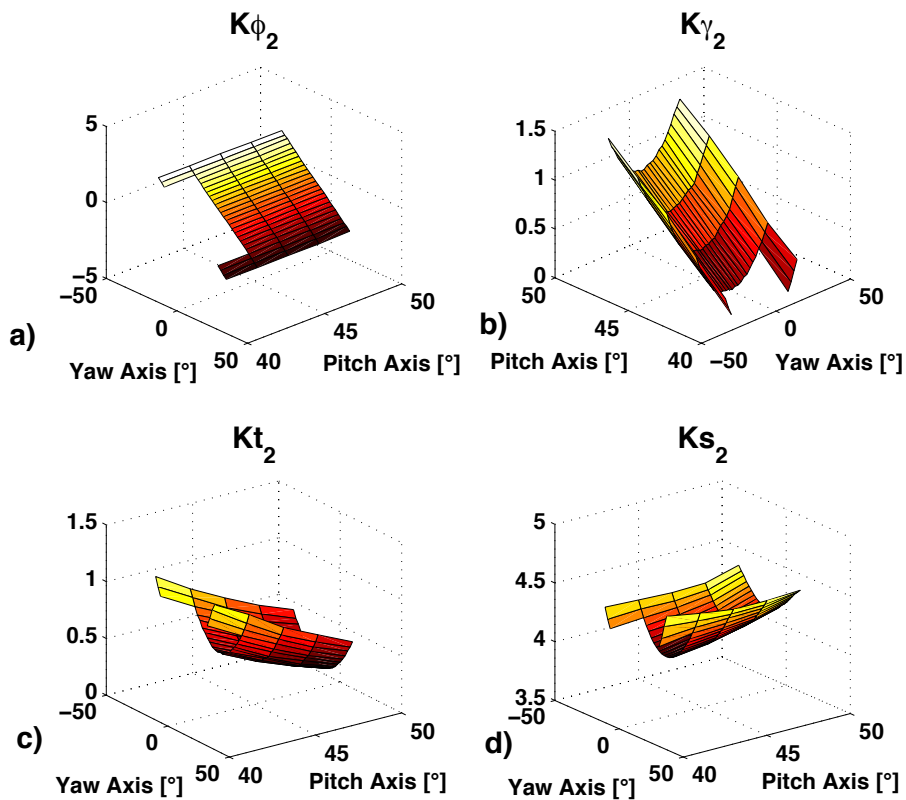


Figure 2–13: Aerodynamic calibration coefficients for sector 2, (a) yaw angle, (b) pitch angle, (c) total pressure, (d) static pressure.



### 2.1.6 Effect of probe tip overheating on measured flow quantities

The probe tip over heat above the flow field saturation temperature might influence the temperature field around the probe and distort the measured streamlines. Therefore, the potential effect of the heater's operation on the flow field around the probe tip was extensively investigated and experimentally tested. As described previously, representative tests for the exit conditions of LP steam turbines were conducted at Freejet facility. The resulting average Nusselt number for the flow conditions found at the last stage of a LP steam turbine is  $\overline{Nu}_D = 50$ . With the Nusselt number analogy the representative flow velocity in air was calculated to be met at  $Ma=0.17$ . Tests were performed at  $Ma=0.17$  for various overheat ratios and a wide range of yaw and pitch angles in order to identify any disturbance on the probe tip over heat on the surrounding flow.

Figure 2–14 shows the deviation of the four aerodynamic calibration coefficients when the heater is activated with  $\Delta T=10K$  overheat and deactivated so that the probe tip temperature is equal to the flow air temperature. As a first observation the error for all calibration coefficients is on average below 0.5%. This practically means that the heater operation has no effect on the measured flow quantities. The streamlines of the flow at the measurement location are not distorted and therefore the flow angles as well as the total and static pressures are not affected. The resulting difference on the measured yaw and pitch angles is, on average, below  $0.03^\circ$  and  $0.07^\circ$  respectively and for the total and static pressures below 10Pa and 30Pa respectively.

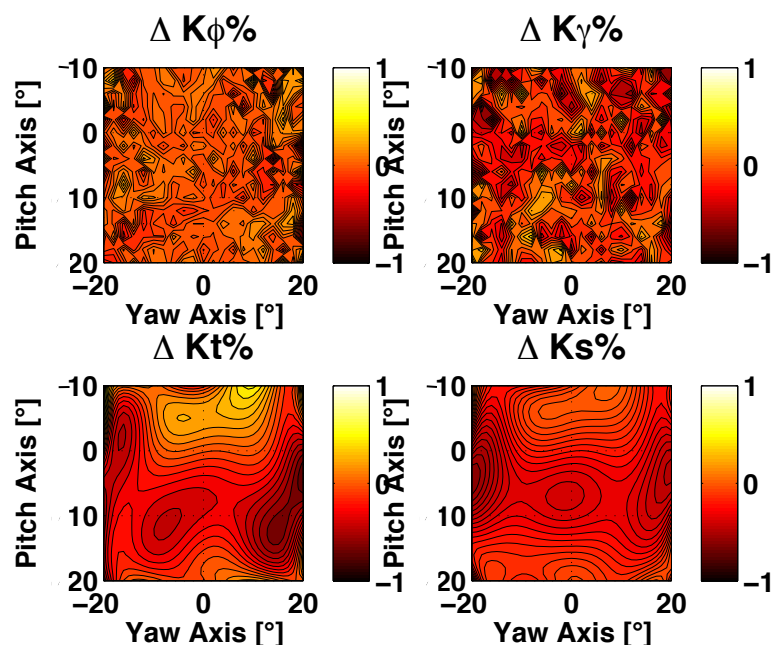


Figure 2–14: Effect of heater's temperature at representative Nusselt flow conditions from tests in Freejet facility for tip temperature overheat  $\Delta T=10K$ .

Additional assessment tests have been performed in MHPS steam turbine test facility. As presented in chapter 5.2.1 the new FRAP-HTH time-averaged measurements were compared to traditional 5HP probe measurements conducted at the same day and at the same measurement plane of the steam turbine. Despite the different spatial resolution of the two probes and the different circumferential measurement location, a good agreement between the FRAP-HTH and the traditional 5HP both in trend and in absolute values was found as described in [77].

These results have demonstrated the ability of the newly developed probe to provide reliable measurements at the last two stages of low-pressure steam turbines under high wetness flow conditions and practically proves that the effect of the heater has no impact on the measured aerodynamic flow quantities.

### 2.1.7 Measurement bandwidth assessment

In order to assess the measurement bandwidth of the probe, measurements were conducted in a shock tube test facility at the Laboratory for Energy Conversion. The experiments were performed in air and in the second step a numerical approach to correct the results for the steam conditions was applied. The shock tube facility has 50mm internal diameter and it is 5 meters long. It consists of a high-pressure and a low-pressure section. The shock step in pressure is achieved by bursting a very thin membrane, which separates the high-pressure section from the low-pressure one. The high-pressure section is open to ambient air pressure of about  $970 \pm 15$  mbar whereas the low-pressure section is controlled by a vacuum pump. A plastic membrane is situated 0.7m upstream of the test section and as its diaphragm breaks under a given pressure difference, a shock wave is generated and propagates with the speed of sound from the membrane location to the probe tip. This shock wave acts as a step function and excites the FRAP-HTH cavity at all frequencies. Figure 2–15.a shows the test section part of the shock test tube facility. The probe (A) is inserted vertically and its shaft is sealed through O-rings, which are installed in the access hole. In order to generate the transfer function of the probe a second in-house built flush mounted sensor probe is installed next to the FRAP-HTH probe as depicted in Figure 2–15.b. As shown in Figure 2–15.a, the membrane which separates the high from low-pressure section is installed at location E. The facility is able to produce up to 600mbar step pressure impulses. Both probes fulfill the intrusion criteria since their diameter is less than 1/10 of the shock tube's internal diameter. The FRAP-HTH and the reference probe are shown in the measurement section (B) of the shock tube in Figure 2–15.b.

The measured step in pressure of the FRAP-HTH probe signal is compared with the reference flush mounted single sensor probe in order to derive the transfer function. The reference probe is installed on the same plane as the FRAP-HTH's pressure tap in the direction of the shock wave propagation. The

signals are acquired with a PCI data acquisition 12 Bit board at 1.6MHz for a time period of 100msec.

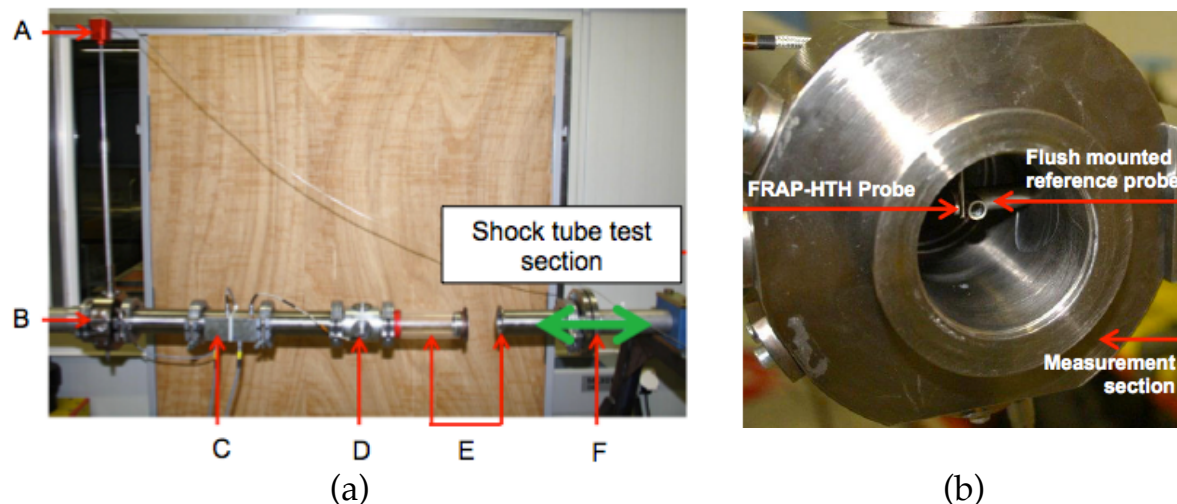


Figure 2–15: Shock-tube test section: (A) FRAP-HTH probe, (B) Reference probe, (C) electronics, (D) triggering sensor, (E) diagraph location, (F) high pressure section (a). FRAP-HTH and flush mounted reference probe (b).

### 2.1.7.1 FRAP-HTH time response

The time signals for the FRAP-HTH and the reference probe after the shock tube tests are presented in Figure 2–16.a. In addition the FFT signal of both probes are shown in Figure 2–16.b. Both probes show a signal amplification at around 560kHz which indicates sensors’ natural frequencies. This agreement of the natural frequencies is because both probes utilize the same type of the piezoresistive silicon transducers. In addition, the eigen-frequency associated with the FRAP-HTH’s pressure tap cavity is visible at 36kHz.

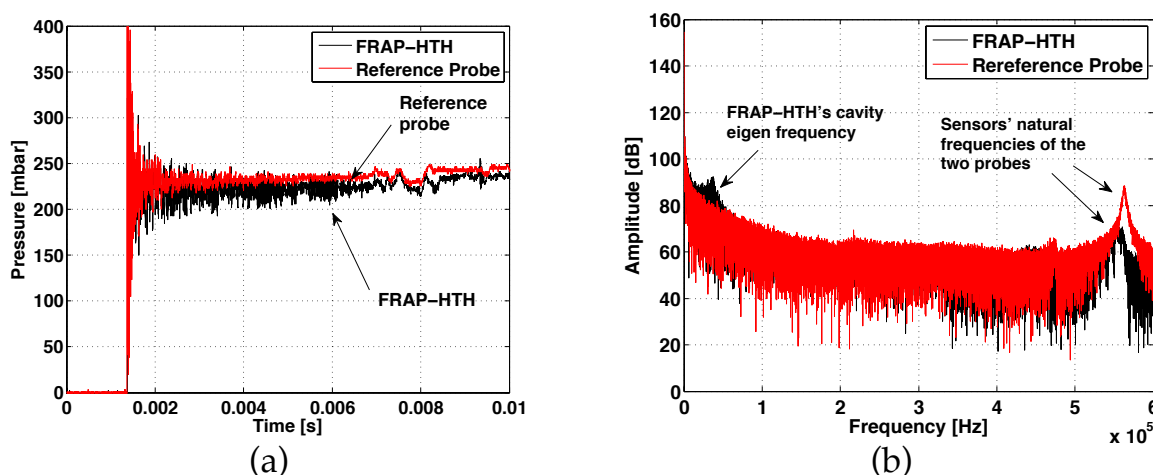


Figure 2–16: Time signal of FRAP-HTH and reference probe in shock tube tests (a) and FFT plots of FRAP and Reference probe signals out of 10 averages (b).

The non-parametric transfer function  $G_n$  of the FRAP-HTH probe is obtained out of the shock tube experiments with the use of the reference flush mounted sensor probe. The parametric transfer function is derived from a second order system, modeled with a polynomial fit into the non parametric transfer function in the frequency domain obtained out of the shock tube data. The parametric transfer function for a time continuous system can be obtained with a curve fitting approach and the mathematical problem can be reduced to a second order system with the Eq.(2-7).

$$G(s) = K \frac{\omega_n^2}{s^2 + 2\zeta\omega_n s + \omega_n^2} \quad (2-7)$$

The values for the coefficients  $\omega_n$  and  $\zeta$  for the parametric transfer function are obtained from the polynomial curve coefficients. The final transfer function is a result of an average out of 15 tests. The main reason for averaging the multiple non-parametric transfer functions, is to reduce the noise levels which are clearly visible in Figure 2–17.a. The average transfer function over 15 individual tests in the shock tube facility is shown in Figure 2–17.b up to 50kHz. The eigen-frequency of the FRAP-HTH cavity is detected in the same figure at a frequency of around 36kHz. The maximum measurement bandwidth of the FRAP-HTH is found to be at 21kHz when the pressure signal is amplified above the value of 3dB. In Figure 2–17.b, the phase plot shows a 90° change in phase at the resonance frequency and both amplitude and phase plots represent a single degree of freedom system.

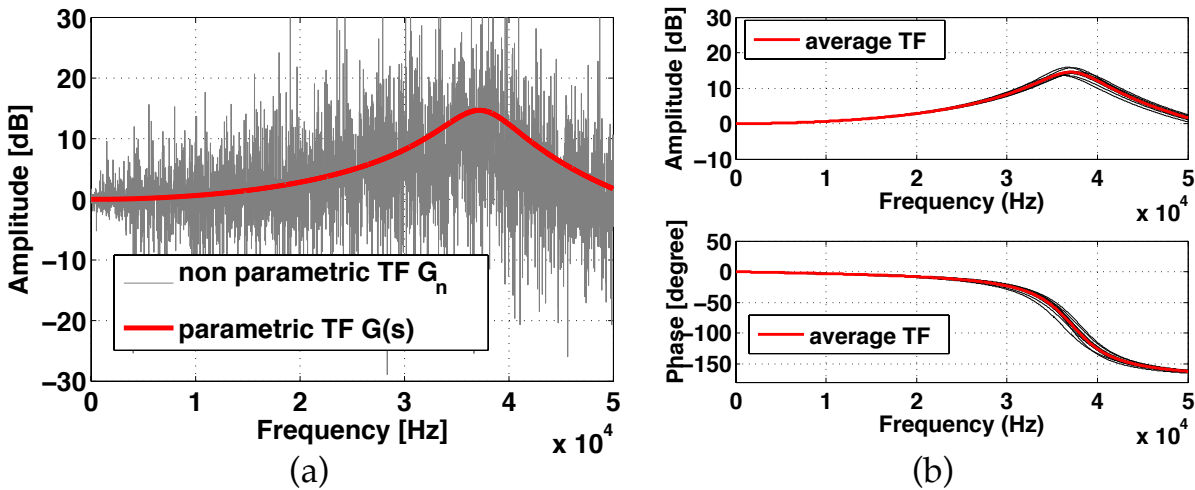


Figure 2–17: Comparison of parametric and non-parametric transfer function (no averaging) from a single experiment (a) and FRAP-HTH averaged transfer function over 15 experiments in shock-tube (b).

### 2.1.7.2 Correction for operation in steam

Since the measurement bandwidth assessment of the probe was conducted in air, a frequency correction for measuring in steam is essential. The use of

the organ pipe frequency approach with Eq.(2-8) is a good approximation because the air and steam are both gases. According to Eq.(2-8) the natural frequency of the probe's pressure tap cavity is proportional to the speed of sound and inversely proportional to the cavity length between the probe surface and the sensor' membrane.

$$f_{nt} = \frac{\sqrt{kRT}}{4 \cdot l_{cavity}} \quad (2-8)$$

Therefore the change in cavity frequency from air to steam is directly proportional to the 20.5% increase in speed of sound as shown below in Eq.(2-9):

$$\frac{\sqrt{kRT}_{steam}}{\sqrt{kRT}_{air}} = \frac{\sqrt{1.13 \cdot 461 \text{ J/kgK} \cdot 330 \text{ K}}}{\sqrt{1.4 \cdot 287 \text{ J/kgK} \cdot 296 \text{ K}}} - 1 = 20.5\% \quad (2-9)$$

As a consequence the calculated measurement bandwidth of the FRAP-HTH probe in steam is 20.5% higher than in air and is set to 25.3kHz (3dB limit).

## 2.2 Uncertainty Analysis

In this section of this chapter, the uncertainties related to flow field measurements in the last stage of low-pressure steam turbine using the FRAP-HTH probe are described. Similar to the work presented by Behr et al. [78], the whole chain of uncertainty sources has been accounted for. This chain starts with the uncertainties resulting from the calibration references, and the polynomial interpolation curves of the calibration models, as well as, the uncertainty sources related to the measurements. The resulting overall uncertainties are calculated by using the Gaussian error propagation formula. The uncertainty calculation was performed using the Guide to the Expression of Uncertainty in Measurement (GUM) [79] which is a commercial workbench for uncertainty calculations.

Figure 2–18.a shows the entire chain of uncertainties considered for calculating the uncertainty in measured flow angles accounting for the uncertainties related to calibration and measurement. According to Figure 2–18.a the uncertainty calculation for the calibration and measurement procedure involves a number of sources of uncertainties:

- Pressure DAQ: the overall uncertainty related to the calibration of the piezo-resistive pressure sensors (yaw and pitch sensors calibration) used to measure P1 to P6 pressure taps. This uncertainty is similar during the aerodynamic calibration and the measurements
- Probe position and reference flow (calibration): the uncertainty in set flow angles during calibration, which depends on the probe installation accuracy on the traversing system and on the traversing system positioning accuracy.

- Model fit: this uncertainty depends on the quality of the polynomial interpolation curve fit used to model the flow angle calibration coefficients  $K_\phi$  and  $K_\gamma$
- Probe position (measurement): the uncertainty in set flow angles during measurement which depends on the probe installation accuracy on the traversing system and on the traversing system positioning accuracy

As described in section 2.1.4, there are two sets of aerodynamic calibration coefficients which are used to measure over the two pitch and yaw angle incidence range of sector 1 and sector 2 as described in Figure 2–10. All above-mentioned uncertainties for the two sectors are summarized in Table 3. The expanded uncertainty resulting from the calibration procedure at  $Ma=0.7$  is  $\pm 0.30^\circ$  and  $\pm 0.49^\circ$  for the yaw and pitch angle respectively in sector 1 and  $\pm 0.14^\circ$  and  $\pm 0.07^\circ$  for the yaw and pitch angle in sector 2, respectively.

Table 3: Sources of uncertainty (expanded with coverage factor 2) for the flow angles.

Source of uncertainty:	Uncertainty		Units
	Sector 1	Sector 2	
Sensor calibration uncertainties (yaw and pitch sensor)	$\pm 25$	$\pm 25$	Pa
Accuracy in probe positioning during aerocalibration	$\phi$	$\pm 0.01$	deg
	$\gamma$	$\pm 0.015$	
Accuracy in probe positioning during measurements	$\phi$	$\pm 0.015$	deg
	$\gamma$	$\pm 0.015$	
Pressure data acquisition uncertainty ( $P_{ref}$ , $P_{atm}$ )	$\pm 20$	$\pm 20$	Pa
Model fit uncertainty for aerocalibration	$\phi$	$\pm 0.15$	deg
	$\gamma$	$\pm 0.24$	
Reference flow uncertainties during aerocalibration	$\phi$	$\pm 0.015$	deg
	$\gamma$	$\pm 0.015$	

When accounting for the uncertainties during measurements, the overall uncertainty in flow angles measurement is  $\pm 0.30^\circ$  and  $\pm 0.49^\circ$  for the yaw and pitch angles respectively in sector 1 and  $\pm 0.20^\circ$  and  $\pm 0.10^\circ$  in sector 2.

The uncertainty evaluation for the total and static pressure follows the same procedure as described for the flow angles. Figure 2–18.b shows a schematic of the uncertainty propagation calculation performed with the GUM workbench for the total and static pressure. The uncertainty calculation uses the same sources of uncertainty as stated in Table 3, except for the uncertainties related to the inter polynomial curve fit of the total and static pressure coefficients  $K_{t,r}$  and  $K_{s,r}$ , which are summarized in Table 4.

Table 4: Sources of uncertainty (expanded with coverage factor 2) for the total and static pressure.

Source of uncertainty:	Uncertainty		Units
	Sector 1	Sector 2	
Pressure data acquisition uncertainty ( $P_{ref}$ , $P_{atm}$ )	$\pm 20$	$\pm 20$	Pa
Model fit uncertainty for aerocalibration	$\Delta K_{t_{c,T}}$	$\pm 0.0019$	$\pm 0.012$
	$\Delta K_{s_{c,T}}$	$\pm 0.0084$	$\pm 0.036$

The overall uncertainties for the two sectors for the measurement conditions found at the nozzle exit of the last stage of a low-pressure steam turbine are presented in Table 5. Sector 1 exhibits in general greater values of uncertainties in all flow parameters. The main reason is the higher error arising from the aerodynamic calibration model fit. The calibration coefficient curves for sector 1 are three-dimensional resulting in greater errors on the model fit term as presented in Figure 2–18. The total and static pressure uncertainties are 1% and 2.3% of the maximum total and static pressure respectively, which enable accurate measurements in the challenging wet steam environment of LP steam turbines.

Table 5: FRAP-HTH expanded uncertainty (coverage factor 2) calculated for L-0 stator exit for  $Ma=0.7$ (see Table 11, OP-1).

Flow parameter:	Expanded abs. Uncertainty	
	Sector 1	Sector 2
$\phi$	$\pm 0.30^\circ$	$\pm 0.20^\circ$
$\gamma$	$\pm 0.49^\circ$	$\pm 0.10^\circ$
$P_t$	$\pm 210\text{Pa}$ (1.0% $P_t$ )	$\pm 170\text{Pa}$ (0.6% $P_t$ )
$P_s$	$\pm 480\text{Pa}$ (2.3% $P_s$ )	$\pm 390\text{Pa}$ (1.9% $P_s$ )
Ma	$\pm 0.032$	$\pm 0.023$
Ma <sub>rel</sub>	$\pm 0.027$	$\pm 0.017$
$\phi_{rel}$	$\pm 0.76^\circ$	$\pm 0.62^\circ$
C <sub>pt</sub>	$\pm 0.6\text{E-}3$	$\pm 0.5\text{E-}3$
C <sub>ps</sub>	$\pm 1.5\text{E-}3$	$\pm 1.2\text{E-}3$

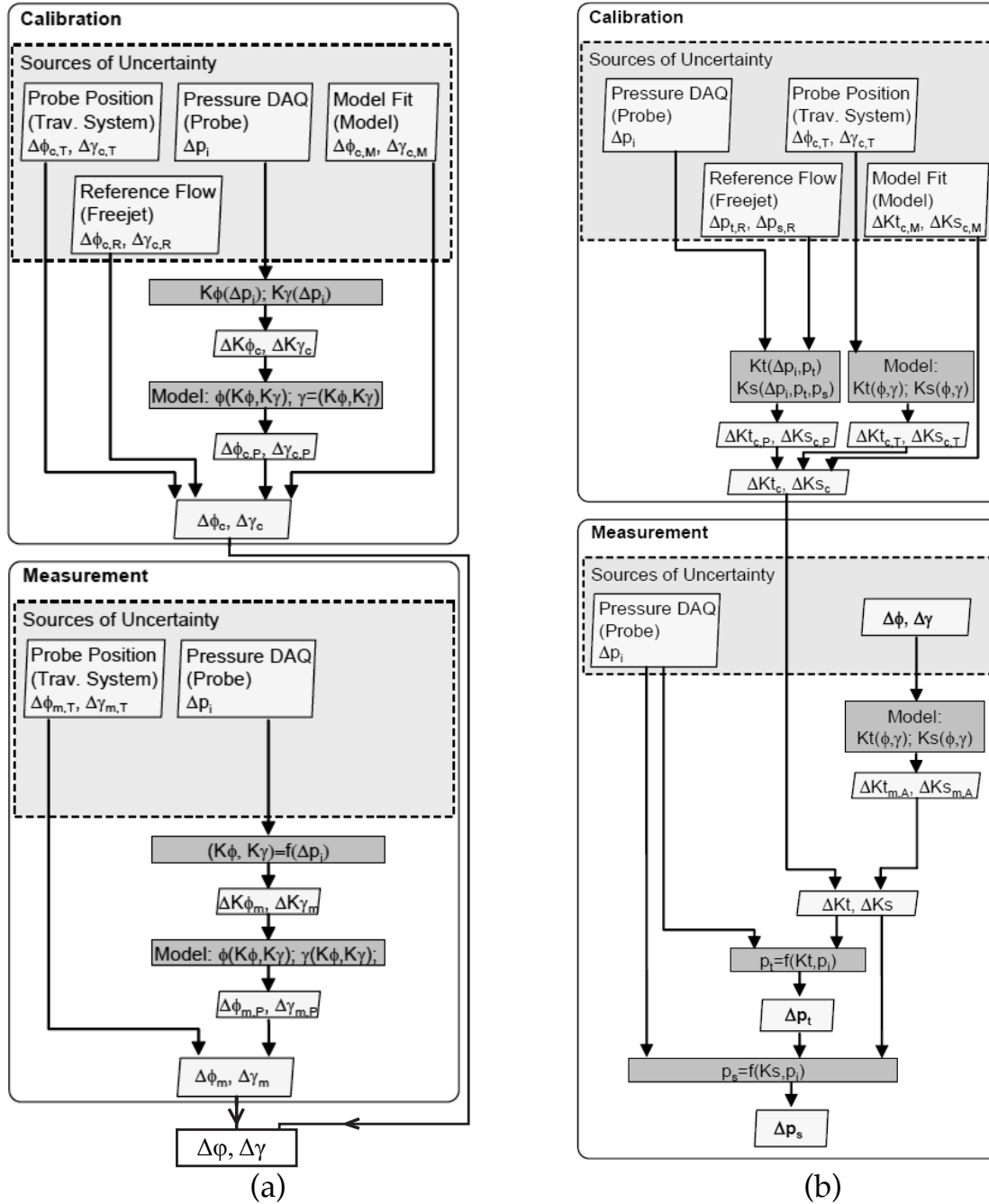


Figure 2–18: Flow angles' uncertainty propagation (a). Pressure uncertainty propagation of total and static pressure measurement (b) [78].



Figure 2–19 summarizes the uncertainties in measured total and static pressure for the Mach number conditions of  $Ma=0.3$ ,  $0.5$  and  $0.7$ . For sector 1, the extended uncertainty of the flow pressures at low Mach number ( $Ma=0.3$ ) are  $\pm 160\text{Pa}$  for the total pressure and  $\pm 180\text{Pa}$  for the static pressure. In most cases, with increasing Mach number the uncertainty of the aerocalibration model increases. The model uncertainty is multiplied with a term representing the partial derivative of the overall uncertainty equation and this term increases as well with higher Mach numbers due to higher absolute pressure levels. As a consequence the model uncertainty contributes more to the overall uncertainty at higher Mach numbers. This effect can be seen in the results shown in Figure 2–19. Nevertheless the relative uncertainties in measured total and static pressure are reducing with increasing Mach number conditions.

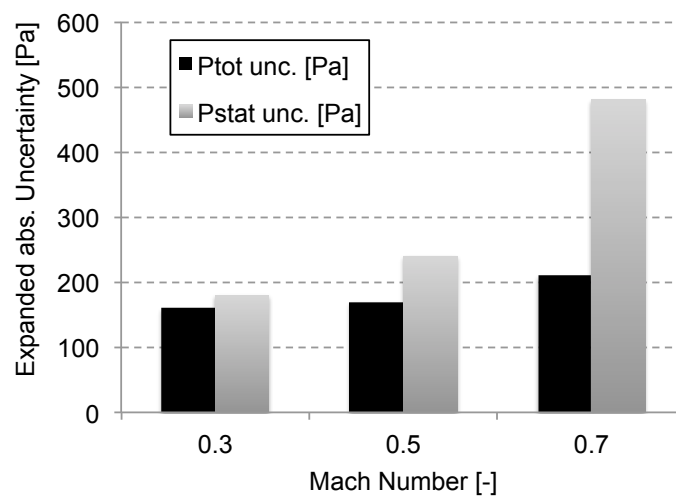


Figure 2–19: Total and static pressure expanded uncertainties as a function of Mach number.

## 2.3 Specific data reduction algorithm for wet steam flows

### 2.3.1 Droplet filtering processing algorithm

As the FRAP-HTH probe operates in wet steam flows with water droplets ranging from  $0.1$  up to  $400\mu\text{m}$  in diameter [9], the interaction of droplets with the pressure taps and the sensors' membrane can alter and corrupt the time-resolved pressure measurements. In particular there are two effects that can occur resulting in a signal corruption. Large droplets that rest inside the pressure tap on top of the sensor shielding interface and affect the local measured static pressure due to latent heat losses during the evaporation process. Small droplets that manage to penetrate through the shielded pressure tap and impact the sensor membrane. Based on the virtual six sensor probe concept (see Figure 2–9), one measurement point with the FRAP-HTH probe consists of three consecutive records for each sensor, all sampled at a sampling rate of  $200\text{kHz}$  with a resolution of 24 Bit. Figure 2–20.a shows the absolute pressure signal from these three consecutive records as measured from the

pitch sensor in wet steam. As presented in the same figure the impact of small droplets can result up to an increase of 280% of the absolute measured pressure, whereas the evaporation of large droplets due to overheating results in a reduction as high as 50% of the absolute measured pressure.

As shown in Figure 2–20.b, the evaporation of the large droplets causing a drop in measured static pressure goes along with a temperature drop of the piezo-resistive sensor. Typical temperature fluctuations related to evaporation phenomena inside the cavity of the probe are presented in Figure 2–20.b, the temperature variation remains less than one degree Celsius.

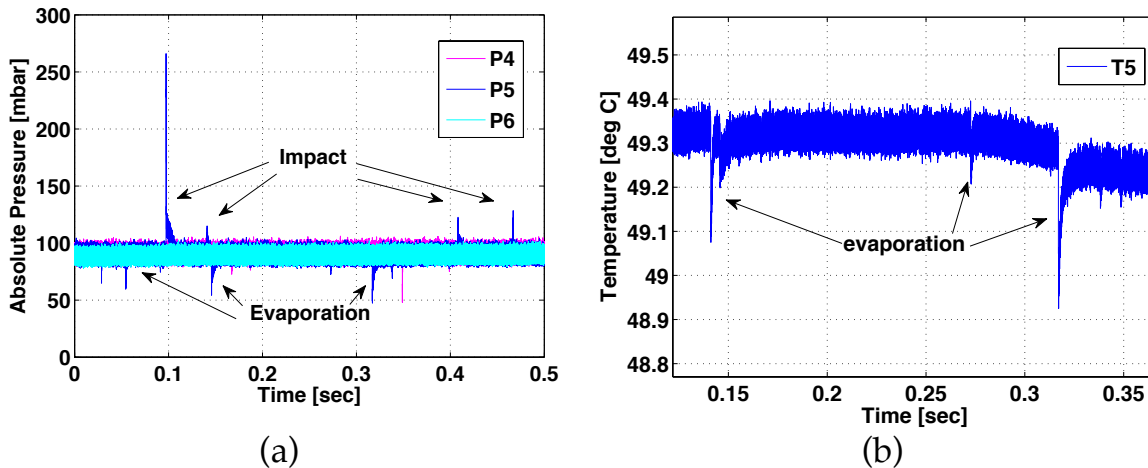


Figure 2–20: Probe’s raw absolute pressure signal from the pitch sensor for the three consecutive records ( $0^\circ$ ,  $-42^\circ$ ,  $+42^\circ$ ) (a). Probe’s raw temperature signal from the pitch sensor for record at  $-42^\circ$  (b).

A filtering algorithm was developed in order to filter out the portions of the raw pressure and temperature signals affected by droplets’ impact or evaporation. Figure 2–21 shows a schematic of the standard in-house data reduction code Herkules as described in [80]. The new droplet filtering subroutine is applied between Step 1 and Step 2, prior to the phasing of the measured data with respect to the turbine’s rotational trigger.

As shown in Figure 2–21, in the first step the droplet filtering code performs a phase-locked averaging (PLA) on the time-resolved pressure voltage signals to quantify the mean level of the pressure signal as well as the peak-to-peak periodical pressure fluctuations triggered by the rotor blade passing frequency. The phase-locked averaged data are used to define the threshold detection boundaries of  $\pm 2\sigma$  around the mean signal value, where  $\sigma$  is the standard deviation of the phase-locked average pressure signal. The raw turbulent data are considered as corrupted when they overshoot the  $\pm 2\sigma$  limit for both impact and evaporation cases.

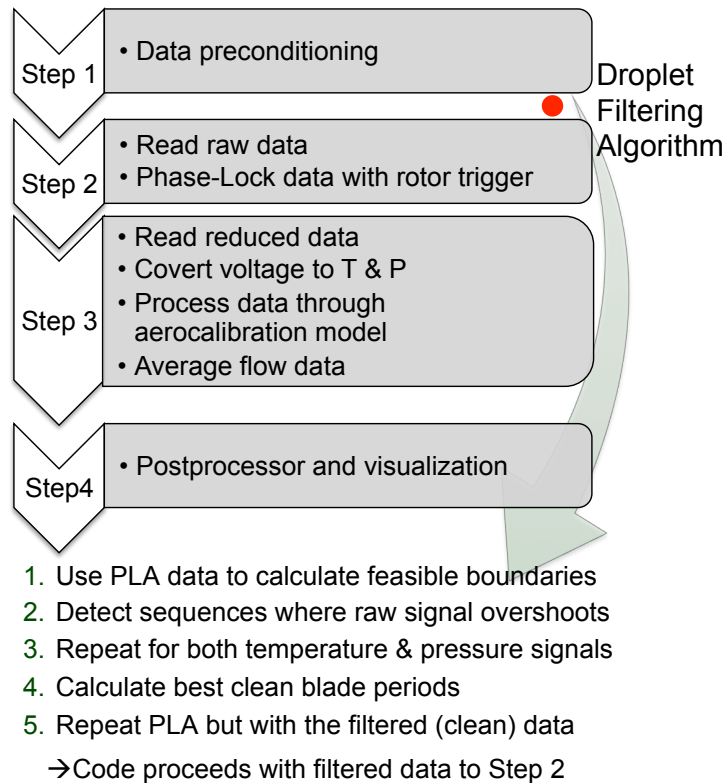


Figure 2–21: Code structure of processing code Herkules with the new subroutine implemented between the first and second step of the initial code.

The case of an evaporation process is described in Figure 2–22.a and b. Figure 2–22.a shows the phase-locked average pressure signal and the derived detection boundaries in conjunction with the measured raw pressure signals. In this particular example of Figure 2–22.a, the mean value of the phase-locked data is 0.88V and the lower and upper threshold boundaries are roughly set to 0.75V and 1.0V respectively. As shown in Figure 2–22.a, the starting point of the corrupted measurement sequence is detected when the raw pressure signal overshoots the lower threshold limit. In the second step, the temperature signal is cross-compared as presented in Figure 2–22.b, and the end of the contaminated sequence is detected when the sensor temperature signal is back to its original average value. This procedure is performed over the entire set of acquired data. The corrupted parts of the measured raw signals are then filtered out and not considered for the following data processing steps, as presented in Figure 2–21.

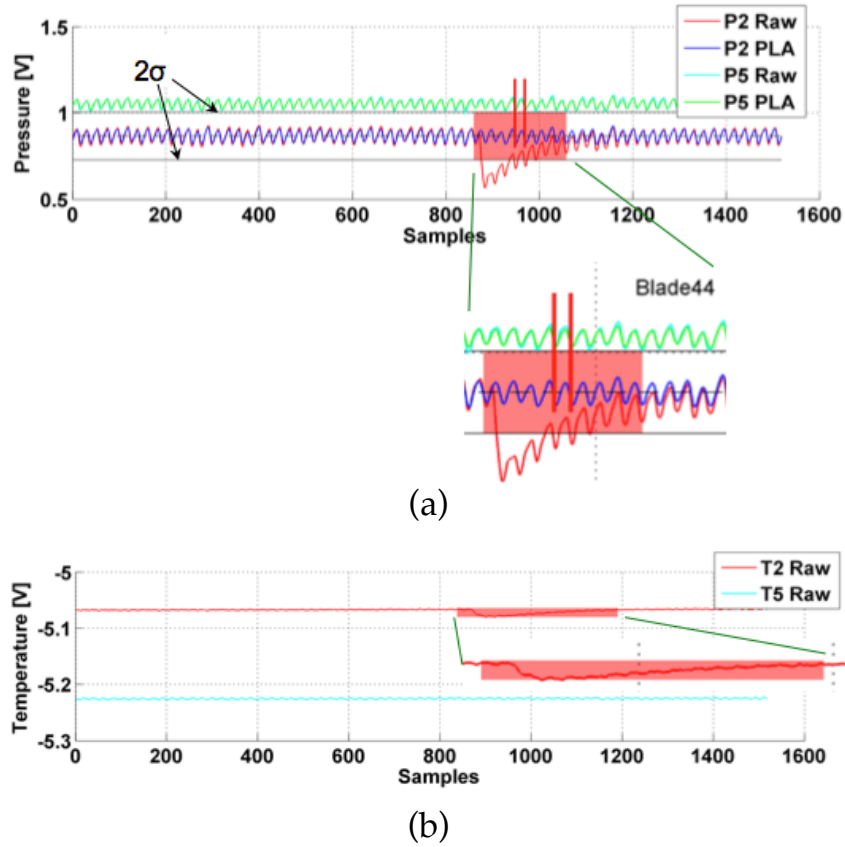


Figure 2-22: Pressure (a) and temperature (b) signals for the yaw sensor for 1 rotor revolution. The signal P2 is corrupted due to water evaporation.

## 2.4 Summary

The development of a fast response probe for time resolved flow field measurements in the wet steam environment was presented in this chapter. A miniature heater with a power density of  $61\text{W}/\text{cm}^2$ , is used to evaporate the concentrated water in the pressure taps of the probe. The heater increases by 5 to  $10^\circ$  the tip temperature of the probe above the flow saturation temperature. As presented in paragraph 2.1.6, test results have shown that the flow quantities when the heater is activated or deactivated are within the uncertainty of the aerocalibration model therefore has no effect on the measured flow quantities. It mainly affects the total pressure and stagnation pressure coefficient distribution due to its higher blockage effect setting the stagnation condition at  $25^\circ$  of the pitch angle instead of  $10^\circ$  for Mach number of 0.7. Nevertheless, this is accounted for through the aerodynamic calibration.

In addition, the detailed calibration procedure is described. A new virtual six-sensor measurement concept was applied to capture the high pitch angles of the flow, due to the large flare angles at the last stages of low-pressure steam turbines. This has broadened the available operating range of the probe up to roughly  $50^\circ$  in pitch angle instead of  $20^\circ$ . Additionally, shock tube tests in air have provided the transfer function of the new probe and a frequency correction for operation in steam has shown that the probe measurement bandwidth is at 25.3kHz. The uncertainty analysis has shown that the total and static pressure uncertainties are 1% and 2.3% of the maximum total and static pressure respectively for the conditions at the last stage of LP steam turbines enabling accurate measurements in the challenging wet steam environment.

The interaction of the droplets with the pressure taps and the sensors' membrane can alter and corrupt the time-resolved pressure measurements. Therefore, a droplet filtering algorithm to exclude any corrupted data due to droplet impact or evaporation from the heating process was developed and presented as well.

As it will be shown in chapters 5 and 6 of the thesis, the probe has demonstrated its ability to perform accurate measurements in severe wet steam conditions with wetness mass fraction up to 8% at the last stages of a LP steam turbine

### 3 Fast response optical backscatter probe for coarse water droplet measurements (FRAP-OB)

This chapter presents the development of an optical backscatter probe for water droplet and speed measurements in turbomachines. The probe utilizes monochromatic wavelength light to illuminate droplets and the measured scattered light provides the information of droplets' size. The effort was focused on a miniature design to minimize the blockage effects and maximize the spatial and temporal resolution, as well as the accuracy.

#### 3.1 General design requirements and operating principle

According to the literature review, the size of the droplets in steam turbines ranges from 0.1 to maximum 400 $\mu\text{m}$ . However, only large droplets ( $D_d > 5\mu\text{m}$ ) are responsible for blade erosion. Thus, the focus on the development for the FRAP-OB probe, is from 20 $\mu\text{m}$  to 120 $\mu\text{m}$  in diameter since larger droplets cannot sustain their size and will further break to smaller sizes. Hence, the new measurement technique should provide diameter and speed measurements of polydispersed coarse water droplets in that particular range. In addition, the probe should be able to use standard access holes that are usually equipped with a guide pipe from the outer casing to the flow path. A typical diameter range for these access holes is 8 to 15mm, therefore this constraint leads to a probe geometry which should be a simple single cylindrical shaft. The probe's measurement volume should be minimized, in order to resolve size and speed distributions across the secondary flow structures present at the endwalls or in the blades' wake. The droplets' trajectories are triggered by the rotor blade-passing period and can be exposed to flow velocities as high as 300m/s depending on their size, which sets the measurement bandwidth requirements to several tenths of MHz.

The FRAP-OB probe presented in the current thesis is a single-particle instrument that measures the light scattered from a droplet passing through an open path focused laser beam. A schematic with the operating principle of the probe is provided in Figure 3–1. The scattered light from the individual droplet is collected with optics over a given range of angles by a photodiode and converted to a digital signal, which is then related to a droplet size by applying the calibration curve. An assembly with optics focuses the beam three probe diameters from the probe surface. The principal reason for this is to avoid the probe disturbing the droplets' path when it is inserted into the machine. When a droplet crosses the measurement sample volume (focused area), light is scattered in all directions and a pair of lenses collects light in the backscatter region as shown in Figure 3–1. The backscattered light is then focused in a miniature photodiode and the signal is transmitted via the electrical circuit to the acquisition equipment. In order to maintain the optics clean from any water contamination and beam deflection as the light exits the probe tip, an active purging system is installed. This provides pressurized air injected

radially on the surfaces of the two lenses as presented in Figure 3–1. The purging flow is attached to the surface of the windows so as to minimize any interaction with the surrounding flow field.

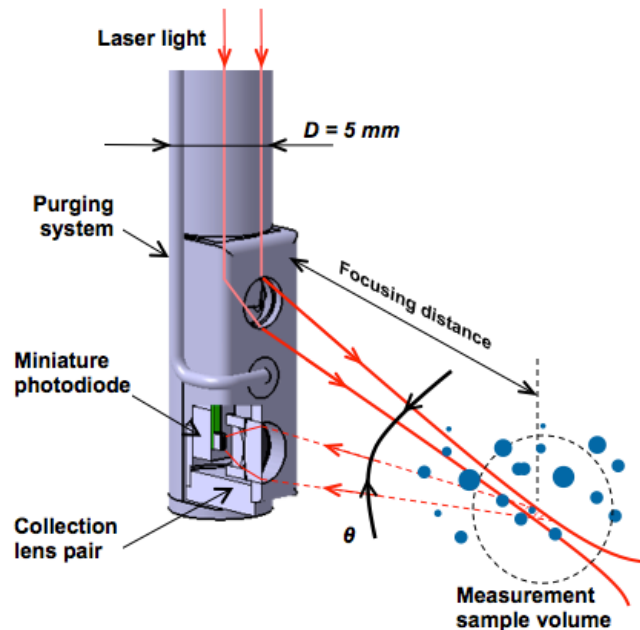


Figure 3–1: Operating principle schematic of the optical backscatter probe.

### 3.2 The FRAP-OB probe

The manufactured optical backscatter probe used in all measurements of the current thesis is presented in Figure 3–2. It has a tip diameter of 5mm and maximum operating temperature up to 120°C. A purging system is installed between the two optical components and pressurized air on the flat surface of the probe keeps the two windows clean from any water contamination. The purging system is controlled through the measurement computer and it is only activated for roughly 0.2sec before each measurement. The control and monitoring system of the probe consists of an integrated signal conditioner, a multi-axis probe traversing system and a laboratory PC that is equipped with an acquisition card with high sampling rate capable of acquiring signals up to 250MHz. The optical fiber at the end of the probe is connected with a 28mW He-Ne laser that is attached to the traversing system. Two channels are recorded during measurements, one is the photodiode signal from the probe and the second is the rotational speed of the machine. The two records are made in order to rephase the measurements with respect to the rotor blade-passing period as it will be shown in the following paragraphs.



Figure 3-2: The optical backscatter probe tip.

### 3.2.1 Optimal light scattering collection angle

Mie simulations were performed with the MiePlot v4.2 code [81] in order to identify the optimum backscatter solid angle  $\theta$  (see Figure 3-1). As presented in Figure 3-3, in the current simulations a Gaussian beam with light intensity  $I_0$  illuminates a water droplet. The droplet scatters light with intensity  $I$  in all directions and creates a scattering pattern. Figure 3-3 presents the scattering pattern from  $0^\circ$ , showing forward scattering (i.e. in the original light direction) of up to  $180^\circ$ , which implies back scattering (i.e. back towards the source of the light). For the case of a water droplet, the shape of this pattern depends on the droplet diameter and the incident wavelength, in this case  $632\text{nm}$ .

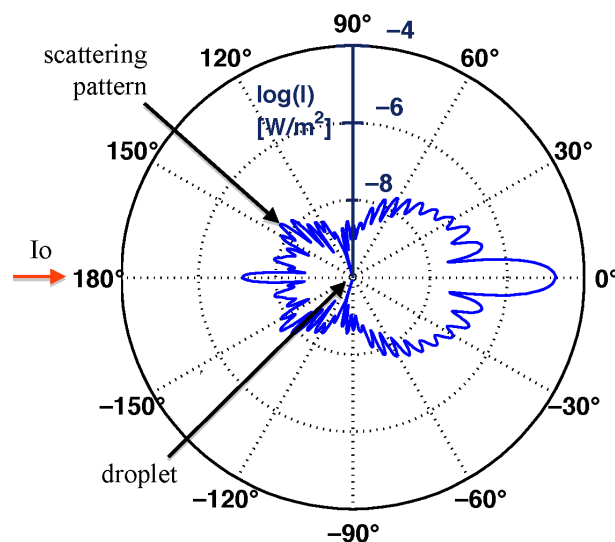


Figure 3-3: Mie simulations schematic. Angular scattering intensity for a water droplet with  $D_d=5$ ,  $\lambda=632\text{nm}$  and  $I_0=1\text{W/m}$ .



Figure 3–4 shows the scattered light intensity for various droplet diameters as a function of the scattering angle  $\theta$ , from  $90^\circ$  to  $180^\circ$ , out of the Mie simulations as depicted in Figure 3–3. The scattered light intensity  $I$  is non-dimensionalized over the incident light intensity  $I_0$  and plotted on a logarithmic scale on the  $y$ -axis. As shown in Figure 3–4, the scattered light in the backscatter region between  $138^\circ$  and  $160^\circ$  shows a high sensitivity over the diameter range of interest. In order to fulfill the requirement of the focusing distance, 15mm away from the probe surface, and at the same time increase the backscattered light sensitivity to the maximum possible, the collecting angle of the probe in the backscatter region was chosen to be between  $150^\circ$  and  $158^\circ$ . In this backscatter angles, the scattered light by a droplet shows a clear sensitivity to the scattered light intensity with increasing droplet diameter. Above  $160^\circ$ , the sensitivity to backscattered light of the droplets is reduced. This is due to scattering only from reflection with the absence of the other scattering phenomena.

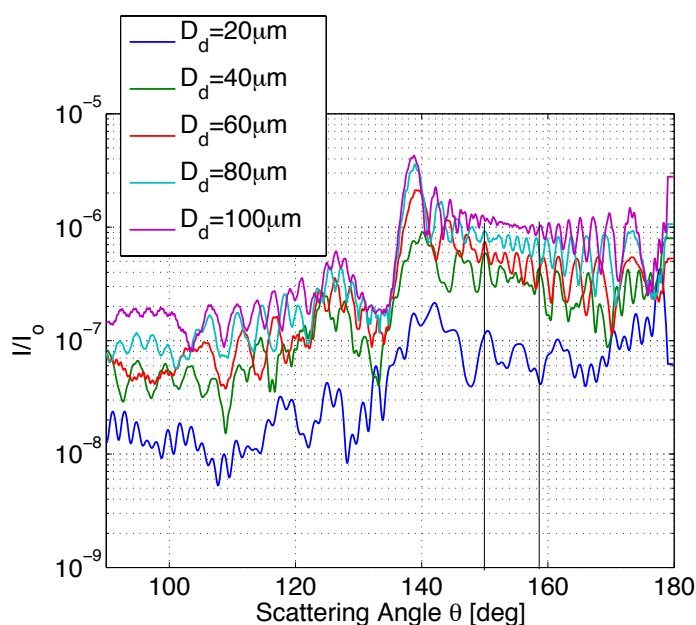


Figure 3–4: Mie calculation of scattering intensity by water droplet ( $m = 1.33 + 1.67 \cdot 10^{-8}i$  at  $20^\circ\text{C}$ ) for unpolarized red light ( $\lambda = 632\text{nm}$ ) for diameters  $D_d = 20, 40, 60, 80$  and  $100\mu\text{m}$ .

### 3.2.2 Sample volume

As presented in Figure 3–1, the intersection of the focused beam with the collecting optics light path, creates a well-defined sample volume in which a single particle scatters light when crossing it. The light is then recorded by the photodiode and converted into droplet diameter and speed using the calibration data (see §3.2.5). The geometrical characteristics of the measurement volume are a crucial factor in the design of an in situ particle instrument since the probe has to operate in a polydispersed droplet laden flow with unknown

particle trajectories and concentrations. As described in [50, 82, 83] two types of errors may occur. The main two uncertainties related to the sample volume geometry are the coincidence and the side effect errors. A schematic with the coincidence and side effect error is presented in Figure 3–5. Coincidence error occurs when more than one droplet crosses the sample volume at the same time. This type of error primarily depends on the droplets' concentration in the flow field and increases as the droplets' concentration increases. The side effect error is caused when a droplet crosses the sample volume of the probe partially. In this case the droplet is partially illuminated by the focused beam and therefore the recorded light signal is reduced, resulting in a fault size of the real droplet diameter. This error is mainly affected by the size of the droplet in the flow path relative to the size of the sample volume. Large droplets relative to the sample volume are most prone to this type of error.

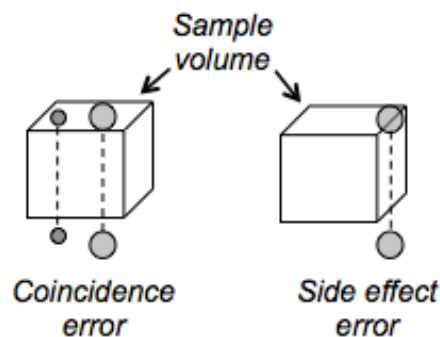


Figure 3–5: Representation of coincidence and side effect error.

The coincidence and side effect errors were calculated as described by Lance et al. in [50] and Avellan et al. in [82] respectively. For the coincidence error, a Poisson probability distribution of droplet inter arrival passing times is used to calculate the probability of more than one droplet crossing the sample volume at the same time. In the probability distribution function the droplet concentration, speed and residence time in the sample volume are used. The side effect error uses the reduced scattered light function when a droplet partially crosses the sample volume. In this calculation the concentration and the apparent diameter cover factors are used. The resulted errors as a function of the sample volume size are shown in Figure 3–6. As expected, the coincidence error increases when the sample volume increases, since the probability of having more than one droplet at the same time in the sample volume increases. On the other hand the probability of a droplet partially crossing the sample volume is reduced as the sample volume is increased.

As shown in Figure 3–6, there is an optimum volume for a particular concentration, which corresponds to the minimum of the sum of the two error curves. This is in the range of  $0.035\text{mm}^3$  resulting in 30% and 18% of the side effect and coincidence error in diameter respectively. In order to reduce the sources of these two errors, the sample volume of the probe was chosen to be

roughly  $0.01\text{mm}^3$ , minimizing the coincidence error to below 5%. The side effect error is minimized through a correction routine, which is described in paragraph 3.2.5.3 of this chapter.

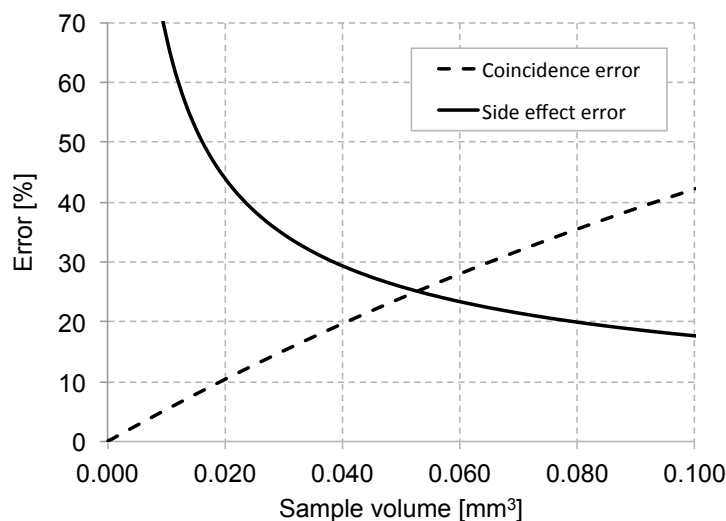


Figure 3–6: Calculated of maximum error due to coincidence and side effect.

In addition to the coincidence and side effect errors there is an additional error due to light extinction of the laser beam. The beam light extinction occurs first when the laser light travels from the probe surface to the focusing point at the location of the sample volume and further light extinction occurs when the light is scattered from a droplet back to the photodiode. In order to select the optical components for the design of the sample volume size, the development was based on the extreme conditions found in the last stage of a typical low-pressure steam turbine. Depending on the operating condition and the backpressure of the turbine the wetness mass fraction is found to be in the range between 6-8%. The condensed water environment consists of very small droplets in the submicron range as well as coarse droplets up to  $100\mu\text{m}$  in diameter [39, 84]. Nevertheless, the small droplets from  $0.1$  to  $1\mu\text{m}$  contribute most to the concentration of the condensed environment. As described in [85], one way to calculate the droplet concentration is to use the specific volume of saturated vapor and liquid together with the wetness mass fraction. The concentration is a function of the droplet diameter and decreases as the droplet diameter increases. Using the analytical calculation of Eq.(3-1),

$$C_n = \frac{3Y\rho_d}{4\pi\rho_s r_d^3(1-Y)} \quad (3-1)$$

the result for an average droplet diameter of  $3\mu\text{m}$  and wetness mass fraction of 6% is about  $10^{11}$  droplets/ $\text{m}^3$ . On the other hand, real measurements with optical extinction probes presented in [86, 87] report a concentration of  $10^{13}$  droplets/ $\text{m}^3$  for a droplet diameter distribution of  $1\mu\text{m}$ . However, a recent

study by Korolev et al. [88] demonstrates the drawback of the extinction technique to underestimate the turbidity on the presence of coarse droplets ( $D_d > 10\mu\text{m}$ ). This implies that the real droplet distribution is shifted towards larger droplet sizes and therefore the actual concentration is overestimated. The beam light extinction was calculated using the Beer-Lambert law as described in Eq.(3-2). When light with initial intensity  $I_0$  passes through an absorbing and scattering medium, in this case the droplets, the intensity decreases along its path  $L$ . Thus, the transmitted light  $I$  that reaches the control volume has a lower intensity, which is a function of the distance  $L$  and turbidity  $\tau$ .

$$I = I_0 e^{-\tau \cdot L} \quad (3-2)$$

The turbidity can be calculated using Eq.(3-3) assuming a droplet distribution of  $N(D)$  and applying the extinction coefficient  $E$  for the water medium.

$$\tau = \int_0^{\infty} \frac{\pi}{4} D^2 N(D) E_{(D,\lambda,m)} dD \quad (3-3)$$

The reduction of incidence light intensity from  $I_0$  to  $I$  results in a proportional decrease of the calibration curve. As a consequence, the error of the probe in measured droplet diameter is calculated below 5%, when the wetness mass fraction is 6%, assuming a Sauter mean droplet diameter of  $10\mu\text{m}$  and a fog droplet concentration of  $10^{10}$  droplets/ $\text{m}^3$ .

### 3.2.3 Photodiode selection

The principal requirement for the photodiode selection is the minimum response time. A sensor with a miniature size is favorable in order to keep the size of the probe as small as possible and minimize the blockage effects around the probe tip. Since particles inside turbomachines can travel up to 300m/s, a high speed PIN photodiode with  $0.25\text{mm}^2$  square active area was chosen. The responsivity at  $\lambda=632\text{nm}$  is 0.49A/W and has a maximum dark current of 0.1nA which allows very low noise levels in the range of  $\pm 0.5\text{mV}$  after amplification on the raw data. The rising time of this silicon miniature sensor is 0.4nsec and is electrically connected to a flexprint with gold wire bond completing the electrical circuit of the fast response optical backscatter probe.

### 3.2.4 Dynamic response

Since the selected photodiode has a very high bandwidth in the range of 3GHz the dynamic response of the probe signal depends on the time response characteristics of the probe's signal conditioning unit that is equipped with the high-speed operational amplifier. When a droplet is crossing the measurement sample volume of the probe, the generated scattered signal is a typical Gaussian curve. For the current studies the probe was exposed to flow velocities of a

maximum of  $Ma=0.5$  (170m/s). This requires a minimum bandwidth of 30MHz in order to collect at least 10 measurement points for each crossing droplet to describe the generated Gaussian curve. As shown in Figure 3–7, in order to achieve this bandwidth, the maximum allowable amplification is roughly 30dB. Thus, with the current electronics, the probe is capable to detect any droplet that travels up to 170m/s without any measurement bandwidth limitation.

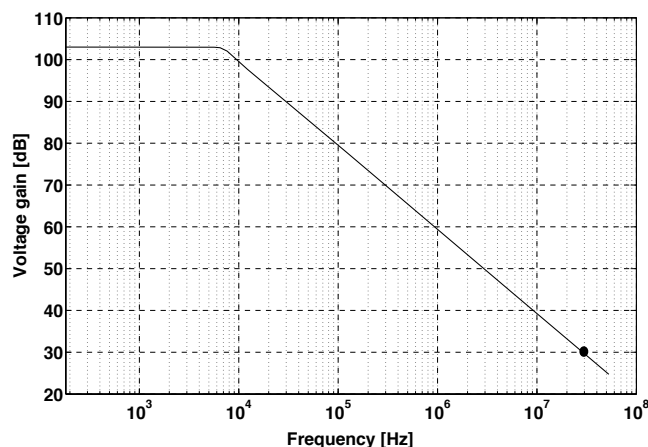


Figure 3–7: Amplitude response of the optical backscatter probe out of simulations.

### 3.2.5 Probe calibration

#### 3.2.5.1 Calibration for droplet size measurements

The FRAP-OB probe is calibrated using a monodispersed droplet calibration facility. A schematic of the calibration facility is shown in Figure 3–8. The probe (A) is mounted on a 2D-XY translation stage system enabling movements on the surface of the optical table (F) with an accuracy of  $5\mu\text{m}$ . The light is generated with the 28mW He-Ne laser (B) and guided through the probe's optical fiber into the probe tip. The probe calibration is performed using an in-house droplet generator (C) developed by Rollinger et al. [89]. The monodispersed droplet generation in the kHz range is based on the Rayleigh breakup jet. A modular design, based on cartridges, which are composed of the water reservoir and the dispensing nozzle, is capable of producing water droplets from 40 to 100 in diameter with a stability of  $\pm 2\mu\text{m}$ . Water droplets are generated continuously with a frequency and air-backpressure set by the user. Depending on the tuning parameters, the droplets' velocity range is from 4 to 12m/s. The performance of the droplet generator device is monitored continuously with a commercial fast response photodiode PDA 100A, annotated with (E) in Figure 3–8, in order to achieve uniform and equally spaced droplets. The monitor photodiode is positioned in the probe's exit light direction; therefore the droplets' signature creates a forward scattering signal. A neutral density filter is attached to the photodiode in order to reduce the intensity of the forward scattered signal.

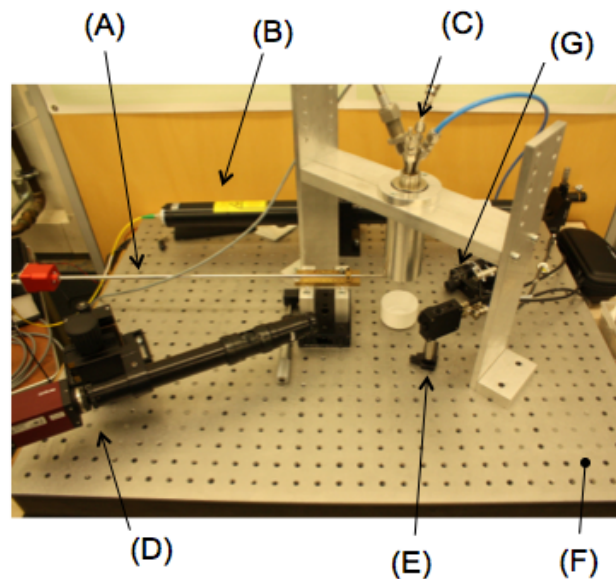


Figure 3–8: Monodispersed calibration facility schematic A: Probe, B: He-Ne Laser, C: Droplet generator, D: Reference camera, E: Droplet monitor diode, F: Optical table, G: Strobe light.

For independent referencing of the droplet diameter the shadow imaging technique is utilized. As shown in Figure 3–8, the droplets are imaged with a high-resolution camera (D). The camera's resolution and pixel size is  $2452 \times 2054$  and  $3.45 \mu\text{m}$  respectively, it has 5x maximum optical magnification (zoom) and is triggered by the strobe light (G). In order to acquire high quality sharp images of the droplets, the camera is mounted on a 3D-XYZ translation stage system. The shadow imaging technique is used to produce pictures of the generated water droplets. In a second step, the obtained pictures are analyzed in MATLAB environment to measure the droplet diameter. The probe's voltage signal is correlated with the droplets' measured diameter in the last step of the post processing analysis.

Two raw images as they are captured with the reference camera when the droplet generator is in operation are shown as examples in Figure 3–9.a and b. Both images have the same magnification factor (optical zoom 2x), which results in  $1.725 \mu\text{m}$  pixel image resolution. In Figure 3–9.a the droplet generator was tuned to operate at 57kHz, producing droplets with a diameter of  $60 \mu\text{m}$ . In Figure 3–9.b the droplet generator was operating at 16kHz and the size of the produced droplets is  $105 \mu\text{m}$ . In order to achieve sufficient statistical data, multiple pictures were recorded and as consequence the droplet count exceeds 100.

The raw signals presented in Figure 3–9 from the optical probe and the monitor photo-diode are presented in Figure 3–10 for the two droplet diameters. The data are acquired at a sampling rate of 62.5MHz over a period of 8 msec with a resolution of 12 Bit. As shown in Figure 3–10, the offset signal of

the FRAP-OB probe (sensor's dark current) is 14.5mV and the RMS noise is  $\pm 0.6\text{mV}$ .

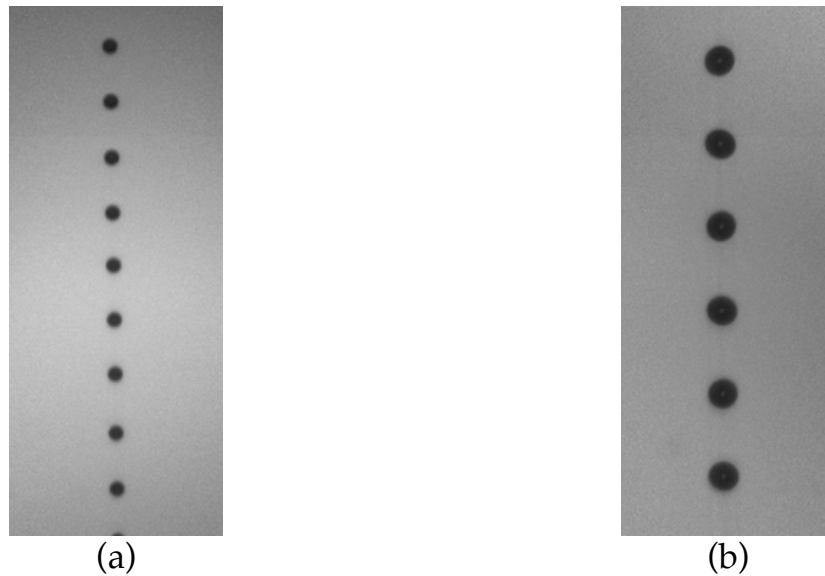


Figure 3-9: Raw images from reference camera for 60 $\mu\text{m}$  droplet diameter (a) and 105 $\mu\text{m}$  droplet diameter (b).

The FRAP-OB signal has a rising slope since it collects back-scattered light when a droplet travels through the sample volume. One can say that in this case the scattered light is “reflected” and afterwards is captured from the probe’s photodiode. On the other hand, the signal from the monitor diode demonstrates a falling slope, since it collects forward scattered light and the droplet “blocks” light, when it crosses the sample volume. As shown in Figure 3-10.a and b, the larger the droplet size is the higher the backscattered light is. Therefore, in order to find the correlation between the droplet diameter and the probe’s output signal, the droplet generator was tuned to produce various droplet sizes with a step of 10 $\mu\text{m}$  and the respective pulse amplitude signals from the probe are compared.

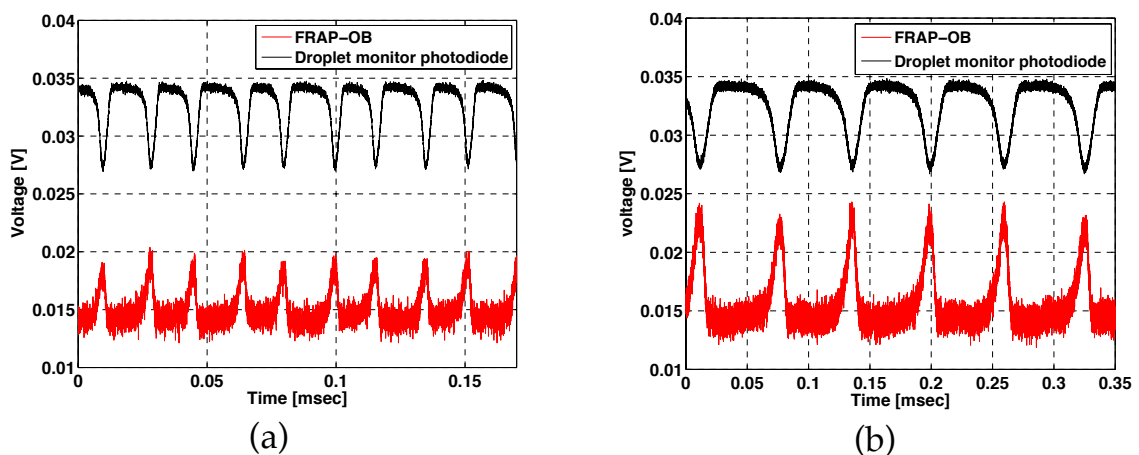


Figure 3-10: Probe and monitor photodiode raw signals during calibration for 60 $\mu\text{m}$  droplet diameter (a) and 105 $\mu\text{m}$  droplet diameter (b).

For each individual droplet the two main parameters that are extracted are the pulse amplitude and the pulse width. Using the reference camera data, the pulse amplitude is correlated to the size of the droplet and the pulse width to the speed that the droplet travels. As presented in Figure 3–11, the pulse amplitude is measured from a threshold value that is  $3\sigma$  of the noise level and the pulse width is calculated at  $1/e^2$  (13.53%) of the peak height.

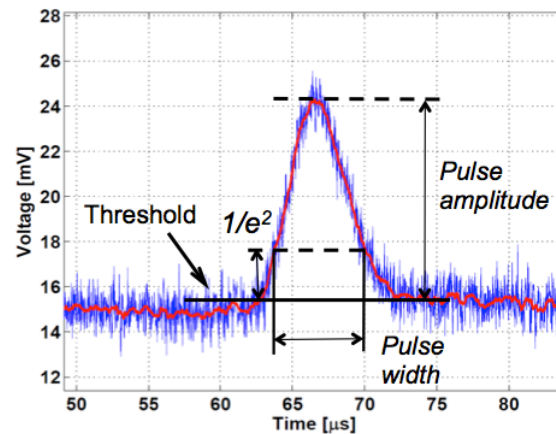


Figure 3–11: Single droplet measured parameters after calibration.

The resulting calibration curve is presented in Figure 3–12. The calibration curve correlates the maximum measured pulse amplitude (probe's output signal) to the respective droplets' diameter obtained using the reference camera. The droplets always cross the two intersecting light paths (laser beam and observer light path, (Figure 3–1) perpendicularly, which implies that the droplet jet and the probe axis are perpendicular to each other.

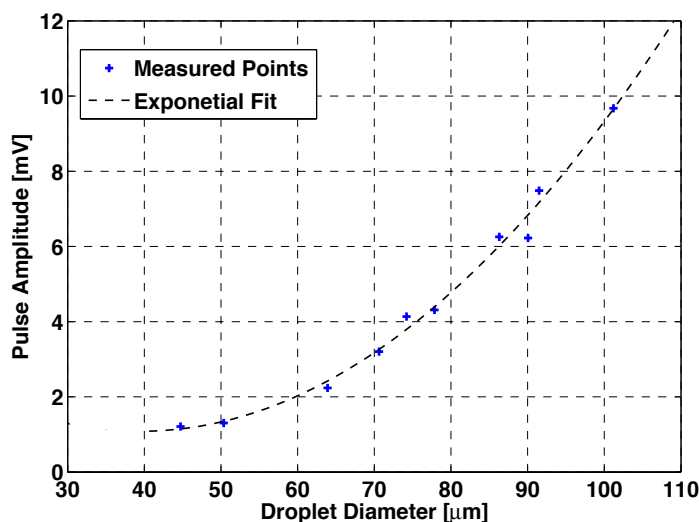


Figure 3–12: Calibration curve of the optical backscatter probe with water droplets obtained from the droplet generator.

The response of the probe as a function of droplet size exhibits some oscillations, resulting in a correlation factor of  $R^2=0.957$  between the exponential



fit and the calibration data. As shown in Figure 3–13, the theoretical response of the backscattered light as a function of water droplet diameter, calculated with the Mie theory, does not increase monotonically. Therefore the relatively poor correlation factor of the calibration curve fit is a direct consequence of the oscillatory behavior of the backscattered light intensity as a function of the droplet diameter. For instance, in Figure 3–13 the dashed line shows an amplitude response signal that corresponds to two different droplet diameters. Simulations have shown, that a response of 0.28 corresponds to the droplet diameters of 53 and 60 $\mu\text{m}$  resulting in an uncertainty of  $\pm 3.5\mu\text{m}$ . Similar trends from simulations or experiments are reported in [50, 54, 90]. The non-monotonic behavior of the theoretical Mie scattering response leads on average to  $\pm 3\mu\text{m}$  uncertainty related to the calibration model exponential curve fit. These uncertainties are taken into account and will be described in paragraph 3.3 (Uncertainty analysis).

The measurements in the turbine test facility (LISA) presented in chapter 4, were conducted at different droplet entry angles compared to the calibration curve. The main droplet direction in the flow path was  $49^\circ$  instead of the  $90^\circ$  that was described in this calibration procedure. Therefore additional sensitivity studies were performed in order to verify the validity of the probe results under various crossing paths of the water droplets. The discrepancies found between the different calibration curves are within the calibration uncertainty bandwidth of the optical backscatter probe and therefore, for the droplet size measurements the same calibration curve was applied for the  $49^\circ$  as well as for the  $90^\circ$  tilting angle.

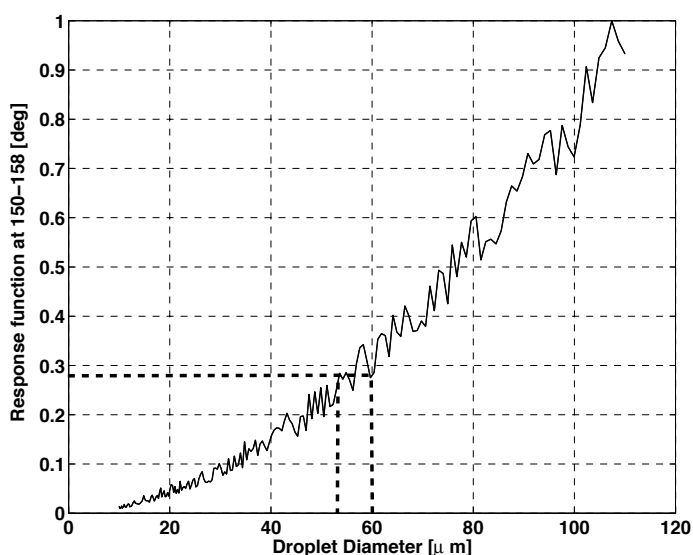


Figure 3–13: Theoretical response function in the backscatter region for water, calculated from the Mie theory out of simulations.

### 3.2.5.2 Calibration for speed measurements

In order to be able to obtain the speed of the droplets in an unknown flow field environment, a calibration procedure was performed with the same calibration set up as presented in Figure 3–8. The velocity of the droplets was calculated from the images taken with the reference camera by multiplying the distance between the two consequent droplets with the droplet generation frequency Eq.(3-4),

$$V_d = L \cdot fg \quad (3-4)$$

Knowing the droplet speed and the pulse width (residence time,  $t_{res}$ ) as depicted in Figure 3–11, one can calculate the effective beam diameter, which is the laser beam diameter that a droplet “sees” when it crosses the sample volume with Eq.(3-5),

$$D_{eff} = V_d \cdot t_{res} \quad (3-5)$$

This effective beam diameter is a function of the droplet diameter since the scattering surface of a large droplet is greater compared to a small one in the same location of the sample volume. This trend is only valid when the laser beam diameter is completely symmetrical in all directions and therefore the scattered signal does not depend on the direction in which the droplets that will cross the sample volume are travelling. The result of the droplet calibration speed is shown in Figure 3–14.a and b for the two calibration cases. Both cases show relatively low scatter around the mean value and constant effective beam diameter as a function of droplet diameter. There is a small change on the linear curve fitting between the two cases as shown in Figure 3–14. This small change on the slope can be attributed to the non-symmetrical shape of the laser beam shape. Nevertheless, the results have shown that the effect on the entry angle of the droplet to the probe’s sample volume can be neglected.

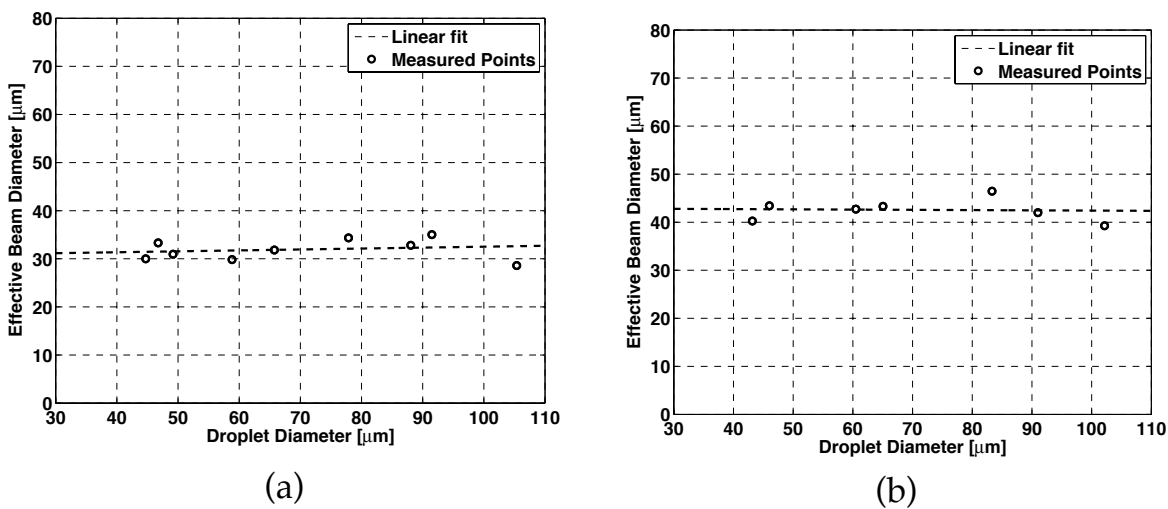


Figure 3–14: Effective beam diameter as a function of droplet diameter for calibration tilting angle 0° (a) and tilting angle 49° (b).

### 3.2.5.3 Correction for side effect error

In this section, the correction routine accounting for the side effect error is described. This error is responsible for the underestimation of droplet size when the droplet crosses the sample volume partially. The calibration set up allows for the quantification of this error and in a second step, the development of a correction algorithm. The calibration curve presented in Figure 3–12 is obtained using monodispersed water droplets ranging from 40 to 110 $\mu\text{m}$  in diameter with step increases of about 10 $\mu\text{m}$ . In order to assess the magnitude of the underestimation in droplet size, the response to the optical backscatter probe was mapped by moving the probe relative to the calibration system using high precision (5 $\mu\text{m}$ ) linear translation stages. During the calibration procedure, described in paragraph 3.2.5.1, the final calibration curve (see Figure 3–12) was a result of the maximum light scattering intensity. In this case the droplets were crossing the sample volume at its center. By moving the probe in the XY plane perpendicularly to the droplet train, the response output across the sample volume was mapped for each droplet diameter used in the calibration of the probe. The results are shown in Figure 3–15, which illustrates that for the same droplet size the probe output varies between a minimum and maximum value (two dashed lines). In the same plot the droplet diameter is non-dimensionalized with the beam diameter. Since the side effect error depends on the droplet size as described above, the deviation of the two curves for large droplets is higher in comparison to small droplets. In other words, the probability of small droplets (up to 50 $\mu\text{m}$ ) partially crossing the sample volume is reduced significantly but the probability of large droplets (range of 100 $\mu\text{m}$ ) partially crossing the sample volume is increased for the current design of the FRAP-OB probe.

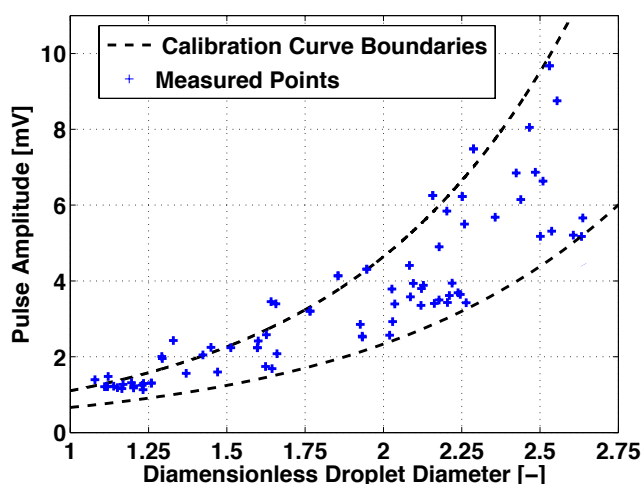


Figure 3–15: Probe's output signal (mapping) when droplets are partially crossing the sample volume.

As a result, it is evident in Figure 3–15 that due to side effect error the response output (pulse amplitude) of the probe for a constant voltage results in a certain range of droplet diameters. As shown in Figure 3–15, this range is set by the two boundaries of the dashed lines. In order to correct this behavior, a probability distribution function was modeled for the whole spectrum of the droplet diameters from  $40\mu\text{m}$  to  $110\mu\text{m}$ . Based on the measured scatter of the calibration data described in Figure 3–15, the probability distributions for the small and large droplets were identified to follow a normal (red) and a skewed normal (blue) distribution as shown in Figure 3–16.

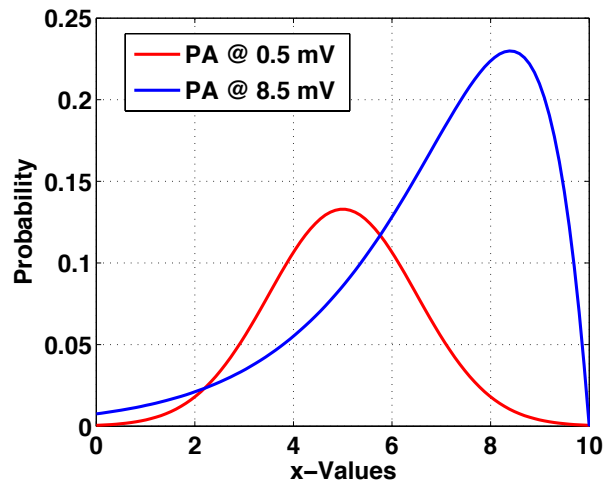


Figure 3–16: Droplet's diameter probability distribution function related to the probe minimum signal amplitude (PA=0.5mV) and maximum signal amplitude (PA=8.5mV).

For the current correction model, an output signal that corresponds to small droplet sizes will be modeled with a normal distribution that has its boundaries between the two dashed lines in Figure 3–15. On the other hand, the output signal for the large droplet sizes will be modeled with a skewed distribution, as presented in Figure 3–16, in order to account for the greater probability of the side effect error with increasing droplet diameter. All intermediate droplet diameters have probability distributions that will gradually vary from normal to normal skewed distribution. The resulting three-dimensional probability distribution correction model is presented in Figure 3–17.

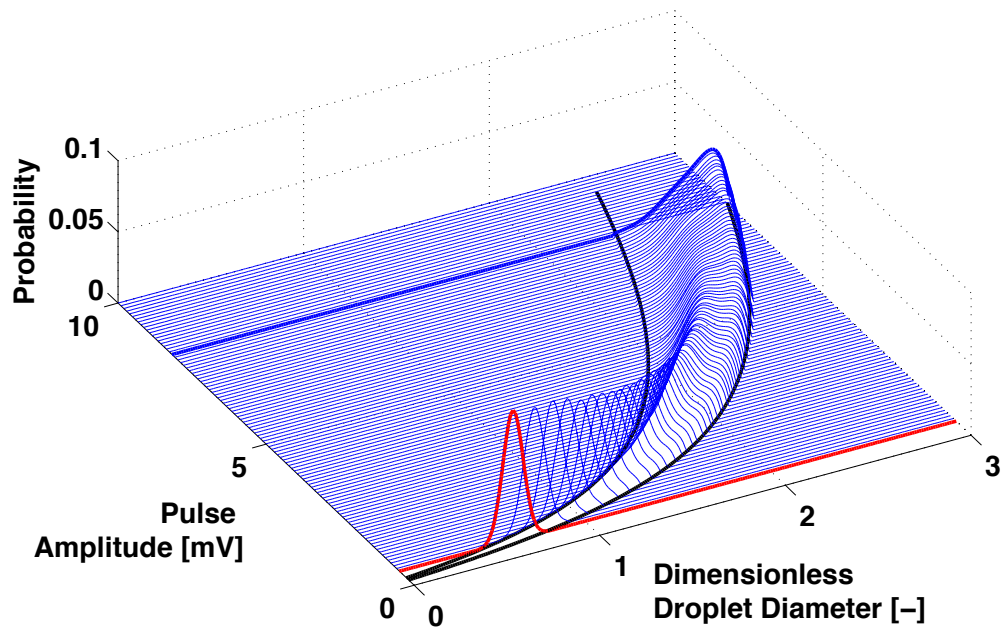


Figure 3–17: Probability distribution model for the calibrated range of the optical backscatter probe.

Each measured droplet distribution is corrected by applying the probability distribution model to the measured distribution described above. The results are shown in Figure 3–18.a and b, and as expected the correction model shifts the distributions towards larger droplet diameters in order to account for the side effect error. As presented in Figure 3–18, in the case of small and large droplet distributions, the Sauter mean diameter has increased from 62 to 70 $\mu\text{m}$  and from 80 to 93 $\mu\text{m}$  respectively. The sample size for the distributions of Figure 3–18.a and b is 200 droplets.

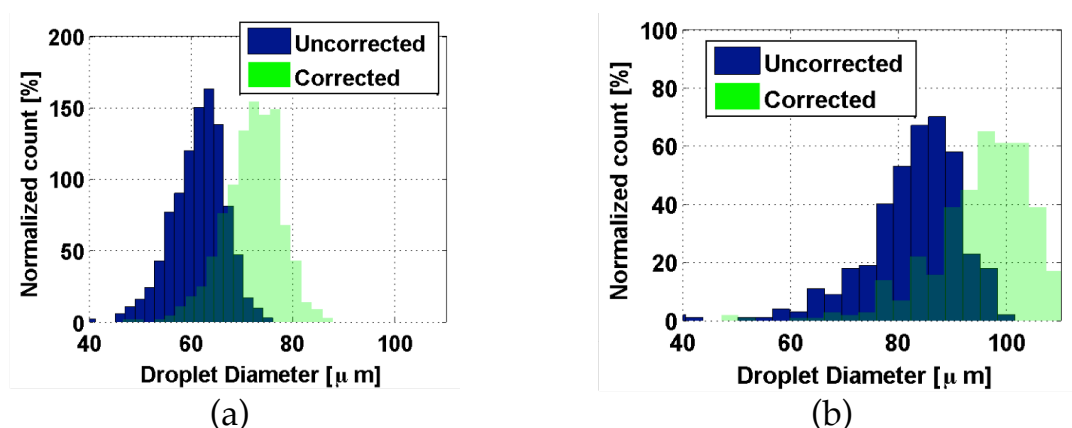


Figure 3–18: Correction example of small (a) and large (b) droplet distribution by applying the probability distribution model.

### 3.3 Uncertainty analysis

In this section the sources of measurement errors related to the optical backscatter probe are identified and the resulting overall uncertainties in derived droplets' diameter and speed are calculated. The whole chain of uncertainty sources has been accounted for starting with the uncertainties resulting from the calibration references as well as the uncertainty sources related to the measurements. The resulting overall uncertainties are calculated using the Gaussian error propagation formula. The uncertainty calculation was performed using the Guide to the Expression of Uncertainty in Measurement (GUM) Workbench [79] as with the FRAP-HTH probe described in 2.2.

#### 3.3.1 Calibration uncertainties

Since the sensitivity of the calibration model curve of the probe is not constant within the calibration range (exponential behavior), the uncertainty analysis for the calibration procedure is divided into three regimes to better describe the uncertainties. These three ranges are from 40 to 65 $\mu\text{m}$ , from 65 to 85 $\mu\text{m}$  and from 85 to 110 $\mu\text{m}$  in droplet diameter. For each calibration range the uncertainty analysis is performed using the mean value in that particular regime. Table 6 lists the sources of uncertainties from the calibration procedure of the optical backscatter probe.

Table 6: Sources of uncertainty (expanded with coverage factor 2) related to the calibration procedure.

Source of uncertainty:	Parameters			Units
	low 40-65	mid 65-85	high 85-110	
Reference camera system	$\pm 0.43$	$\pm 0.56$	$\pm 0.56$	$\mu\text{m}$
Uncertainty due to non monotonic behavior	$\pm 3.5$	$\pm 4$	$\pm 3$	$\mu\text{m}$
He-Ne power laser drift stability	$\pm 2$	$\pm 2$	$\pm 2$	%
Voltage measurement with DAQ system	$\pm 0.02$	$\pm 0.02$	$\pm 0.02$	mV

The uncertainty for the reference camera system is derived from the ratio of the minimum pixel size divided by the magnification factor (camera zoom). The second source of uncertainty is derived from the non-monotonic behavior of the light scattering from the droplet in the backscatter region. As shown in Figure 3-13 and described in the corresponding paragraph, the theoretical response of the backscattered light as a function of the water droplet diameter does not increase monotonically. In order to have a model that describes this relationship monotonically, the fluctuations on the response signal have to be accounted for. Therefore, the uncertainty in droplet diameter from the model is  $\pm 3.5\mu\text{m}$ ,  $\pm 4\mu\text{m}$  and  $\pm 3\mu\text{m}$  for the low, middle and high regime respectively. In addition, the power drift of the laser is included in the uncertainty chain analysis. According to the manufacturer, this is  $\pm 2\%$  over a period of 8 hrs.

and corresponds to backscatter signal fluctuations during calibration. Last but not least, the uncertainty on the voltage measurement is set by the 12 Bit acquisition system used over an analogue input range of  $\pm 100\text{mV}$ , which provides a maximum signal voltage resolution of  $\pm 0.02\text{mV}$  and is constant for all regimes. Combining the above sources of uncertainties, the absolute error in droplet's diameter from the calibration procedure for the low, central and high regime is calculated to  $\pm 4.1$ ,  $\pm 4.7$  and  $\pm 3.5\mu\text{m}$  respectively.

### 3.3.2 Measurement uncertainties

In addition to the calibration uncertainties, the uncertainties during the measurements in the axial turbine test facility LISA are presented in the current paragraph. The main sources of uncertainties during measurements are the coincidence error as well as the laser drift stability as described above. The side effect error is not included in the current calculation since the correction model is applied in the post processing code to account for it (see §3.2.5.3). In addition, the resulting errors from the calibration procedure for the three distinct regions are included in the error propagation calculations for the measurements. The uncertainties from the measurements are presented in Table 7 and the overall uncertainty of the probe for the three regimes is calculated to  $\pm 4.7$ ,  $\pm 5.4$  and  $\pm 4.0\mu\text{m}$  respectively. In the current measurement campaign the averaged droplet speed results are in the range of 40 to 50m/s. The calculated uncertainty of the speed measurements is  $\pm 2.3\text{m/s}$ .

Table 7: Sources of uncertainty (expanded with coverage factor 2) from the measurements.

Source of uncertainty:	Parameters			Units
	low 40-65	mid 65-85	high 85-110	
Calibration procedure	$\pm 4.1$	$\pm 4.7$	$\pm 3.5$	$\mu\text{m}$
Coincidence error	$\pm 2.5$	$\pm 2.3$	$\pm 2$	%
He-Ne power laser drift stability	$\pm 2$	$\pm 2$	$\pm 2$	%
Voltage measurement with DAQ system	$\pm 0.02$	$\pm 0.02$	$\pm 0.02$	mV
Overall uncertainty	$\pm 4.7$	$\pm 5.4$	$\pm 4.0$	$\mu\text{m}$

### 3.4 Single measurement point processing algorithm

For the new optical backscatter probe a multi-step post-processing algorithm for droplet detection was developed. As mentioned previously, the FRAP-OB probe is a single particle detector. This implies that every droplet that crosses the sample volume of the probe (see Figure 3–1) will generate an output signal. The backscatter signal from small droplets is at least three to four orders of magnitude lower than the respective forward scattering signal, which leads to a relatively low signal-to-noise ratio for droplets in the lower diameter range. In addition, as mentioned previously, in order to detect droplets with high velocities, the probe is equipped with a high bandwidth amplifier. As a consequence, the probe signal collects noise from surrounding devices affecting the signal-to-noise ratio over a wide range of frequencies. A flow chart of the post-processing algorithm is presented in Figure 3–19. The pulse amplitude and width are extracted from the raw data of the probe following the procedure described in the following paragraphs.

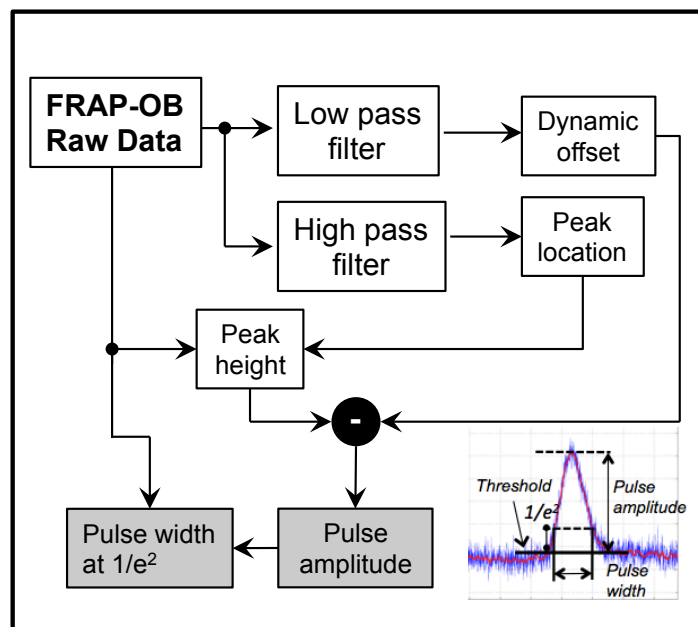


Figure 3–19: Flow chart of the post processing algorithm for the optical backscatter probe.

A typical raw data file is shown in Figure 3–20.a. Over a measurement time period of 320msec the droplets appear as single vertical lines. Figure 3–20.b shows the signal over a reduced time period of 6 msec and it illustrates that the detected droplets as well as external periodical noise signatures fall into the same amplitude response. In order to allow for accurate measurements and extend the lower droplet diameter detection range several signal-filtering and detection steps have to be applied as presented below.



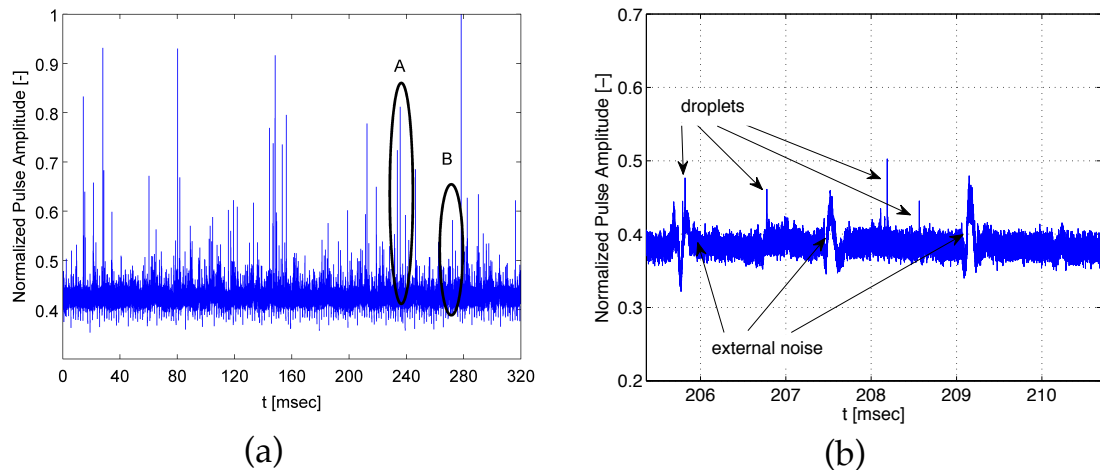


Figure 3–20: Single measurement point raw data file over 14 rotor revolutions (a) and the same raw file zoom in over 4 detected droplets (b).

The filtering steps include the utilization of a high pass filter to locate the droplets by filtering out low frequency external noise content while keeping fast droplets' signals content. The utilization of a low pass filter is performed in a second step in order to get the dynamic ground signal of the probe (sensor's dark current) by keeping the external low frequency periodic noise. The steps are the following.

Apply High Pass filter:

- Calculate the mean value ( $\mu$ ) and the standard deviation ( $\sigma$ ) of the ground noise of the signal
- Locate the droplets on the high pass filtered data as shown in Figure 3–21.a. When the peak voltage is above the value of  $\mu+3\sigma$  from the ground noise the sample (time) of that peak is stored

Apply Low Pass filter:

- Get the dynamic ground signal of the probe that follows any external noise (Figure 3–21.b)

Calculate the pulse amplitude of each droplet:

- Check on the raw data (Figure 3–21.b) the location (sample) where the droplets were recorded in the first step with the HP filter
- Calculate at that location the voltage difference between the peak and the dynamic ground signal obtained from the LP filter.

The dynamic ground signal is indicated as a red line in Figure 3–21.b and the droplets, which have been tracked are highlighted in the same figure with a black triangle. In the post-processing step the considered peaks are checked for reliability. There are several criteria that have to be fulfilled in order to consider the measured signal as a valid droplet. The droplets that fulfill these criteria are marked with a triangle at their signal peak height.

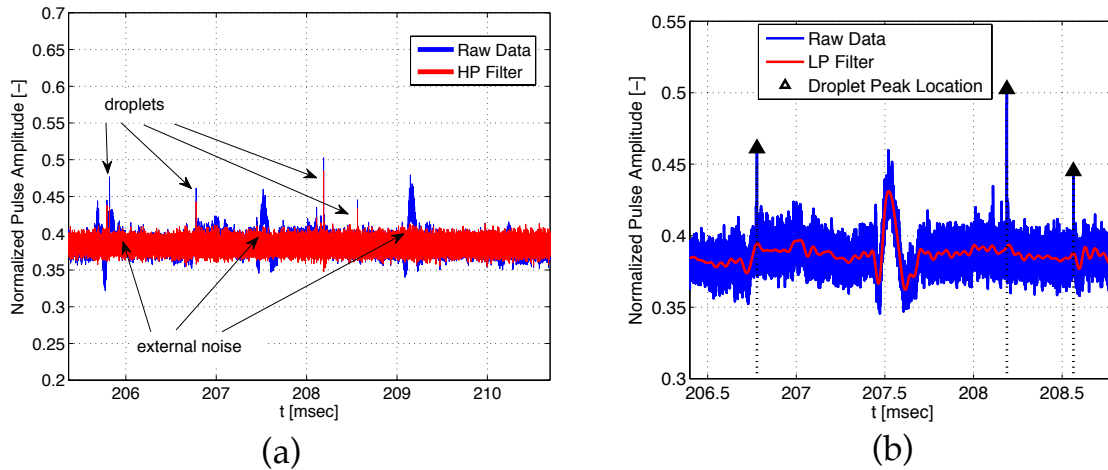


Figure 3–21: Utilization of high pass filter (a) and low pass filter (b) in raw data.

A valid detected droplet at time location A (see Figure 3–20.a) is presented in Figure 3–22.a. The signal is a symmetrical Gaussian profile as recorded during the calibration procedure implying a valid droplet. For each valid droplet the pulse amplitude is measured as well as the pulse width at  $1/e^2$  of the total peak height. The peak height in Figure 3–22.b that shows the detected droplet at time location B (see Figure 3–20.a) is not valid. The signal pattern reveals that this particular droplet is not spherical since the shape of the signal does not match with the calibrated one. Therefore in the last step of the data processing this droplet is not counted. The detection criteria of the post-processing algorithm are mainly related to shape, size and signal-to-noise ratio of the recorded signals. At this measurement location of Figure 3–20.a, 352 droplets were detected and plotted in the same graph.

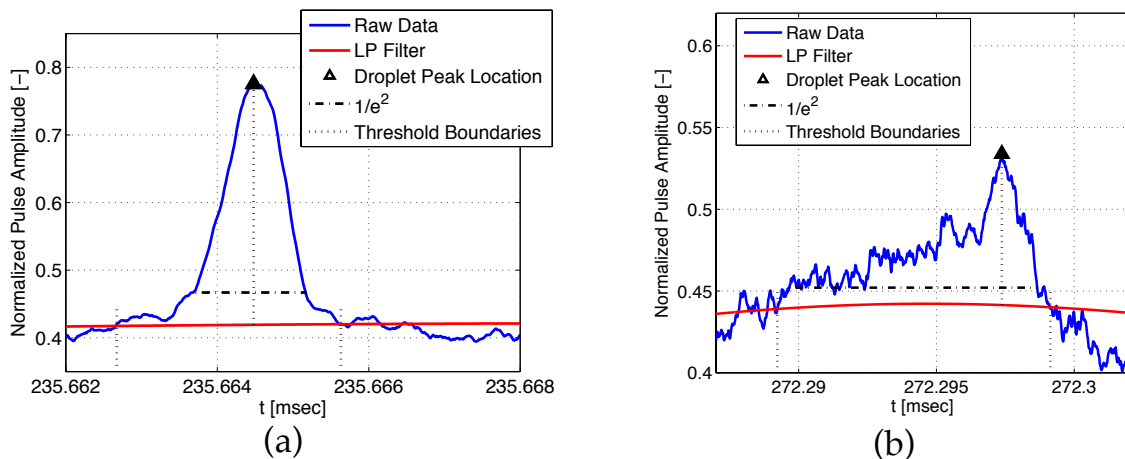


Figure 3–22: Zoom in a single valid droplet at time location A (a) and a non valid droplet at time location B (b) of Figure 3–20.

In the last step of the post-processing routine the voltage signals of the valid droplets are converted to droplet diameters and speed and are plotted in a histogram distribution graph for each single measurement point. Figure 3–23 and Figure 3–24 show the droplet size and speed distributions respectively

from the raw data file as presented in Figure 3–20.a. The three main parameters that can be extracted for the size are the  $D_{10}$ ,  $D_{32}$  and  $D_M$  and for the velocity the average value ( $V_{10}$ ) as well as the most frequent value  $V_M$ .

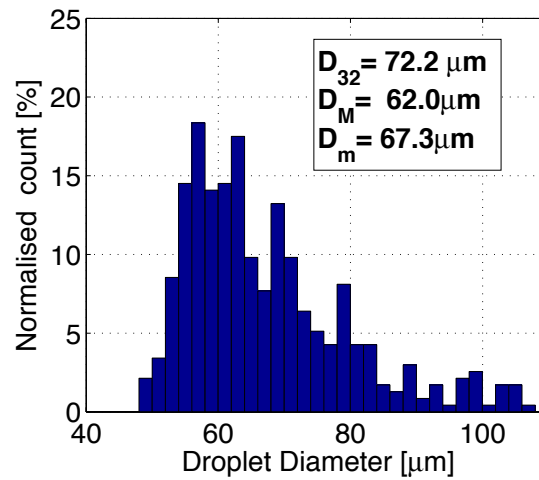


Figure 3–23: Single measurement point probe representation results. Voltage peak heights that fulfil the detection criteria are converted into droplet size and presented as a size distribution histogram.

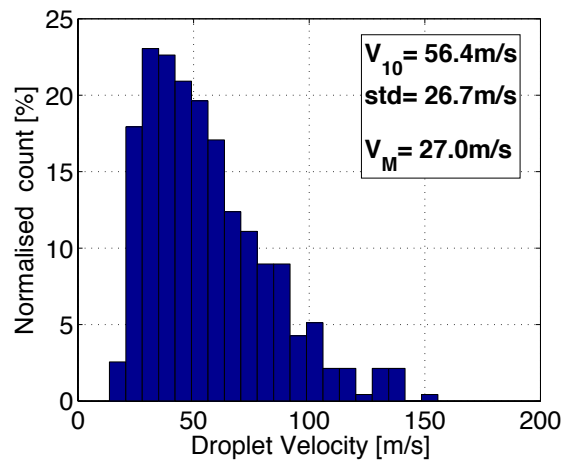


Figure 3–24: Single measurement point probe representation results. Voltage pulse widths that fulfil the detection criteria are converted into droplet velocity and presented as velocity distribution histogram.

### 3.5 Phase lock averaging concept for droplet measurements

The phase lock-averaging concept for coarse water droplets with the FRAP-OB probe is described in the current paragraph of the thesis. When implementing the phase lock-averaging concept, there is a principal difference between the two probes due to their different signal type. The FRAP-HTH probe provides a continuous pressure signal with time intervals of  $1/200,000$  seconds. On the other hand, the FRAP-OB probe has discrete measurement points for every detected droplet that has crossed its sample volume. Figure 3–25 shows the measured droplets with the FRAP-OB probe for 2 rotor revolutions. The detected droplets are marked with the triangle and the rotor trigger with the blue curve. In addition, Figure 3–25 shows the number of the rotor blades with red, which is 54 for one rotor revolution (one-and-one-half-stage axial turbine LISA, see chapter 4).

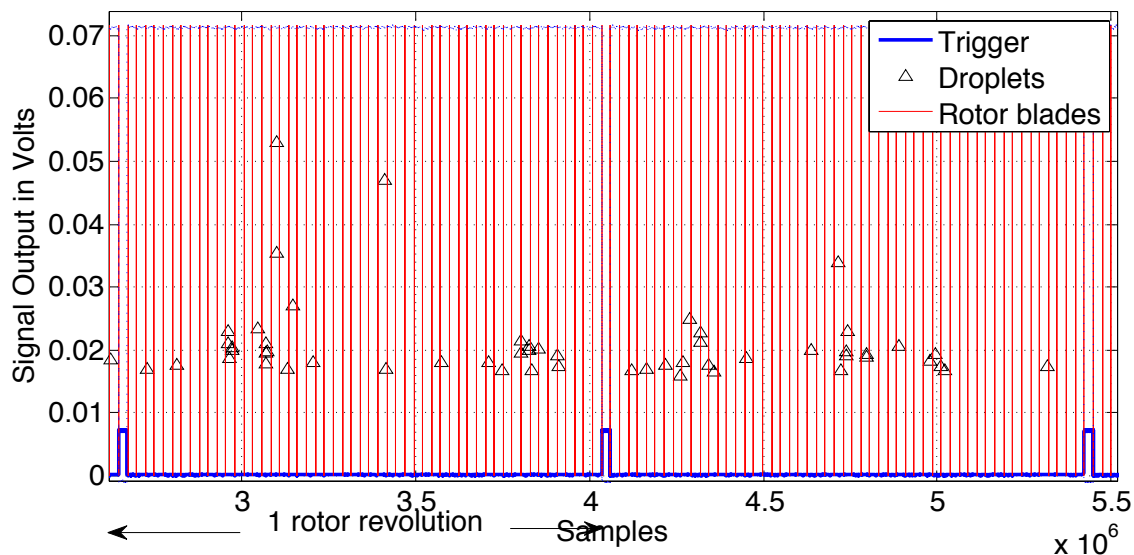


Figure 3–25: Detected droplets for two rotor revolutions as they are spread among the difference blade passages.

In order to phase lock average the FRAP-OB data, each rotor blade passage is partitioned into 10 sections. Figure 3–26 shows the rotor blade passage, which is indicated as “1 rotor blade passing period”. This passage is divided, into 10 equal time portions and the individual droplets that were found in each of these sections are superimposed for 90 blade passage events, phase locked with reference to rotor trigger. There are cases where there is marginal number of detected droplets and the total number of droplets for each section does not exceed 30 when superimposed over 90 revolutions. For example the first rotor passage (samples:  $4.04 \times 10^6$  to  $4.06 \times 10^6$ ) for this particular rotor revolution in Figure 3–26, has no detected droplets. Nevertheless droplets are detected in the 4<sup>th</sup>, 6<sup>th</sup> and 8<sup>th</sup> rotor passages as indicated in Figure 3–26. In order to increase the accuracy of the results in this case, the detected droplets in every section are summed up for all rotor blades over one rotor revolution. As

a consequence, the data that are phased locked over 90 revolutions in the second step, contain sufficient amount of droplets to increase the accuracy of the FRAP-OB results.

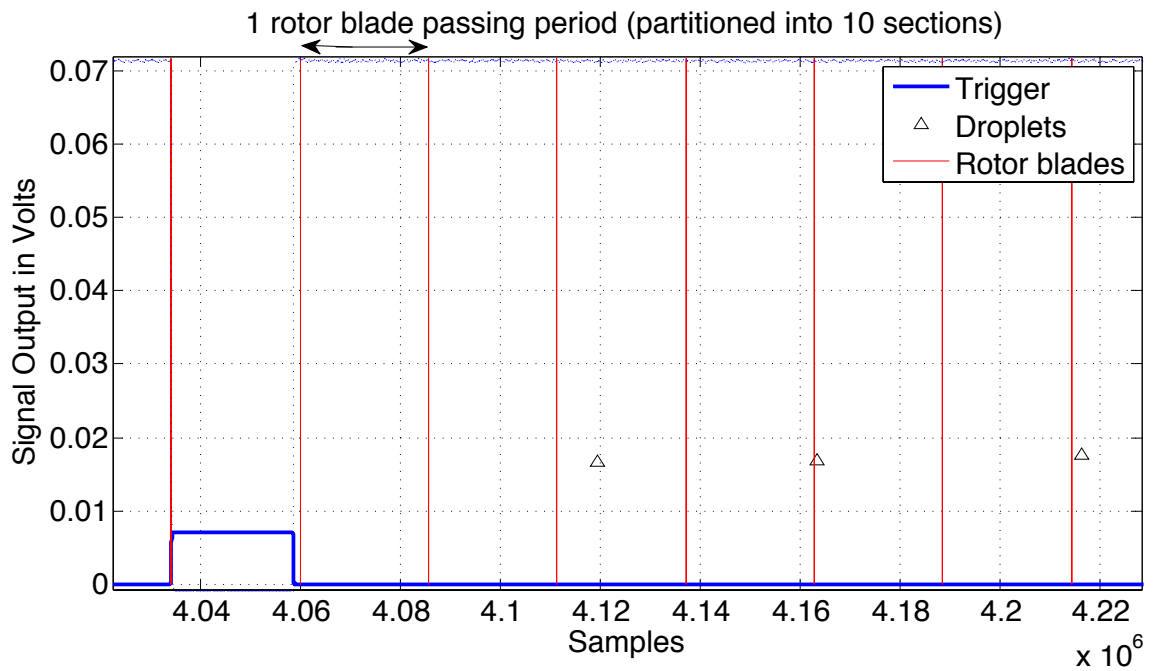


Figure 3–26: Rotor blade passing period as it is partitioned into ten sections.

### 3.6 Summary

The design and development of a novel fast response optical backscatter probe for coarse water droplets was presented in this chapter. The novel miniature probe has a tip diameter of 5mm and comprises of optical components for focusing a laser beam and collecting the backscattered light from droplets when crossing the probe's sample volume. The fast response photodiode used, enables droplet measurements in the range of 40 to 110 $\mu$ m in diameter in an environment with droplet concentration up to  $10^{11}$  droplets/m<sup>3</sup>. The design of the probe provides high spatial and temporal resolution suitable for unsteady measurements in the flow path of a large range of turbomachines.

In addition, the detailed calibration procedure is described. The calibration is conducted with a droplet generator capable of producing monodispersed water droplets from 40 to 110 $\mu$ m in diameter. The measurement bandwidth of the new probe is 30MHz, which is capable of resolving droplet speeds up to 170m/s. Substantial effort to reduce errors related to the operating principle of the probe was made. This sets the overall calculated uncertainty, accounting for all sources of errors for the diameter and speed measurements, to  $\pm 4.7\mu$ m and 2.3m/s respectively.

Finally a post-processing algorithm to allow for droplet measurements in working environments with high surrounding noise is described. The developed routine increases the signal to noise ratio by a factor of 2, enabling accurate measurements in the low droplet range below 50 $\mu$ m in diameter.

As it will be shown in chapters 4 and 6 the probe has demonstrated its ability to performed accurate measurements in severe environments with droplet-laden flows in several measurement campaigns

## 4 Measurements in one-and-half-stage axial turbine equipped with a spray generator

This chapter presents the experimental results obtained with the FRAP-OB probe from one-and-half-stage axial turbine test facility operating with air. The facility was equipped with a spray generator and two different operating conditions were measured at two different axial locations downstream of the stator. Time averaged and time resolved results are presented with the droplet diameter and concentration measured data.

### 4.1 Experimental set up

The experimental study was carried out in the research axial turbine facility "LISA" in the Laboratory for Energy Conversion at ETH Zurich. The one-and-a-half stage, unshrouded, highly loaded axial turbine with 3D blading is a representative of modern high-pressure gas turbine. The research turbine facility consists of a quasi-closed air loop, which includes a single stage radial compressor, a two stage water-to-air heat exchanger and a calibrated venturi nozzle for accurate mass flow measurements. Upstream of the turbine test section there is a 3m long flow conditioning stretch in order to ensure a homogeneous flow field. A DC generator absorbs the turbine's power and controls the rotational speed with an accuracy of  $\pm 0.02\%$  ( $\pm 0.5\text{rpm}$ ). The water-to-air heat exchanger controls the inlet total temperature to  $\pm 0.3\text{K}$ . The compressor ratio can be regulated in order to operate in design or part load conditions. A schematic of the experimental facility is shown in Figure 4–1.

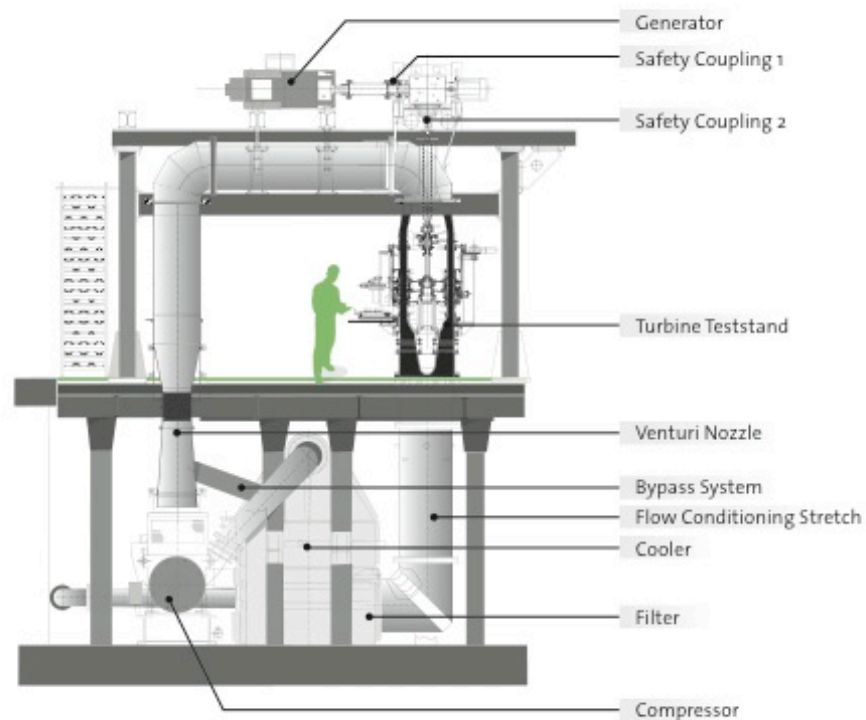


Figure 4–1: Schematic of LISA turbine test facility.

For the current measurements, the facility was equipped with a 1.5 stage of an axial turbine that is described in Behr et al. [91]. Two operating conditions were studied, one at nominal operating design point and one at part load to investigate the droplet formation at reduced relative flow velocities. The rotor rotational speed for all operating conditions was kept constant at 2700rpm, which corresponds to a rotor blade passing frequency of 2430Hz. The FRAP-OB results presented in this chapter were made at two axial downstream locations from the trailing edge of stator 1, one at 2% and the second at 8% stator axial chord. As shown in Figure 4–2, the measurement grid is comprised of 21 points in the radial direction covering the stator span from 10% up to 90%. In the circumferential direction the measurement grid consists of 41 equally spaced traverses that cover one stator pitch (10°). The data were acquired at a sampling rate of 62.5MHz over a period of 320msec and the main operating parameters and conditions are summarized in Table 8.

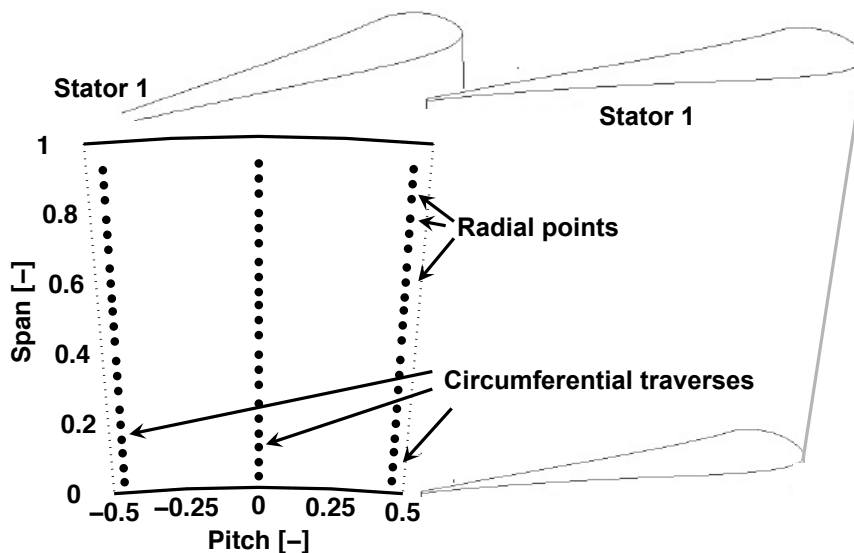


Figure 4–2: Measurement grid schematic at the experiments performed in LISA test rig. The observer looks upstream. The measurement grid consists of 21 x 41 points equally spaced in the radial and circumferential direction respectively, and covers one full stator pitch (10°) from 5% to 90% of the blade span.

Figure 4–3 shows, the custom-made water spray generator which was installed 5 stator chords upstream of the test section. The current droplet generator is capable to generate a spray with droplet diameters from 1 to 200 $\mu$ m covering one and half stator passage and injecting at mid-span location with a mass flow of 0.16lt/min. As presented in Figure 4–4.b, the spray generator was embedded in a support strut with a standard symmetrical NACA profile to create an aerodynamic shape and minimize any interactions of the injector body with the generated water spray and airflow. Measurements were performed at the inlet plane as well as the stator 1 exit plane for the two different



operating conditions. The test facility, with the FRAP-OB probe installed on the traversing system, during the measurements is shown in Figure 4–4.a.

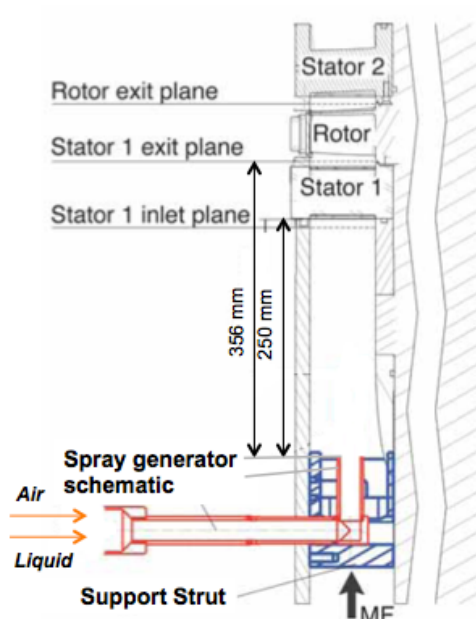


Figure 4–3: Cross section of the test segment (Turbine Teststand).

Table 8: Operating conditions and geometrical characteristics.

	Design point	Part load	Units
Rotor Rotational Speed	2700	2700	rpm
Rotor/Stator Blades	54/36	54/36	-
Rotor Blade Passing Frequency	2430	2430	Hz
Pressure Ratio 1.5-Stage,tot-stat	1.65	1.33	-
Turbine Entry Temperature	55	55	°C
Total Inlet Pressure	1.4	1.2	abs bar
Stator 1 Exit Mach number (average)	0.52	0.42	-
Stator 1 Exit Flow Angle	73.1	72.8	deg
Mass Flow	12.13	8.4	kg/s
Shaft Power	288	132	kW
Hub/Tip diameter	660/800	660/800	mm

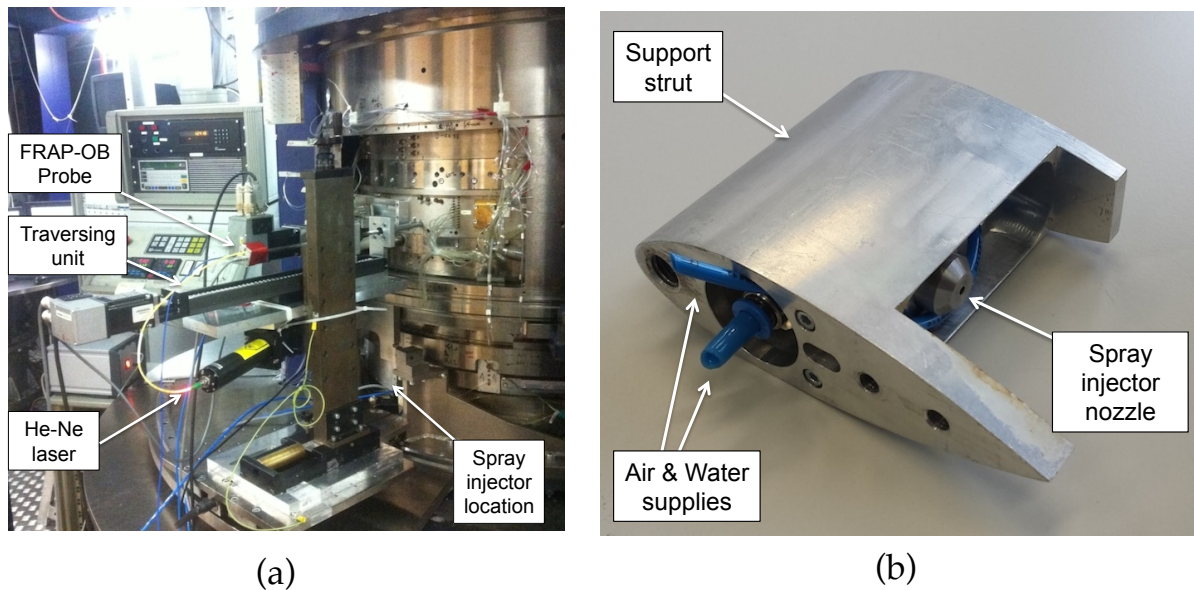


Figure 4-4: FRAP-OB probe installed on traversing unit (a) and support strut with the spray generator (b).

## 4.2 Results and discussion

### 4.2.1 Results for design and part load conditions at the location of $x/c=2\%$

In this paragraph the design and part load operating conditions results at  $x/c=2\%$  downstream of stator 1 (see Figure 4-3: Stator 1 exit plane) are presented. As shown in Figure 4-5.a all droplets above  $45\mu\text{m}$  in diameter are located at the stator's trailing edge between 20 and 85% in the spanwise direction covering approximately 20% pitch in circumferential direction. Figure 4-6 shows the time-averaged results of the Mach number downstream of the same stator. The stator wake and therefore the location of the trailing edge can be identified at  $0^\circ$  pitch from 0 to 100% span. In the same figure one can locate the hub and tip passage vortices located on stator's suction side between 0 and +0.25 pitch at 10% and 85% span respectively. In all plots the observer looks upstream. The results of Figure 4-5.a show that coarse droplets are impacting the suction side of the stator and create a film of water on its surface. As a result they exit the stator trailing edge with significant lower velocity compared to the flow field velocity as it will be shown in the next paragraphs. The same behavior is observed in Figure 4-5.b, for the part load condition, but with a wider circumferential coverage (25% pitch) and a small migration towards the center of the blade span.

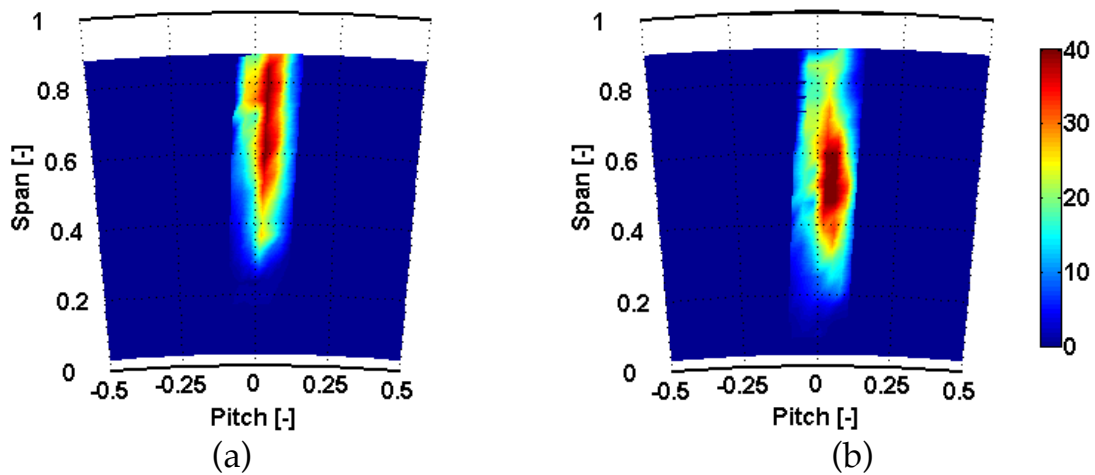


Figure 4–5: Droplet rate [droplets/rev] at Stator 1 exit plane for design point (a) and part load condition (b). Observer looks upstream.

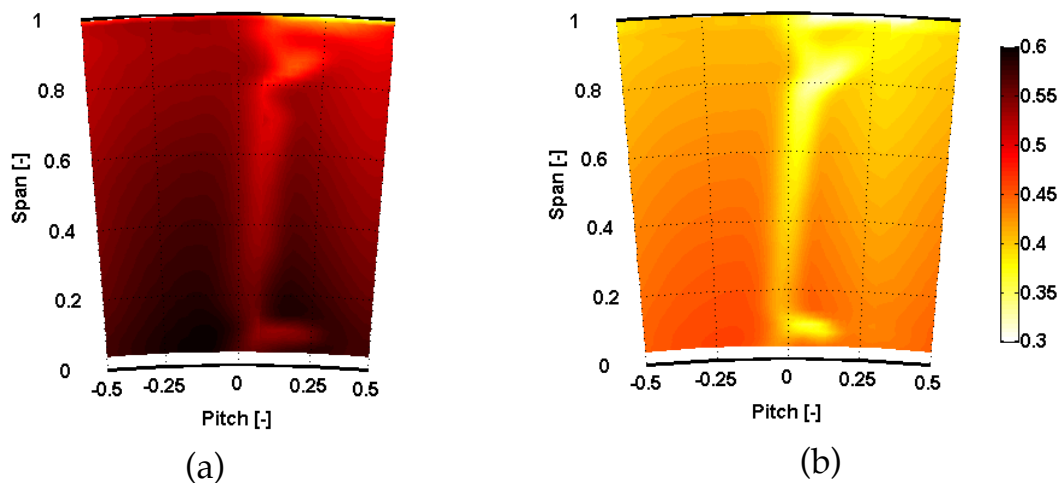


Figure 4–6: Absolute Mach number [-] at Stator 1 exit plane for design operating condition (a) and part load (b). Observer looks upstream.

In order to analyze and understand the difference in droplet size and location, the droplet size distribution is investigated at three distinct blade span locations, hub, mid and tip region at 25, 50 and 75% blade span respectively. Figure 4–7 summarizes the droplets' size distribution related to the three measured points for all operating points. Each plot contains the droplet Sauter mean diameter, Mode value of the diameter, as well as the mean value of the distribution. The droplet size distribution follows a skewed normal distribution for all cases. As depicted in Figure 4–7, two main observations emerge. The first is the reduction of the droplet size, by shifting the distributions to the left, when the relative flow velocity increases from part load to design speed. The Sauter Mean Diameter is reduced by 8%, 10% and 10.5% for the tip, mid and hub span locations respectively when the absolute Mach number increases from 0.42 to 0.52. The second observation is the increase of droplet's diameter from hub to the blade tip region. In this case, the Sauter Mean Diameter

has increased by 10.3% and 8% for the design and part load condition respectively.

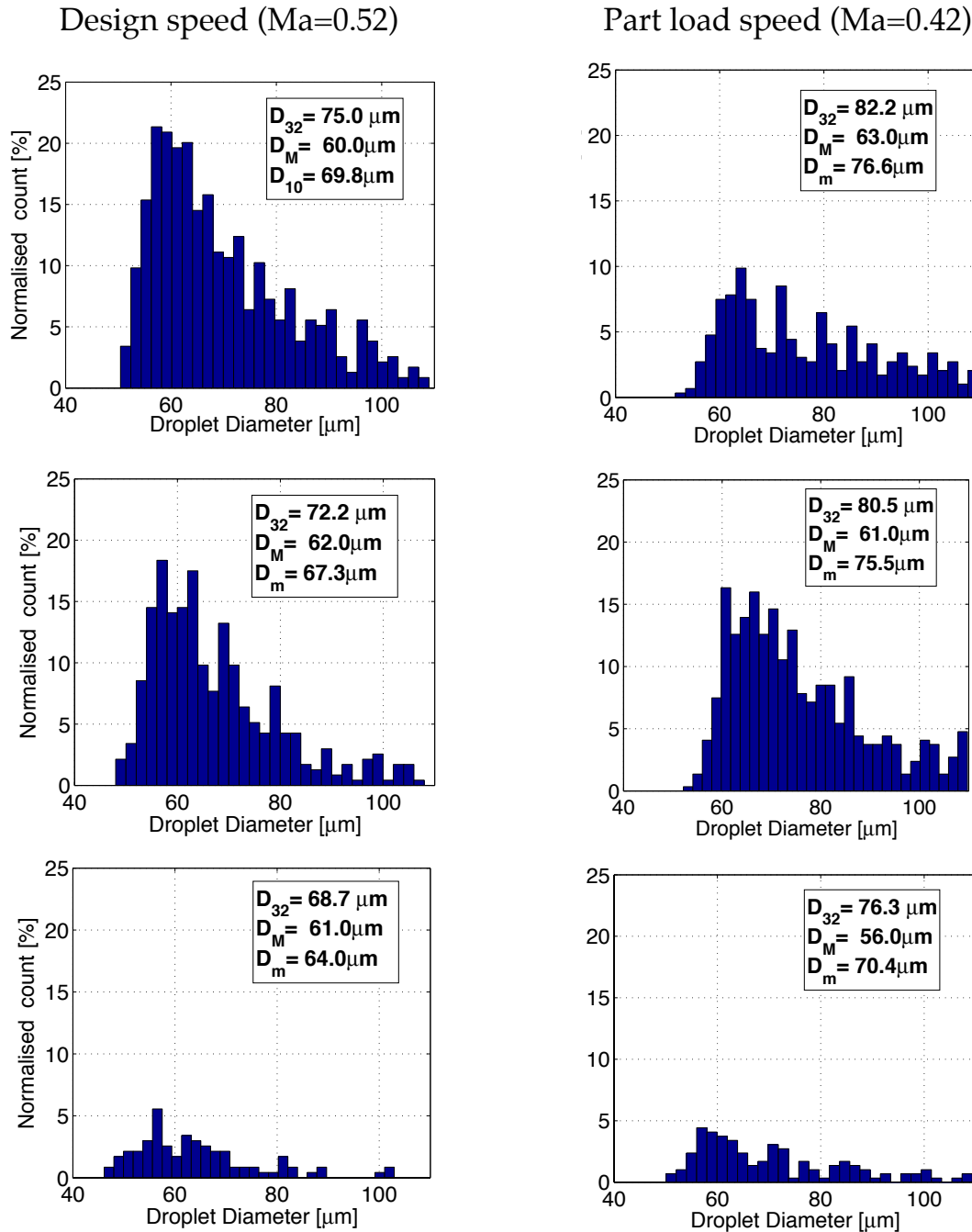


Figure 4-7: Size droplet distribution at tip (upper), midspan (center) and hub (bottom) spanwise locations for design and part load conditions at  $x/c=2\%$  downstream of stator 1 exit.

In order to explain these trends, the Weber number as expressed in Eq.(4-1) is used. The Weber number is defined as the ratio of the dynamic to the surface-tension force acting on a drop and it is a measure of the droplet stability for i.e. the ability of the droplet to maintain a spherical geometry while shear forces try to tear it apart.

$$We = \frac{D_d \cdot \rho_f \cdot |\overline{V}_d - \overline{V}_f|^2}{\sigma_d} \quad (4-1)$$

When  $We \ll 20$  the droplets are spherical and stable in size. As the Weber number increases above the value of 20 to 23 the droplets begin to deform and break up into smaller sizes [17, 43]. Following this theoretical analysis on the current results, one can say that the principal cause for the reduction on the droplet size from part load to the design operating condition is due to the increase of  $|\overline{v}_d - \overline{v}_f|^2$  term in Eq.(4-1). As consequence higher shear forces between the flow and the droplets are generated, which lead to greater values of Weber numbers resulting in larger droplets' break up.

The lower mean flow velocities at the tip region, on an average by 8% for the design condition as shown in Figure 4–8 and locally by 18% as shown in Figure 4–6, result on smaller values of We number and therefore on larger droplet diameters. This can explain the second observation where the droplet diameters are larger in the tip region of the blade span compared to the hub span locations. Additional aerodynamic results for the design operating condition can be found in [91].

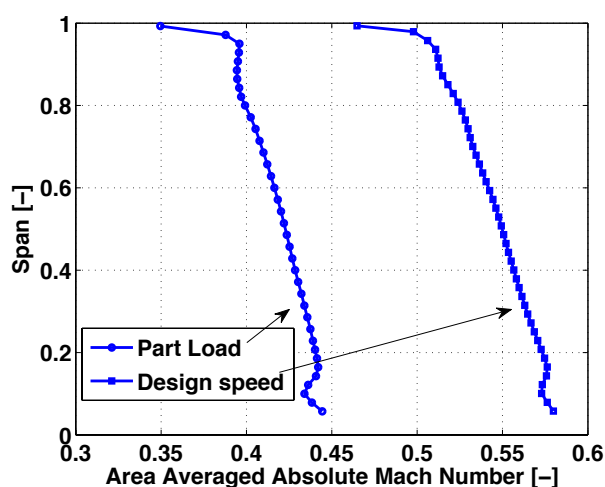


Figure 4–8: Area averaged absolute Mach number for design and part load operating conditions at Stator 1 exit plane.

Many research studies address the significance of the droplet velocity magnitude relative to the rotor tip speed velocity [11, 38, 92]. This is due to the fact that erosion rate on rotor blades is proportional to the droplet velocity and momentum described with a power law equation  $R_e \sim V_d^n$ , where  $n$  is between 3-5 [38, 92] and is a factor which is material dependent. Figure 4–9 shows a schematic of the velocity triangles at stator 1 exit plane. As depicted in Figure 4–9, the absolute droplet velocity ( $V_{d,abs}$ ) is assumed to have the same exit angle as the main absolute flow field angle ( $V_{f,abs}$ ) [39]. Following this as-

sumption, the droplet relative velocity ( $V_{d,rel}$ ) can be calculated through the rotor rotational velocity ( $\omega \times r$ ) for each radial location. The time averaged absolute flow yaw angle velocity is  $73.1^\circ$  and  $72.9^\circ$  for design and part load conditions respectively.

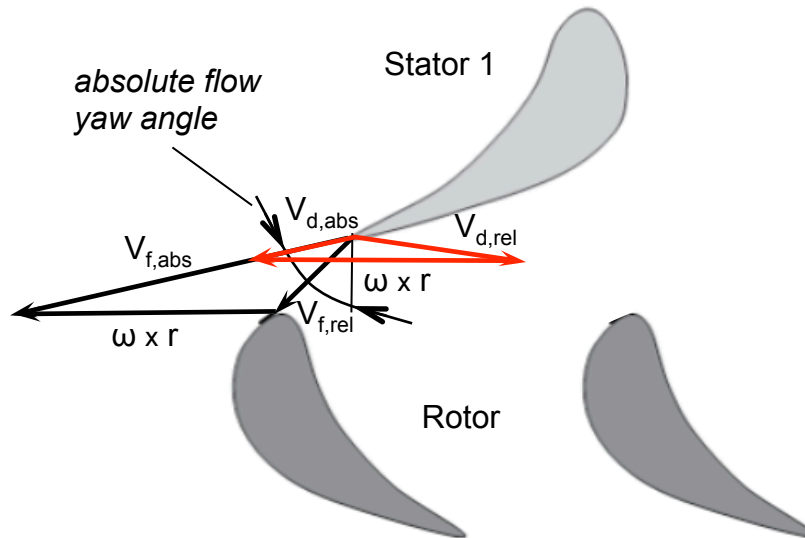


Figure 4–9: Velocity triangles flow field (black) and droplets (red) at Stator 1 exit.

Results of Figure 4–10.a show that for both operating conditions the droplets ranging from  $55$  up to  $100\mu\text{m}$  diameter have on an average a deficit of  $80\%$  in absolute velocity compared to the flow. Therefore the large water droplets will impact the rotor blade on the suction side of the leading edge. On the other hand Figure 4–10.b shows that the droplets' relative velocity is on an average two times larger for part load condition compared to design operating point. At part load condition, the droplets in the range of  $50\mu\text{m}$  in diameter have approximately the same relative velocity as the flow field relative velocity ( $V_{d,rel} \sim V_{f,rel}$ ), and the droplets at the range of  $100\mu\text{m}$  have  $20\%$  higher relative velocity compared to the flow field relative velocity for the part load condition. For the design operating point there is no dependency of the relative droplet velocity with the droplet size and the relative droplet velocity is  $40\%$  lower compared to the part load condition as shown in Figure 4–10.b. The droplets will further accelerate, due to aerodynamic drag forces, and reach a maximum velocity depending on the available axial gap between the stator and rotor blades [38, 93]. In order to further understand the formation mechanisms and be able to assess the droplets' maximum velocity before impacting the rotor leading edge additional measurements were performed at a second downstream location of stator 1.

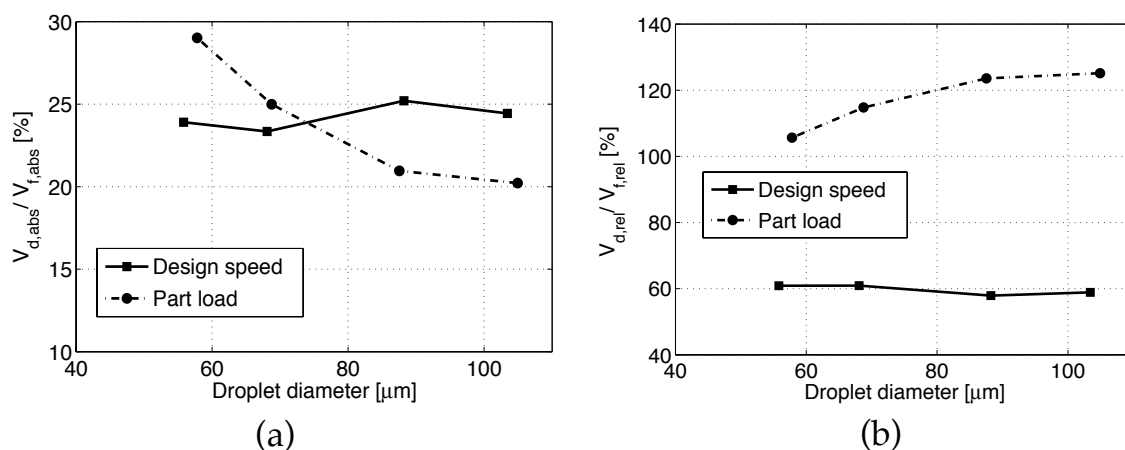


Figure 4–10: Absolute (a) and relative (b) droplet velocity at midspan location for design and part load conditions.

#### 4.2.2 Results for part load condition at locations of $x/c=2\%$ and $8\%$

Since the part load condition has greater impact on the erosion mechanisms as shown in Figure 4–10.b, results are presented only from this operating point in this paragraph for two different axial locations downstream of Stator 1. As shown in Figure 4–11, the droplet size is significantly reduced while they accelerate from the stator trailing edge towards the rotor leading edge. This is expressed by the reduction on the actual value of the diameter as well as by the reduction in detected coarse droplet count. The Sauter Mean Diameter has been reduced by 10%, 11.3% and 3% for the tip, mid and hub span locations respectively.

As described previously the velocity and the droplet size are the two main parameters affecting the erosion process at rotor leading edge. Therefore, in order to verify the size of the droplets at the time when they impact the rotor leading edge, the Weber number as a function of droplet diameter is presented in Figure 4–12 for the midspan location. Similar results were obtained for the tip and hub regions. Measurements at  $8\%c$  downstream of stator 1 show that the Weber number is below the critical value of 22 for all droplet diameters. This implies that the droplets have reached a stable regime and they will not break up into smaller size. The final distributions are those depicted in Figure 4–11 ( $8\%c$  downstream) and the Sauter Mean Diameter is  $73.9\mu\text{m}$ ,  $71.2\mu\text{m}$  and  $73.9\mu\text{m}$  for the tip, mid and hub span locations respectively.

The droplet speed results for the two downstream locations are presented in Figure 4–13.a and b. As shown in Figure 4–13.a the droplets accelerate by 10% for the range of  $50\mu\text{m}$  in diameter and by 40% for the large range of  $100\mu\text{m}$ . Using the same assumptions as described in Figure 4–9, the relative droplet diameter is calculated and plotted in Figure 4–13.b. The relative droplets' speed is about 105% of relative flow field velocity and roughly constant

for all droplet sizes from 45 up to 110 $\mu\text{m}$  in diameter. Having measured the current droplet speeds and diameter, according to the power law equation  $R_e \sim V_d^n$  the erosion rate at part load condition is increased exponentially and can reach 16 up to 32 times higher rates depending on the blade material.

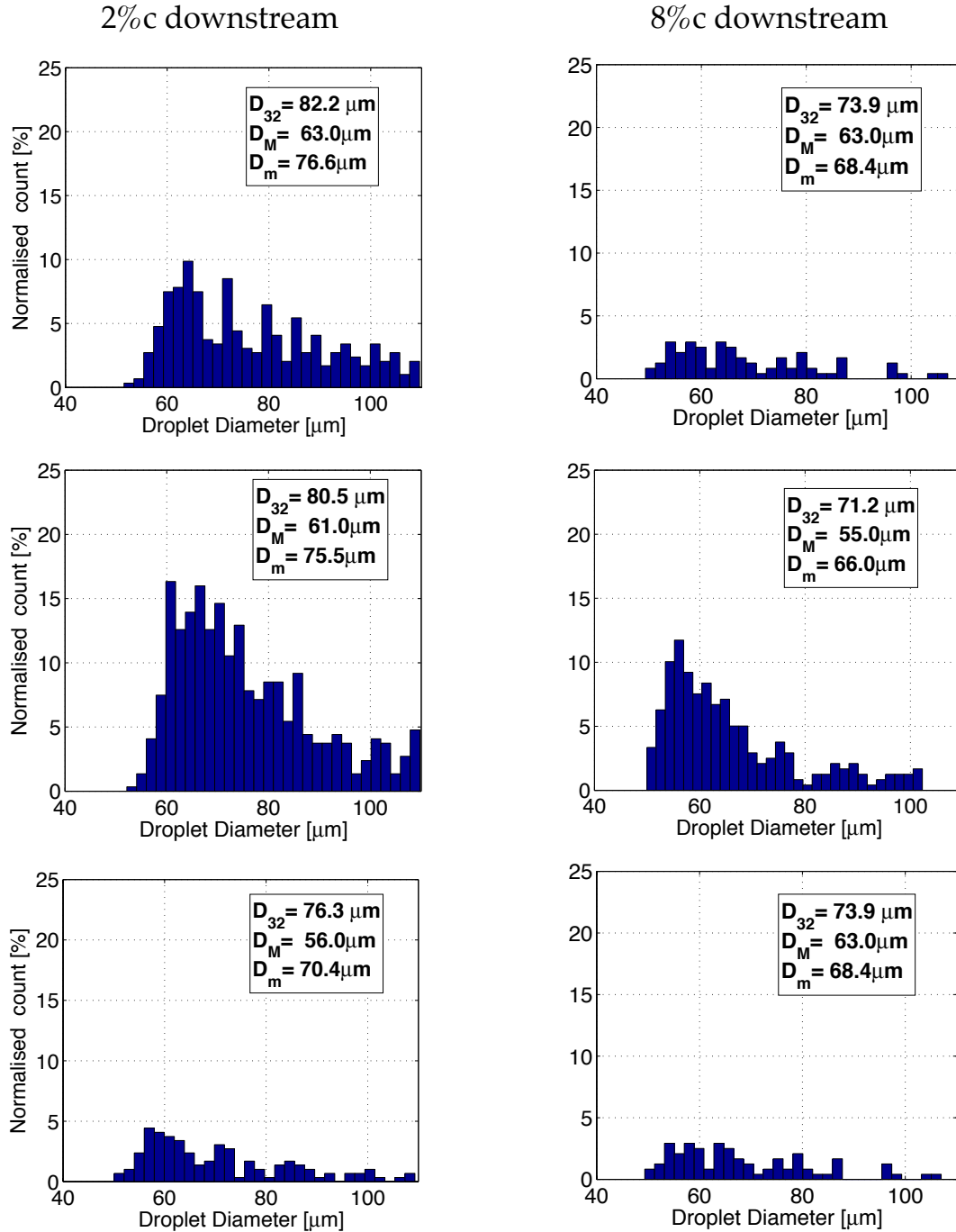


Figure 4–11: Size droplet distribution at tip (upper), midspan (center) and hub(bottom) spanwise locations for part load condition at  $x/c$  2% and 8% downstream of stator 1 exit.



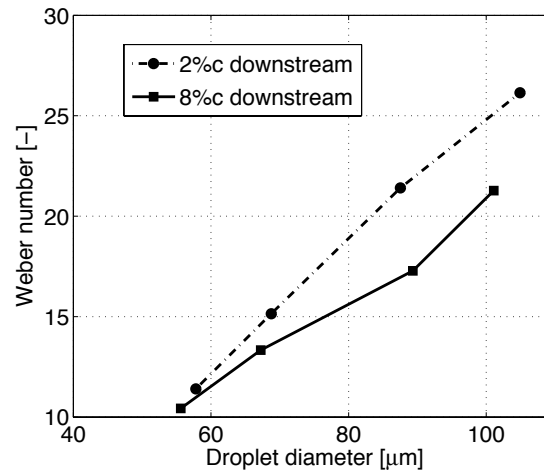


Figure 4-12: Weber number as a function of droplet diameter for the two different downstream axial locations of Stator 1 at mid span.

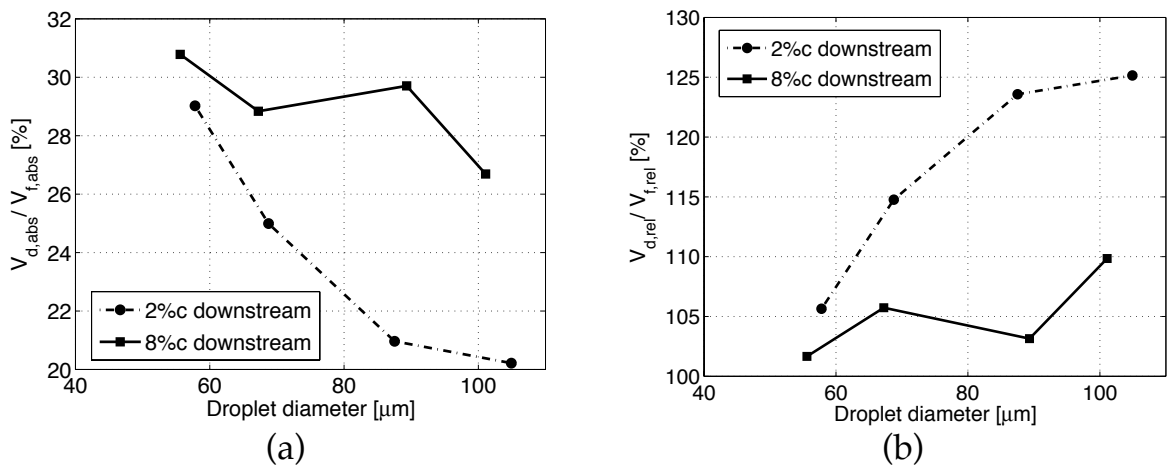


Figure 4-13: Absolute (a) and relative (b) droplet velocity at midspan location at  $x/c=2\%$  and  $8\%$  for part load condition.

### 4.2.3 Time resolved results for design and part load condition

The time-resolved results of the droplet mass rate as defined in Eq.(4-2) downstream of stator 1 are presented and discussed in the current paragraph. The droplet mass rate is the product of the droplet mass by the droplet count.

$$DR = N \left( \frac{4}{3} \pi r_d^3 \rho_d \right) \quad (4-2)$$

Figure 4-14 shows the droplet mass rate contour plots at the exit plane of stator 1 over 4 rotor blade passing sub-periods equal to  $t/T = 0.25$ , where  $T$  is the respective rotor blade passing time period. At the left hand side of Figure 4-14 the results from the design point are presented, at the center and right hand side the results from the part load condition are displayed. It can be seen

that the droplet mass rate is modulated by the downstream rotor blading passing period for all test cases. This modulation is due to the flow field periodical interaction with the downstream rotor potential field as reported by Behr et al. [91].

When the design condition is studied, at  $t/T=0$  the droplet mass rate gets its maximum value of about  $2 \times 10^{-4}$  mg covering from 30% up to 90% of the span and 20% of the stator pitch. At time  $t/T=0.25$  the droplet rate is reduced by 23% and as consequence the actual area that the droplets cover is reduced covering a lower range in spanwise and pitchwise direction. At  $t/T=0.5$  the droplet rate increases by 16%, which again results in the same increase on the area coverage and finally at time  $t/T=0.75$  the droplet rate exhibits a similar distribution as at  $t/T=0$ . This modulation with time implies that the potential field of the downstream rotor, which generates a periodical static pressure fluctuation, results in the droplet impact rate with a variation of 15% around the mean value. This unsteady static pressure field decelerates the droplets when it is high (droplet mass rate reduction) and allows the droplets to continue in the flow when it is low (droplet mass rate increase).

Similar unsteady behavior, which is modulated with the rotor blade-passing period, is observed at part load condition but with a phase shift most probably due to the reduced flow field velocity. As shown in Figure 4-14 at the central plots, the maximum droplet mass rate is found at  $t/T=0.25$  (Figure 4-14.b, center) approximately at  $2.2 \times 10^{-4}$  mg. At part load condition the unsteady peak-to-peak fluctuations of the droplet mass rate have been increased by 10% mainly due to increase of droplets' diameter as presented in Figure 4-7. This implies that the droplets' count  $N$  in Eq.(4-2) has remained fairly constant but the droplets' mass has increased due to an increase in the droplet diameter.

When the part load condition is studied at two different downstream locations, at 2% and 8% downstream of the axial stator chord, the results demonstrate a very interesting behavior. At  $x/c=8\%$  the droplet mass rate is modulated again by the rotor blade passing period however the peak-to-peak fluctuations have increased by 80% from  $2\%c_x$  to  $8\%c_x$  leading to unsteady values of  $\pm 40\%$  of the mean value. The principal reason is the greater potential field, as the droplets approach the rotor leading edge.

In addition, the plots for the part load condition at  $x/c=8\%$  in Figure 4-14, demonstrate a very small deviation on droplet's trajectory of about  $\pm 0.3^\circ$  which is not so clear in the current plots. However the unsteady aerodynamic results from Behr et al. in [91] have showed that the circumferentially averaged unsteady flow yaw angle is  $\pm 2^\circ$ . When the unsteady yaw angle is probed at specific circumferential locations the unsteady fluctuations become even greater reaching  $\pm 5^\circ$ . The fact that the droplets' deviation is  $\pm 0.3^\circ$  when the flow field unsteady yaw angle is deviating up to  $\pm 5^\circ$ , implies that the droplet trajectories do not follow the flow field streamlines. This is further supported

with the calculation of the Stokes number in Eq.(4-3). For a mean droplet diameter of  $70\mu\text{m}$  that travels at  $45\text{m/s}$  and a characteristic length of  $r_{ch}=0.005\text{m}$  (rotor blade leading edge radius) the calculated Stokes number is 124. Such a high value of the Stokes number,  $St \gg 1$ , implies that the droplet is dominated by its inertia and continues along its initial trajectory without following the streamlines of the flow.

$$St = \frac{\rho_d \cdot D_{d,m}^2 \cdot V_{d,abs}}{18 \cdot \mu_f \cdot r_{ch}} \quad (4-3)$$

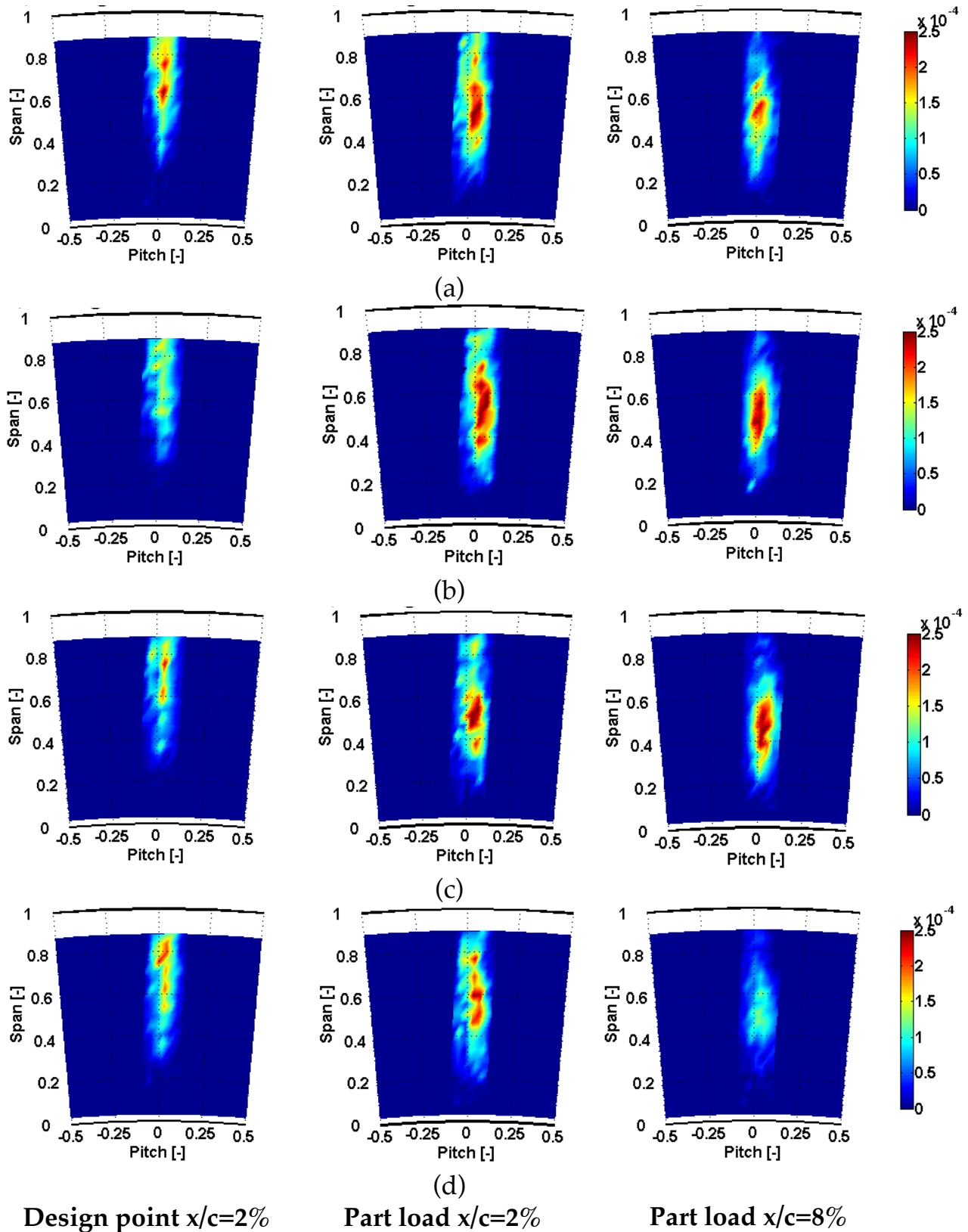


Figure 4-14: Time resolved droplet mass rate [mg/s] at Stator 1 exit plane for design point (left) and part load condition (center) at  $x/c=2\%$  and part load condition at  $x/c=8\%$  (right) for four instants of the rotor blade passing period: a)  $t/T=0.00$ , b)  $t/T=0.25$ , c)  $t/T=0.50$  and d)  $t/T=0.75$ .

### 4.3 Summary

In this chapter of the thesis the optical backscatter probe for coarse water droplet measurements was demonstrated at the stator exit of the axial turbine facility LISA equipped with a water droplet spray generator. The custom made spray generator was installed five stator chords upstream of the test section and the spray was injected at midspan covering one and a half stator pitch. The measurements were performed under two different operating conditions at two different axial locations downstream of the first stator.

The coarse water droplets were found to be maximum at the stator's trailing edge. This is due to the impact of the droplets at the stator's pressure side and the formation of a water film, which is periodically torn from the trailing edge. In addition, measurements have shown that the droplets increase by 10% in size when the flow velocity is reduced from  $Ma=0.52$  to  $Ma=0.42$ , due to significant reduction on the shear forces between the droplets and the stream flow. Droplet speed measurements have shown that the coarse water droplets suffer from a deficit in absolute velocity at the stator exit and they will therefore impact the downstream rotor leading edge on the suction side. This is due the variation on the velocity triangles where they show a change on the relative droplet velocity. Part load condition results in an increase of the relative droplet velocity by 40% compared to the design operating point. As a consequence, the erosion rate increases by a factor of 16 depending on the material used for the rotor blades.

The time-resolved measurements, with the droplet mass rate distribution at stator 1 exit plane, have shown that the droplet mass rate is modulated by the downstream rotor blade-passing period in all test cases. This is due to the unsteady static pressure field, which is generated from the stator-rotor interaction. In particular, at part load condition the peak-to-peak fluctuations have increased by 80%, from 2% and 8% downstream of the axial stator chord, leading to unsteady values of  $\pm 40\%$  of the mean value. The large increase of the unsteady droplet mass rate as the rotor leading edge is approached is due to the stronger potential field that drives the droplets' motion.

## 5 Measurements in a 7MW steam turbine test facility

This chapter presents a set of time resolved steam flow field measurements from the exit of the last two stages of a low-pressure steam turbine equipped with subsonic rotor blades in the last stage. The FRAP-HTH probe is used for the first time in wet steam conditions with wetness mass fraction up to 8%. The probe demonstrates its ability to perform accurate measurements under various wet steam conditions and provides valuable unsteady data for the unsteady flow field analysis.

### 5.1 Experimental test facility

The measurements presented in the current chapter were conducted at MHPS research steam turbine test facility for thermal power generation in Hitachi city, Japan. As shown in Figure 5–1, the experimental test facility is a four stage (L-3 to L-0) low-pressure steam turbine with a scale ratio of 1/2.2. The steam is generated in the boiler and then guided to the inlet of the turbine through a control valve. The inlet pressure and temperature can be adjusted in order to change the operating point and therefore the loading conditions of the machine. Downstream of the last stage of the turbine the steam condensates and returns back to the boiler to complete the cycle. An orifice flowmeter and flow nozzle are installed in order to measure the mass flow in the main steam pipe and the condensation pipe respectively. A generator and a hydraulic (water) break (dynamometer) absorb the turbine's power and control the rotational speed of the machine.

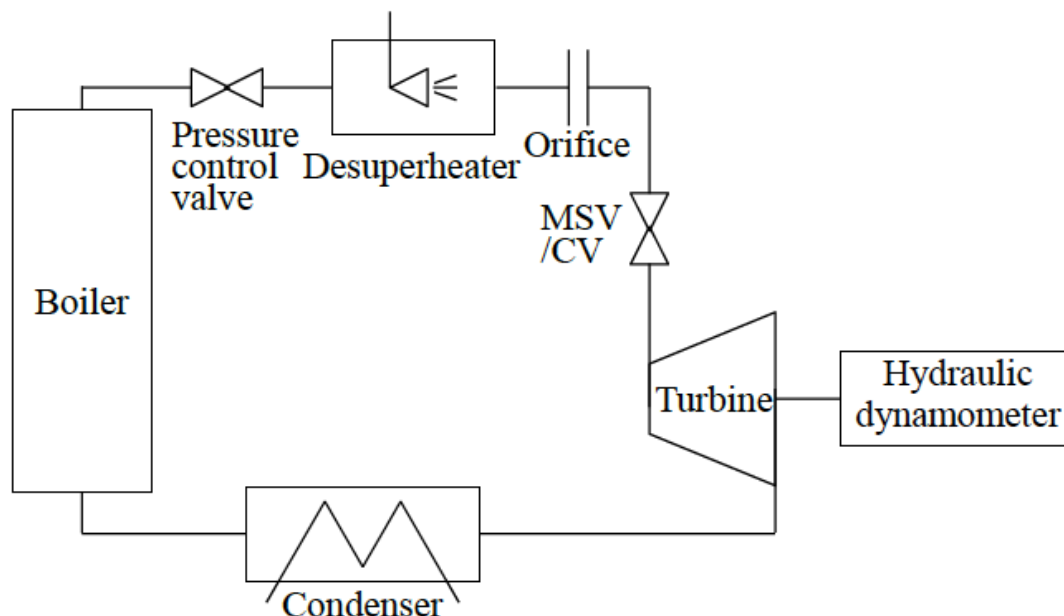


Figure 5–1: Schematic of experimental test facility [94].

The rated speed of the machine is 7920rpm and the three different operating conditions tested in this measurement campaign are summarized in Table 9. Figure 5–2 shows the steam turbine facility with the FRAP-HTH probe installed at L-1 measurement plane. Additional information from the test facility can be found in [15].

Table 9: Operating tested conditions.

		OP-3	OP-2	OP-1
Massflow [t/h]		67	52	52
Exit pressure [kPa]		8.0	8.0	10.7
Inlet temperature [°C]		266	266	266
Calculated Wetness mass fraction at midspan [%]	L-1	3.1	2.5	2.3
	L-0	8.0	6.5	4.5

The measurement planes of the current experimental work are presented in Figure 5–3. All measurements were performed at the exit of L-1 and L-0 stages. The number of the rotor blades is 96 and 70 for L-1 and L-0 respectively. Both stages are equipped with a part span connector (PSC) located at 52% and 50% span at L-1 and L-0 rotor blades respectively. The PSC is elliptical snubber, which is integrally manufactured with the blade. The data are acquired at a sampling rate of 200kHz over a period of 2s with a resolution of 24Bit. The post-processing is done for three consecutive rotor pitches. The sampling rate resolves 16 points in the rotor relative frame of reference.

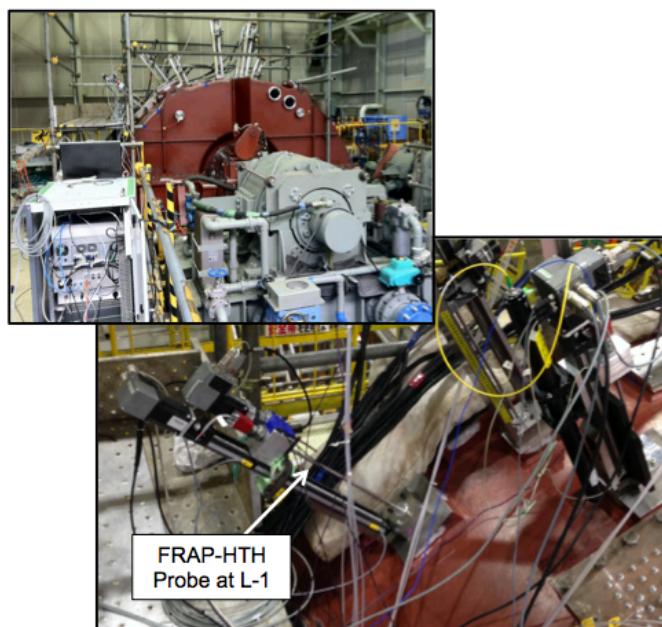


Figure 5–2: Low-pressure steam turbine test facility where FRAP-HTH measurements were conducted.

The probe was mounted on a two axis traversing system enabling a single traverse at each plane from blade hub to tip with the possibility of rotation around its axis. The spatial resolution of the measurement grid at the traverse planes consisted of 33 and 41 radial points for L-1 and L-0 planes respectively and all points were equally distributed.

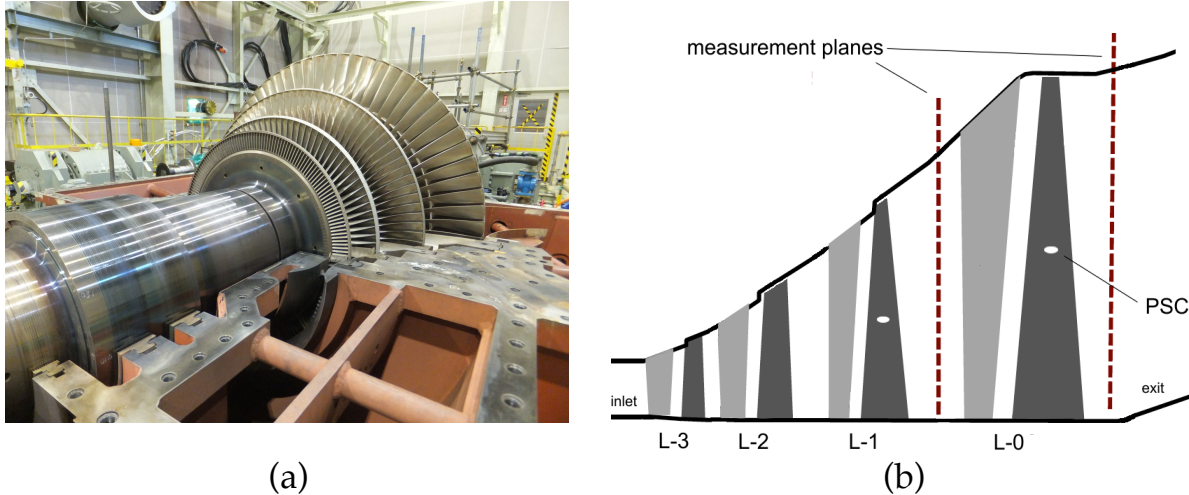


Figure 5-3: Four stage rotor (a) and schematic of the four stages with the respective probe measurement locations (b).

As indicated in Figure 5-4.a, at L-1 plane the total traverse length is 192mm and consists of 33 points with the first measurement point located at 74mm (30% span) from the hub and the last measurement point located at 266mm (103%span). At L-0 plane, Figure 5-4.b, the total traverse length is 418mm and consists of 41 discrete points. The first measurement point is at 32mm (7% span) from the hub and the last point at 482mm (103% span).

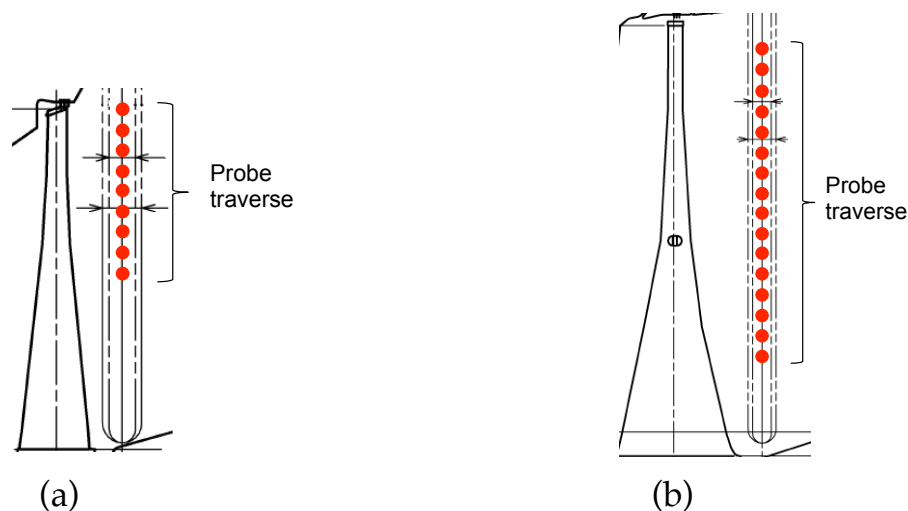


Figure 5-4: Probe traverse path at (a) L-1 and (b) L-0 stage.



## 5.2 Results and discussion

### 5.2.1 Time-averaged measurement comparison between FRAP-HTH and five hole probe

In this paragraph, the FRAP-HTH time-averaged measurements are compared to 5HP measurements conducted on the same day at L-1 and L-0 stages' exit. The 5HP consists of a typical cobra shape probe with a tip diameter of 5mm and is equipped with a standard air purging system. The FRAP-HTH and the 5HP measurements were performed along a single radial traverse, and it should be noted that the 5HP access hole is located at a different upstream stator clocking position compared to the FRAP-HTH. The 5HP measurements were performed with a radial spatial resolution of 33mm. The FRAP-HTH measurements are time-averaged over 80 rotor revolutions for three rotor blade passing events. The two sets of measurements are compared at L-0 and L-1 rotor exit for operating condition OP-3, which exhibits the most severe conditions with an average wetness mass fraction of 8.0% and 3.1% at L-0 and L-1 respectively.

#### 5.2.1.1 Time-averaged results comparison at L-1 rotor exit

Figure 5–5 shows the FRAP-HTH and the 5HP relative yaw flow angle as well as the absolute Mach number across the blade span at L-1 rotor exit. There is good overall agreement between the two probes, both in the trend and in absolute values across the span. Both probes capture the two peaks of local flow overturning located at 58% and 45% span, which are generated by the presence of the PSC at 52%. The effect of the PSC can also be seen in Figure 5–5.b, where the FRAP-HTH measurements show two clear local peaks of absolute Mach number. They occur at 58% and 45% span, and are caused by the blockage generated by the PSC. The RMS value of the yaw angle difference is 2.8deg and 0.03 in the absolute Mach number. It is believed that the offset in the measured relative yaw angle is in part due to probe alignment error during installation.

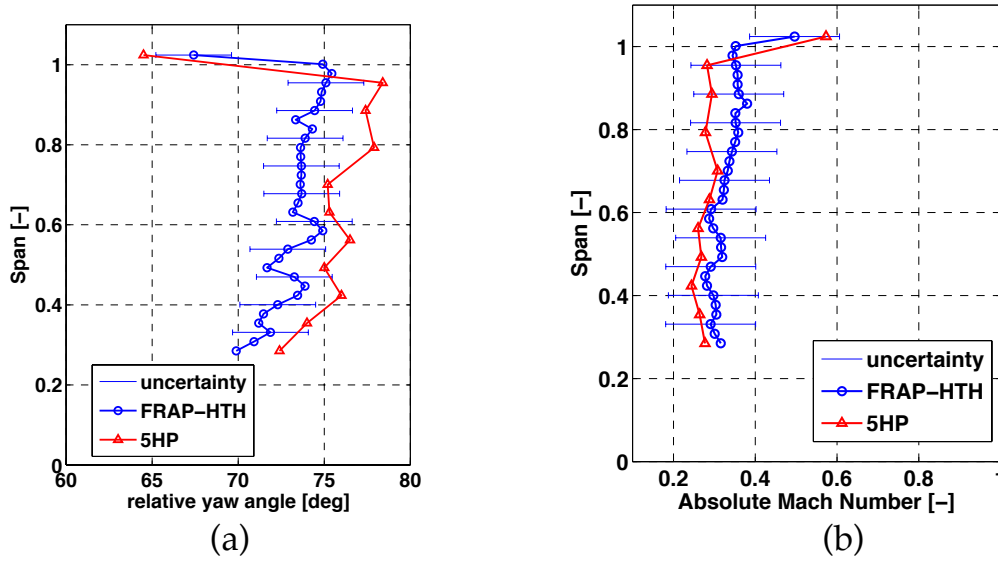


Figure 5–5: Relative flow yaw angle (a) and absolute Mach number (b) measured by the 5HP and FRAP-HTH probes at rotor exit of L-1 stage

5.2.1.2 Time-averaged results comparison at L-0 rotor exit

Figure 5–6 shows the FRAP-HTH and the 5HP measured relative yaw flow angle as well as the absolute Mach number across the blade span at the L-0 rotor exit.

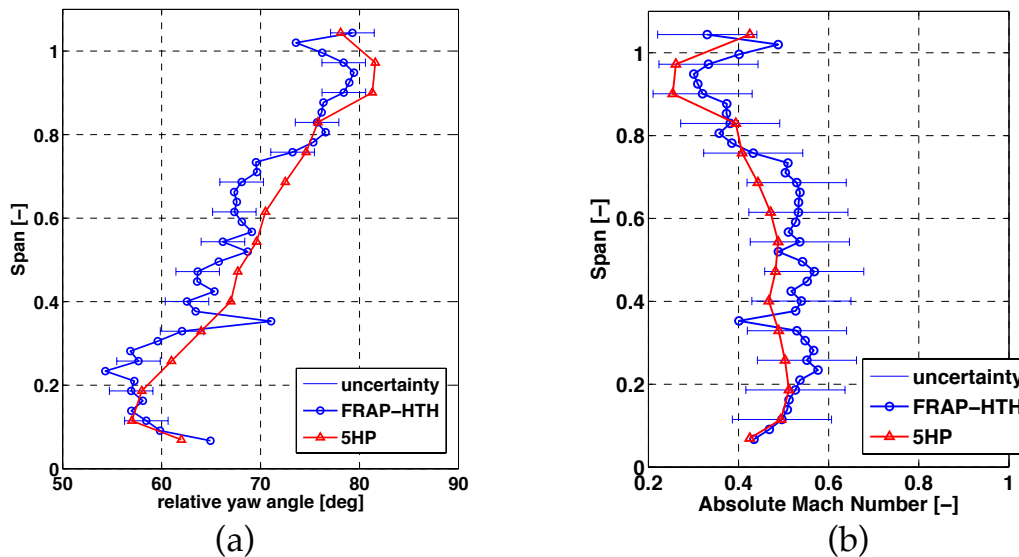


Figure 5–6: Relative flow yaw angle (a) and absolute Mach number (b) of 5HP and FRAP-HTH probes at rotor exit of L-0 stage

In general there is a good agreement between the two probes, both in the trend and in absolute values. As shown in Figure 5–6.a, both probes capture the overturning, centered at 95% span related to the presence of the tip secondary flow structures. Unlike the 5HP measurements, the denser FRAP-HTH

radial measurement grid allows to capture two peaks of local flow overturning at 57% and 35% span, which are generated by the presence of the PSC located at 50%, as reported in [95]. The effect of the PSC can also be seen in Figure 5–6.b, where the FRAP-HTH measurements show two local peaks of absolute Mach number, at 52% and 35% span, due to the redistribution of the flow around the PSC. The RMS value difference between the FRAP-HTH and 5HP measurements is 1.6 deg for the relative yaw angle and 0.1 for the absolute Mach number. These measured deviations are within both probes' measurement uncertainty bandwidth. This is despite the fact that both probes have different radial measurement spacing and are located at different upstream stator clocking position.

### 5.2.2 Steady flow field at rotor exit of L-1 stage

In this paragraph the time-averaged FRAP-HTH measurement results at the rotor exit of L-1 stage are presented for the 3 different operating conditions listed in Table 9. All plots show measurement results from 1.03 down to 0.3 span. Figure 5–7.a shows the spanwise distribution of the time averaged total pressure coefficient, as defined in Eq.(5-1), in the rotor relative frame of reference. The inlet and exit refer to the conditions at the inlet exit of the steam turbine respectively (see Figure 5–3.b). In the same graphs the maximum and minimum values obtained from the time resolved data are plotted as well. OP-3 has on an average a 2% deficit in the mean value of the  $C_{pt,rel}$  across the whole span compared to the other 2 conditions. On the other hand OP-1 and OP-2 demonstrate very similar  $C_{pt,rel}$  distribution.

$$C_{pt,rel} = \frac{P_{t,rel,FRAP-HTH} - P_{s,exit}}{P_{t,inlet} - P_{s,exit}} \quad (5-1)$$

In order to analyze the flow field further, the blade span was subdivided in 4 main regions. These are: the hub region from 0.28 to 0.4 span; the mid-span region containing the snubber interface from 0.4 to 0.6 span; the tip region from 0.6 to 1 span and finally the shroud region up to 1.03 span. Eq.(5-2) is used to compare the magnitude of the periodical fluctuations along the blade span between the 3 measured operating conditions. For each span location  $i$ , the difference of the peak-to-peak fluctuations is divided by the averaged  $\overline{C_{pt,rel}}$  value. Table 10 summarizes the results for OP-1, OP-2 and OP-3.

$$\frac{\widetilde{C_{pt,rel,max}} - \widetilde{C_{pt,rel,min}}}{\overline{C_{pt,rel}}} \times 100\% \Big|_{span(i)} \quad (5-2)$$

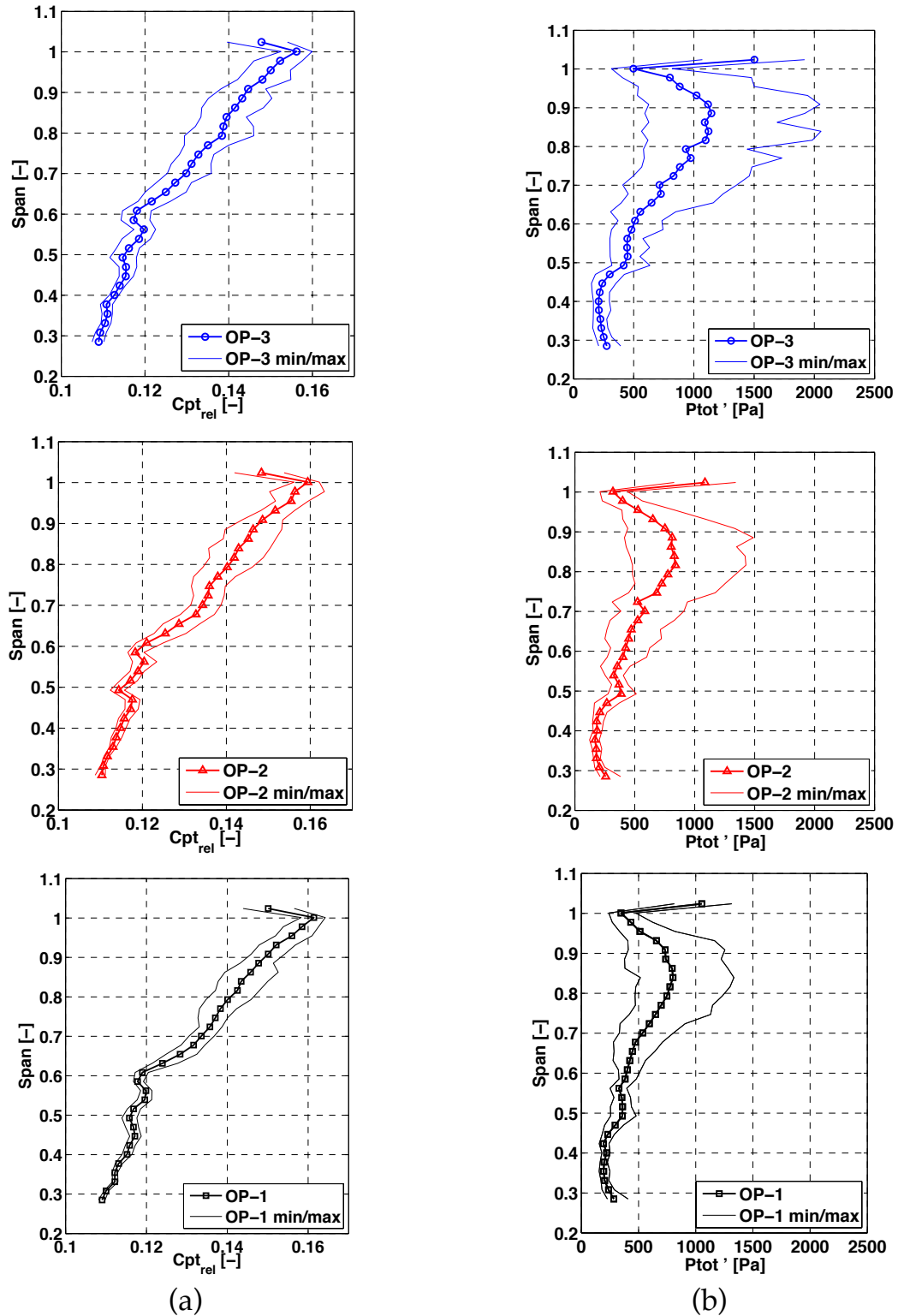


Figure 5-7: Time averaged spanwise distribution of  $C_{pt\_rel}$  (a) and time averaged RMS of  $P_{tot}'$  [Pa] (b) at rotor exit of L-1 stage for OP-3, OP-2 and OP-1 with their respective minimum and maximum values obtained from the time resolved data.

Table 10: Spanwise distribution of peak-to-peak fluctuation of  $C_{pt\_rel}$  as a function of the local mean value for OP-1, OP-2 and OP-3 conditions.

Region:	Span [%]	OP-1 [%]	OP-2 [%]	OP-3 [%]
Hub	28-40	1.3	1.6	2.4
Mid-span	40-60	2.5	3.1	4.1
Tip	60-98	5.9	6.9	8.1
Shroud	98-103	5.9	6.7	7.4

As shown in Table 10, all conditions experience the highest  $C_{pt\_rel}$  variation at the tip and shroud locations with gradually decreasing levels of fluctuations until the hub region. OP-3 shows the highest amplitude of unsteady fluctuations at all spanwise locations compared to OP-2 and OP-1. In the tip region OP-3 shows periodical fluctuations in  $C_{pt\_rel}$ , which are 37% and 14.8% higher than for OP-1 and OP2, respectively. At the mid-span location between 40 and 60% span, the variation in  $C_{pt\_rel}$  is found to be higher in OP-3 by 64% and 32% compared to OP-1 and OP-2 respectively, which signifies more intense flow interactions with the PSC for the high massflow operating condition. In the shroud region, the labyrinth leakage flow also generates total pressure losses that strongly depend on the operating condition and it will be shown in the subsequent paragraphs that the stochastic unsteadiness are also maximized at that location for this measurement plane. Finally at the hub section between 28 and 40% span, OP-3 condition demonstrates 2.4% peak to peak oscillations of the mean value, which is still 85% greater compared to OP-1 and 50% higher compared to OP-2.

The averaged losses are triggered by unsteady secondary flow structures. As Porreca et al. [96] describe, the RMS value of the random part of the pressure signal acquired with the FRAP-HTH, as defined in Eq.(5-3), has shown to be an appropriate indicator to identify regions of elevated total pressure losses. Based on the triple decomposition of the time-resolved pressure signal, the random part of the signal can be calculated as the difference between the raw pressure signal  $P(t)$  of the FRAP-HTH probe and the phase-locked averaged one ( $\bar{P}(t) + \tilde{P}(t)$ ), as presented in Eq. (5-3),

$$P(t)' = P(t)_{FRAP} - (\bar{P}(t) + \tilde{P}(t)) \quad (5-3)$$

Figure 5–7.b shows the time-averaged distribution RMS of  $P_{tot}'$ , for OP-1, 2 and 3 with their respective maximum and minimum values resulting from the time resolved measurements. In all cases, the tip region of the blade span exhibits the highest levels of RMS of  $P_{tot}'$  and  $C_{pt\_rel}$  values. This observation is in good agreement with location and with the order of magnitude of the pressure fluctuations with [97]. As shown in Figure 5–7.b, the highest values of RMS of  $P_{tot}'$  are located at 103% and 80% span for all conditions. Their origins

will be further analyzed in the subsequent time-resolved results. At the mid-span region, the small kink present at 50% span is linked to the presence of the PSC. Below 45% span the RMS of  $P_{tot}'$  remains almost constant and gets its smallest value.

As indicated in Figure 5–7.b one can see that OP-3 shows higher values of stochastic unsteadiness at the tip region compared to OP-1 (maximum range of max-min values). At midspan, OP-3 shows an increase of 41% compared to OP-1. Below 40% span the differences between the two conditions are relatively small. It is worth mentioning that there is more than a 50% change in RMS of  $P_{tot}'$  between the two conditions in the area above 100% span associated with the shroud leakage flow.

Similar observations can be made in Figure 5–7.b when OP-3 and OP-2 conditions are compared. The differences between the two conditions are in the same levels as the variations observed between OP-3 and OP-1, as described in the previous paragraph. However in this case, OP-2 shows higher stochastic unsteadiness in the region from 55% to 75% span, with 15% higher peak-to-peak variations in  $P_{tot}'$  compared to OP-1. This change might be related to the variations in the unsteady aerodynamic performance of the PSC among the different operating points.

### 5.2.3 Time resolved flow field at rotor exit of L-1 stage

In order to further analyze the discrepancies of the flow field along the blade span, the time resolved data are discussed in this paragraph. As mentioned previously, the temporal resolution is limited to 16 measurement points for a rotor blade passage. Therefore it is possible that very small flow features (i.e. blade wake) are resolved with limited samples. The corresponding time-resolved relative total pressure coefficient for OP-3 is shown in Figure 5–8. This is a space-time diagram for three consecutive blade passing events (phase lock averaged data) with the three dashed vertical lines representing the approximate position of the rotor blade trailing edges at  $t/T=0.75$ , 1.75 and 2.75 respectively. The pressure and suction side of each blade passage is indicated as well. The rotation is from left to right and the observer “looks” upstream. The measured total relative pressure variations are generally lowered adjacent to the hub and mid-span relative to the tip. This is in good agreement with Figure 5–7.b and evidence that the flow field interaction with the rotor blades is predominant at the blade tip region (blade span > 65%).

This observation is shown as well in Figure 5–9 with the unsteady absolute total pressure downstream of L-1 rotor. The radial axis represents the blade span and the circumferential axis the time for one rotor revolution. The results have been non-dimensionalized with the mean pressure value measured in the traverse over this one rotor revolution.

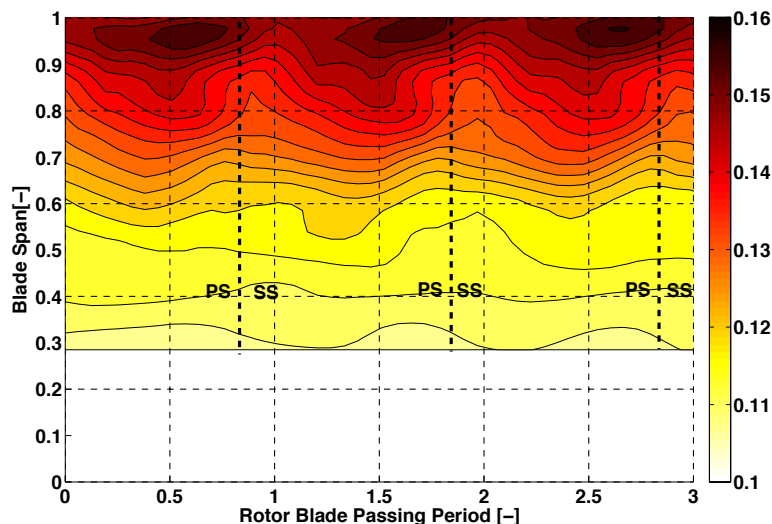


Figure 5–8: Time resolved  $C_{pt\_rel}$  [-] at rotor exit of L-1 stage for OP-3.

Besides the modulation in total pressure triggered by the upstream rotor blades, it worth noting the highly distorted flow field, around 24 and 72 of the rotor blade passing period. The large fluctuations at the rotor exit of L-1 for these particular blades are induced by the strain gauges attached on the blade surfaces for the blade vibration measurements as described in [94].

In order to identify the secondary flow structures and assess their impact on the flow field among the different measured operating conditions, the unsteady results of the RMS of  $P_{tot}'$  are presented in Figure 5–10. For compactness of the thesis, only the results of conditions OP-1 and OP-3 are analyzed. Three regions of elevated RMS of  $P_{tot}'$  can be identified over the measured blade span. The first are the regions A and B highlighted in Figure 5–10.a located at 90%, and occurring periodically at blade passing periods of  $t/T=0.1$ , 1.1, and 2.1 and at  $t/T=0.6$ , 1.6 and 2.6. The third region labeled as C is related to the tip labyrinth leakage flow and results in the highest values in the region of 103% span.

As presented in Figure 5–10, it is believed that out of the 2 features located at 90% span, the one with the most elevated values (A) located on the suction side of the rotor blade can be associated to the tip passage vortex. The second feature (B) is associated with the upstream stator's tip passage vortex. Similar secondary flow structure generated from the upstream stator, with lower intensity compared to the tip passage vortex, at 75% span, is reported by Chaluvadi et al. [98].

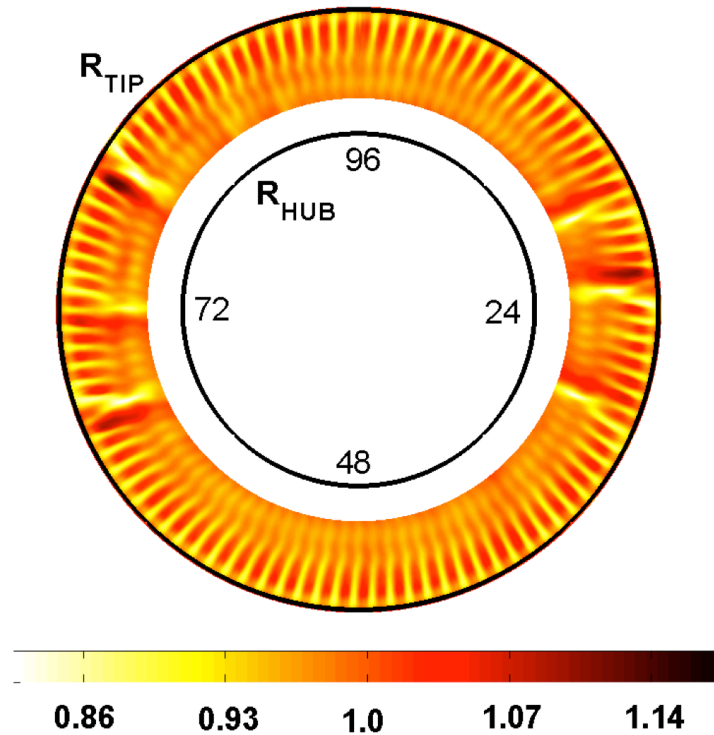


Figure 5–9: Time resolved total pressure  $P/P_{avg}$  obtained from the single traverse at the exit of L-1 rotor for OP-3. The radial axis refers to the blade span and the azimuthal axis to the blade count over one rotor revolution.

Figure 5–11 shows the respective time-resolved relative flow yaw angle at the rotor exit. In this graph the relative flow yaw angle is subtracted from the blade metal angle in order to decouple the effect of the high twisting angle of the blade design. Positive values imply overturning, and negative values underturning. For this particular circumferential traverse location the unsteady flow field distribution is rather complex. It is most probably affected by the secondary flow structures generated in the two upstream stages. The tip passage vortex can be identified at the tip region at 90% span where the high alteration of the yaw angle ( $\pm 4.5^\circ$ ) is present in the suction side at the rotor blade passing period of  $t/T=0.1, 1.1$  and  $2.1$ . This vortex rotates counter clockwise as highlighted in Figure 5–11.a. Since this region between 80 and 100% span is dominated by secondary flow structures, the RMS of  $P_{tot}'$  (stochastic total pressure fluctuation) is maximum in the same location. This is confirmed in Figure 5–10 where the highest values of  $P_{tot}'$  RMS are centered at 90% span on the suction side of the rotor blade. Further evidences of the presence of the tip passage vortex are shown in Figure 5–12, where the unsteady flow yaw angle, pitch angle, total pressure and static pressure at 86% blade span are shown for OP-1 and OP-3 conditions for three rotor blade passing periods. As previously described, the presence of the tip passage vortex at this spanwise location at the time instants  $t/T=0.1, 1.1$  and  $2.1$  results in variation of the yaw angle of  $\pm 4.5^\circ$  for OP-3 and  $\pm 2^\circ$  for OP-1, across the tip passage



vortex. Accordingly the pitch variation is  $\pm 3^\circ$  for OP-3 and  $\pm 2^\circ$  for OP-2. In Figure 5–12 the peak-to-peak variation in relative total pressure is 14% of the average relative total pressure level for OP-3 and 11% for OP-1.

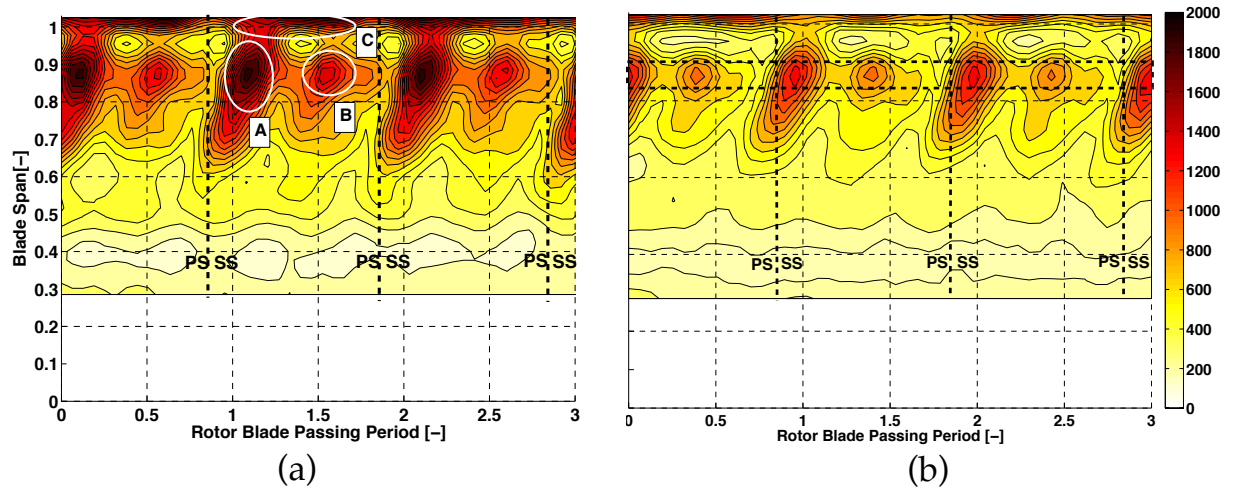


Figure 5–10: Time resolved RMS of  $P_{tot}'$  [Pa] in stationary frame of reference at rotor exit of L-1 stage for (a) OP-3 and (b) OP-1.

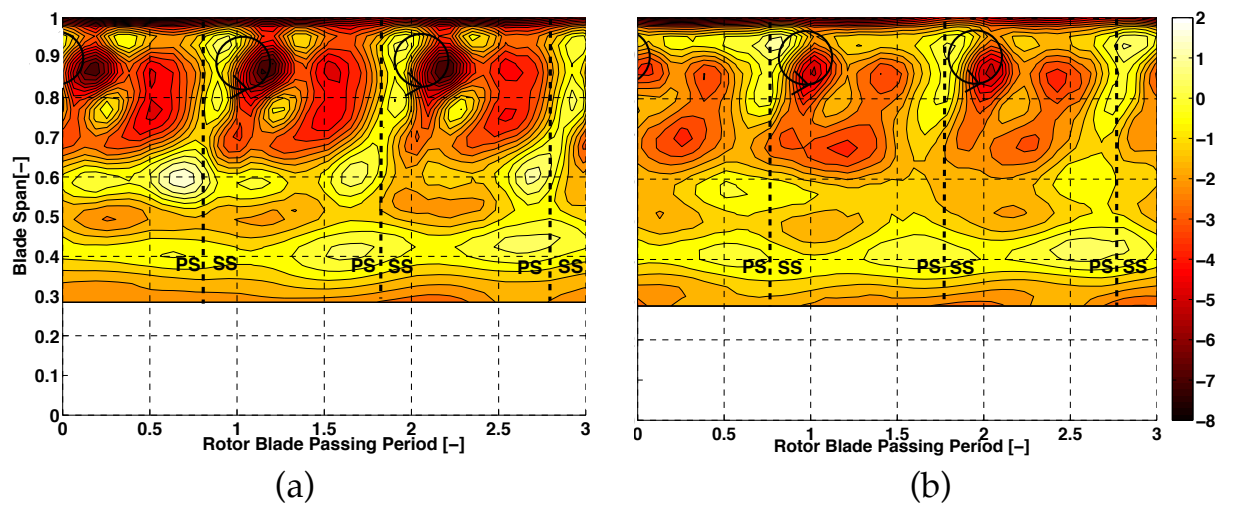


Figure 5–11: Time resolved relative yaw flow angle [deg] at rotor exit of L-1 stage for (a) OP-3 and (b) OP-1 (relative to blade metal angle).

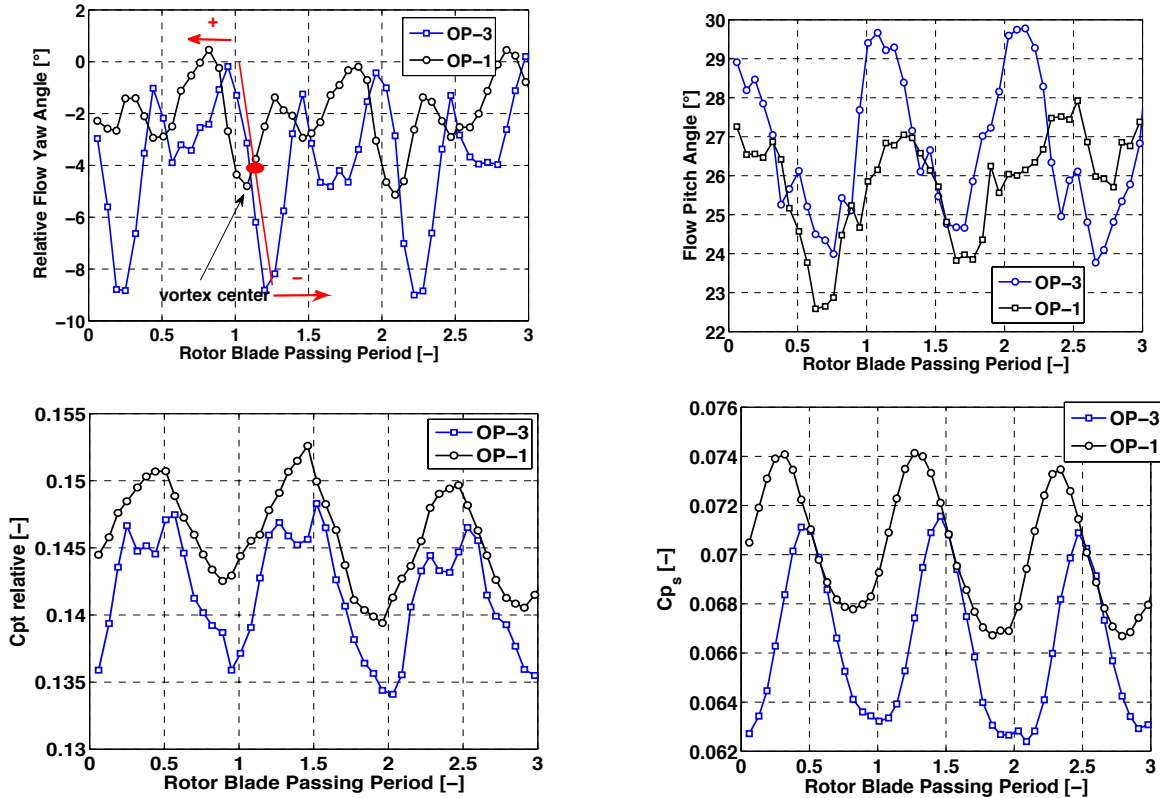


Figure 5-12: Unsteady relative flow yaw and pitch angles, relative total and static pressure coefficients at 86% span for OP-3 and OP-1.

One more observation worth noting is related to the presence of the PSC in Figure 5-11. The snubber results in a small alternation of the yaw angle of  $\pm 1^\circ$ , and its influence on the flow is  $\pm 10\%$  in span from its design location (52% span). Häfele et al. [95] have reported similar values for the impact of the PSC downstream of the rotor blade in steam turbine measurements.

As shown in Figure 5-11.a, the flow at the operating condition 3 in the region from 65 up to 100% span exhibits higher underturning compared to the flow at OP-1. The result is that the secondary flow structures are more enhanced and therefore generate higher aerodynamic losses in that particular regime, as previously described in Figure 5-7.b. This is in good agreement with the results in Figure 5-10, where OP-1 creates 25% less  $P_{tot}'$  RMS in the structures A and B.

#### 5.2.4 Steady flow field at rotor exit of L-0 stage

This paragraph presents the time-averaged results of the FRAP-HTH probe at the exit of L-0 stage for two different operating points. All plots show measurement results from 1.04 down to 0.33 span. Figure 5-13.a depicts the time averaged spanwise distribution of the relative pressure coefficient for OP-2 and OP-3 as described in Eq.(5-1). Condition OP-3 shows on an average 4.7% lower relative  $C_{pt}$  value and this can be attributed to the higher relative velocity across the span, which results in greater viscous losses. However, as

shown in Figure 5–13.b an inversion of the  $Cpt_{rel}$  is observed at 95% span, where OP-2 shows 5% greater  $Cpt_{rel}$  compared to OP-3 for this measurement plane. The results in Figure 5–13.b are derived with Eq.(5-4) for each radial measurement point.

$$\frac{\overline{Cpt}_{rel,OP-3} - \overline{Cpt}_{rel,OP-2}}{\overline{Cpt}_{rel,OP-3}} \times 100 \quad (5-4)$$

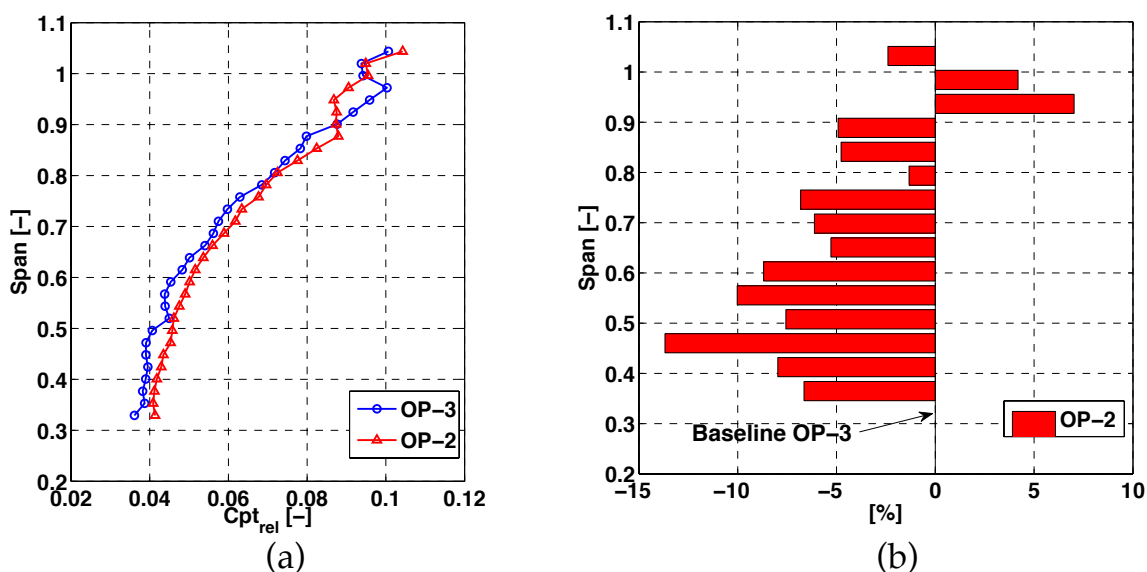


Figure 5–13: Time averaged spanwise distribution of the  $Cpt$  in relative frame of reference for 2 operating conditions (a) and difference in  $Cpt_{rel}$  between OP-2 with OP-3 (b),  $\dot{m}_{OP-2} = 78\% \dot{m}_{OP-3}$ .

In order to understand the reason for this variation at the blade tip of the L-0 stage, the time-resolved peak-to-peak variations of  $Cpt_{rel}$  for OP-2 and OP-3 are shown in Figure 5–14.a together with their respective time-averaged distribution across the span. It can be seen that at the region of 95% span, the peak-peak fluctuations of the  $Cpt_{rel}$  are 3 times larger for OP-2, the condition with the reduced mass flow, compared to OP-3. The maximum peak-to-peak fluctuations are 33% of the mean value for OP-2 at 92% span. On the other hand below 80% span, as seen in Figure 5–14.a, both conditions show very similar and low unsteady relative total pressure behavior.

In Figure 5–14.b the RMS of  $P_{tot}'$  are presented for OP-2 and OP-3. At 95% span, OP-2 gets the highest  $P_{tot}'$  RMS value, highlighting the presence of enhanced secondary flow structures compared to OP-3. This observation is in good agreement with Figure 5–14.a representing the region of high periodical unsteadiness at 92 to 95% span. The results of L-1 and L-0 stages for OP-2 and OP-3 contradict each other. The reason for this phenomenon is the sensitivity to the operating condition of the last stage in a steam turbine. In the current study OP-2 operates with 22.4 % reduced mass flow compared to OP-3.

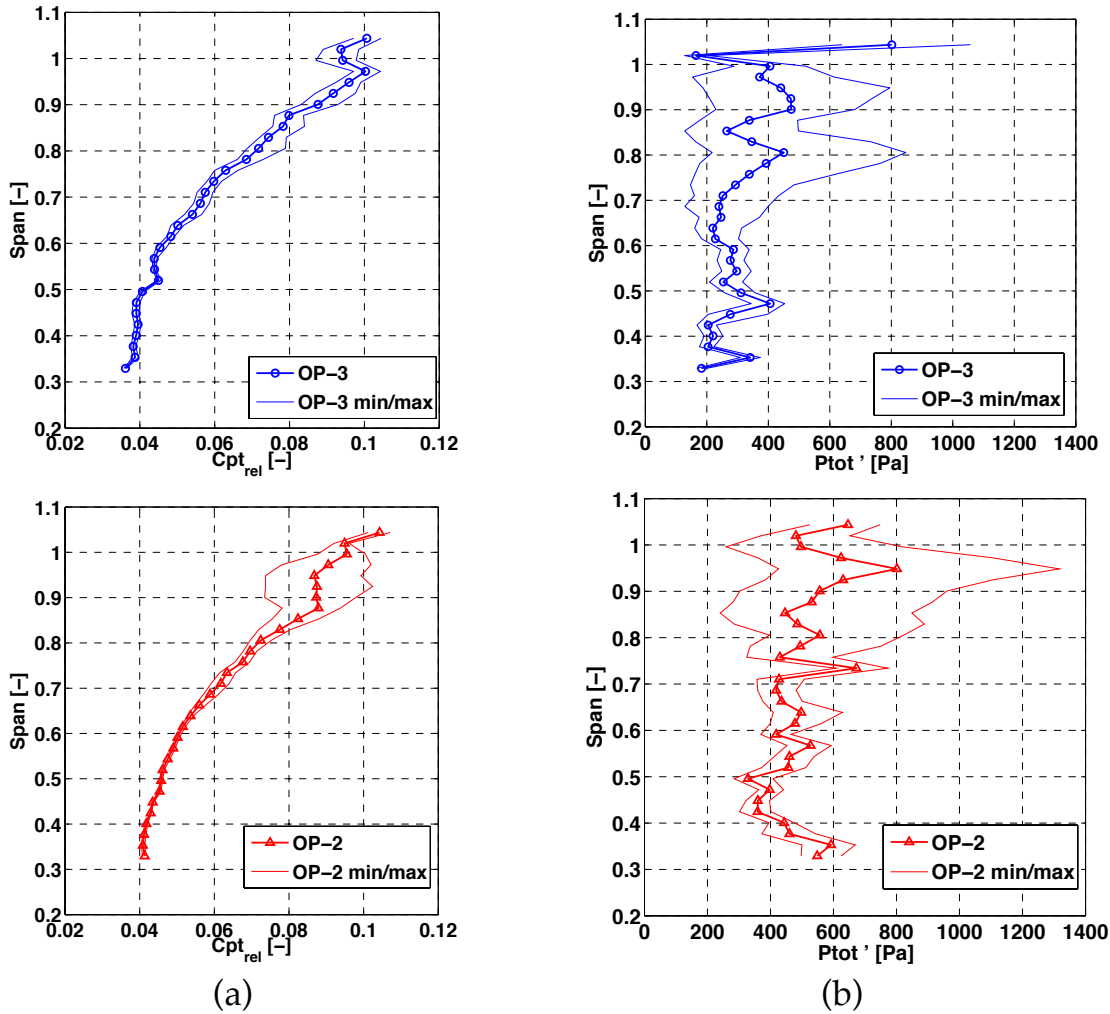


Figure 5–14: Time averaged spanwise distribution of  $C_{pt\_rel}$  (a) and time averaged  $P_{tot}'$  RMS [Pa] (b) at rotor exit of L-0 stage for OP-2 and OP-3 with their respective minimum and maximum values obtained from the time resolved data,  $m_{OP-2} = 78\% m_{OP-3}$ .

As shown in Figure 5–15, when the volume flow of the machine is reduced (OP-2), the fluid is redirected towards the tip region of the blade, which will strengthen the intensity of the three-dimensional turbulent flow structures present at the tip as shown in Figure 5–14 a. and b. This behavior normally is related to the very early stages of windage [31, 33, 35] as described in the introduction chapter of the thesis. According to [35], the first characteristic changes of the flow field appear below 50% of the high volume flow conditions. However, in this case the reduction of the mass flow is only 23%, therefore this flow redirection is not associated to windage but post probably to negative incidence angle or shock waves at the low reaction zone in the blade hub.

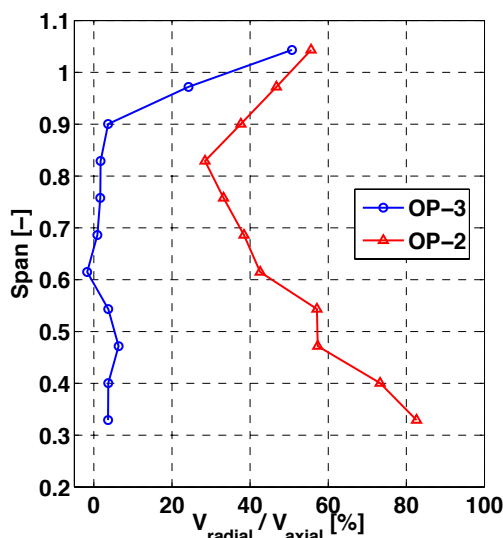


Figure 5–15: Time-averaged spanwise distribution of  $V_{\text{radial}}/V_{\text{axial}}$  at exit of L-0 stage,  $\dot{m}_{OP-2} = 78\% \dot{m}_{OP-3}$ .

### 5.2.5 Time resolved flow field at rotor exit of L-0 Stage

The time-resolved measurements performed at the rotor exit are presented in this paragraph for a single circumferential traverse. Figure 5–16 shows the spanwise distribution of the  $P_{\text{tot}}'$  RMS plotted over three consecutive blade passing events for OP-3 and OP-2. As seen in Figure 5–16 a and b, the  $P_{\text{tot}}'$  RMS distribution across the span exhibits multiple cores of highly turbulent flow structures located between 75% and 95% span, which are most likely generated from the rotor as well as from upstream stator. However, the single traverse type of measurement does not allow a clear identification of their origin. Nevertheless, one can identify that the high values of  $P_{\text{tot}}'$  RMS located between 80% and 95% span, for both operating conditions are driven periodically by the rotor blade passing period. OP-2 presented in Figure 5–16.b shows 60% higher values of  $P_{\text{tot}}'$  RMS compared to OP-3 for the turbulent structures located at 95% span, and 25% higher for the features located at 80% span.

Figure 5–17 shows the time-resolved relative flow yaw angle at the rotor exit for the conditions OP-2 and 3. In this figure the relative flow yaw angle is subtracted from the blade metal angle. Positive values infer to flow overturning and negative values to flow under-turning. As a general observation, the flow regions of high  $P_{\text{tot}}'$  RMS in Figure 5–16, located between 80% to 95%, result in local flow underturning in Figure 5–17, which is a typical signature of secondary flow structures. In Figure 5–17, the peak-to-peak fluctuations of the relative flow yaw angle between 80 to 95% span is of  $\pm 4^\circ$  for OP-3 and of  $\pm 5^\circ$  for OP-2. The higher levels of relative yaw angle periodical unsteadiness found in OP-2 compared to OP-3, are in good agreement with the observed variations in  $P_{\text{tot}}'$  RMS between the two conditions. If we now extend the analysis to the  $C_{\text{pt,rel}}$  temporal distribution, one can see that the magnitude of the

observed periodical unsteadiness in  $C_{pt,rel}$  presented in Figure 5–18 a and b is in line with the  $P_{tot}'$  RMS temporal and spatial distribution.

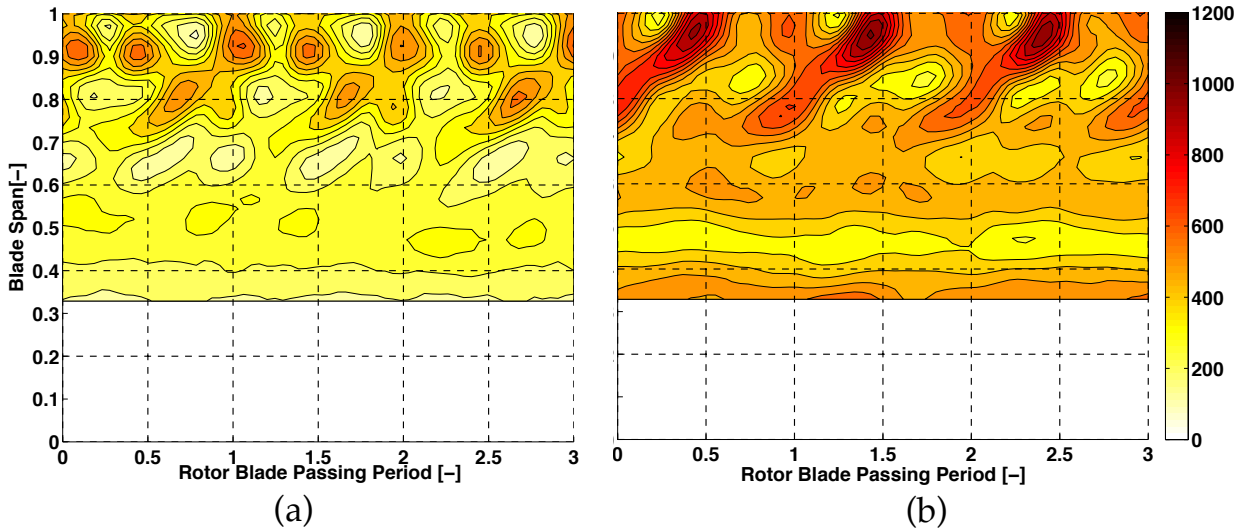


Figure 5–16: Time resolved RMS of  $P_{tot}'$  [Pa] in stationary frame of reference at rotor exit of L-0 stage for (a) OP-3 and (b) OP-2,  $\dot{m}_{OP-2} = 78\% \dot{m}_{OP-3}$ .

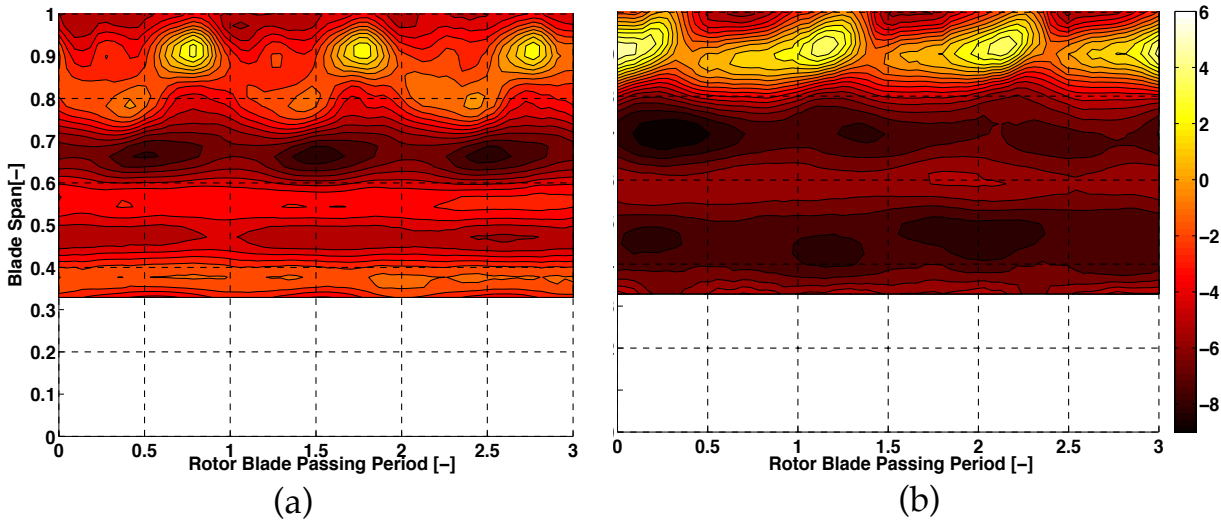


Figure 5–17: Time resolved relative flow yaw angle [deg] (relative to the blade metal angle) at rotor exit of L-0 stage for (a) OP-3 and (b) OP-2,  $\dot{m}_{OP-2} = 78\% \dot{m}_{OP-3}$ .

In Figure 5–18.a, it can be seen that the peak-to-peak variation in  $C_{pt,rel}$  at 92% span is 11% of the mean value for OP-3; whereas in Figure 5–18.b the peak-to-peak fluctuations at 92% span is 33% of the mean value for OP-2. Therefore, it can be concluded that due to the flow redirection to the blade tip, OP-2 shows 3 times higher relative total pressure fluctuations at the region of 95% span compared to OP-3. This is also the reason for the 5% deficit in relative total pressure around the tip, as shown in Figure 5–13.b.

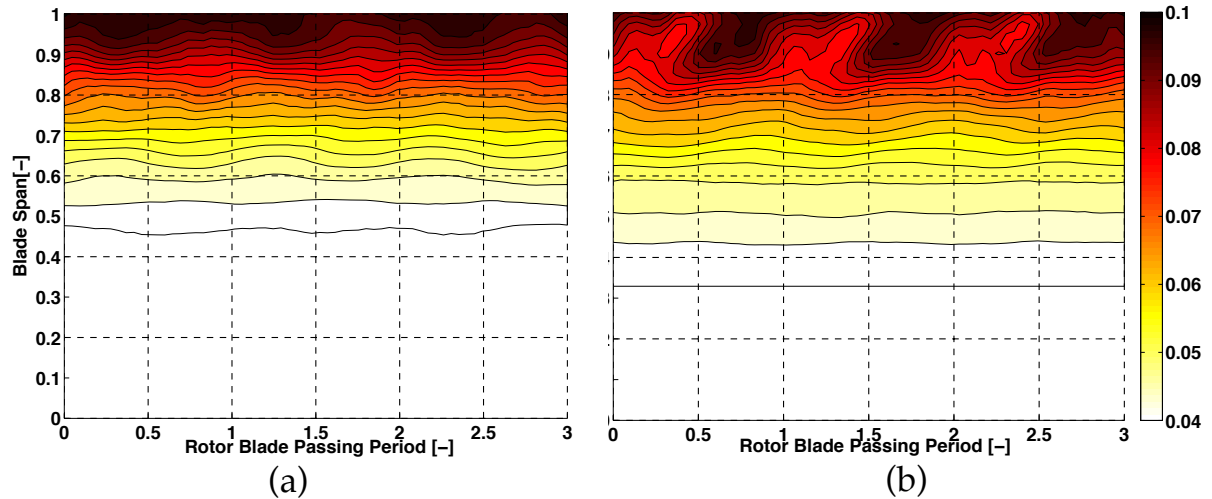


Figure 5–18: Time resolved  $C_{pt\_rel}$  [-] at rotor exit for (a) OP-3 and (b) OP-2,  $\dot{m}_{OP-2} = 78\% \dot{m}_{OP-3}$ .

### 5.3 Summary

A set of time-resolved flow field measurements with the FRAP-HTH probe at the inlet and exit of the last stage of a low-pressure steam turbine were presented in this chapter of the thesis. The measurements were performed in a steam turbine test facility in Japan equipped with subsonic rotor blades in the last stage. Three different operating points, including two reduced massflow conditions, were compared and a detailed analysis of the unsteady flow structures under various blade loads and wetness mass fractions was presented. A good level of agreement in trend and absolute values was found between the FRAP-HTH probe and the commonly used 5HP probe. The FRAP-HTH probe has demonstrated its reliability for accurate measurements in severe wet steam conditions with wetness mass fraction up to 8%.

The measurements have shown that the secondary flow structures at the tip region (shroud leakage and tip passage vortices) are the predominant sources of unsteadiness over the last 30% of the blade span for all operating conditions. At the exit of the second to last stage (L-1), the intensity of periodical fluctuations is found to be maximum for the high massflow condition (OP-3), with 8% fluctuation in relative total pressure. In contrast, at the exit of the last stage, the reduced mass flow operating condition (OP-2) exhibits up to 3 times higher pressure fluctuations between 85 to 100% span as compared to OP-3, causing 5% deficit in total pressure. The reason for this phenomenon is the redirection of the flow towards the blade tip region, resulting in the strengthening of the secondary flow structures.

## 6 Measurements in a 10MW steam turbine test facility with supersonic airfoils near the blade tip

The FRAP-OB and FRAP-HTH probes have demonstrated their ability to perform accurate measurements, in particle-laden flows, in chapters 4 and 5 respectively. In this chapter of the thesis a unique unprecedented set of time-resolved steam flow field measurements, in the last stage of a LP steam turbine, with relative supersonic inlet conditions at the last rotor is presented. All measurements were conducted at the stator exit at the top 30% of the blade span.

### 6.1 Experimental test facility

The results of the current chapter are from MHPS' 10MW research steam turbine test facility in Hitachi, Japan. As shown in Figure 6–1.a and b, it is a four-stage low-pressure steam turbine (L-3 to L-0) rig with a scale ratio of 1/3. The newly developed last stage rotor blades are a downscaled model of actual 50in steam turbine blades, enabling supersonic relative flow speeds at the tip region. Regarding the operation of the facility, the steam is generated in the boiler and directed into the turbine inlet. The inlet pressure and temperature are controlled in order to test different operating conditions and loads. At the exit of the last stage of the machine the condenser controls the exit absolute static pressure and the condensate water is guided back to the boiler to close the cycle. The facility also includes an inverter motor to drive the turbine shaft during low load tests. The inverter motor generator and a water brake dynamometer absorb the turbine's generated power and control the rotational speed of the machine through a gearbox. The measurements were performed at a rated speed of 10,800rpm, which is representative of a 60Hz power plant mainly used in USA as well as in Korea and Japan. The operating tested conditions presented in this chapter are summarized in Table 11.

Table 11: Operating tested conditions.

	OP-1	OP-2	OP-3	OP-4
Massflow [t/h]	47.5	35	35	15
Exit pressure [kPa]	5.0	5.0	5.0	5.0
Inlet temperature [°C]	272	272	220	272
Calculated wetness mass fraction at L-0 stator exit @ 80% span [%]	4.0	3.6	6.2	1.0

As shown in Figure 6–1.b, all measurements of the current experimental work were conducted at the stator exit of the last stage (L-0). The last stage of this LP steam turbine has 58 and 48 stator and rotor blades respectively. In addition, the stator blades are equipped with moisture separating slits (suction slits). This specific feature is installed at the outer range of the blade span and it is located on stator's pressure side. Its main goal is to remove the water



film, which builds up on the blade surface and then periodically tears from the trailing edge generating large droplets responsible for the erosion in the blade tip region (see Figure 1–12).

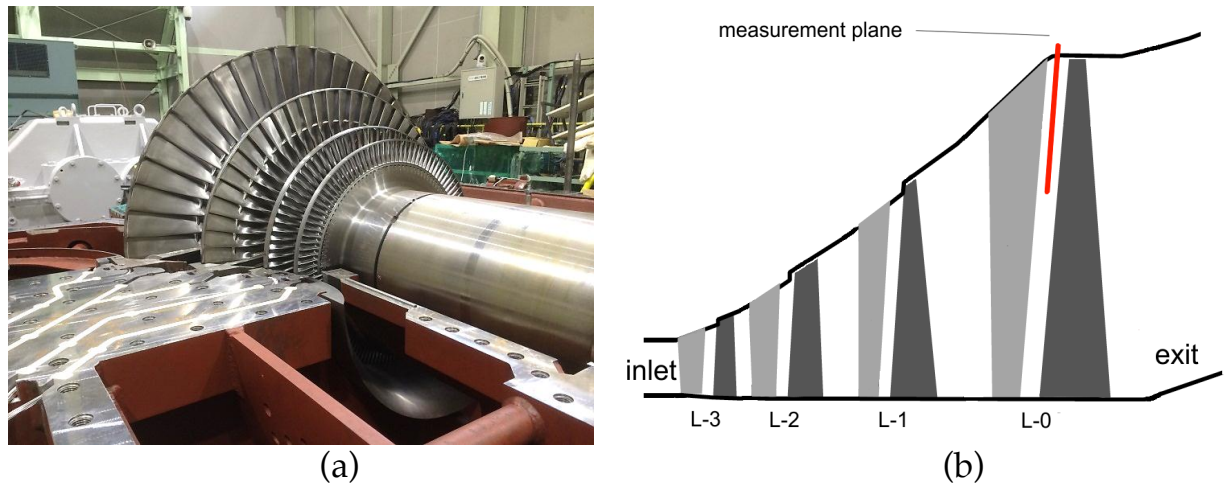


Figure 6–1: MHPs' low-pressure steam turbine test facility where FRAP-HTH and FRAP-OB measurements were conducted (a). Schematic of test facility, the measurement plane of the probe is marked in red (b).

The data are acquired at a sampling rate of 200kHz for the FRAP-HTH probe and 1MHz for the FRAP-OB probe over a time period of 2 and 1s respectively. All measurements approximately cover the last 30% of the blade span for one stator pitch. As shown in Figure 6–2, the grid at the measurement plane consists of 21 radial traverses with each traverse including 19 points in the radial direction. This is performed with the additional circumferential traversing axis which was installed specifically for this measurement campaign. In the radial direction, the 19 points are cluster towards the end wall in order to improve the spatial resolution at the region of the bow shock. The FRAP-HTH measurement plane is located at  $x/s=0.35$  between L-0 stator and rotor and the FRAP-OB plane is located at  $x/s=0.02$ . This practically implies that the plane of the FRAP-OB probe is located less than 2mm downstream in the axial direction from the trailing edge of L-0 stator.

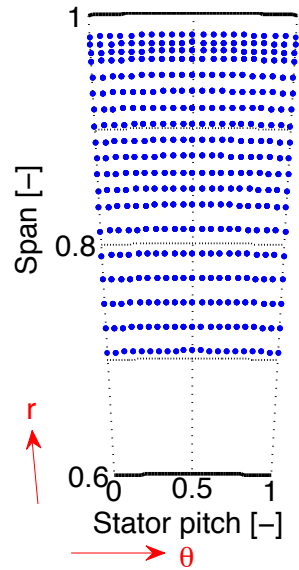


Figure 6–2: Measurement grid with 21 equally spaced points in the circumferential direction and 19 points in the radial direction clustered towards the end wall.

## 6.2 Results and discussion

### 6.2.1 Flow field analysis with FRAP-HTH results

#### 6.2.1.1 Time averaged results at L-0 stator exit

This paragraph presents the time averaged results of the flow field for operating point OP-1 as they were measured with the FRAP-HTH probe. The operating conditions for OP-1 are presented in Table 11. The results are circumferentially area averaged over one stator pitch and the first measurement point is at 96% of the blade span, which eliminates the influence of the probe access hole on the mainstream flow. Additionally, the minimum and maximum values obtained with the time resolved data are plotted on the current graphs with solid lines. These data are not circumferentially averaged.

Figure 6–3.a and b show the spanwise distribution of the total and static pressure coefficients for OP-1 according to Eq.(6-1) and Eq.(6-2) respectively. The inlet and exit refer to the conditions at the inlet and exit of the machine respectively (see Figure 6–1.b).

$$C_{pt} = \frac{P_{t,FRAP-HTH} - P_{s,exit}}{P_{t,inlet} - P_{s,exit}} \quad (6-1)$$

$$C_{ps} = \frac{P_{s,FRAP-HTH} - P_{s,exit}}{P_{t,inlet} - P_{s,exit}} \quad (6-2)$$

As shown in Figure 6–3.a, the total pressure coefficient is 0.06, up to 80-85% span and increases progressively to 0.07, up to 96% of the blade span. The stat-

ic pressure coefficient presented in Figure 6–3.b is 0.035, up to 80-85% and remains fairly constant up to 96% of the blade span with a small reduction at 87% span. The peak-to-peak fluctuations are relatively low in the lower region of the top 30% of the blade span and are increased up to 3 times in the outer region for both coefficients  $C_{pt}$  and  $C_{ps}$ , as shown in Figure 6–3.a and b.

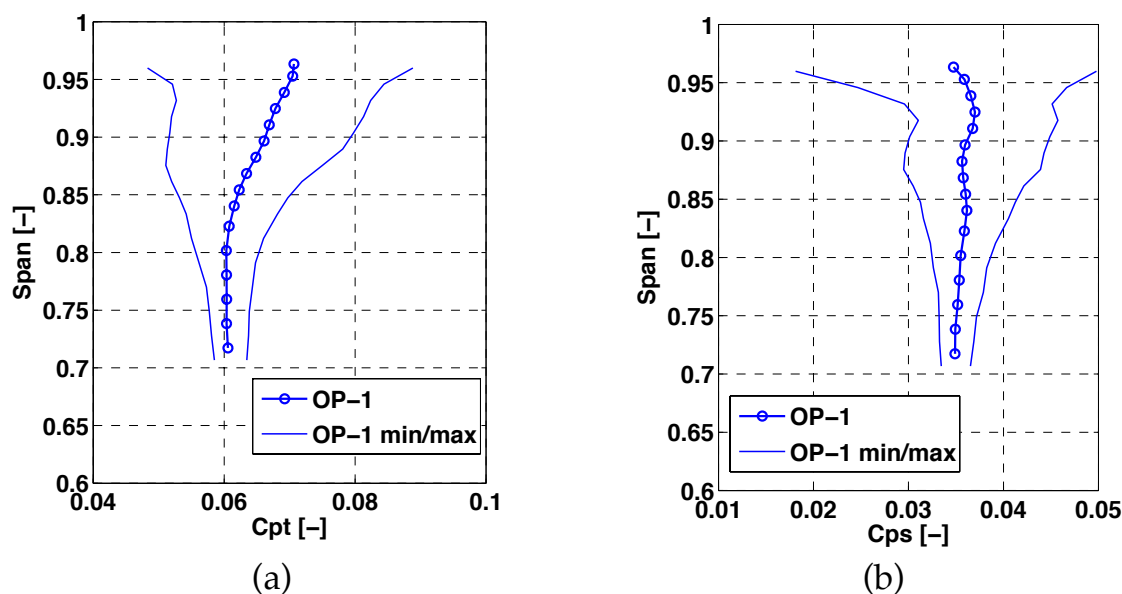


Figure 6–3: Circumferentially area averaged spanwise distribution of  $C_{pt}$  [-] (a) and  $C_{ps}$  [-] (b) with the minimum and maximum values obtained from the time resolved data.

Figure 6–4.a and b show the delta yaw angle and the pitch angle respectively. In Figure 6–4.a the absolute yaw angle, measured with the FRAP-HTH probe, is subtracted from the mean value of the blade metal angle according to Eq.(6-3).

$$\Delta\varphi = \varphi_{ma} - \varphi_{abs,FRAP-HTH} \quad (6-3)$$

Negative values imply flow underturning while positive values imply flow overturning. In general, the flow follows the blade metal angle with a small underturning of  $2.5^\circ$  on average at 93% span. The flow pitch angle percentage in Figure 6–4.b is the ratio of the measured pitch angle with the FRAP-HTH probe to the flare angle of the turbine, expressed with Eq.(6-4) (annulus angle at the meridional plane of the steam turbine casing). Values of 100% pitch angle imply that the flow has the same angle as the flare angle of the steam turbine and values of 0% pitch angle indicate that the flow is parallel to the rotating axis of the machine.

$$\gamma = \frac{\gamma_{FRAP-HTH}}{\gamma_{Flare\ angle}} \times 100\% \quad (6-4)$$

As depicted in Figure 6–4.b the flow pitch angle is approximately 60% of the flare angle up to 90% span, and it reaches approximately 80% of the flare angle from 90 to 96% of the blade span indicating the high radial component of the flow due to the specific geometry of the turbine annulus.

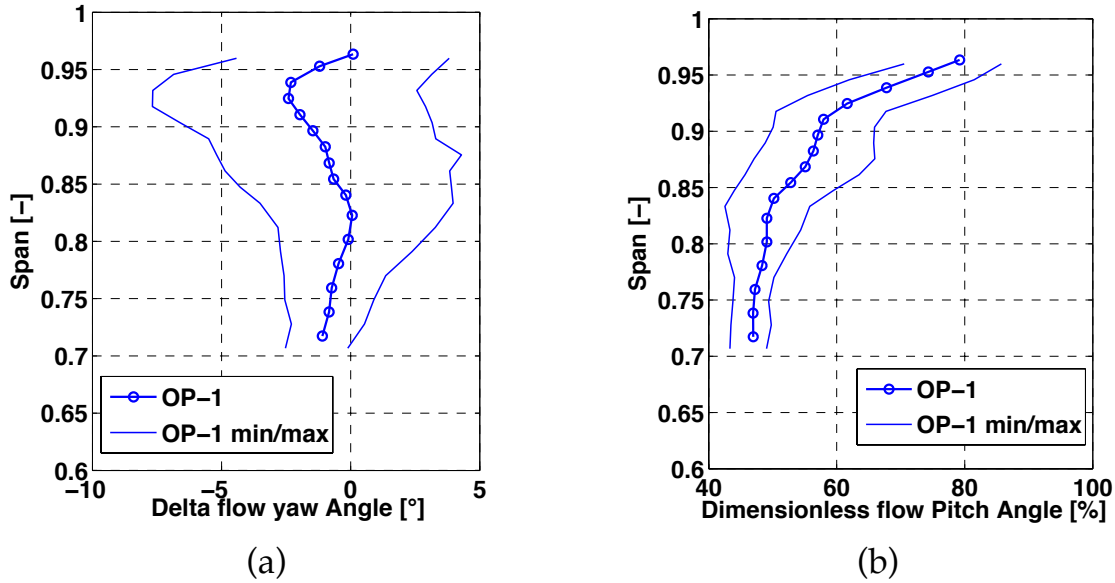


Figure 6–4: Circumferentially area averaged spanwise distribution of delta flow yaw angle [deg] (a) and dimensionless flow pitch angle [-] (b) with the minimum and maximum values obtained from the time resolved data.

In order to analyze the flow field further, the blade at the top 30% of the span is divided into two regions:

- Supersonic region (span > ~0.85)
- Subsonic region (span < ~0.85)

In the outer part (supersonic region) of the blade span the time averaged flow is supersonic relative to the rotor blade ( $Ma_{rel} > 1.0$ ) and in the inner part (subsonic region) the time averaged flow is subsonic ( $Ma_{rel} < 1.0$ ). Table 12 demonstrates the percentage of the peak-to-peak fluctuations over the mean value for the four flow quantities  $C_{pt}$ ,  $C_{ps}$ , delta yaw angle and the dimensionless flow pitch angle as presented in Figure 6–3 and Figure 6–4. Eq.(6-5) was used in order to calculate these quantities.

$$\frac{rms(\widetilde{Fq}_{max} - \widetilde{Fq}_{min})}{\overline{Fq}} 100\% \Big|_{\substack{span \\ region}} \quad (6-5)$$

In Table 12 all flow quantities are in percentage except the delta yaw angle, where the peak-to-peak difference is used, since the denominator of Eq.(6-5) gets values very close to zero for this particular flow quantity. In addition, the same data are presented in Figure 6–5 with a bar plot, in order to provide to the reader a better view of the two flow regimes. As expected and presented in Table 12 the supersonic region experiences greater peak-to-peak fluctua-

tions in all flow quantities. In particular, the total and static pressure coefficient is about 3.5 times larger in the supersonic region as compared to the subsonic. Regarding the flow angles, the peak-to-peak fluctuations in yaw and pitch angles have been doubled in the supersonic region compared to the subsonic. The variations in the yaw angle are approximately  $\pm 4.5^\circ$  and variations in flow pitch angle  $\pm 11.9\%$ . It is worth noting that the unsteady fluctuations in the subsonic region are in the range of 5-10% of the mean value for each flow quantity. Nevertheless, according to the author's knowledge, this is the first time that time resolved measurements in wet steam conditions are reported in the open literature with relative supersonic flows at the inlet of the last stage rotor. Therefore, the presented data cannot be compared with any other experimental measurements and the only possible comparison is with CFD results from the open literature.

Due to the high rotational speed, the long blade length of the last rotor has a supersonic tip speed, which results in a attached bow shock travelling with the rotor leading edge and interacting with the stator exit flow, as described by Senoo in [14, 99] and by Havakechian and Denton in [27]. This bow shock is presented in paragraph 1.2.2 of the introduction chapter and is annotated with S1 in Figure 1–8. As described in the following paragraphs, the bow shock is responsible for the large flow unsteadiness measured in the supersonic region and presented in Table 12 and induces up to 2 times higher rotor relative inflow angles' variation in comparison to the subsonic region. Still, the specific design of the blade airfoil allows an oblique shock wave to be generated in order minimize the losses and keep the efficiency at its maximum [14]. The time resolved data presented in the following paragraphs would be of use for the study of differences between the subsonic and supersonic region of the L-0 rotor blade and further analysis of the complicated flow field.

Table 12: Peak to peak fluctuations of the main flow field quantities as a function of the mean value for OP-1 for supersonic and subsonic region of the span.

Flow quantity ( $Fq$ ):	Region	OP-1 [%]
Cpt	Supersonic	$\pm 20.1$
	Subsonic	$\pm 5.8$
Cps	Supersonic	$\pm 22.5$
	Subsonic	$\pm 6.6$
Delta yaw angle	Supersonic	$\pm 4.5^\circ$
	Subsonic	$\pm 1.9^\circ$
Dimensionless pitch angle	Supersonic	$\pm 11.9$
	Subsonic	$\pm 6.1$

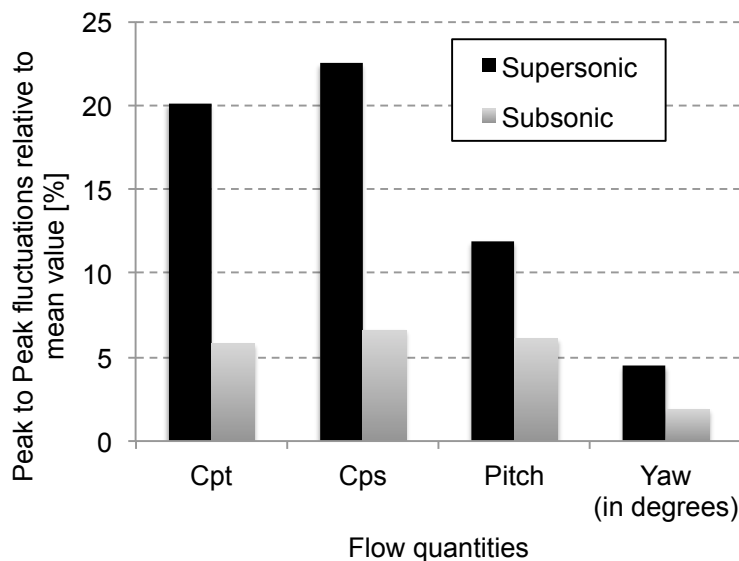


Figure 6–5: Bar plot of the peak-to-peak fluctuations of the main flow field quantities as presented in Table 12 for OP-1 for the supersonic and subsonic region of the blade span.

#### 6.2.1.2 Bow shock interaction with the L-0 stator's boundary layer

In order to further interpret the results from Figure 6–3 and Figure 6–4 and be able to assess the underlying flow mechanism responsible for the increased levels of unsteadiness in the supersonic region, the interaction of the rotor's bow shock with the upstream stator is studied in this section. While this kind of unsteady flow field was expected since the static pressure gradients become very large with the presence of a compressive shock wave, from the design point of view, it is important to minimize the interaction of the shock wave with the upstream stator and avoid any flow separation zone on the stator's suction side. Therefore, the first analysis is investigating the effect of the shock wave on the boundary layer of the upstream stator.

Figure 6–6.a and b show the time averaged total pressure coefficient and absolute Mach number respectively at three spanwise locations over one stator pitch. Following the stator's exit mean flow angle, the location of the intersecting wake with the measurement plane is found to be approximately between 0.1 to 0.17 of the stator pitch over the analyzed blade span region. As indicated in Figure 6–6.a for the results at 90% span, the Cpt value is minimum at the stator wake region. Nevertheless, as shown in Figure 6–6.a, no major Cpt losses related to the stator wake can be found. In particular, the total pressure coefficient is reduced only by 7% in the wake region (0.15 stator pitch) compared to the freestream (0.3 to 0.6 stator pitch). The circumferential extend of the wake signature remains rather small covering less than 0.1 stator pitch. The absolute Mach number shown in Figure 6–6.b agrees with this finding since the stator wake does not experience a large velocity deficit.

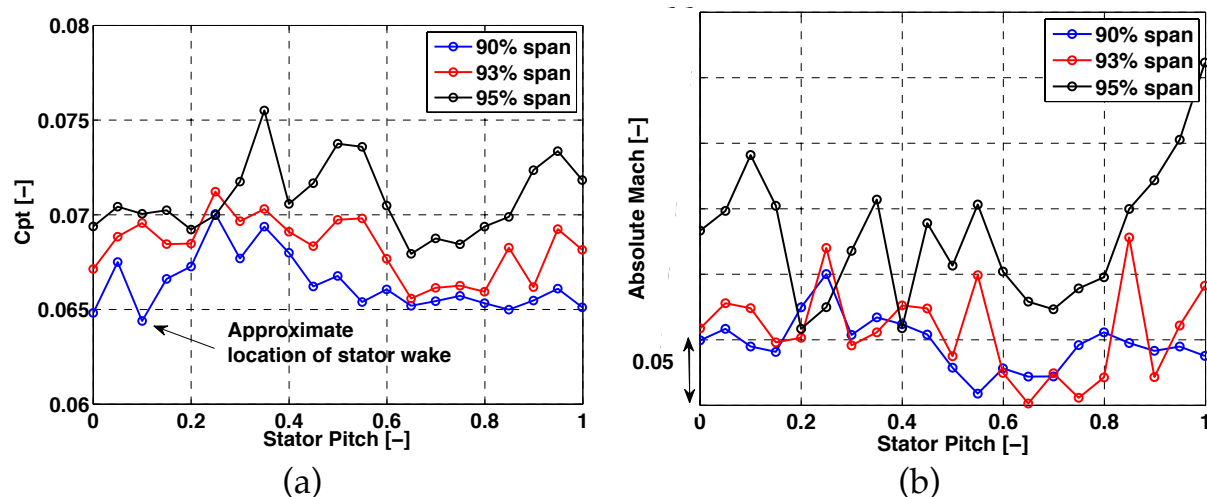


Figure 6-6: Total pressure coefficient (a) and absolute Mach number (b) at three blade span locations for one stator pitch, OP-1.

As a first observation, a large-scale boundary layer separation, associated to high aerodynamic losses at the stator exit, could not be identified. Nevertheless, in order to understand deeper this interaction and the cause of elevated unsteadiness, the time distance plots obtained from the time resolved results are used in the following paragraphs. A schematic of a space time diagram for a particular span location (at 87.5% span) is shown in Figure 6-7. In the time distance plots, fixed flow features relative to the stationary frame appear as vertical lines (i.e. stator wake) and features traveling with the downstream rotor are visible as inclined parallel structures, which are assigned to different L-0 rotor blades. The interaction of the downstream rotor influence flow and the stator can be observed in the crossing of those lines. The graphs are plotted for four L-0 rotor blade passing periods (y-axis) since within this time five full L-1 rotor blade-passing periods will have been completed.

Figure 6-8 shows the time resolved results of the total pressure coefficient at 90% span as obtained with the FRAP-HTH probe. As indicated in the same figure, there is a small modulation of the Cpt value with time in the stator wake at 0.17 stator pitch. This is shown at 0.12 stator pitch at  $t/T$ : 0.8, 1.8, 2.8 and 3.8 with a small reduction on Cpt. This variation implies that the attached bow shock results in a small wake widening when it interacts with the stator's suction side. Nevertheless, the white dashed lines in Figure 6-8 indicate how a large-scale separation should affect the total pressure coefficient. A large Cpt modulation with time would be present and associated to high losses. In addition to the Cpt results, the time resolved results of the absolute Mach number at 90% span are plotted in Figure 6-9. The features traveling with the downstream rotor are well visible as inclined parallel structures, which are assigned to different rotor blades. The two white dashed lines, in Figure 6-9, highlight one complete rotor pitch for a fixed time period of  $t/T$ . The entire rotor pitch could not be visible in this plot since the number of the rotor blades is less than those of the stator and therefore the rotor passage is

bigger compared to the stator passage. As shown in Figure 6–9, only a minor modulation with time of the velocity at the stator wake region was identified. This can be found at 0.17 stator pitch at  $t/T:0.2, 1.2, 2.2$  and  $3.2$ .

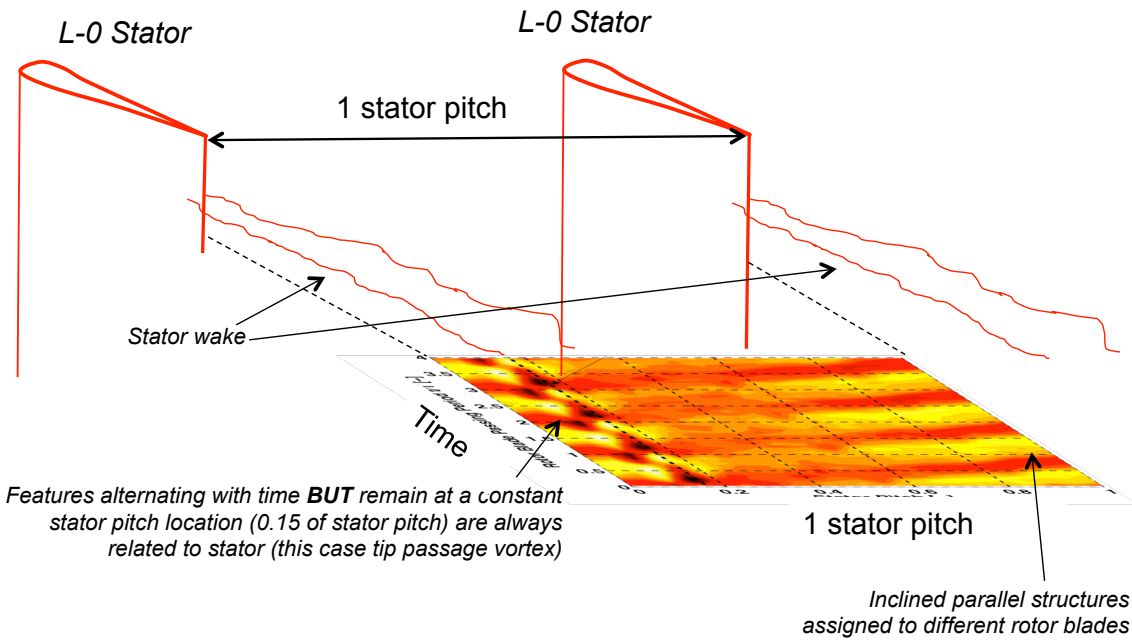


Figure 6–7: Representation of a time space diagram for the absolute yaw angle at a specific span location (87.5% span) for one stator pitch and four rotor blade passing periods.

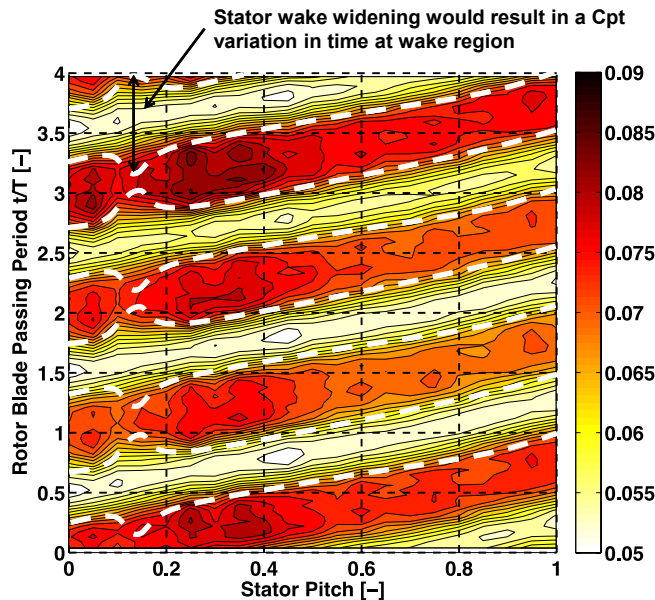


Figure 6–8: Circumferential distribution of  $C_{pt}$  [-] at L-0 stator exit for OP-1 at 90% span from measurements with the theoretical increase of the stator wake due to large scale separation.



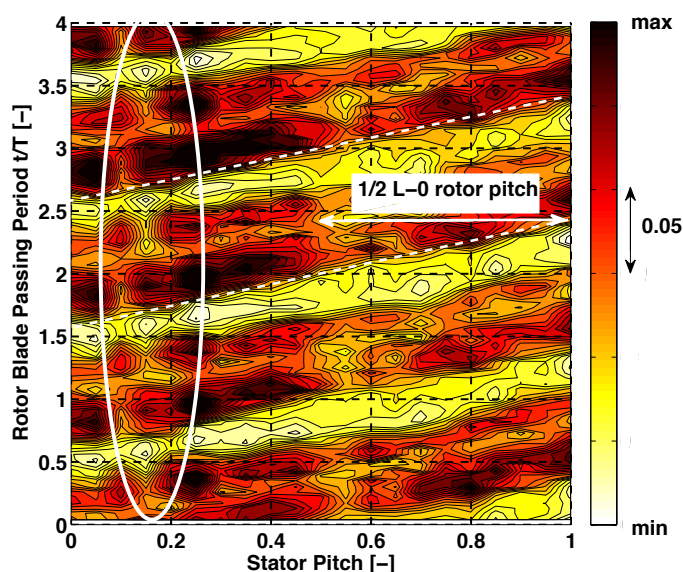


Figure 6–9: Circumferential distribution of absolute Mach number at L-0 stator exit for OP-1 at 90% span. The stator wake region where a high velocity modulation is expected in the case of a large-scale separation is marked with the white ellipse.

Considering always that the spatial resolution of the current measurements is  $0.3^\circ$  ( $6.2^\circ$  stator pitch/21 traverses), a large-scale separation on the suction side of the stator, triggered by the presence of the shock wave, was not found. This kind of boundary layer separation would reduce the total pressure coefficient as well as the velocity in the stator wake region (as a function of time, rotor blade passing period), due to increased losses. As a result, one could say that the thickness of the boundary layer is modulated by the presence of the shock wave, however the high unsteady values are not a major source of total pressure losses, and there is no clear evidence of a large scale separation that could be attributed to the high unsteady values at the top 15% of the blade span (supersonic region).

### 6.2.1.3 Bow shock unsteadiness analysis

In fluid mechanics a shock wave is a type of propagating disturbance. Like an ordinary wave, a shock wave carries energy, and can propagate through a medium; however it is characterized by an abrupt, nearly discontinuous change in pressure, temperature and density of the medium [100]. Since the density and static pressure increase rapidly along a compressive wave, the approximate location of the bow shock, present on the rotor, can be found with the results of the static pressure coefficient. The static pressure coefficient is directly proportional to the density field. Upstream of the shock wave the density and therefore the static pressure are low and downstream of the shock wave the density and thus the static pressure are high. This is

shown as well in Figure 6–10.a with the Schlieren visualization technique for a supersonic airfoil with a diamond shape. As explained by Kundu and Cohen in [100] the shock wave is in fact a very small boundary layer and the analysis shows that the thickness  $\delta$  of the shock wave is given by

$$\frac{\delta \cdot \Delta u}{\nu} \sim 1 \quad (6-6)$$

where the left-hand side is a Reynolds number based on the velocity change across the shock, its thickness, and the average value of the viscosity. The kinematic viscosity of steam for the current static pressure conditions is  $\nu \sim 80 \times 10^{-6} \text{ m}^2/\text{s}$ , and the velocity jump was measured in the range of  $\Delta u \sim 70 \text{ m/s}$ , therefore the thickness which is obtained is in the order of  $\delta \sim 10^{-6} \text{ m}$  resulting to a step increase in density as illustrated in Figure 6–10.b (Ideal case).

When measuring with the FRAP-HTH probe with a sampling rate of 200kHz, the total acquired samples for one rotor blade passing period are 24. In this discrete case the density field variation should have the profile of the green curve, as shown in Figure 6–10.b, due to sampling and spatial resolution limitations related to the probe's tip size.

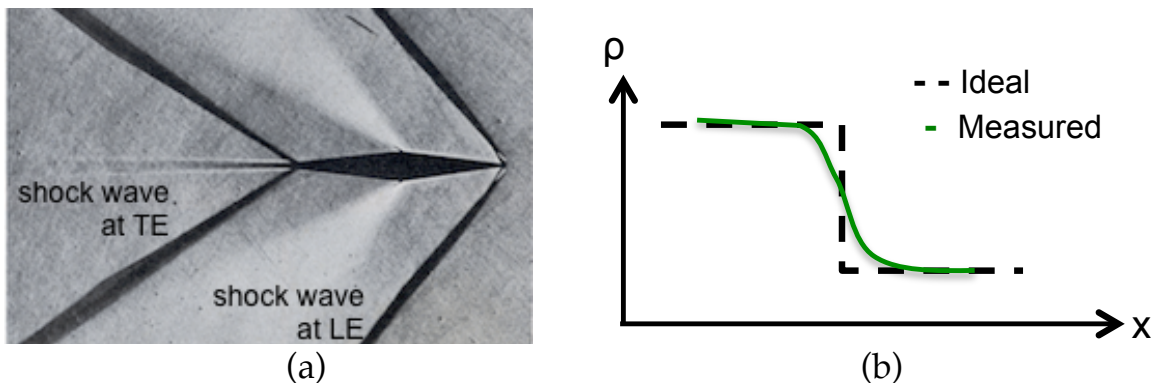


Figure 6–10: Shock wave attached at the leading edge of a diamond airfoil type (a) [101]. Density profile along the shock wave for ideal and measured case.

In the following paragraphs the unsteady flow field is further studied, in order to understand the origin of the peak-to-peak fluctuations of the flow at the supersonic region of the stator exit. As presented in Figure 6–3 and Figure 6–4, the supersonic and subsonic regions exhibit a large difference in the flow unsteadiness, which clearly sets two distinct flow regimes. The results are focused on 90% and 75% of the blade span. Although the attached bow shock becomes stronger at higher blade span locations and therefore it would be reasonable to select a higher span location for the analysis. The position at 90% was chosen since the pitch angle component becomes very large (see Figure 6–4.b) from this blade span and above.

The static pressure coefficient for the supersonic (90% span) and subsonic (75% span) spanwise locations is plotted in Figure 6–11.a and b respectively for one stator passage. As mentioned previously, following the stator's exit flow mean angle, the location of the intersecting stator wake is found at approximately 0.15 of the stator pitch. The stator suction and pressure sides are located on the left and right of the wake respectively and the observer looks upstream. As shown in Figure 6–11.a, the  $C_{ps}$  variation and therefore static pressure variation in a fixed stator pitch location is due to the downstream rotor rotation. High values of  $C_{ps}$  indicate the potential field of the downstream rotor and low values of  $C_{ps}$  indicate the field from the downstream rotor passage. The flow field in the subsonic region exhibits lower unsteadiness than presented earlier and shown in Figure 6–11.b. In particular, the peak-to-peak fluctuations in the stator's wake region are below 5% of the mean value and remain fairly constant in the entire stator passage. It should be noted that the variation of  $C_{ps}$  at different blade passing periods (i.e.:  $t/T=1.75$  compared to 2.25 at 0.4 stator pitch) is most probably related to the complex flow field of the upstream stages (L-1 stators: 88, rotors: 60). Their signature print in this spanwise location with the absence of the downstream bow shock was expected to be more evident than it is.

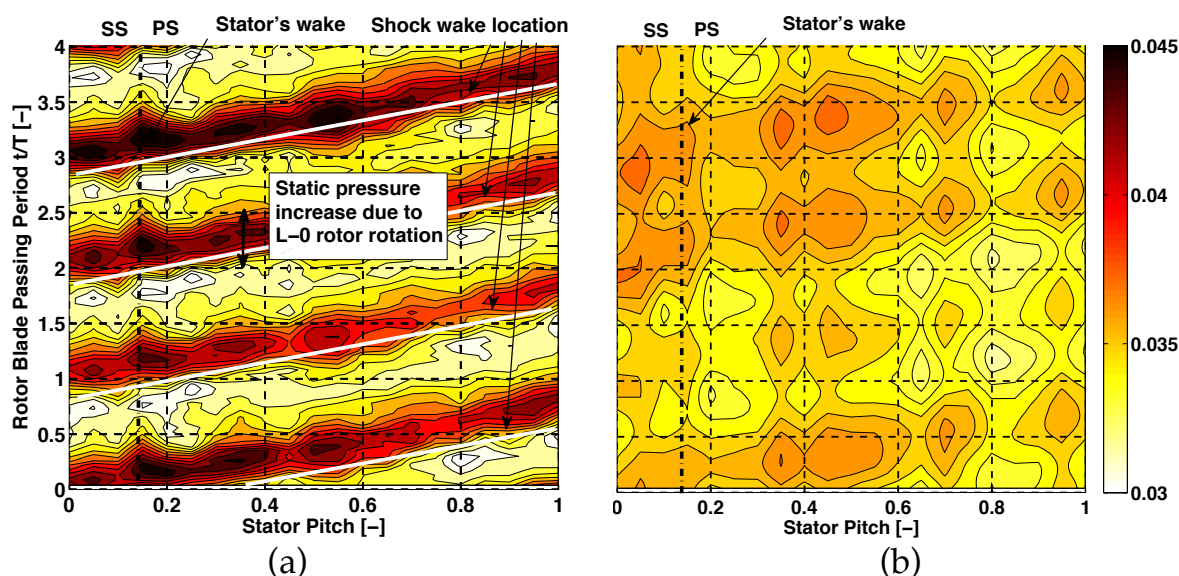


Figure 6–11: Circumferential distribution of  $C_{ps}$  [-] at L-0 stator exit for OP-1 at 90% (a) and 75% (b) span.

Regarding the unsteady flow yaw angle, regions of high and low static pressure, as presented in Figure 6–11.a, correspond well with flow overturning and underturning respectively as indicated in Figure 6–12 for the supersonic region at 90% span. This implies that the flow unsteadiness is driven by the high static pressure gradients generated by the moving bow shock. As shown in the same figure, the peak-to-peak fluctuations of the yaw angle in the vicinity of the stator wake are  $\pm 5.1^\circ$  indicating the influence of the L-0 rotor

potential field. In contrast, the peak-to-peak fluctuations at the stator passage, between 0.3 to 0.7 stator pitch, do not exceed the value of  $\pm 1.1^\circ$ .

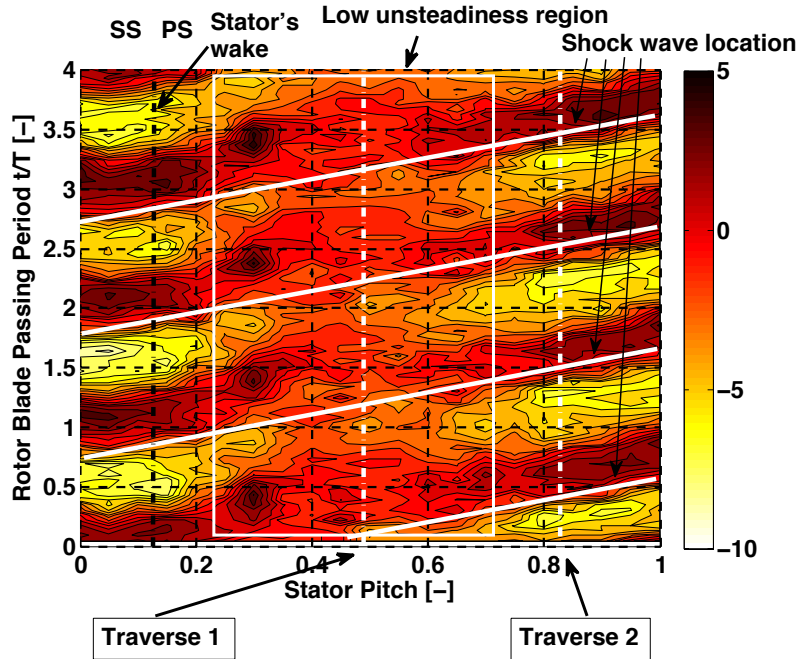


Figure 6–12: Circumferential distribution of delta yaw angle [deg] at 90% span at L-0 stator exit for OP-1. The region of low unsteadiness is marked with a white frame.

According to the definition given in Figure 6–10, for the following analysis the shock wave location is considered when the static pressure coefficient gets the average value between the minimum and the maximum as the  $C_{ps}$  curve increases from right to left on the plot. This is the inflection point of the  $C_{ps}$  curve. The effect of the bow shock on the flow field and its interaction with the upstream stator are shown in Figure 6–13 for four time instants of the rotor blade-passing period. It should be mentioned that the measured flow field (yaw angle) at the measurement plane is a result of the left stator passage flow out of the two that are always present in the schematics of Figure 6–13. This is due to the pronounced curvature of the stator's suction side, which results to high turning of the flow in the circumferential direction. In Figure 6–13, the plots at the right hand side show the absolute yaw angle as well as the static pressure coefficient,  $C_{ps}$ , for one complete stator pitch at 90% span. As previously mentioned, the yaw angle is relative to the blade metal angle, positive values imply flow overturning and negative values flow underturning. On the left hand side of Figure 6–13 qualitative schematics of the rotor blade location relative to stator's trailing edge for four time instants are presented as well. The results of Figure 6–13 will help to further understand this interaction, as the rotor blade moves circumferentially with time at constant rotational speed.

At time  $t/T=0$  in Figure 6–13, the maximum and minimum value of the static pressure coefficient is at 0.05 and 0.7 of the stator pitch respectively. This implies that the approximate location of the bow shock is at 0.3 of the stator pitch. As presented in Figure 6–13, the regions upstream (right side) and downstream (left side) of the shock wave correspond well to flow underturning and overturing respectively. At this time step the unsteady fluctuations of the absolute yaw angle relative to the blade metal angle are  $\pm 2.5^\circ$ .

At time  $t/T=0.25$  the approximate location of the bow shock, which has traveled with the rotor blade, is now at 0.6 of the stator pitch, and the regions upstream and downstream correspond well to flow under and overturing respectively. It is worth noting, that the relative yaw angle has increased to  $-5^\circ$ , and the peak-to-peak fluctuations of the static pressure coefficient by 10%, compared to the previous time instant.

At the later time,  $t/T=0.5$ , the approximate location of the attached bow shock has moved to 0.9 of the stator pitch. The regions upstream and downstream of the shock wave correspond again to flow under- and overturing respectively. The yaw angle gets its minimum value of  $-6^\circ$  relative to the blade metal angle and the static pressure coefficient the maximum gradient since the curve gets its highest steepness.

At time  $t/T=0.75$  the shock wave has just over taken the stator's trailing edge, and both shocks from two consecutive rotors are outside of the measurement plane. This is due to the greater number of stator blades (58) compared to the rotor blades (48) which makes the rotor passage 20% larger compared to the stator passage. The static pressure field, due to the absence of the shock in the measurement plane, is depicted as well in the static pressure coefficient in Figure 6–13. The  $C_{ps}$  value is increased from 0.031 up to 0.041 monotonically from 0 to 1 of the stator pitch, with no step as in the previous time instants.

From this analysis the stator passage flow seems to be constrained as the shock wave moves towards the trailing edge of the stator. While the attached bow shock travels together with the blade, the available area that the shock has, between the stator and rotor, is reduced progressively due to the curved profile of the stator's suction side (see Figure 6–16). The interaction of the shock wave with the stator's suction side intensifies the static pressure field. As a consequence, the unsteady static pressure results in high unsteadiness of the yaw angle. The results have shown that the available axial distance that the bow shock has seems to be the principal cause for the intense fluid motion at the stator exit of the last stage.

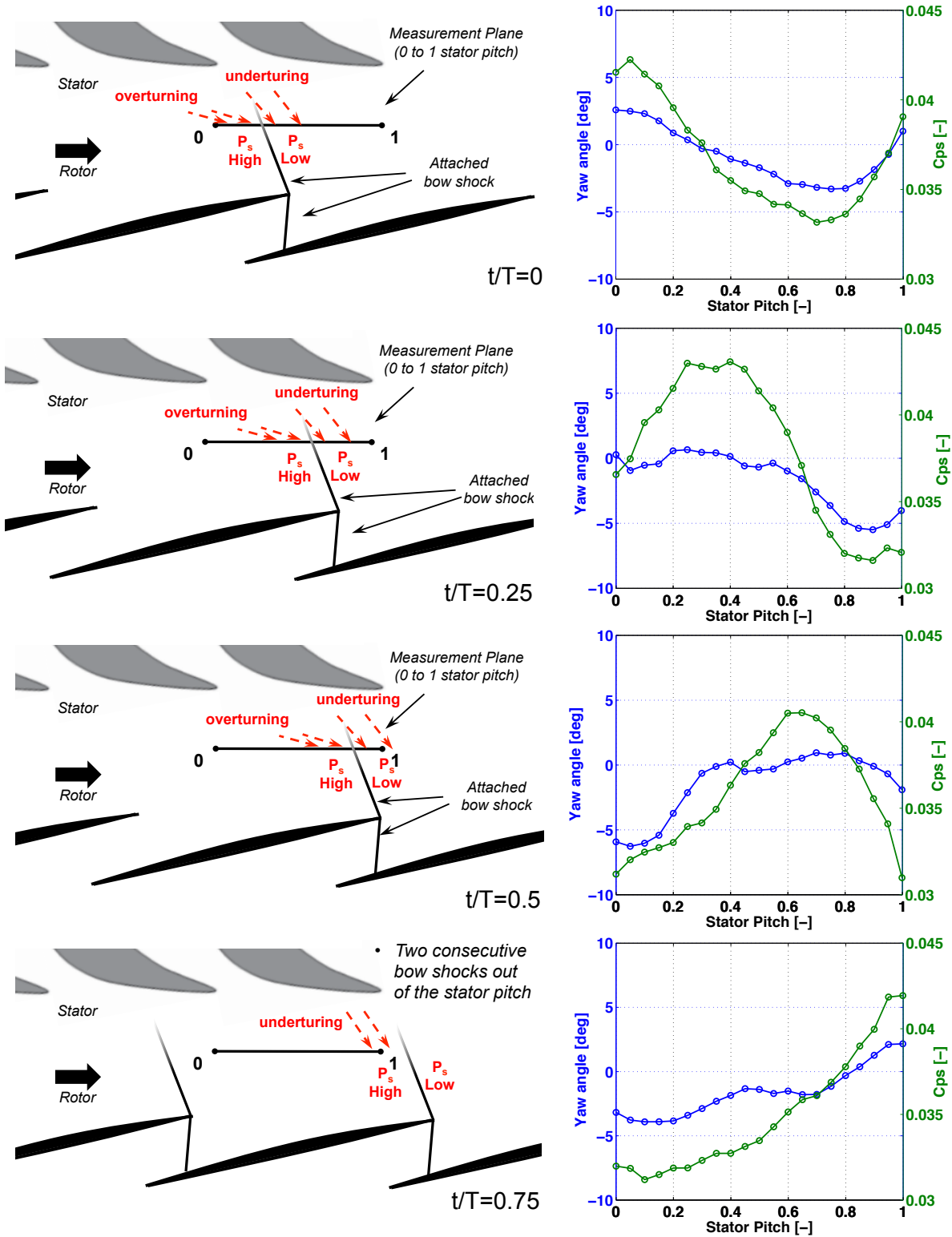


Figure 6-13: Left: Bow shock interaction with the stator trailing edge of L-0 stage for four instants of the rotor blade passing period ( $t/T=0$ ,  $t/T=0.25$ ,  $t/T=0.5$  and  $t/T=0.75$ ) at 90% span. Right: absolute flow yaw angle and Cps coefficient according to Eq.(6-3) and Eq.(6-2) respectively for the same time instants over one stator pitch.

Since the flow field unsteadiness is driven by the high static pressure gradients induced by the shock wave in the circumferential direction, the yaw angle unsteadiness in the stator passage region, between 0.3 and 0.7 stator pitch as presented in Figure 6–12, is strongly reduced. According to the previous analysis, one could say that there is no obvious reason why the yaw angle unsteadiness in the region from 0.3 to 0.7 of the stator pitch is reduced. The principal reason seems to be the redirection of the flow towards higher spanwise locations. This is shown in Figure 6–14 with the dimensionless pitch angle space time diagram. 100% pitch angle imply that the flow is parallel to the casing and 0% pitch angle indicates that the flow is parallel to the rotating axis of the machine. As indicated in Figure 6–14, the flow pitch angle has the maximum peak-to-peak fluctuations at the center of the stator passage from 0.3 to 0.7 of the stator pitch and this is the region where the absolute yaw angle experiences the minimum unsteadiness as shown in Figure 6–12.

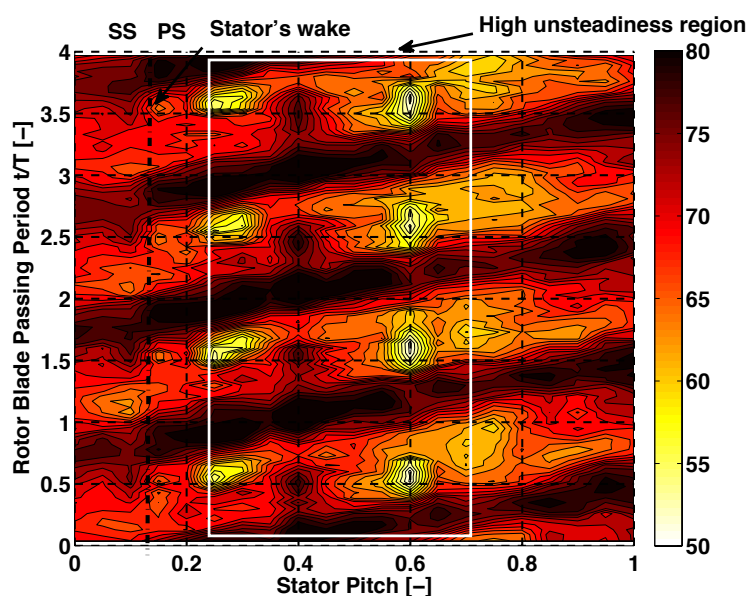


Figure 6–14: Circumferential distribution of dimensionless pitch angle [%] at 95% at L-0 stator exit for OP-1. The region of high unsteadiness is marked with a white frame.

The flow redirection towards the blade tip is shown as well in Figure 6–15, where the time resolved pitch angle is plotted for the top 20% of the blade span for four consecutive blade passing events. As shown in Figure 6–15, two different traverses were chosen out of the 21 that comprise one stator pitch. The results from the first traverse (Figure 6–12: Traverse 1) in Figure 6–15.a show the unsteady pitch angle variations from 80 to 100% span for 4 rotor blade passing events in the low yaw angle unsteadiness region. The same results are presented in Figure 6–15.b (Figure 6–12: Traverse 2) for the region where the yaw angle peak-to-peak fluctuations start increasing. In the region with the reduce yaw angle unsteadiness (Figure 6–12: Traverse 1) the pitch

angle has increased not only in magnitude, as shown in Figure 6–15.a, but also in the spanwise extent starting from 0.85 span. A relaxation of the static pressure field in the axial upstream direction reduces the yaw angle unsteadiness and increases the pitch angle unsteadiness.

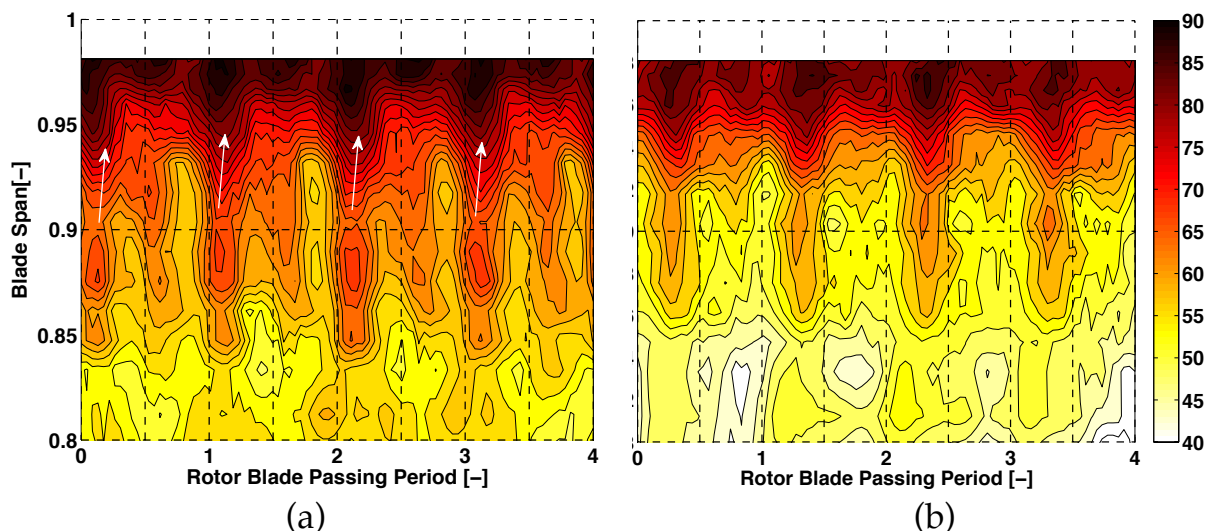


Figure 6–15: Time resolved flow pitch angle [%] (Blade span vs. Time) for two individual traverses: (a) region of low yaw angle unsteadiness (0.5 stator pitch) and (b) region where yaw angle unsteadiness starts increasing (0.85 stator pitch) as shown in Figure 6–12.

The axial distance between the bow shock and the stator suction side (see Figure 6–16) is reduced up to the stator trailing edge, causing the high alternation of the yaw angle. Once the shock has overtaken the stator's trailing edge, the flow is pushed towards the blade tip once again as a result of the local static pressure reduction (relaxation of the static pressure in the axial direction upstream). At this point, it is worth noting that the unsteady pitch angle does not show any intercepted region with low unsteadiness over the entire stator pitch, as shown in Figure 6–14. The pitch flow angle unsteadiness, induced by the rotating bow shock, is always present over the entire stator pitch and is only getting more intense in the region from 0.3 to 0.7 of the stator pitch. The principal reason is the specific geometry of the turbine's casing in the measurement plane. As shown in Figure 6–17, the high flare angle at the casing is constant over the entire annulus of the turbine ( $360^\circ$ ). Thus, the bow shock is always interacting with the wall, and therefore this is depicted with the parallel features traveling with the downstream rotor in Figure 6–14. However, once the shock wave has overtaken the stator's trailing edge, after being compressed from reduction in the area of the stator suction side in combination with the inclined wall, there is a mass flux towards the blade tip that transfers the unsteadiness of the flow in the radial direction.



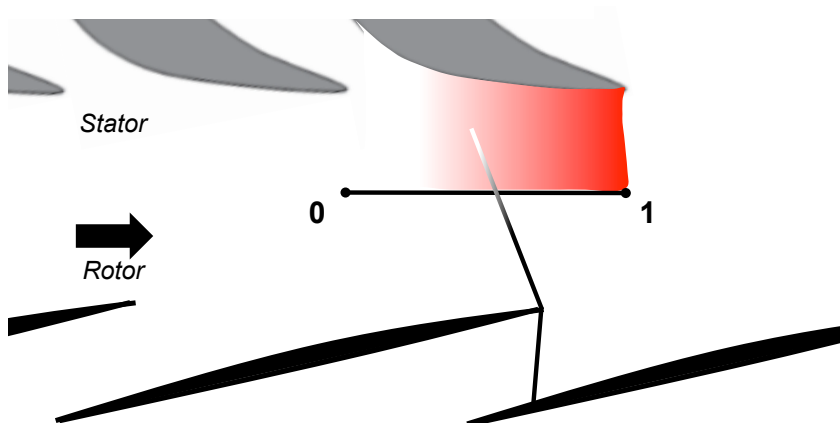


Figure 6–16: Reduction of the effective area due to stator’s suction side profile (marked with red) while the shock wave travels within the stator passage.

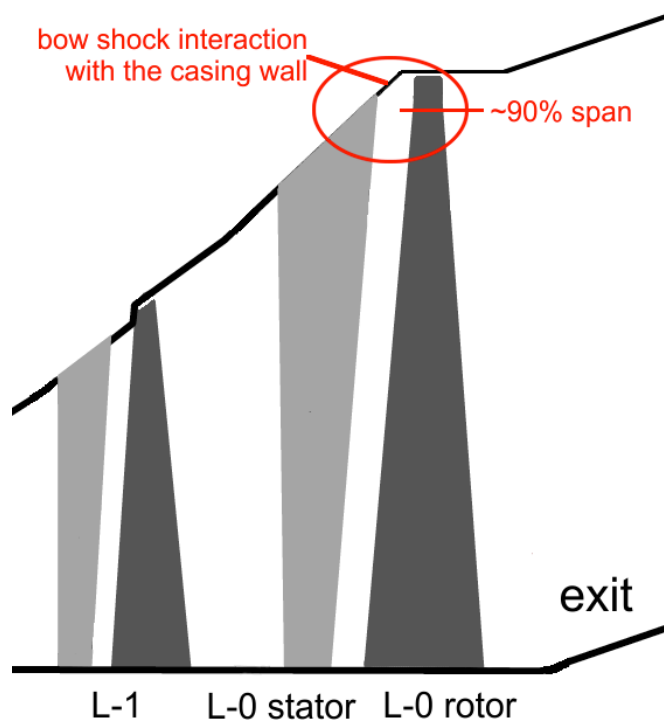


Figure 6–17: Meridional view of the last two stages. The bow shock interacts always with the casing wall at the very top of the blade span.

#### 6.2.1.4 Sensitivity analysis of energy loss across supersonic rotor passage to flow unsteadiness

As presented in the previous paragraphs, fluctuations on the flow angles as well as on the total and static pressure are induced by the presence of the attached bow shock at the inlet of the supersonic rotor section. However, the design of a supersonic airfoil has some special features that might be affected from the unsteady flow field. In this paragraph, a sensitivity analysis on the added losses across the rotor passage is performed.

In order to accelerate the flow within the rotor passage, the flow path should be divergent. Therefore, the throat is located at the inlet in the supersonic blade airfoil and defines the maximum mass flow rate. The flow acceleration, expressed with the Mach number increase, specifies uniquely the flow turning with the Prandtl-Mayer relation [100]. As a consequence, the inlet flow quantities are more important than the exit choked properties. Thus, the relative flow yaw angle, relative Mach number and pressure ratio  $P_{s,exit}/P_{t,inlet}$  are selected as predetermined inlet design parameters to satisfy the design mass flow rate. When the inflow velocity is supersonic, the relative yaw angle and relative Mach number at the inlet are not independent of each other. This relationship is called unique incidence, and a supersonic airfoil should correspond to it [14]. The unsteady fluctuations at the inlet, result in a deviation from this unique incidence. Therefore, it is important to assess the additional losses induced by the unsteady behavior of the flow.

Figure 6–18 shows the relative yaw angle and relative Mach number at the inlet and exit of L-0 rotor blade for the ideal case assuming an airfoil without thickness.

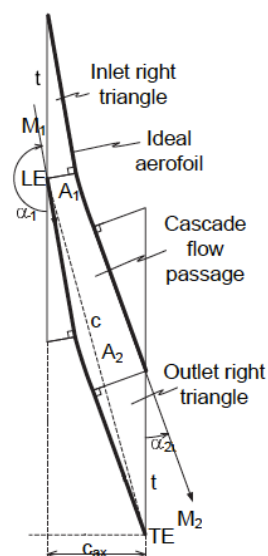


Figure 6–18: L-0 rotor inlet and exit velocity and Mach number relationship. The subscripts 1 and 2 refer to the inlet and exit of the rotor passage respectively [14].

Since there are no measurements with the FRAP-HTH probe at the rotor exit, the relative yaw angle can be calculated with Eq.(6-7), based on the quasi-one-dimensional theory. This equation provides the relative exit yaw angle,  $\alpha_2(t)$ , as function of the relative inlet,  $M_1(t)$ , and relative exit,  $M_2(t)$ , Mach numbers. The optimum isentropic relative yaw angle at the outlet is achieved when the supersonic flow at the inlet accelerates smoothly to the isentropic supersonic outflow in the cascade passage presented in Figure 6–18. In this case the strong trailing edge shock wave (see Figure 1–8, shock wave S3) can be avoided.

$$\alpha_2(t) = \sin^{-1}\left(\frac{A_1}{pitch}\right) = \sin^{-1}\left[\sin(\alpha_1(t))\frac{M_1(t)}{M_2(t)}\left(\frac{1 + \frac{\gamma+1}{2}M_2^2(t)}{1 + \frac{\gamma+1}{2}M_1^2(t)}\right)^{\frac{\gamma+1}{2(\gamma-1)}}\right] \quad (6-7)$$

For the following calculations, the FRAP-HTH time-resolved data are circumferentially area averaged. The resulting span distribution of relative yaw angle and relative Mach number at the inlet of the last rotor are shown in Figure 6–19.a and b respectively. Since the exit Mach number,  $M_2(t)$ , is unknown, the time averaged results from the measurements with the 5HP are used. In a second step, a sensitivity analysis of the exit flow angle,  $\alpha_2(t)$ , to this variable is performed. It is worth noting, that the phase between  $\alpha_1(t)$  and  $M_1(t)$  in Eq.(6-7), is taken into consideration for the calculation of  $\alpha_2(t)$ .

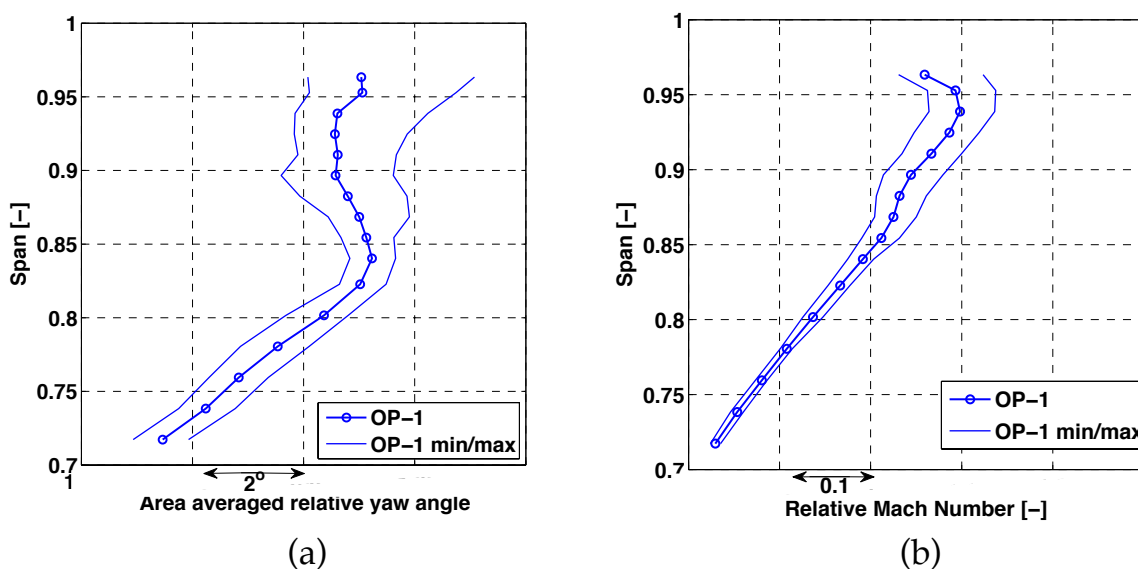


Figure 6–19: Circumferentially area averaged spanwise distribution of relative yaw angle (a) and relative Mach number (b) for OP-1 at the rotor inlet. The solid lines show the circumferentially area averaged time resolved results.

The calculated relative yaw angle,  $\alpha_2(t)$ , at the exit of L-0 rotor is presented in Figure 6–20. In this plot the solid line shows the pitchwise averaged relative yaw angle, and the dashed lines represent the instantaneous maximum and minimum values along the blade span. The peak-to-peak fluctuations in the supersonic region, above 85% span are approximately  $\pm 1.3^\circ$  from the average value.

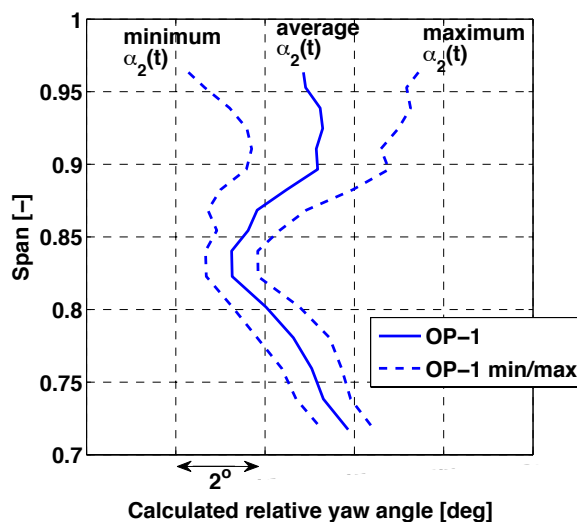


Figure 6–20: Calculated relative yaw angle at the rotor exit for OP-1 according to Eq.(6-7). The dashed lines show the instantaneous maximum and minimum values along the blade span.

The correlation of the relative yaw angle, at the rotor exit, with the energy loss coefficient is given by Senoo in [14]. In this numerical study, the effect of the outlet blade metal angle on the relative energy loss coefficient for various supersonic turbine airfoils, with constant pitch-to-chord ratio, is presented. As explained in [14], the smaller the outlet metal angle is, the smaller is the flow passage and vice versa. However, a smaller outlet flow passage width results in insufficient flow acceleration, not enough to reach the isentropic Mach number, at the exit of the blade, as shown in Figure 6–18. This results in an oblique shock wave with higher energy losses (see Figure 1–8, shock wave S3). Thus, in order to increase the corresponding exit Mach number,  $M_2$ , and reduce the losses, the outlet metal angle should increase.

This effect is presented in Figure 6–21 for various trailing wedge angles,  $WE_{TE}$ , of the L-0 rotor blade. High and low  $WE_{TE}$  imply large and small trailing edge radius respectively. The optimum design case is when the  $WE_{TE}=16$ , and the increment of the outlet metal angle is  $10^\circ$ . Any deviation from the design point, results in additional energy losses. Assuming the flow follows the blade metal angle, the additional losses due to the unsteady relative yaw angle at the exit can be calculated with the results from Figure 6–21.

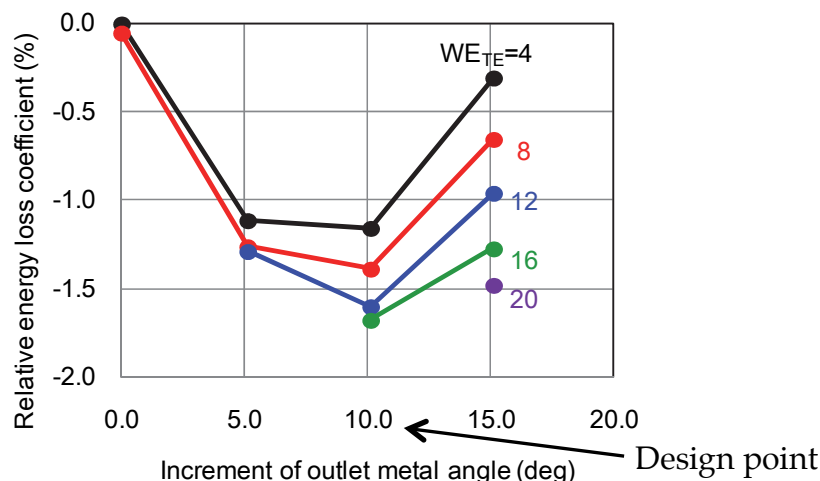


Figure 6–21: Energy loss coefficient out of simulations presented by Senoo in [14]. The optimum design case is for an increment of 10° in the outlet metal angle relative to the initial quasi-one-dimensional design result.

Considering the maximum deviation of the relative yaw angle,  $\alpha_2(t)_{\max}$ , from the average value,  $\alpha_2(t)_{\text{average}}$ , along the blade span (see Figure 6–20), the instantaneous maximum losses are calculated with the results from Figure 6–21 for  $WE_{TE}=16$ . The results are shown in Figure 6–22.a for the supersonic region. Nevertheless, since the maximum losses occur at a specific time instant, it is worth calculating the time averaged losses with Eq.(6-8),

$$\Delta\xi = \beta_{16} \cdot \frac{\sum (\tilde{\alpha}_2(t) - \bar{\alpha}_2(t))}{\bar{\alpha}_2(t)} \quad (6-8)$$

where  $\beta_{16}$  is equal to the derivative of the relative loss coefficient for  $WE_{TE}=16$  in Figure 6–21. As depicted in same figure, the large wedge trailing edge ( $WE_{TE}=16$ ) could not be applied to the airfoil with small increments of outlet metal angle because the angle on the suction surface approaches to zero, thus the smooth suction surface cannot be formed. Therefore, for the current calculations the same slope was assumed from 5° to 10° of the increment metal angle when  $\tilde{\alpha}_2(t) - \bar{\alpha}_2(t) < 0$ . The relative increase of energy loss, attributed to the flow unsteadiness, is presented in Figure 6–22.b from 85 to 96% span. This sensitivity analysis shows, that the added losses, due to flow unsteadiness induced by the shock wave in the supersonic region, are 0.04% greater from the design point.

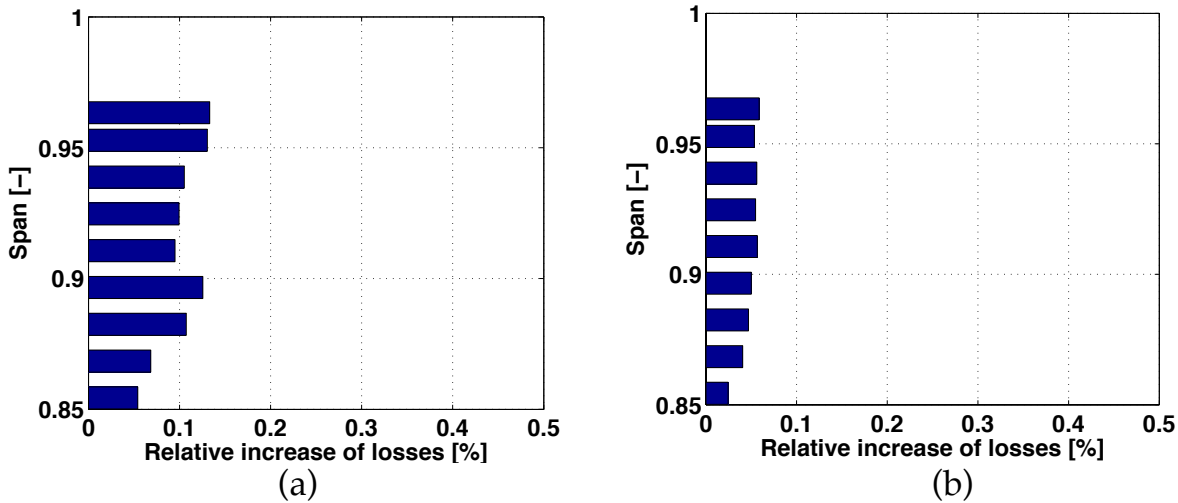


Figure 6–22: Calculated instantaneous maximum losses (a) and time averaged losses (b) in the supersonic region for OP-1. These plots present the relative increase of the losses compared to the design point as indicated in Figure 6–21.

### *Energy loss sensitivity to exit Mach number unsteadiness*

In order to assess the validity of the assumption that the Mach number at the exit remains constant, the same calculations were performed imposing  $\pm 0.15$  unsteadiness in the  $M_2(t)$ . The amplitude of unsteady relative Mach number at the rotor exit is assumed to be  $\pm 0.15$ . The calculated time averaged losses for the two extreme cases, where the exit Mach number is  $\pm 0.15$  from the average value, are presented in Figure 6–23. As shown in the same figure, the influence of the exit Mach number to Eq.(6-7) and thus to the results is small. In particular, when  $M_2$  is  $\bar{M}_2 - 0.15$  (Figure 6–23.a), the overall time averaged losses induced by the shock wave in the supersonic region are 0.033% greater from the design point, and when  $M_2$  is  $\bar{M}_2 + 0.15$  (Figure 6–23.b), the overall time averaged losses are 0.045% greater from the design point. Therefore, the sensitivity results for the exit Mach number have shown that the unsteadiness of  $\pm 0.15$  induces up to  $\pm 0.005\%$  losses, compared to the case with the average value of Mach number at the rotor exit.

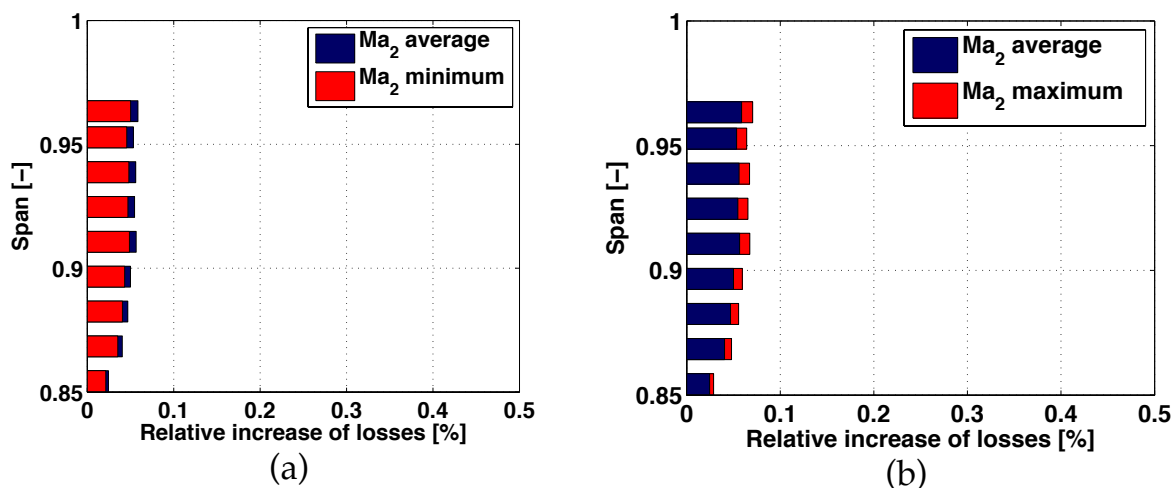


Figure 6–23: Calculated time averaged losses for  $Ma_2 + \Delta Ma$  (a) and  $Ma_2 - \Delta Ma$  (b) in the supersonic region for OP-1. These plots present the relative increase of the losses compared to the design point.

## 6.2.2 Flow field analysis at reduced mass flow operation

The results from the part load condition, when the mass flow has been reduced by 68%, are presented in this paragraph. The analysis is based on the comparison between the high and low mass flow operating points OP-1 and OP-4 respectively (see Table 11). Both conditions have the same inlet temperature and exit vacuum pressure, but they differ on the operating mass flow. Together with the time averaged results, the minimum and maximum values obtained from the time resolved results are plotted in the following plots. At this point it has to be mentioned that the FRAP-HTH probe operates outside the calibration range for the spanwise location above 80% for the operating point OP-4. At low mass flow condition, the absolute Mach number of the flow was found to exceed the probe's maximum aerocalibration range Mach 0.82. Nevertheless, the results of the total pressure as well as the absolute yaw angle are not affected, as they are independent of the flow velocity (see §2.1.5 FRAP-HTH aerodynamic calibration). The measured absolute Mach numbers, above 0.82 are underestimated, when processed with the available aerocalibration model, due to an underestimation of the compressibility affecting the static pressure aerocalibration coefficient. It implies that the low mass flow condition might experience even higher absolute Mach numbers at L-0 stator exit.

Figure 6–24.a and b show a comparison of the total pressure coefficient and the absolute yaw angle respectively for the two operating points. As illustrated in Figure 6–24.a, both operating points demonstrate the same trend: low unsteadiness below 0.8 span, and a gradual increase above 0.8 span.

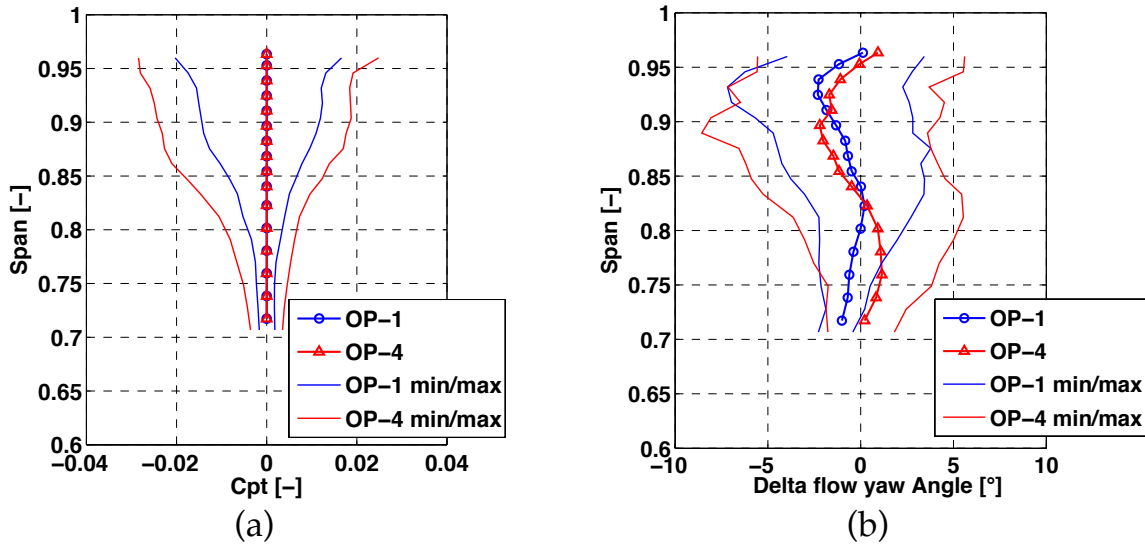


Figure 6-24: Circumferentially area averaged spanwise distribution of total pressure coefficient (a) and absolute yaw angle (b) with the minimum and maximum values obtained from the time resolved data for OP-1 and OP-4 (part load,  $32\% \dot{m}_{OP-1}$ ).

However, the peak-to-peak fluctuations of the Cpt are increased in OP-4 (low mass flow condition) by 65% and 95% at 90% and 75% span respectively. The results from the absolute yaw angle in Figure 6-24.b show an increase of  $\pm 2.3^\circ$  and  $\pm 1.5^\circ$  at 90% and 75% span respectively, indicating higher levels of flow unsteadiness at operating point OP-4 when the mass flow is decreased by 60%.

In order to explain the greater peak-to-peak fluctuations at OP-4 compared to OP-1, one should study the sensitivity of the operating condition of the last stage to the mass flow reduction. As explained in the motivation chapter of this thesis and observed in paragraph 5.2.5 with the measurements in the 7MW case, when the volume flow of the machine is reduced sufficiently (OP-4), the massflow of the last stage is being redirected towards the blade tip region, due to the onset of turbine windage [31, 33, 35], strengthening the intensity of the secondary flow structures. Depending on the intensity of this phenomenon, the resulting recirculation bubble, present near the hub, can propagate upstream, sometimes reaching the second to last stage, L-1 [31]. Figure 6-25 shows the flow pitch angle at the L-0 stator exit for the high and low mass flow conditions, OP-1 and OP-4 respectively.

As presented in Figure 6-25, the flow pitch angle has been increased by 10% from OP-4 to OP-1 from 70% to 90% of the blade span. Such an increase of the pitch angle at the very top of the blade span shows that the flow is redirected to the tip, most probably due to the onset of windage [35] responsible for the supersonic absolute flow conditions measured near the blade tip, as indicated in Figure 6-26.a.



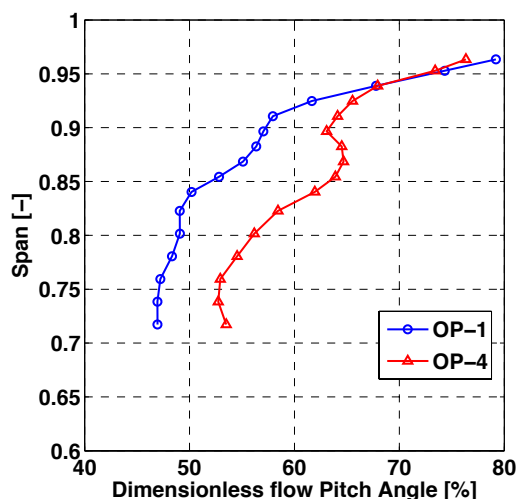


Figure 6–25: Circumferentially area averaged spanwise distribution of dimensionless flow pitch angle for high mass flow (OP-1) and low mass flow (OP-4,  $32\% \dot{m}_{OP-1}$ ) operating points.

In the same figure, one can see that the Mach number remains fairly constant from 0.7 to 0.8 span for both operating points, however for operating point OP-4 the Mach number starts increasing above 0.8 span. The reduced mass flow condition shows a 25% greater value from 0.85 to 0.95 span in the time averaged domain, generating sonic absolute flow conditions at the exit of the stator. When the peak-to-peak fluctuations are analyzed, OP-4 shows two times higher unsteadiness, compared to OP-1 from 0.85 to 0.9 of the blade span at the absolute Mach number.

As indicated in Figure 6–26.b, OP-4 operates under subsonic relative flow conditions, which results most probably an intermittent presence of bow shock at the rotor leading edge compared to OP-1. Nevertheless, it is believed that the high unsteady values measured at the low mass flow condition could be linked to the presence of a shock wave at the trailing edge of the stator, at the blade tip region, due to the supersonic flow conditions as measured with the FRAP-HTH probe. As explained by Stürer et al. in [24], the large blade height to hub diameter ratio, typical for steam turbines, generates large static pressure gradient across the blade span. This leads to a strong negative Mach number gradient at the stator exit with supersonic flow speed at the root of the stator. As a consequence, a shock wave is generated at the trailing edge, which causes extremely high unsteadiness at the root region. A convergent divergent blade profile is then chosen to minimize the high aerodynamic losses from the trailing edge shock at hub.

Although the flow unsteadiness induced by the stator trailing edge shocks generates high unsteady blade loading, the fact that this is located at the root of the fixed blade will cause the least excitation to the rotating blade. However, in the case of operating point OP-4, when such shock wave could be

present at the tip region of the trailing edge with a convergent stator profile, the flow unsteadiness becomes high as shown in Figure 6–24.a. Subsequently, the interaction with the downstream rotor can become critical in terms of blade vibrations and aerodynamic losses.

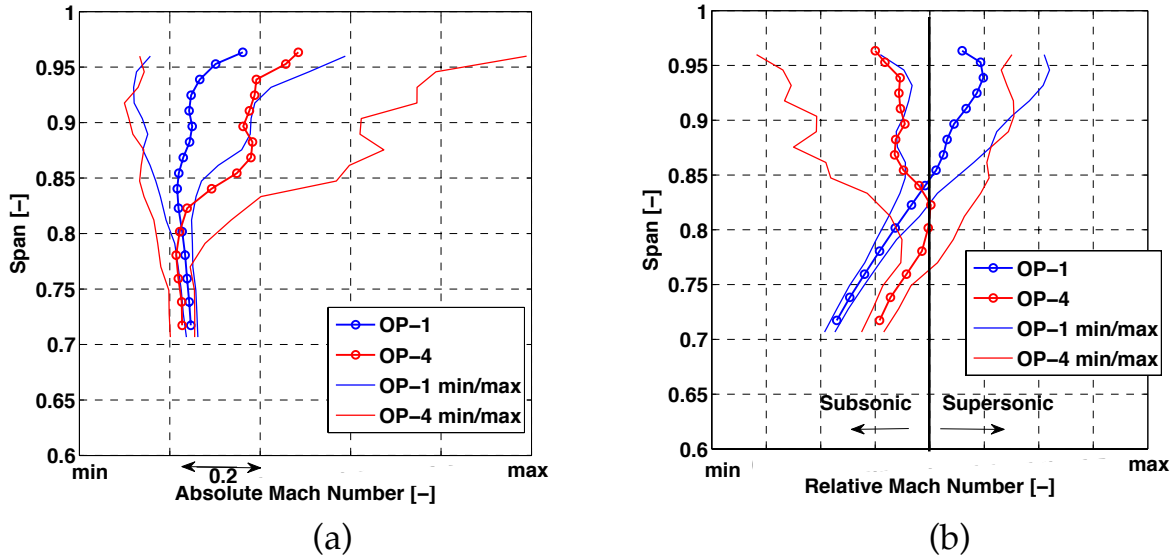


Figure 6–26: Circumferentially area averaged spanwise distribution of absolute (a) and relative (b) Mach number with the minimum and maximum values obtained from the time resolved data for high the mass flow (OP-1) and low mass flow (OP-4,  $32\% \dot{m}_{OP-1}$ ) operating points.

## 6.2.3 Coarse water droplet analysis with FRAP-OB results

### 6.2.3.1 Time averaged results at L-0 stator exit

This section presents the time-averaged results of the coarse water droplets distribution downstream of L-0 stator for two operating conditions, OP-2 and OP-3 as presented in Table 11. As mentioned previously, the measurement plane of the droplet measurements is located at approximately  $x/s=0.02$  downstream of the stator and the observer looks upstream. In addition, stator schematics with the approximate location of their trailing edges are plotted in order to provide a better view of the stator passage to the reader. Although the measurements were conducted at the last 30% of the blade span for one stator pitch, the results presented in the current paragraph are focused at the blade span between 68-82%, since this region has a substantial droplet count within the operating range of the FRAP-OB probe. Results from operating point OP-3 cover 1.2 of the stator pitch, in order to further support the discussion of the droplet spatial distribution analysis. It has to be mentioned that all results comprise droplet sizes above the minimum probe's detection limit of  $D_d > 30\mu\text{m}$ .

Figure 6-27 shows the time averaged contour plots of the droplet rate for the two operating points, OP-2 and OP-3. The droplet rate is the number of coarse water droplets recorded for each measurement point of the grid for one rotor revolution. The observer looks upstream and the measurement plane is roughly 2mm downstream of the stator trailing edge. As presented in Figure 6-27.a and b, all droplets above 30 $\mu\text{m}$  in diameter cover the entire stator passage for both operating points of the steam turbine. At specific locations in the stator wake region droplets were not detected. These locations are indicated in Figure 6-27.a at 0.3 pitch and at 70% span and in Figure 6-27.b at 0 pitch and at 70-75% span.

The results of the Sauter mean diameter for OP-3 and OP-2 are plotted in Figure 6-28.a and b respectively. As shown in the two figures, the largest droplets were detected in the vicinity of the stator suction side and the smallest droplets were measured closer to the pressure side of the last stage stator. The coarse water droplets were reassured in the range from 37  $\mu\text{m}$  to 80 $\mu\text{m}$  in Sauter mean diameter and they were found to be present mainly between 68% to 82% span.

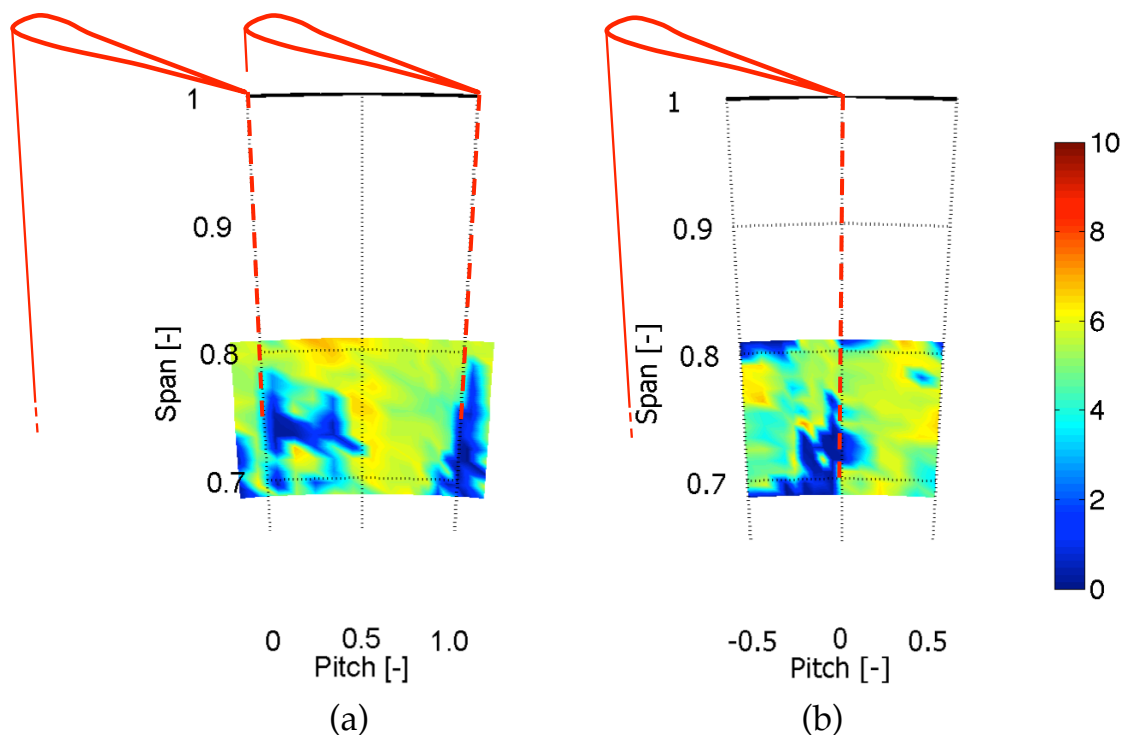


Figure 6-27: Time averaged results of droplet rate [#droplet/rev] for (a) OP-3 and (b) OP-2 at L-0 stator exit ( $T_{in,OP-3}=220^{\circ}\text{C}$  &  $T_{in,OP-2}=270^{\circ}\text{C}$ ).

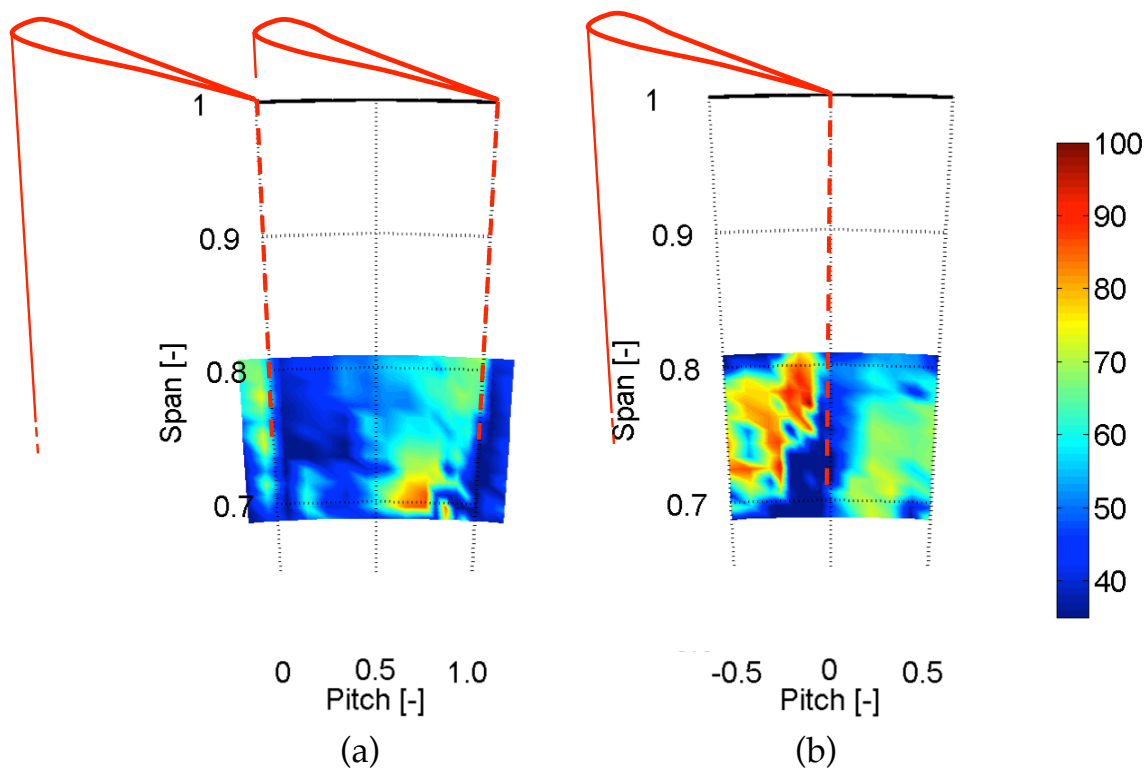


Figure 6-28: Time averaged results of Sauter mean droplet diameter [ $\mu\text{m}$ ] for (a) OP-3 and (b) OP-2 at L-0 stator exit ( $T_{in,OP-3}=220^{\circ}\text{C}$  &  $T_{in,OP-2}=270^{\circ}\text{C}$ ).

In order to further understand the droplet formation mechanism for the given operating conditions, the time averaged droplet mass rate was calculated according to Eq.(6-9).

$$DR_d = N_i \frac{4}{3} \pi r_{d10,i}^3 \rho_d \quad (6-9)$$

The droplet mass rate is calculated by multiplying the number of droplets measured at each measurement grid location with their respective volume and density. The droplet volume is calculated using the measurements of the droplet diameter obtained with the FRAP-OB probe. Thus, the droplet mass rate is a measure of the water content and as a consequence should be proportional to the wetness mass fraction.

The results from the droplet mass rate for operating points OP-3 and OP-2 are presented in Figure 6–29.a and b respectively. The Figures show that the droplet mass rate increases at the vicinity of the stator's suction side in both operating conditions. Further evidences of this particular distribution are found in Figure 6–29.a, since the results cover 1.2 of the stator pitch for this particular operating point. At OP-3 (Figure 6–29.a) there is a high rate of water content between 0.5 and 1 of the stator pitch for the measured spanwise range. The results for OP-2 (Figure 6–29.b) also demonstrate high levels of water content in the vicinity of the stator's suction side between -0.5 and 0 of the stator pitch and in particular in the spanwise region between 70 to 82%. The values have been increased by 50% from the operating point OP-3 to OP-2, as shown in Figure 6–29.a and b respectively.

On average, the wetness mass fraction in OP-3 is greater than in OP-2, since the turbine inlet temperature is reduced. However, as stated by Crane in [39], the contribution of coarse water droplets to the total wetness fraction is only 5-10% of the overall droplet mass. This implies that the fog droplets primarily determine the wetness fraction at a specific operating condition. In addition, the wetness mass fraction, which is stated in Table 11, is only a single value calculated from the inviscid flow theory at the meridional plane using the steam tables. Based on these two facts it is believed that the reduced droplet mass rate in OP-3 compared to OP-2 is most probably due to a shift in the total droplet distribution (Fog and Coarse) towards smaller sizes. The final size of the droplet diameter cannot be depicted in the current results, since the FRAP-OB only measures droplets with a diameter greater than  $D_d > 30 \mu\text{m}$ . However this trend is also shown on the Sauter mean diameter, as indicated in Figure 6–30, with a change from  $65 \mu\text{m}$  to  $55 \mu\text{m}$  when the operating point of the steam turbine changes from OP-2 to OP-3.

When comparing the total mass of the coarse droplets for OP-2 or OP-3, results show that more than 99% of the water content is due to fine droplets. However, the simplified calculation of the average wetness in Table 11 does not including any secondary flow features or local flow structures that might

alter significantly the actual distribution of the wetness mass fraction. Thus, it is believed that the correct approach is to have concurrent measurements of fine droplets, for example with an extinction probe together with the FRAP-OB measurements. Unfortunately this was not possible in the current measurement campaign.

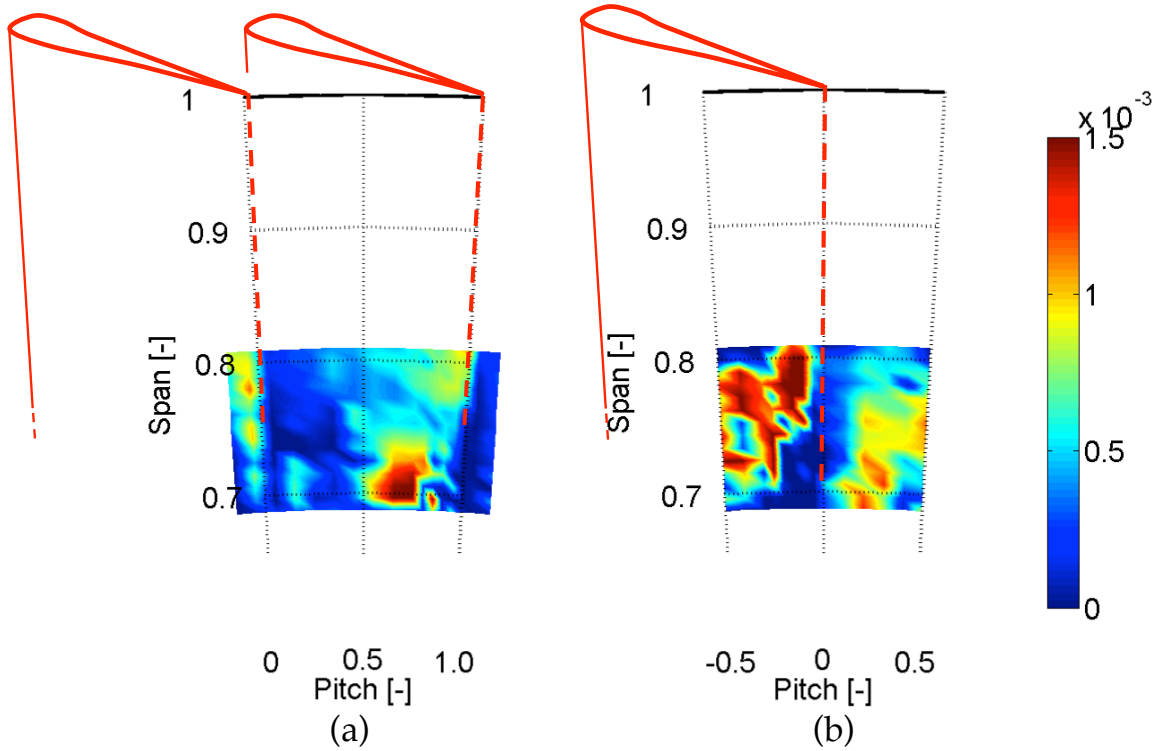


Figure 6-29: Time averaged results of droplet mass rate [mg/rev] for (a) OP-3 and (b) OP-2 at L-0 stator exit ( $T_{in,OP-3}=220^{\circ}C$  &  $T_{in,OP-2}=270^{\circ}C$ ).

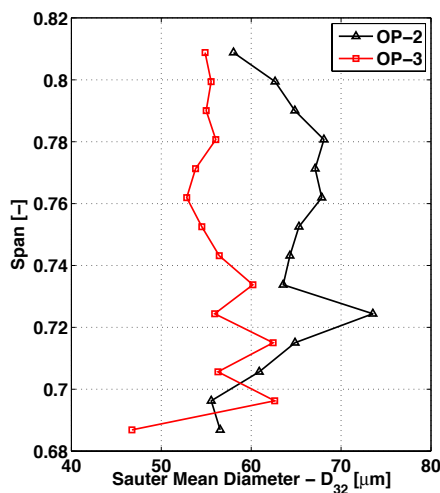


Figure 6-30: Sauter mean droplet diameter for OP-2 and OP-3 at L-0 stator exit ( $T_{in,OP-3}=220^{\circ}C$  &  $T_{in,OP-2}=270^{\circ}C$ ).

According to Eq.(6-9), the elevated values of water content at the vicinity of the stator's suction side imply that coarse water droplets are located in that region (see Figure 6-28), since coarse droplets were found almost uniformly in the entire stator pitch as indicated in Figure 6-27. This is also depicted in Figure 6-31 with the distributions of the droplet diameter for a fixed spanwise location at 75% span for OP-2.

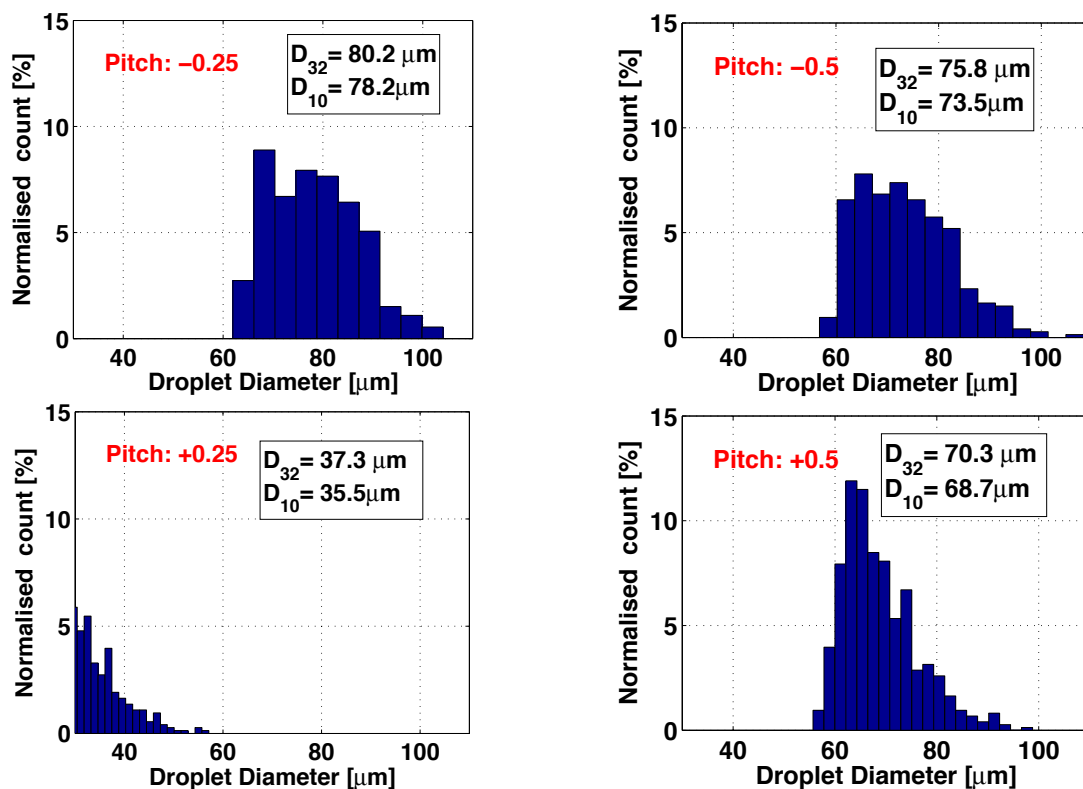


Figure 6-31: Droplet diameter distribution for OP-2 at 75% for four different circumference locations at Pitch: -0.25, -0.5, +0.5 and +0.25 (see Figure 6-29.b).

The Sauter mean diameter is decreased progressively, starting at  $80.2\mu\text{m}$  at the vicinity of the stator suction side (pitch=-0.25), until it reaches its minimum value in the vicinity of the stator's pressure side (pitch=+0.25) with  $D_{32}=37.3\mu\text{m}$ . This is the first time according to the authors' knowledge that droplet plane measurements have been conducted at the stator exit of the last stage for the entire stator pitch. The current results are aiming to supplement the existing theory [9, 11, 37, 39], which states that large droplets are generated from the development of a liquid thin film on the stationary blades, due to the deposition of submicron droplets formed by nucleation in the main steam flow and later sheds from the trailing edge of the stator. It is believed that the presence of suction slits at the pressure side of the stator reduces the size of the coarse droplets and they are beneficial for the erosion process. As a result, the droplet coagulation mechanism described by Moore and et. in [7] as well as coarse droplets generated from the break up film on the stator's suction side, could potentially result in the droplet spatial distribution, which was

measured in the current work and presented in this section of the thesis in Figure 6–29.a and b.

### 6.2.3.2 Time resolved results at L-0 stator exit

Further evidence of the droplet locations are presented with time resolved results obtained with the FRAP-OB probe. Figure 6–32 shows the circumferential distribution at 78% of the stator span of the time resolved droplet mass rate as it was measured with the FRAP-OB probe for operating OP-2. For this operating point the unsteady flow field measured with the FRAP-HTH probe is available. In order to calculate this quantity four rotor blade passages are partitioned into 15 sections with a time interval of  $t_{int}=4/(15 \times \text{BPF})$ , and the individual droplets that were found in each of these sections were phase-locked over 88 rotor revolutions. As presented in Figure 6–32, the time resolved droplet mass rate is modulated by the rotor blade-passing period. This is highlighted with the features A, located at -0.15 of the stator pitch, which are repeated at  $t/T=0.25, 1.25, 2.25$  and  $3.25$ . As presented in Figure 6–29.b, the water content has been reduced by 60% on average between 0 and +0.5, thus the unsteady fluctuations shown in Figure 6–32 are also reduced between 0 and +0.5. The discontinuity in color scale in Figure 6–32, between -0.5 and +0.5 stator pitch is due to insufficient droplet count resulting in this step.

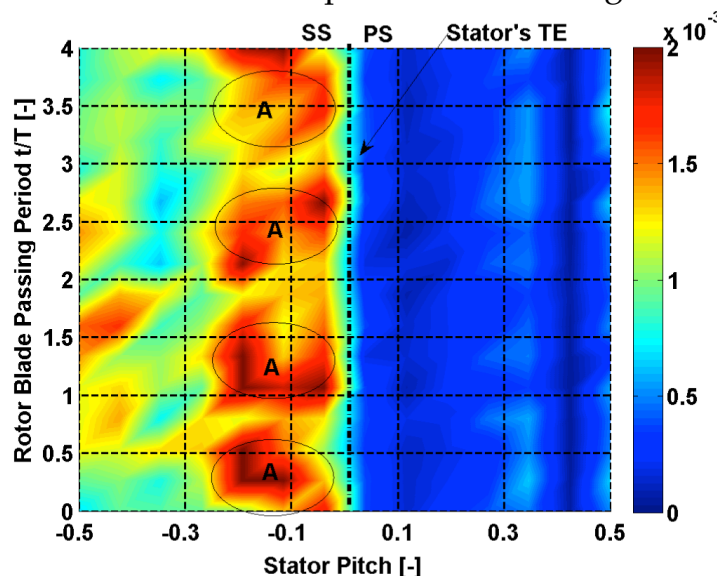


Figure 6–32: Circumferential distribution of measured droplet mass rate [mg/sec] at L-0 stator exit for OP-2 at 78% span.

In order to further analyze the droplet spatial distribution, the time resolved static pressure coefficient is plotted for the same operating point and spanwise location in Figure 6–33. The L-0 stator wake intersection for two consecutive stator blades is found at 0 and 1 stator TE pitch for this operating condition. The features A with high water content at -0.15 stator pitch, as indicated in Figure 6–32, correspond to regions A with low local static pressure at 0.85 stator pitch, as shown in Figure 6–35. The location of -0.15 (0, trailing



edge-0.15=0.15) stator pitch of Figure 6–32 corresponds to 0.85 (1, stator wake-0.15=0.85) in Figure 6–33 as the two measurement planes are not in the same axial downstream distance from the stator trailing edge to each other. The unsteady interaction of the downstream rotor blades with the stator wake and freestream, results in pressure fluctuations, which could potentially influence the condensation process [102] and might affect the coarse droplet coagulation mixing mechanism. As a consequence it is believed that the regions where coarse droplets were measured could be a result of a mixing process mainly due to coagulation and will depend on the stator rotor interactions as presented in Figure 6–32 and Figure 6–33.

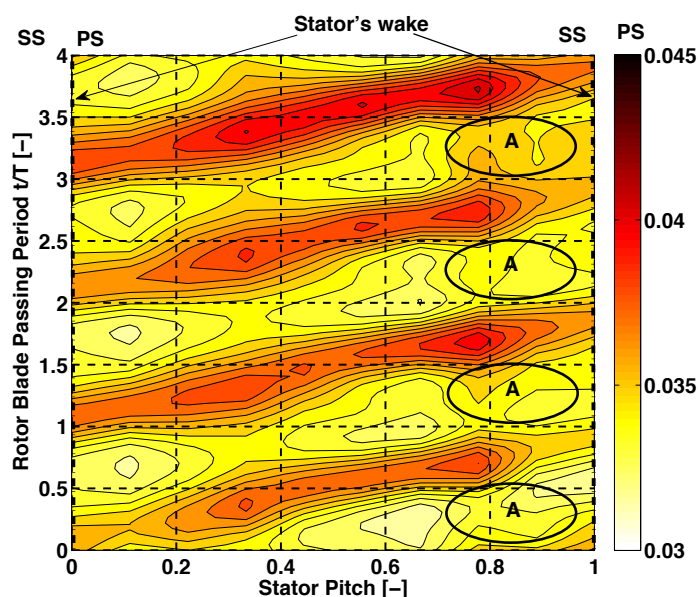


Figure 6–33: Circumferential distribution of Cps [-] at L-0 stator exit for OP-2 at 78% span.

The novel measures with the FRAP-OB probe revealed a spatial distribution for the coarse droplets for two different operating points that are also modulated by the downstream rotor blade-passing period. Since the droplet formation mechanism is strongly dependent on the operating point of the machine, as well as on the stator geometry (suction slits, trailing shape, etc.), it has to be further investigated and cross-compared with measurements at different LP steam turbine stator blades and various operating conditions.

It is worth noting the correlation of high streamwise vorticity with regions of high water content measured with the FRAP-OB probe. This is depicted in Figure 6–34 with the dimensionless streamwise vorticity at 78% span for OP-2. As presented in Figure 6–32, the locations of high water content (features A, Figure 6–32) coincide with regions of high alternating streamwise vorticity in Figure 6–34. One could associate the regions of high vorticity with regions of high mixing in the flow field and suggest that this pattern occurs as a result of fog and coarse water droplet coagulation, as described earlier. In the same graph there is a location at 0.4 stator pitch with even greater values

of streamwise vorticity, which are most probably associated to the complex flow field generated from the upstream four stages.

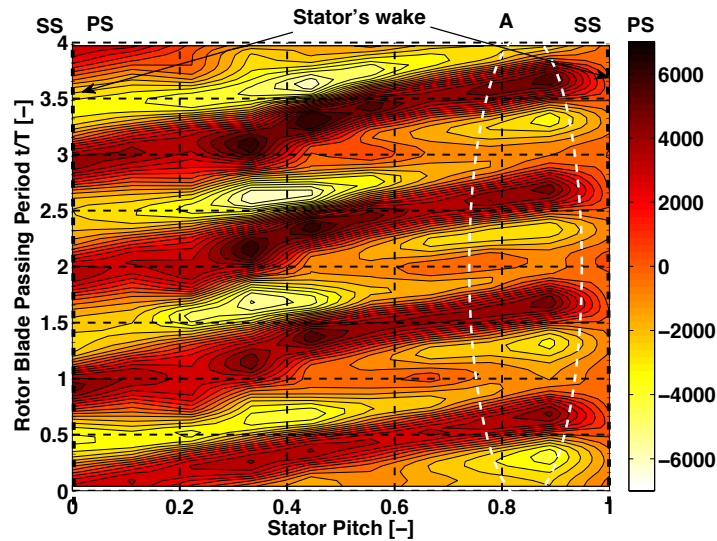


Figure 6–34: Circumferential distribution of non dimensional streamwise vorticity [-] at L-0 stator exit for OP-2 at 78% span.

Similar results and trends for the spanwise location at 71% are presented in Figure 6–35 and Figure 6–36. Figure 6–35 shows the coarse droplet mass rate for operating point OP-2 for four consecutive rotor blade passing periods.

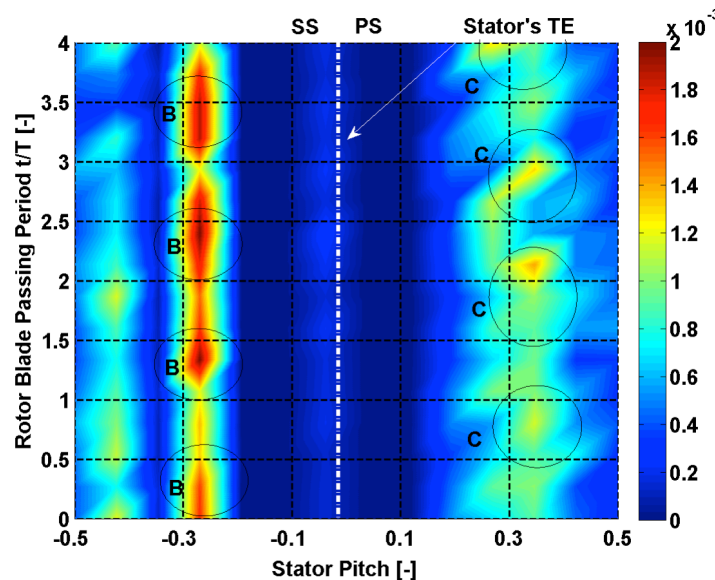


Figure 6–35: Circumferential distribution of measured droplet mass rate [mg/sec] at L-0 stator exit for OP-2 at 71% span.

The features B and C, located at -0.25 and +0.35 stator pitch respectively, are modulated with the rotor blade passing period. The results at 71% span show the same behavior as the previous spanwise location. The features with high water content B, as indicated in Figure 6–35, correspond to regions B with low

local static pressure at 0.75 stator pitch, as indicated in Figure 6–36. On the other hand, the features highlighted as C in Figure 6–35 correspond to regions with low  $C_{ps}$  (features C) at 0.35 stator pitch in Figure 6–36.

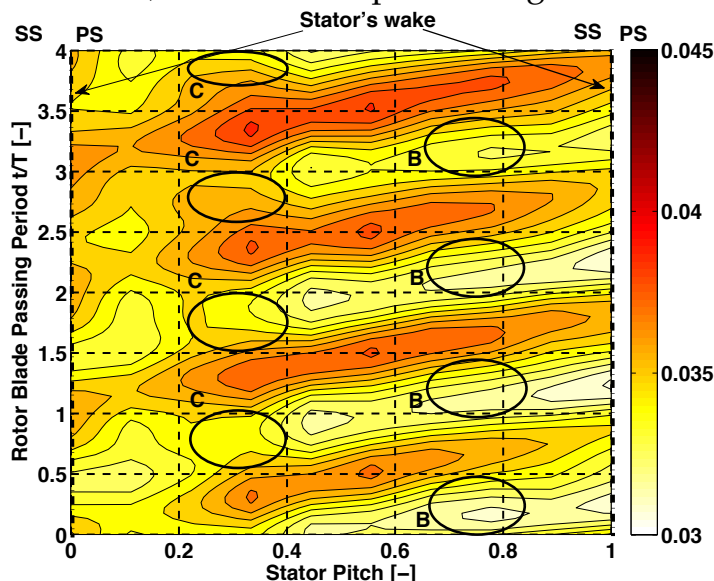


Figure 6–36: Circumferential distribution of  $C_{ps}$  [-] at L-0 stator exit for OP-2 at 71% span.

The streamwise vorticity for this spanwise location is shown in Figure 6–37. As presented in Figure 6–35, the locations of high water content (features B and C, Figure 6–35) coincide with regions of high alternating streamwise vorticity in Figure 6–37. Again, the regions of high vorticity could be associated to regions of high mixing in the flow field, as a consequence of fog and coarse water droplet coagulation. The current results have demonstrated the complexity of the coarse water droplet phenomena and further investigation is needed understand better the formation mechanisms in LP steam turbines.

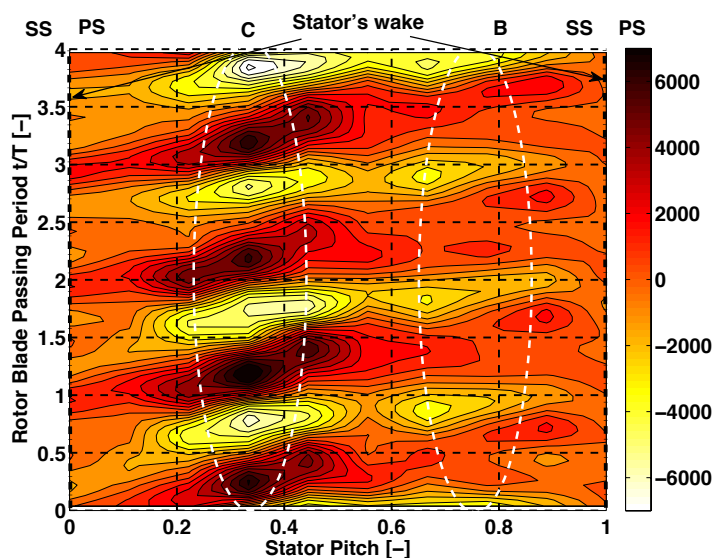


Figure 6–37: Circumferential distribution of non dimensional streamwise vorticity [-] at L-0 stator exit for OP-2 at 71% span.

### 6.3 Summary

A combined time-resolved coarse water droplet and flow field measurements at the nozzle exit of the last stage of a low-pressure steam turbine with supersonic relative inflow conditions at the blade tip was presented in this chapter of the thesis. Both probes have demonstrated their ability to perform measurements under severe wet steam conditions met at the last stage of the machine.

The flow field measurements were conducted for two operating points, one with a high volumetric flow and one low volumetric flow where the mass flow was reduced by 68%. For the high mass flow condition, results have shown that the attached bow shock at the rotor leading edge increases the flow unsteadiness in the top 15% of the blade span compared to lower subsonic region. It increases the rotor relative inflow angles' unsteadiness up to 3 times higher than in the subsonic region. The static pressure unsteadiness for the supersonic and subsonic region is  $\pm 22.5\%$  and  $\pm 6.6\%$  of the mean value respectively and the yaw angle unsteadiness for the supersonic and subsonic region is  $\pm 4.5^\circ$  and  $\pm 1.9^\circ$  of the mean value respectively.

The periodical impingement of the rotor attached bow shock on the upstream stator suction side modulates the stator wake. However, no major aerodynamic losses expressed with the total pressure coefficient could be related to the stator wake. Considering always the spatial resolution of the FRAP-HTH probe, there was no clear evidence of any large scale boundary layer separation. However, regions of high and low static pressure, corresponded well with flow overturning and underturning respectively for the supersonic region above 85% span. This implies that the flow unsteadiness is driven by the high static pressure gradients generated by the moving bow shock. The sensitivity analysis of energy loss across the supersonic rotor to the flow unsteadiness induced by the shock wave, showed an increase of 0.04% from the design point in the energy loss coefficient. The axial gap between the stator trailing edge and rotor leading edge is the factor influencing the unsteady stator rotor interaction intensity and therefore the flow unsteadiness at the rotor inlet above 85% span.

The low mass flow operating point exhibits 65% greater peak-to-peak fluctuations of total pressure coefficient. A redirection of the flow to the blade tip due to the onset of windage has generated sonic flow conditions at the stator exit and subsonic at the rotor inlet. This has resulted most probably on a trailing edge shock at the stator blade generating aerodynamic losses and being responsible for the large unsteady interactions between the rotor and stator blades at the top 20% of the blade span.

The coarse water droplets' range was measured from 37 to 80 $\mu\text{m}$  in Sauter mean diameter and they were found to be present mainly between 68-82% span and over the entire stator pitch. The major finding was the location for the large droplets at the vicinity of the stator suction side. The coagulation

mechanism together with the film break on the stator's suction side could be responsible for the location of the droplets at the vicinity of the stator's suction side. The low inlet temperature seems to exhibit droplets with a lower Sauter mean diameter, however further investigations are needed to understand the coarse water droplet formation mechanism. The suction slit seems to perform well in reducing the amount of coarse droplets present in the pressure side of the stator wake. In addition, unsteady coarse water droplet measurements at the stator exit of the last stage showed that the droplet mass rate is modulated by the downstream rotor blade-passing period.

## 7 Conclusions and outlook

### 7.1 Summary

The fast response instrumentation for unsteady flow field and droplet measurements in the wet steam environment of low-pressure steam was presented in this thesis. Two novel fast response probes have been developed, manufactured and tested – a fast response aerodynamic probe for time resolved aerodynamic measurements and an optical backscatter probe for coarse water droplet measurements.

Both probes have demonstrated their ability to provide accurate measurements under severe wet steam conditions. Significant data were obtained to fulfil the objectives of the current work and improve the understanding of the flow field and droplet mechanisms affecting the performance and lifetime of LP steam turbines.

#### **Fast response aerodynamic probe for time resolved measurements in wet steam (FRAP-HTH)**

The miniature FRAP-HTH probe has a tip diameter of 2.5mm and utilizes two piezoresistive pressure transducers to measure the flow angles as well as the total and static pressure of the flow.

In order to avoid any water contamination on the sensing part of the probe, a custom-made miniature heater was developed. This component overheats the tip few degrees above the flow saturation temperature to operate the probe with dry pressure taps. Test results have shown that the heater's operation has no effect on the measured flow quantities. The error for all calibration coefficients is on average below 0.5%, well within the uncertainty of the aerocalibration model.

Due to the high flare angles in low-pressure steam turbines, a new virtual six-sensor measurement concept was applied to capture the high flow pitch angles. This has broadened the available operating range of the probe from 20° to 50° in pitch angle.

A detailed uncertainty analysis, accounting for errors from the calibration procedure and measurements, has shown that the maximum total and static pressure uncertainties are 1% and 2.3% of the average total and static pressure respectively at the nozzle exit of the last stage in a LP steam turbine. Thus, accurate measurements in the challenging wet steam environment are possible.

In order to exclude any possible corrupted data, due to droplet's impact or evaporation from the heating process, a filtering algorithm was developed.

#### **Fast response optical backscatter probe for coarse water droplet measurements (FRAP-OB)**

The novel miniature probe uses the light scattering technique to illuminate droplets with a laser source and measure the backscattered light with fast response gallium arsenide photodiode. During the development of the FRAP-

OB probe an entirely new packaging solution had to be implemented. The miniature FRAP-OB probe has a tip diameter of 5mm and enables droplet measurements in the range of 30 $\mu$ m to 110 $\mu$ m in diameter. The measurement bandwidth of the probe is 30MHz, capable of resolving droplet speeds up to 170m/s. In order to avoid the deflection of the laser beam as it exists the sapphire window, the probe is equipped with an air purging system.

The calibration of the probe is conducted with a monodispersed droplet generator with an accuracy of  $\pm 0.6\mu$ m. Substantial effort to reduce errors related to the operating principle of the probe was made. This sets the overall calculated uncertainty, accounting for all sources of errors for the diameter and speed measurements, to  $\pm 5.4\mu$ m and  $\pm 2.3$ m/s respectively.

In order to make possible droplet measurements in a working environment with high surrounding electromagnetic noise, a sophisticated post-processing routine that increases the signal to noise ratio by a factor of 2 had to be developed.

## 7.2 Concluding remarks

### **Coarse water droplet formation downstream of the stator of an axial turbine test facility**

The FRAP-OB proof of concept to provide steady and unsteady measurements is demonstrated, in the flow field of the axial turbine test facility, LISA. In this measurement campaign the facility was equipped with a water spray generator, working in the submicron range, to create representative conditions of the droplets' formation onto the stator blades. Two different operating points, including one reduced massflow condition, are compared, at two different axial locations downstream of the first stator.

For all test cases, the maximum concentration of coarse water droplets, over the entire stator pitch, was found at the trailing edge of the stator. This is due to the water film formation on the stator's pressure side, which sheds from the trailing edge and generates coarse droplets. In addition, measurements have shown that the droplets increase by 10% in size when the flow velocity is reduced 15% due to significant reduction on the shear forces between the droplets and the stream flow. Droplet speed measurements have shown that the coarse water droplets impact the suction side of the downstream rotor, due to their deficit in absolute velocity. Part load condition results in an increase of the relative droplet velocity by 40% compared to the design operating point, and as a consequence the erosion rate is increased up to 16 times depending on the material used for the rotor blades.

The time-resolved droplet measurements, performed for a first time, have shown that the droplet mass rate at the stator exit is modulated by the downstream rotor blade-passing period. In particular, when the droplets approach the downstream rotor leading edge, the unsteady droplet mass rate

fluctuates  $\pm 40\%$  around the mean value. This is due to the enhanced unsteady potential field that drives the droplets' motion.

### **Effect of mass flow reduction on the performance of the last two stages of a LP steam turbine (Subsonic case)**

A set of time-resolved flow field measurements with the FRAP-HTH at the inlet and exit of the last stage of a low-pressure steam turbine was presented. The FRAP-HTH probe has demonstrated its reliability for accurate measurements in severe wet steam conditions with averaged wet-mass fractions up to 8%. Three different operating points, including two reduced mass-flow conditions (part load conditions), were measured.

The measurements have shown that the secondary flow structures at the tip region (shroud leakage and tip passage vortices) are the predominant sources of unsteadiness over the last 30% of the blade span for all operating conditions. At the exit of the second to last stage (L-1), the intensity of periodical fluctuations is found to be maximum for the high massflow condition, with 8% fluctuation in relative total pressure. In contrast at the exit of the last stage (L-0), the reduced mass flow operating condition exhibits up to 3 times higher pressure fluctuations between 85 to 100% span, causing 5% deficit in total pressure. The reason is the redirection of the flow towards the blade tip region, resulting in the strengthening of the secondary flow structures.

### **Concluding remarks on the flow field and coarse water droplet formation at the last stage of LP steam turbine with supersonic turbine blades (Supersonic case)**

Combined time-resolved coarse droplet and flow field measurements at the nozzle exit of the last stage of a LP steam turbine with supersonic flow conditions near the blade tip have been performed. Both probes (FRAP-HTH and FRAP-OB) have demonstrated their ability to perform accurate measurements, and significant data were obtained in order to improve the understanding of the stator rotor interaction and the droplet formation mechanisms.

#### **Flow field analysis**

The flow field measurements were conducted for two operating points, one with a high volumetric flow and one a low volumetric flow where the mass flow is reduced by 68%.

For the high mass flow condition, results have shown that the attached bow shock at the rotor leading edge increases the flow unsteadiness by a factor of 3 in the top 15% of the blade span compared to the lower subsonic region. The unsteady interaction of the attached bow shock with the upstream stator suction side modulates the stator's wake. Nevertheless, there was no clear evidence of any large-scale boundary layer separation on the stator's suction side. Regions of high and low static pressure correspond well with flow overturning and underturning respectively for the supersonic region. This implies that the flow unsteadiness is driven by the high static pressure gradi-



ents, generated across the moving bow shock. A sensitivity analysis to the losses across the rotor blade showed an increase of 0.04% relative to the design point, due to the elevated flow fluctuations. The axial gap between the stator trailing edge and rotor leading edge is the main factor influencing the unsteady stator rotor interaction intensity and thus the flow unsteadiness at the rotor inlet above 85% span in the presence of the bow shock

The low mass flow operating point exhibits 65% greater peak-to-peak fluctuations of total pressure coefficient, compared to the high mass flow condition. A redirection of the flow to the blade tip, due to the onset of windage was measured. This generates supersonic flow conditions at the stator exit (stationary frame of reference) and subsonic at the rotor inlet (relative frame of reference), resulting most probably in a trailing edge shock at the stator exit above 85% span. Thus, higher aerodynamic losses are generated responsible for the large unsteady fluctuations found at the blade tip section.

#### **Coarse water droplet analysis**

The coarse water droplets were measured in the range from 37 $\mu\text{m}$  to 80 $\mu\text{m}$  in Sauter mean diameter and were found to be present mainly between 68-82% span and over the entire stator pitch. The suction slit located on the stator pressure side, seems to perform well in reducing the amount of coarse droplets present in the pressure side of the stator wake. The maximum droplet concentration at the vicinity of the stator suction side is the major finding of these measurements. The coagulation mechanism together with the film break from the stator's suction surface could be responsible for the location of the droplets at the vicinity of the stator's exit suction side. The low inlet temperature exhibits droplets with a lower Sauter mean diameter, however further investigations are needed to understand this droplet formation mechanism. In addition, unsteady coarse water droplet measurements at the stator exit of the last stage showed that the droplet mass rate is modulated by the downstream rotor blade-passing period as a result of the stator rotor interaction.

### 7.3 Future work

The outcome of the current study has revealed the potential for future development and improvements. The discussion is focused on the potential improvements of FRAP-HTH and FRAP-OB probes in order to enlighten more the mechanisms, which govern the unsteady wet steam flows.

#### FRAP-OB

One of the most important challenges is the quantification of light extinction along the light beam caused by the fog droplets for concentrations above  $10^{11}$  droplets/m<sup>3</sup>. The extinction of light affects both the minimum droplet size resolution as well as the measurement accuracy of the FRAP-OB probe. Therefore light extinction measurements are required under high wetness mass fraction conditions.

Currently the FRAP-OB probe can measure coarse water droplets from 30 to 110 $\mu$ m in diameter. However, as presented in the current thesis and reported in literature, the droplets found in the last stages of steam turbines responsible for erosion can be as low as 10 $\mu$ m in diameter. Although the scattering technique is suitable for such a small size; the high power laser, required to resolve these particles, makes practically this method impossible. Reducing the losses or increasing the scattering signal, either by decreasing distance between the probe and the sample volume or using forward scattering, are possible ways to cope with this challenge. According to the author's opinion, a future development, which can improve both the measurement range and accuracy due to light extinction, is a combination of an optical scattering probe with the optical extinction probe. The issue with light extinction along the laser beam as well as the increase in measurement range can be solved with this kind of probe design. Nevertheless, an increase in laser power is essential unless forward scattering technique is adopted.

The second priority is the reduction of the uncertainty related to the side effect error. The small sample volume of the current probe minimizes the coincidence errors but is detrimental to the side effect error, when a droplet is partially crossing the sample volume. Currently a numerical correction method based on a probability distribution function is applied to account for it and correct the droplets size distribution. The optimum solution requires improvements on the measurement procedure. This could be achieved by illuminating the droplets with a second light beam but with a different wavelength and measuring the backscattered light with a second photodiode. The two resulted signals could be used, after calibration, to provide the actual droplet diameter and the relative position of the droplet from the center axis of the sample volume.

Last but not least, the extent of the probe application to different media or even solid particles will contribute to the efficiency improvement of turbomachines in various fields beside the challenging environment of steam turbines.

## **FRAP-HTH**

Regarding the FRAP-HTH probe, the well established FRAP technology, which is based on, has contributed to develop a probe that meets the expectations for wet steam measurements. Nevertheless, the measurements revealed three major improvements to increase the accuracy of the results and expand the operation of the probe to even more severe wet steam conditions.

As previously described, the two pressure taps are equipped with a shield to protect the miniature piezoresistive sensor from direct particle impacts. However, this shield has a clearance of 80 $\mu$ m allowing particles to enter the pressure taps and reach the sensor's membrane. The resulting signal is then corrupted with a penalty on the post processing time. An improved design where the shield reduces the access gap would be therefore beneficial.

Additionally, an increase in heating power should be considered to enable measurements at higher Mach number and wetness mass fraction than currently presented. On the other hand, the sensor packaging into the tip should be revised to further reduce the thermal stresses induced to the piezo resistive sensors and impacting the DC accuracy of the measured total and static pressures.

Finally, as presented in chapter 6, the flow at the tip region of the last stage in LP steam turbines can reach supersonic velocity even in the absolute frame of reference. It is therefore proposed to develop a supersonic wedge probe, since the static pressure aerocalibration coefficient of the current cylindrical design exhibits a high sensitivity to Mach number under transonic flow conditions.

## **Suggestions for numerical studies (CFD)**

The outcome of the current work has shown that one of main design parameters, on the inter-blade row interaction with the presence of a bow shock, is the axial gap between the stator trailing and rotor leading edge. Therefore, a parametric numerical study on the relationship of the axial distance with the stage efficiency is proposed. When combined with coarse water droplet analysis, the study will not only reveal the optimum axial gap at the top 15% of the blade span, but the final droplet size and speed responsible for the erosion at the rotor blade leading edge.

Finally, the sensitivity of the flow field to part load conditions in LP steam turbines is high, and further analysis to investigate the performance of the machine has to be made. Measurements have shown that the complex flow field at the last stages is driven by the fixed vacuum conditions, set by the condenser. Unsteady numerical calculations at various operating points are proposed. This will allow the better understanding of the unsteady flow phenomena at part load conditions and improve the efficiency of low-pressure steam turbines in the future.



# Appendix

## References

- [1] Hoeven, M. v. d., "Energy Climate and Change," International Energy Agency, Paris 2015. Available: <http://www.iea.org/publications/freepublications/publication/weo-2015-special-report-energy-climate-change.html> (accessed, July 2015).
- [2] Anderegg, W. R. L., Prall, J. W., Harold, J., and Schneider, S. H., 2010, "Expert credibility in climate change," *Proceedings of the National Academy of Sciences*, 107(27), pp. 12107-12109.
- [3] "Renewables 2015 Global Status Report," 2015. Available: <http://www.ren21.net> (accessed, October 2015).
- [4] SE4ALL, "Tracking Progress," 2015. Available: <http://www.se4all.org/tracking-progress/> (accessed, October 2015).
- [5] "BP Energy Outlook 2035," 2014. Available: <http://www.bp.com/energyoutlook> (accessed, July 2015).
- [6] Çengel, Y. A., Boles, M. A., and Kanoğlu, M., *Thermodynamics : an engineering approach*, 8th ed. in SI Units edition.: New York : McGraw-Hill, 2015.
- [7] Moore, M. J. and Sieverding, C. H., *Two-phase steam flow in turbines and separators : theory - instrumentation - engineering*: Washington & London: Hemisphere New York a.o.: McGraw-Hill, 1976.
- [8] Young, J. B., Yau, K. K., and Walters, P. T., 1988, "Fog Droplet Deposition and Coarse Water Formation in Low-Pressure Steam Turbines: A Combined Experimental and Theoretical Analysis," *Journal of Turbomachinery*, 110(2), pp. 163-172.
- [9] Li, C., Wang, X., Cheng, D., and Sun, B., 2008, "Experimental Study on Effects of Slot Hot Blowing on Secondary Water Droplet Size and Water Film Thickness," *Journal of Engineering for Gas Turbines and Power*, 131(3)
- [10] Dousti, S., Cao, J., Younan, A., Allaire, P., and Dimond, T., 2012, "Temporal and Convective Inertia Effects in Plain Journal Bearings With Eccentricity, Velocity and Acceleration," *Journal of Tribology*, 134(3), pp. 031704-031704.
- [11] Cai, X., Ning, D., Yu, J., Li, J., Ma, L., Tian, C., *et al.*, 2014, "Coarse water in low-pressure steam turbines," *Proceedings of the Institution of Mechanical Engineers, Part A: Journal of Power and Energy*, 228(2), pp. 153-167.
- [12] Cook, S. S., 1928, "Erosion by Water-Hammer," *Proceedings of the Royal Society of London A: Mathematical, Physical and Engineering Sciences*, 119(783), pp. 481-488.
- [13] Aldo Antonio Rueda Martínez, F. R. M., Miguel Toledo Velázquez, Florencio Sánchez Silva, Ignacio Carvajal Mariscal, Juan Abugaber Francis, 2012, "The Density and Momentum Distributions of 2-Dimensional Transonic Flow in an LP-Steam Turbine," *Energy and Power Engineering*, 04(05), pp. 365-371.
- [14] Senoo, S. and Ono, H., 2013, "Development of Design Method for Supersonic Turbine Aerofoils Near the Tip of Long Blades in Steam Turbines Part 2: Configuration Details and Validation," San Antonio, Texas, Vol. 5B: Oil and Gas Applications; Steam Turbines, GT2013-94039.
- [15] Haraguchi, M., Nakamura, T., Yoda, H., Kudo, T., and Senoo, S., 2013, "Nuclear Steam Turbine With 60 inch Last Stage Blade," Volume 1: Plant Operations, Maintenance, Engineering, Modifications, Life Cycle and Balance of Plant; Nuclear Fuel and Materials; Radiation Protection and Nuclear Technology Applications, ICONE21-16600.
- [16] Shibukawa, N., Iwasaki, Y., Takada, Y., Murakami, I., Suzuki, T., and Fukushima, T., 2014, "An Experimental Investigation of the Influence of Flash-Back Flow on Last Three Stages of Low Pressure Steam Turbines," ASME, Düsseldorf, Vol. 1B, GT2014-26897.
- [17] Ow, C. S. and Crane, R. I., 1979, "On the Critical Weber Number for Coarse Water Formation in Steam Turbines," *Journal of Mechanical Engineering Science*, 21(5), pp. 353-356.

- [18] Dixon, S. L., *Fluid Mechanics and Thermodynamics of Turbomachinery*, Fifth edition. Oxford, UK: Elsevier, 2005.
- [19] Miyake, S., Koda, I., Yamamoto, S., Sasao, Y., Momma, K., Miyawaki, T., *et al.*, 2014, "Unsteady Wake and Vortex Interactions in 3-D Steam Turbine Low Pressure Final Three Stages," ASME, Düsseldorf, Vol. 1B, GT2014-25491.
- [20] Behr, T., 2007, "Control of Rotor Tip Leakage and Secondary Flow by Casing Air Injection in Unshrouded Axial Turbines," Diss. ETH No. 17283, ETH Zurich.
- [21] Vogt, H. F. and Zippel, M., 1996, "Sekundärströmungen in Turbinengittern mit geraden und gekrümmten Schaufeln; Visualisierung im ebenen Wasserkanal," *Forschung im Ingenieurwesen - Engineering Research*, 62(9), pp. 247-253.
- [22] Langston, L. S., 2001, "Secondary Flows in Axial Turbines—A Review," *Annals of the New York Academy of Sciences*, 934(1), pp. 11-26.
- [23] Sharma, O. P. and Butler, T. L., 1987, "Predictions of Endwall Losses and Secondary Flows in Axial Flow Turbine Cascades," *Journal of Turbomachinery*, 109(2), pp. 229-236.
- [24] Stüer, H., Truckenmüller, F., Borthwick, D., and Denton, J. D., 2005, "Aerodynamic Concept for Very Large Steam Turbine Last Stages," Volume 6: Turbo Expo 2005, Parts A and B
- [25] Havakechian, S. and Denton, J., 2015, "Three-Dimensional Blade-Stacking Strategies and Understanding of Flow Physics in Low-Pressure Steam Turbines—Part I: Three-Dimensional Stacking Mechanisms," *Journal of Engineering for Gas Turbines and Power*, 138(5), pp. 052603-052603.
- [26] Parvizinia, M., Berlich, C., Truckenmüller, F., and Stüer, H., 2004, "Numerical and Experimental Investigations Into the Aerodynamic Performance of a Supersonic Turbine Blade Profile," ASME, Vienna, Vol. 5, GT2004-53823.
- [27] Havakechian, S. and Denton, J., 2015, "Three-Dimensional Blade Stacking Strategies and Understanding of Flow Physics in Low-Pressure Steam Turbines—Part II: Stacking Equivalence and Differentiators," *Journal of Engineering for Gas Turbines and Power*, 138(6), pp. 062601-062601.
- [28] Troyanovskii, B. M., Lagun, V. P., Maiorskii, E. V., Noiman, K., and Simoyu, L. L., 1970, "Designing Steam Turbine Last Stages," *Teploenergetika* 17(2), pp. 16-20.
- [29] Lagun, V. P., Simoyu, L. L., Frumin, Y. Z., Povolotskii, L. V., and Sukharev, F. M., 1971, "Distinguishing features of the operation of LPC last stages at low load and under no-load conditions," *Teploenergetika*, 18(2), pp. 21-24.
- [30] Megerle, B., Rice, T. S., McBean, I., and Ott, P., 2014, "Unsteady Aerodynamics of Low-Pressure Steam Turbines Operating Under Low Volume Flow," *Volume 5B: Oil and Gas Applications; Steam Turbines*, 136, p. 9.
- [31] Segawa, K., Senoo, S., Kudo, T., Nakamura, T., and Shibashita, N., 2012, "Steady and Unsteady Flow Measurements Under Low Load Conditions in a Low Pressure Model Steam Turbine," ASME, Anaheim, California, Vol. 3: Thermal-Hydraulics; Turbines, Generators, and Auxiliaries, ICONE20-POWER2012-54862.
- [32] Gerschütz, W., Casey, M., and Truckenmüller, F., 2005, "Experimental investigations of rotating flow instabilities in the last stage of a low-pressure model steam turbine during windage," *Proceedings of the Institution of Mechanical Engineers, Part A: Journal of Power and Energy*, 219(6), pp. 499-510.
- [33] Sigg, R., Heinz, C., Casey, M. V., and Sürken, N., 2009, "Numerical and experimental investigation of a low-pressure steam turbine during windage," *Journal of Power and Energy*, 223(6), pp. 697-708.
- [34] Binner, M. and Seume, J. R., 2013, "Flow Patterns in High Pressure Steam Turbines During Low-Load Operation," *Journal of Turbomachinery*, 136(6), pp. 061010-061010.
- [35] Megerle, B., Stephen Rice, T., McBean, I., and Ott, P., 2012, "Numerical and Experimental Investigation of the Aerodynamic Excitation of a Model Low-Pressure Steam Turbine Stage Operating Under Low Volume Flow," *Journal of Engineering for Gas Turbines and Power*, 135(1), p. 012602.

- [36] Gerber, A. G. and Mousavi, A., 2007, "Representing Polydispersed Droplet Behavior in Nucleating Steam Flow," *Journal of Fluids Engineering*, 129(11), pp. 1404-1414.
- [37] Christie, D. G., Hayward, G. W., Lowe, H. J., MacDonald, A. N., and Sculpher, P., 1965, "The Formation of Water Drops Which Cause Turbine Blade Erosion," *Proceedings of the Institution of Mechanical Engineers, Conference Proceedings*, 180(15), pp. 13-22.
- [38] Lam, T. C. T. and Dewey, R., 2003, "A Study of Droplet Erosion on Two L-0 Turbine Stages," International Joint Power Generation Conference, Atlanta USA, Vol. IJPGC2003-40082
- [39] Crane, R. I., 2004, "Droplet deposition in steam turbines," *Proceedings of the Institution of Mechanical Engineers, Part C: Journal of Mechanical Engineering Science*, 218(8), pp. 859-870.
- [40] Hammitt, F. G., *Cavitation and multiphase flow phenomena*: New York a.o. : McGraw-Hill, 1980.
- [41] Hammitt, F., Krzeczowski, S., and Krzyżanowski, J., 1981, "Liquid film and droplet stability consideration as applied to wet steam flow," *Forschung im Ingenieurwesen A*, 47(1), pp. 1-14.
- [42] Xinjun, W., Tingxiang, X., and Yanfeng, L., 2005, "Effects of water suction on water film tearing at trailing blade edges," *Heat Transfer—Asian Research*, 34(6), pp. 380-385.
- [43] Lee Black, D., McQuay, M. Q., and Bonin, M. P., 1996, "Laser-based techniques for particle-size measurement: A review of sizing methods and their industrial applications," *Progress in Energy and Combustion Science*, 22(3), pp. 267-306.
- [44] Völker, L., Casey, M., Dunham, J., and Stürer, H., 2008, "The Influence of Lean and Sweep in a Low Pressure Steam Turbine: Throughflow Modelling and Experimental Measurements," ASME, Berlin, Vol. 6: Turbomachinery, Parts A, B, and C, GT2008-50161.
- [45] Tsukuda, T., Sato, H., Nomura, D., Kawasaki, S., and Shibukawa, N., 2014, "An Experimental Investigation of Thermal Wetness Loss in the Full Scale Size Low Pressure Turbine," ASME, Düsseldorf, Vol. 1B, GT2014-26012.
- [46] Cai, X., Ning, T., Niu, F., Wu, G., and Song, Y., 2009, "Investigation of wet steam flow in a 300 MW direct air-cooling steam turbine. Part 1: Measurement principles, probe, and wetness," *Proceedings of the Institution of Mechanical Engineers, Part A: Journal of Power and Energy*, 223(5), pp. 625-634.
- [47] Baumgardner, D., Brenguier, J. L., Bucholtz, A., Coe, H., DeMott, P., Garrett, T. J., et al., 2011, "Airborne instruments to measure atmospheric aerosol particles, clouds and radiation: A cook's tour of mature and emerging technology," *Atmospheric Research*, 102(1–2), pp. 10-29.
- [48] Wendisch, M., Keil, A., and Korolev, A. V., 1996, "FSSP Characterization with Monodisperse Water Droplets," *Journal of Atmospheric and Oceanic Technology*, 13(6), pp. 1152-1165.
- [49] Fugal, J. P., Shaw, R. A., Saw, E. W., and Sergeyev, A. V., 2004, "Airborne digital holographic system for cloud particle measurements," *Applied Optics*, 43(32), pp. 5987-5995.
- [50] Lance, S., Brock, C. A., Rogers, D., and Gordon, J. A., 2010, "Water droplet calibration of the Cloud Droplet Probe (CDP) and in-flight performance in liquid, ice and mixed-phase clouds during ARCPAC," *Atmos. Meas. Tech.*, 3(6), pp. 1683-1706.
- [51] Ellis, R. A., Sandford, A. P., Jones, G. E., Richards, J., Petzing, J., and Coupland, J. M., 2006, "New laser technology to determine present weather parameters," *Measurement Science and Technology*, 17(7), p. 1715.
- [52] Roques, S., 2007, "An airborne icing characterization probe: nephelometer prototype," *Smart Materials and Structures*, 16(5), p. 1784.
- [53] Knox, K. J., Reid, J. P., Hanford, K. L., Hudson, A. J., and Mitchem, L., 2007, "Direct measurements of the axial displacement and evolving size of optically trapped aerosol droplets," *Journal of Optics A: Pure and Applied Optics*, 9(8), p. S180.



- [54] Holve, D. and Self, S. A., 1979, "Optical particle sizing for in situ measurements Part 1," *Applied Optics*, 18(10), pp. 1632-1645.
- [55] Lemaitre, P., Porcheron, E., Grehan, G., and Bouilloux, L., 2006, "Development of a global rainbow refractometry technique to measure the temperature of spray droplets in a large containment vessel," *Measurement Science and Technology*, 17(6), p. 1299.
- [56] Paul Lawson, D. R., Andy Heymsfield, Darrel Baumgardner, Olaf Stetzer, Greg McFarquhar, Linnea Avallone, Markus Petters, 2007, "Instrument Limitations and Uncertainties," Workshop on In Situ, Airborne Instrumentation, Oregon, USA
- [57] Walters, P. and Skingley, P., 1979, "An optical instrument for measuring the wetness fraction and droplet size of wet steam flows in LP turbines," *Proc. Inst. Mech. Eng., Part C*, 141(79), pp. 337-348.
- [58] Tatsuno, K. and Nagao, S., 1986, "Water Droplet Size Measurements in an Experimental Steam Turbine Using an Optical Fiber Droplet Sizer," *Journal of Heat Transfer*, 108(4), pp. 939-945.
- [59] Walters, P. T., 1987, "Wetness and Efficiency Measurements in L.P. Turbines With an Optical Probe As an Aid to Improving Performance," *Journal of Engineering for Gas Turbines and Power*, 109(1), pp. 85-91.
- [60] Hayashi, K., Shiraiwa, H., Yamada, H., Nakano, S., and Tsubouchi, K., "150 kW Class Two-Stage Radial Inflow Condensing Steam Turbine System," presented at the Volume 4: Cycle Innovations; Fans and Blowers; Industrial and Cogeneration; Manufacturing Materials and Metallurgy; Marine; Oil and Gas Applications, Vancouver, Canada, 2011, GT2011-46192.
- [61] Kerchel, S. W., Simpson, M. L., Azar, M., and Young, M., 1993, "An optical technique for characterizing the liquid phase of steam at the exhaust of an LP turbine," *Office of Scientific and Technical Information (OSTI)*, 24(22)
- [62] Schatz, M. and Casey, M., 2007, "Design and testing of a new miniature combined optical/pneumatic wedge probe for the measurement of steam wetness," *AIP Conference Proceedings*, 914(1), pp. 464-479.
- [63] Wu, G., Song, Y., Ning, T., Su, M., Li, J., Niu, F., *et al.*, 2010, "Investigation of wet steam flow in a 300 MW direct air-cooling steam turbine. Part 2: flow field and windage," *Proceedings of the Institution of Mechanical Engineers, Part A: Journal of Power and Energy*, 224(1), pp. 129-137.
- [64] Fan, X., Jia, Z., Zhang, J., and Cai, X., 2009, "A video probe measurement system for coarse water droplets in LP steam turbine," *Journal of Physics: Conference Series*, 147(1), p. 012065.
- [65] Leizerovich, A. S., *Steam Turbines for Modern Fossil-fuel Power Plants*: Fairmont Press, 2008.
- [66] Kuperfshried, P., Köppel, P., Roduner, C., and Gyarmathy, G., 2000, "On the Development and Application of The FRAP (Fast-Response Aerodynamic Probe) System for Turbomachines - Part 1: The Measurement System," *Journal of Turbomachinery*, 122(3), pp. 505-516.
- [67] Pfau, A., Schlienger, J., Kalfas, A. I., and Abhari, R. S., 2002, "Virtual Four Sensor Fast Response Aerodynamic Probe (FRAP) " 16th Symposium on measuring techniques in transonic and supersonic flow in cascades and turbomachines, Cambridge, UK
- [68] Mansour, M., Chokani, N., Kalfas, A. I., and Abhari, R. S., 2008, "Time-Resolved Entropy Measurements Using a Fast Response Entropy Probe," *Meas. Sci. Technol.*, 19
- [69] Lenherr, C., Kalfas, A. I., and Abhari, R. S., 2010, "High Temperature Fast Response Aerodynamic Probe," *Journal of Engineering for Gas Turbines and Power*, 133(1), pp. 011603-011613.
- [70] Mansour, M., Kocer, G., Lenherr, C., Chokani, N., and Abhari, R. S., 2011, "Seven-Sensor Fast-Response Probe for Full-Scale Wind Turbine Flowfield Measurements," *Journal of Engineering for Gas Turbines and Power*, 133(8), pp. 081601-081601.

- [71] Lenherr, C., 2010, "High temperature fast response aerodynamic probe," Diss. ETH No. 19367, ETH Zürich.
- [72] Microstar Laboratories, Ziegler-Nichols tuning rule. Available: <http://www.mstarlabs.com/control/znrule.html> (accessed, November 2014).
- [73] Schaedler, R., 2013, "A Heated FRAP-Shaped 4-Hole Probe for Measurements in Wet Steam," Master Thesis LEC (06-911-432), ETH Zurich.
- [74] Gossweiler, C. R., Kupferschmied, P., and Gyarmathy, G., 1995, "On Fast-Response Probes: Part 1—Technology, Calibration, and Application to Turbomachinery," *Journal of Turbomachinery*, 117(4), pp. 611-617.
- [75] Gallington, R. W., 1980, "Measurement of Very Large Flow Angles With Non-Nulling Seven-Hole Probe," *Aeronautics Digest*, USAFA-TR-80-17, pp. 60-80.
- [76] Bohn, D. and Simon, H., 1975, "Mehrparametrische Approximation der Eichraeume und Eichflaechen von Unterschall- und Ueberschall-5-Loch-Sonden," *ATM - Technisches Messen*, 468-479(JG)
- [77] Bosdas, I., Mansour, M., Kalfas, A. I., Abhari, R. S., and Senoo, S., 2015, "Unsteady Wet Steam Flow Field Measurements in the Last Stage of Low Pressure Steam Turbine," *Journal of Engineering for Gas Turbines and Power*, 138(3), pp. 032601-032601.
- [78] Behr, T., Anestis, I. K., and Abhari, R., 2006, "A Probabilistic Uncertainty Evaluation Method For Turbomachinery Probe Measurements," XVII Symposium on Measuring Techniques in Turbomachinery. Transonic and Supersonic Flow in Cascades and Turbomachines, Thessaloni Greece, September 21-22
- [79] 1995, "Guide to the Expression of Uncertainty in Measurement (GUM)", International Organisation for Standardisation, Geneva, Switzerland
- [80] Schlienger, J., 2003, "Evolution of Unsteady Secondary Flow in a Multistage Shrouded Axial Turbine," Ph. D ETH, Zurich.
- [81] Laven, P., Mie Plot. Available: <http://www.philiplaven.com> (accessed, November 2013).
- [82] Avellan, F. and Resch, F., 1983, "A scattering light probe for the measurement of oceanic air bubble sizes," *International Journal of Multiphase Flow*, 9(6), pp. 649-663.
- [83] Baumgardner, D., Strapp, W., and Dye, J. E., 1985, "Evaluation of the Forward Scattering Spectrometer Probe. Part II: Corrections for Coincidence and Dead-Time Losses," *Journal of Atmospheric and Oceanic Technology*, 2(4), pp. 626-632.
- [84] Martinez, F., Velazquez, M., Silva, F., Martinez, A., Montes, S., and Chavez, O., 2011, "Theoretical and Numerical Analysis of the Mechanical Erosion in Steam Turbine Blades. Part I," *Energy and Power Engineering*, 03(03), pp. 227-237.
- [85] Kleitz, A. and Dorey, J. M., 2004, "Instrumentation for wet steam," *Proceedings of the Institution of Mechanical Engineers, Part C: Journal of Mechanical Engineering Science*, 218(8), pp. 811-842.
- [86] Petr, V. and Kolovratnik, M., 2000, "Modelling of the droplet size distribution in a low-pressure steam turbine," *Proceedings of the Institution of Mechanical Engineers, Part A: Journal of Power and Energy*, 214(2), pp. 145-152.
- [87] Cai, X., Niu, F., Ning, T., Wu, G., and Song, Y., 2010, "An investigation of wet steam flow in a 300MW direct air-cooling steam turbine. Part 3: heterogeneous/homogeneous condensation," *Proceedings of the Institution of Mechanical Engineers, Part A: Journal of Power and Energy*, 224(4), pp. 583-589.
- [88] Korolev, A., Shashkov, A., and Barker, H., 2013, "Calibrations and Performance of the Airborne Cloud Extinction Probe," *Journal of Atmospheric and Oceanic Technology*, 31(2), pp. 326-345.
- [89] Rollinger, B., Morris, O., and Abhari, R. S., 2011, "Stable tin droplets for LPP EUV sources," *Extreme Ultraviolet (EUV) Lithography II*, (7969), p. 79692W.
- [90] Damaschke, N., Nobach, H., Semidetnov, N., and Tropea, C., 2002, "Optical particle sizing in backscatter," *Applied Optics*, 41(27), pp. 5713-5727.

- [91] Behr, T., Kalfas, A. I., and Abhari, R. S., 2007, "Unsteady Flow Physics and Performance of a One-and-1/2-Stage Unshrouded High Work Turbine," *ASME Journal of Turbomachinery*, 129, pp. 348-359.
- [92] Ahmad, M., Casey, M., and Sürken, N., 2009, "Experimental assessment of droplet impact erosion resistance of steam turbine blade materials," *Wear*, 267(9-10), pp. 1605-1618.
- [93] Eisfeld, T. and Joos, F., 2009, "Experimental Investigation of Two-Phase Flow Phenomena in Transonic Compressor Cascades," Volume 7: Turbomachinery, Parts A and B, Orlando, Florida, USA, GT2009-59365.
- [94] Duan, C., Ishibashi, K., Senoo, S., Bosdas, I., Mansour, M., Kalfas, A., *et al.*, "Unsteady Wet Steam Flow Measurements in a Low-Pressure Test Steam Turbine," presented at the 13th Asian International Conference on Fluid Machinery, Tokyo Japan, September 2015
- [95] Häfele, M., Starzmann, J., Grübel, M., Schatz, M., Vogt, D. M., Drozdowski, R., *et al.*, 2014, "Numerical investigation of the impact of part-span connectors on aerothermodynamics in a low pressure industrial steam turbine," ASME, Düsseldorf, Vol. 1B: Marine; Microturbines, Turbochargers and Small Turbomachines; Steam Turbines, GT2014-25177.
- [96] Porreca, L., Hollenstein, M., Kalfas, A. I., and Abhari, R. S., 2007, "Turbulence Measurements and Analysis in a Multistage Axial Turbine," *Journal of Propulsion and Power*, 23(1), pp. 227-234.
- [97] Qi, M., Yang, J., Yang, R., and Yang, H., 2013, "Investigation on Loading Pulsation of LP Long Blade Stage in Steam Turbine," ASME, San Antonio, Texas, Vol. 5B: Oil and Gas Applications; Steam Turbines, GT2013-94652.
- [98] P. Chaluvadi, V. S., Kalfas, A. I., Banieghbal, M. R., Hodson, H. P., and Denton, J. D., 2001, "Blade-Row Interaction in a High-Pressure Turbine," *Journal of Propulsion and Power*, 17(4), pp. 892-901.
- [99] Senoo, S., 2012, "Development of Design Method for Supersonic Turbine Aerofoils Near the Tip of Long Blades in Steam Turbines Part 1: Overall Configuration," Copenhagen, Denmark, Vol. GT2012-68218
- [100] Kundu, P. K., Cohen, I. M., Dowling, D. R., and Tryggvason, G., *Fluid mechanics*, 6th ed. edition.: Amsterdam : Elsevier, 2016.
- [101] Duncan, W. J., Thom, A. S., and Young, A. D., *Mechanics of fluids*, [Second ed., reprinted 1981] edition.: London : Arnold, 1981.
- [102] Starzmann, J., Schatz, M., Casey, M. V., Mayer, J. F., and Sieverding, F., 2011, "Modelling and Validation of Wet Steam Flow in a Low Pressure Steam Turbine," Volume 7: Turbomachinery, Parts A, B, and C, GT2011-45672.

## Nomenclature

### Symbols

$c$	Stator's chord	[mm]
$C$	Concentration	[droplets/cm <sup>3</sup> ]
$C_{ps}$	Static pressure coefficient	[-]
$C_{pt}$	Total pressure coefficient	[-]
$D$	Diameter	[m]
$DR$	Droplet mass rate	[mg]
$E$	Extinction coefficient	[-]
$f$	Frequency	[kHz]
$f_g$	Droplet frequency generator	[kHz]
$G$	Transfer function	[-]
$H$	Blade height	[m]
$I$	Light intensity	[Watts/m <sup>2</sup> ]
$k$	Adiabatic gas constant	[-]
$k$	Thermal conductivity	[W/m K]
$K$	Aerodynamic calibration coefficient	[-]
$l$	Length	[m]
$L$	Distance	[mm]
$m$	Refractive index	[-]
$Ma$	Mach number	[-]
$N$	Distribution	[-]
$N$	droplet count	[#droplets/rev]
$PA$	Pulse Amplitude	[mV]
$P, p$	Pressure	[Pa]
$r$	Radius	[mm]
$R$	Erosion Rate	[-]
$R$	Resistance	[Ohms]
$s$	Axial gap between L-0 stator rotor	[mm]
$S$	Laplace complex angular frequency	[-]
$St$	Stokes number	[-]
$t$	Time instant	[sec]
$t$	Blade pitch	[-]
$T$	Temperature	[°C]
$T$	Time period	[sec]
$U$	Voltage	[volts]
$V$	Velocity	[m/s]
$We$	Weber number	[-]
$WE$	Wedge angle of L-0 rotor blade	[deg]
$x$	Stator's axial downstream location	[mm]
$x$	Axial distance downstream stator	[mm]

**Greek symbols**

$\alpha$	<i>Polynomial calibration coefficient</i>	<i>[-]</i>
$\alpha$	<i>Relative flow yaw angle</i>	<i>[deg]</i>
$\beta$	<i>slope of loss energy coefficient</i>	<i>[%/deg]</i>
$\gamma$	<i>Flow pitch angle</i>	<i>[deg]</i>
$\delta$	<i>Shock wave thickness</i>	<i>[<math>\mu\text{m}</math>]</i>
$\zeta$	<i>Damping</i>	<i>[-]</i>
$\theta$	<i>Scattering angle</i>	<i>[deg]</i>
$\lambda$	<i>Wavelength</i>	<i>[nm]</i>
$\mu$	<i>Dynamic viscosity</i>	<i>[Pa s]</i>
$\nu$	<i>kinematic viscosity</i>	<i>[m<sup>2</sup>/s]</i>
$\xi$	<i>Energy loss coefficient</i>	<i>[-]</i>
$\rho$	<i>Density</i>	<i>[kg/m<sup>3</sup>]</i>
$\sigma$	<i>Standard deviation</i>	<i>[-]</i>
$\sigma$	<i>Surface tension</i>	<i>[N/m]</i>
$\tau$	<i>Turbidity</i>	<i>[cm<sup>-1</sup>]</i>
$\varphi$	<i>Flow yaw angle</i>	<i>[deg]</i>
$\omega$	<i>Rotational speed</i>	<i>[rad/s]</i>

**Subscripts**

10	<i>Arithmetic mean diameter</i>
32	<i>Sauter mean diameter</i>
abs	<i>Absolute</i>
atm	<i>Atmospheric</i>
avg	<i>Average value</i>
ax	<i>axial</i>
c	<i>Calibration</i>
ch	<i>Characteristic length (rotor blade leading edge radius)</i>
d	<i>Droplet</i>
dyn	<i>Dynamic</i>
e	<i>Erosion</i>
e	<i>excitation</i>
eff	<i>Effective beam diameter of the FRAP-OB probe</i>
f	<i>Flow</i>
heater	<i>Heater location</i>
i	<i>Measurement point at specific grid location</i>
int	<i>interval</i>
m	<i>Measurements</i>
M	<i>Model</i>
M	<i>Most frequent value in a data set (i.e. diameter)</i>
ma	<i>L-0 stator metal angle (average value)</i>
n	<i>Number</i>
nt	<i>Natural</i>

<i>o</i>	<i>Incident light intensity</i>
<i>p</i>	<i>Probe</i>
<i>ref</i>	<i>Reference back pressure</i>
<i>rel</i>	<i>Relative</i>
<i>res</i>	<i>Residence</i>
<i>s</i>	<i>Static</i>
<i>sat</i>	<i>Saturation</i>
<i>st</i>	<i>Steam</i>
<i>t</i>	<i>Total</i>
<i>T</i>	<i>Traversing system</i>
<i>TE</i>	<i>Trailing edge</i>
<i>tip</i>	<i>Probe tip location</i>

### Superscripts

~	<i>Time resolved data (phase locked)</i>
–	<i>Time averaged data (mean value)</i>
'	<i>Random part of pressure signal</i>
<i>i,j</i>	<i>Polynomial order</i>

### Abbreviations

5HP	<i>Pneumatic 5-hole probe (Cobra shape)</i>
BPF	<i>Blade passing frequency</i>
CFD	<i>Computational Fluid Dynamics</i>
FFT	<i>Fast Fourier Transform</i>
<i>F<sub>q</sub></i>	<i>Flow field quantity (i.e: yaw, pitch angle, etc.)</i>
FRAP-HT	<i>High temperature fast response aerodynamic probe</i>
FRAP-HTH	<i>High temperature fast response aerodynamic heated probe</i>
FRAP-OB	<i>Fast response optical backscatter probe</i>
GEP	<i>Gaussian error propagation</i>
GUM	<i>Guide to expression of uncertainty in measurement</i>
IEA	<i>International Energy Agency</i>
INDC	<i>Intended nationally determined contributions</i>
IPCC	<i>Intergovernmental panel on climate change</i>
LE	<i>Leading edge</i>
LEC	<i>Laboratory for energy conversion</i>
LP	<i>Low-pressure</i>
Mtoe	<i>Million tonnes of oil equivalent</i>
MBDOE	<i>Million barrels per day of oil equivalent</i>
MHPS	<i>Mitsubishi Hitachi Power Systems</i>
OEP	<i>Optical extinction probe</i>
OP	<i>Operating Point</i>
PDA	<i>Phase Doppler Anemometry</i>
PLA	<i>Phase lock averaged data</i>

<i>PPM</i>	<i>Parts per million</i>
<i>PS</i>	<i>Pressure side</i>
<i>PSC</i>	<i>Part-span connector</i>
<i>RMS</i>	<i>Root mean square</i>
<i>SS</i>	<i>Suction side</i>
<i>TE</i>	<i>Trailing edge</i>
<i>TF</i>	<i>Transfer function</i>

## List of Figures

Figure 1–1: World energy demand to 2030 in Mtoe [1]. INDC scenario: Intended Nationally Determined Contributions. 450 scenario: limit concentration of greenhouse gases in the atmosphere to 450ppm of CO <sub>2</sub> .....	1
Figure 1–2: Estimated fossil fuel energy share of global final energy consumption in year 2013 [3].....	2
Figure 1–3: World energy demand to 2030 by sector in MBDOE [5]. .....	3
Figure 1–4: Schematic of Rankine cycle (left) with the respective temperature (T)-entropy (s) diagram of a steam turbine (right)[6]. .....	4
Figure 1–5: Blade erosion in a steam turbine [13]. .....	4
Figure 1–6: Secondary flow model described in [20]......	7
Figure 1–7: Sketch of Mach number and static pressure radial distribution in the last stage of a low-pressure steam turbine [24]......	9
Figure 1–8: Losses associated to shock waves at the tip region of a supersonic rotor blade profile [14]. .....	10
Figure 1–9: Side view of a forward swept stator blade at tip region from the last stage simulated by Stüer et al. [24]......	12
Figure 1–10: Flow field distribution at the last stages of LP steam turbine under ventilation [30] (a) and comparison with experiments from [31] (b). .....	12
Figure 1–11: Topology of phase transition in a LP steam turbine presented by Gerber in [36]. Stator and rotor components are labelled with S and R, respectively. ....	14
Figure 1–12: Water film formation on last stage stator in a LP steam turbine [7]. .....	15
Figure 1–13: Tearing modes of water film according to Li et al. [9]. The three different modes are: (a) film tearing, (b) spindle tearing, and (c) rivulet tearing. ....	16
Figure 1–14: Single sensor fast response probe by Gerschütz et al. [32]......	18
Figure 1–15: Optical probes used in atmospheric research mounted on aircraft's fuselage and wing [56]. .....	19
Figure 1–16: The tip from a combined optical and pneumatic probe by Wu et al. [63]. .....	20
Figure 1–17: Photograph of the combined optical and pneumatic probe by Cai et al. [11]. .....	21
Figure 2–1: Front part and tip schematics of the FRAP-HT probe developed by Lenherr [71].....	26
Figure 2–2: Temperature-entropy diagram for a steam turbine operating cycle and the respective probe tip operating temperature. ....	27
Figure 2–3: FRAP-HTH probe tip schematic. A: Probe tip ( $D_p=2.5\text{mm}$ ), B: Heating elements ( $D_{\text{Heating-spot}}=4.7\text{mm}$ ), C: Tip temperature monitoring ( $T_{\text{tip}}$ ), D: 8mm shaft.....	28
Figure 2–4: PID block diagram for FRAP-HTH's miniature heater control. ....	28
Figure 2–5: Tip temperature overheat for two different heater locations. Case A: $10 \times D_p$ from the pressure taps, Case B: $4.5 \times D_p$ from the pressure taps.....	30
Figure 2–6: Actual temperature of yaw and pitch sensors as well as heater temperature along the blade span for the exit of the last stage of 7MW LP steam turbine with an average wetness mass fraction of 8% for the final version of FRAP-HTH (a). Same results zoomed in for 30 to 72°C (b). .....	31
Figure 2–7: Wheatstone bridge schematic (a) and silicon pressure transducer with a cross-section at the diaphragm region(b). .....	32



Figure 2–8: Calibration curve in volts for yaw sensor, (a) is the U output and (b) is the Ue output.....	32
Figure 2–9: Virtual 6-Hole measurement concept with a 2-Hole Probe.....	33
Figure 2–10: FRAP-HTH extended calibration section’s schematic for Ma=0.7.....	34
Figure 2–11: Extended aerodynamic probe calibration at Freejet facility.....	35
Figure 2–12: Aerodynamic calibration coefficients for sector 1, (a) yaw angle, (b) pitch angle, (c) total pressure, (d) static pressure.....	38
Figure 2–13: Aerodynamic calibration coefficients for sector 2, (a) yaw angle, (b) pitch angle, (c) total pressure, (d) static pressure.....	38
Figure 2–14: Effect of heater’s temperature at representative Nusselt flow conditions from tests in Freejet facility for tip temperature overhead $\Delta T=10K$ .....	39
Figure 2–15: Shock-tube test section: (A) FRAP-HTH probe, (B) Reference probe, (C) electronics, (D) triggering sensor, (E) diagraph location, (F) high pressure section (a). FRAP-HTH and flush mounted reference probe (b).....	41
Figure 2–16: Time signal of FRAP-HTH and reference probe in shock tube tests (a) ad FFT plots of FRAP and Reference probe signals out of 10 averages (b). ....	41
Figure 2–17: Comparison of parametric and non-parametric transfer function (no averaging) from a single experiment (a) and FRAP-HTH averaged transfer function over 15 experiments in shock-tube (b). ....	42
Figure 2–18: Flow angles’ uncertainty propagation (a). Pressure uncertainty propagation of total and static pressure measurement (b) [78]. ....	46
Figure 2–19: Total and static pressure expanded uncertainties as a function of Mach number.....	47
Figure 2–20: Probe’s raw absolute pressure signal from the pitch sensor for the three consecutive records (0°, -42°, +42°) (a). Probe’s raw temperature signal from the pitch sensor for record at -42° (b).....	48
Figure 2–21: Code structure of processing code Herkules with the new subroutine implemented between the first and second step of the initial code.....	49
Figure 2–22: Pressure (a) and temperature (b) signals for the yaw sensor for 1 rotor revolution. The signal P2 is corrupted due to water evaporation. ....	50
Figure 3–1: Operating principle schematic of the optical backscatter probe.....	53
Figure 3–2: The optical backscatter probe tip.....	54
Figure 3–3: Mie simulations schematic. Angular scattering intensity for a water droplet with $D_d=5$ , $\lambda=632nm$ and $I_o=1W/m$ .....	54
Figure 3–4: Mie calculation of scattering intensity by water droplet ( $m=1.33+1.67 \cdot 10^{-8}i$ at 20°C) for unpolarized red light ( $\lambda=632nm$ ) for diameters $D_d=20, 40, 60, 80$ and $100\mu m$ .....	55
Figure 3–5: Representation of coincidence and side effect error.....	56
Figure 3–6: Calculated of maximum error due to coincidence and side effect.....	57
Figure 3–7: Amplitude response of the optical backscatter probe out of simulations.....	59
Figure 3–8: Monodispersed calibration facility schematic A: Probe, B: He-Ne Laser, C: Droplet generator, D: Reference camera, E: Droplet monitor diode, F: Optical table, G: Strobe light.....	60
Figure 3–9: Raw images from reference camera for 60 $\mu m$ droplet diameter (a) and 105 $\mu m$ droplet diameter (b).....	61

Figure 3–10: Probe and monitor photodiode raw signals during calibration for 60 $\mu$ m droplet diameter (a) and 105 $\mu$ m droplet diameter (b). .....	61
Figure 3–11: Single droplet measured parameters after calibration.....	62
Figure 3–12: Calibration curve of the optical backscatter probe with water droplets obtained from the droplet generator. ....	62
Figure 3–13: Theoretical response function in the backscatter region for water, calculated from the Mie theory out of simulations. ....	63
Figure 3–14: Effective beam diameter as a function of droplet diameter for calibration tilting angle 0° (a) and tilting angle 49° (b). ....	64
Figure 3–15: Probe’s output signal (mapping) when droplets are partially crossing the sample volume. ....	65
Figure 3–16: Droplet’s diameter probability distribution function related to the probe minimum signal amplitude (PA=0.5mV) and maximum signal amplitude (PA=8.5mV).....	66
Figure 3–17: Probability distribution model for the calibrated range of the optical backscatter probe. ....	67
Figure 3–18: Correction example of small (a) and large (b) droplet distribution by applying the probability distribution model. ....	67
Figure 3–19: Flow chart of the post processing algorithm for the optical backscatter probe. ....	70
Figure 3–20: Single measurement point raw data file over 14 rotor revolutions (a) and the same raw file zoom in over 4 detected droplets (b). ....	71
Figure 3–21: Utilization of high pass filter (a) and low pass filter (b) in raw data. ....	72
Figure 3–22: Zoom in a single valid droplet at time location A (a) and a non valid droplet at time location B (b) of Figure 3–20.....	72
Figure 3–23: Single measurement point probe representation results. Voltage peak heights that fulfil the detection criteria are converted into droplet size and presented as a size distribution histogram. ....	73
Figure 3–24: Single measurement point probe representation results. Voltage pulse widths that fulfil the detection criteria are converted into droplet velocity and presented as velocity distribution histogram. ....	73
Figure 3–25: Detected droplets for two rotor revolutions as they are spread among the difference blade passages.....	74
Figure 3–26: Rotor blade passing period as it is partitioned into ten sections.....	75
Figure 4–1: Schematic of LISA turbine test facility. ....	77
Figure 4–2: Measurement grid schematic at the experiments performed in LISA test rig. The observer looks upstream. The measurement grid consists of 21 x 41 points equally spaced in the radial and circumferential direction respectively, and covers one full stator pitch (10°) from 5% to 90% of the blade span. ....	78
Figure 4–3: Cross section of the test segment (Turbine Teststand).....	79
Figure 4–4: FRAP-OB probe installed on traversing unit (a) and support strut with the spray generator (b). ....	80
Figure 4–5: Droplet rate [droplets/rev] at Stator 1 exit plane for design point (a) and part load condition (b). Observer looks upstream.....	81
Figure 4–6: Absolute Mach number [-] at Stator 1 exit plane for design operating condition (a) and part load (b). Observer looks upstream. ....	81

Figure 4–7: Size droplet distribution at tip (upper), midspan (center) and hub (bottom) spanwise locations for design and part load conditions at $x/c=2\%$ downstream of stator 1 exit.....	82
Figure 4–8: Area averaged absolute Mach number for design and part load operating conditions at Stator 1 exit plane.....	83
Figure 4–9: Velocity triangles flow field (black) and droplets (red) at Stator 1 exit.....	84
Figure 4–10: Absolute (a) and relative (b) droplet velocity at midspan location for design and part load conditions.....	85
Figure 4–11: Size droplet distribution at tip (upper), midspan (center) and hub(bottom) spanwise locations for part load condition at $x/c$ 2% and 8% downstream of stator 1 exit.....	86
Figure 4–12: Weber number as a function of droplet diameter for the two different downstream axial locations of Stator 1 at mid span.....	87
Figure 4–13: Absolute (a) and relative (b) droplet velocity at midspan location at $x/c=2\%$ and 8% for part load condition. ....	87
Figure 4–14: Time resolved droplet mass rate [mg/s] at Stator 1 exit plane for design point (left) and part load condition (center) at $x/c=2\%$ and part load condition at $x/c=8\%$ (right) for four instants of the rotor blade passing period: a) $t/T=0.00$ , b) $t/T=0.25$ , c) $t/T=0.50$ and d) $t/T=0.75$ .....	90
Figure 5–1: Schematic of experimental test facility [94].....	92
Figure 5–2: Low-pressure steam turbine test facility where FRAP-HTH measurements were conducted.....	93
Figure 5–3: Four stage rotor (a) and schematic of the four stages with the respective probe measurement locations (b).....	94
Figure 5–4: Probe traverse path at (a) L-1 and (b) L-0 stage. ....	94
Figure 5–5: Relative flow yaw angle (a) and absolute Mach number (b) measured by the 5HP and FRAP-HTH probes at rotor exit of L-1 stage .....	96
Figure 5–6: Relative flow yaw angle (a) and absolute Mach number (b) of 5HP and FRAP-HTH probes at rotor exit of L-0 stage .....	96
Figure 5–7: Time averaged spanwise distribution of $C_{pt,rel}$ (a) and time averaged RMS of $P_{tot}'$ [Pa] (b) at rotor exit of L-1 stage for OP-3, OP-2 and OP-1 with their respective minimum and maximum values obtained from the time resolved data. ....	98
Figure 5–8: Time resolved $C_{pt,rel}$ [-] at rotor exit of L-1 stage for OP-3.....	101
Figure 5–9: Time resolved total pressure $P/P_{avg}$ obtained from the single traverse at the exit of L-1 rotor for OP-3. The radial axis refers to the blade span and the azimuthal axis to the blade count over one rotor revolution.....	102
Figure 5–10: Time resolved RMS of $P_{tot}'$ [Pa] in stationary frame of reference at rotor exit of L-1 stage for (a) OP-3 and (b) OP-1. ....	103
Figure 5–11: Time resolved relative yaw flow angle [deg] at rotor exit of L-1 stage for (a) OP-3 and (b) OP-1 (relative to blade metal angle).....	103
Figure 5–12: Unsteady relative flow yaw and pitch angles, relative total and static pressure coefficients at 86% span for OP-3 and OP-1.....	104
Figure 5–13: Time averaged spanwise distribution of the $C_{pt}$ in relative frame of reference for 2 operating conditions (a) and difference in $C_{pt,rel}$ between OP-2 with OP-3 (b), $\dot{m}_{OP-2} = 78\% \dot{m}_{OP-3}$ .....	105

Figure 5–14: Time averaged spanwise distribution of $C_{pt,rel}$ (a) and time averaged $P_{tot}'$ RMS [Pa] (b) at rotor exit of L-0 stage for OP-2 and OP-3 with their respective minimum and maximum values obtained from the time resolved data, $\dot{m}_{OP-2} = 78\% \dot{m}_{OP-3}$ .....	106
Figure 5–15: Time-averaged spanwise distribution of $V_{radial}/V_{axial}$ at exit of L-0 stage, $\dot{m}_{OP-2} = 78\% \dot{m}_{OP-3}$ .....	107
Figure 5–16: Time resolved RMS of $P_{tot}'$ [Pa] in stationary frame of reference at rotor exit of L-0 stage for (a) OP-3 and (b) OP-2, $\dot{m}_{OP-2} = 78\% \dot{m}_{OP-3}$ .....	108
Figure 5–17: Time resolved relative flow yaw angle [deg] (relative to the blade metal angle) at rotor exit of L-0 stage for (a) OP-3 and (b) OP-2, $\dot{m}_{OP-2} = 78\% \dot{m}_{OP-3}$ .....	108
Figure 5–18: Time resolved $C_{pt,rel}$ [-] at rotor exit for (a) OP-3 and (b) OP-2, $\dot{m}_{OP-2} = 78\% \dot{m}_{OP-3}$ .....	109
Figure 6–1: MHPS' low-pressure steam turbine test facility where FRAP-HTH and FRAP-OB measurements were conducted (a). Schematic of test facility, the measurement plane of the probe is marked in red (b). .....	111
Figure 6–2: Measurement grid with 21 equally spaced points in the circumferential direction and 19 points in the radial direction clustered towards the end wall. ....	112
Figure 6–3: Circumferentially area averaged spanwise distribution of $C_{pt}$ [-] (a) and $C_{ps}$ [-] (b) with the minimum and maximum values obtained from the time resolved data. ....	113
Figure 6–4: Circumferentially area averaged spanwise distribution of delta flow yaw angle [deg] (a) and dimensionless flow pitch angle [-] (b) with the minimum and maximum values obtained from the time resolved data. ....	114
Figure 6–5: Bar plot of the peak-to-peak fluctuations of the main flow field quantities as presented in Table 12 for OP-1 for the supersonic and subsonic region of the blade span. ....	116
Figure 6–6: Total pressure coefficient (a) and absolute Mach number (b) at three blade span locations for one stator pitch, OP-1. ....	117
Figure 6–7: Representation of a time space diagram for the absolute yaw angle at a specific span location (87.5% span) for one stator pitch and four rotor blade passing periods. ....	118
Figure 6–8: Circumferential distribution of $C_{pt}$ [-] at L-0 stator exit for OP-1 at 90% span from measurements with the theoretical increase of the stator wake due to large scale separation. ....	118
Figure 6–9: Circumferential distribution of absolute Mach number at L-0 stator exit for OP-1 at 90% span. The stator wake region where a high velocity modulation is expected in the case of a large-scale separation is marked with the white ellipse. ....	119
Figure 6–10: Shock wave attached at the leading edge of a diamond airfoil type (a) [101]. Density profile along the shock wave for ideal and measured case. ....	120
Figure 6–11: Circumferential distribution of $C_{ps}$ [-] at L-0 stator exit for OP-1 at 90% (a) and 75% (b) span. ....	121
Figure 6–12: Circumferential distribution of delta yaw angle [deg] at 90% span at L-0 stator exit for OP-1. The region of low unsteadiness is marked with a white frame. ....	122
Figure 6–13: Left: Bow shock interaction with the stator trailing edge of L-0 stage for four instants of the rotor blade passing period ( $t/T=0$ , $t/T=0.25$ , $t/T=0.5$ and $t/T=0.75$ ) at 90% span. Right: absolute flow yaw angle and $C_{ps}$ coefficient according to Eq.(6-3) and Eq.(6-2) respectively for the same time instants over one stator pitch. ....	124

Figure 6–14: Circumferential distribution of dimensionless pitch angle [%] at 95% at L-0 stator exit for OP-1. The region of high unsteadiness is marked with a white frame.....	125
Figure 6–15: Time resolved flow pitch angle [%] (Blade span vs. Time) for two individual traverses: (a) region of low yaw angle unsteadiness (0.5 stator pitch) and (b) region where yaw angle unsteadiness starts increasing (0.85 stator pitch) as shown in Figure 6–12. ....	126
Figure 6–16: Reduction of the effective area due to stator’s suction side profile (marked with red) while the shock wave travels within the stator passage. ....	127
Figure 6–17: Meridional view of the last two stages. The bow shock interacts always with the casing wall at the very top of the blade span.....	127
Figure 6–18: L-0 rotor inlet and exit velocity and Mach number relationship. The subscripts 1 and 2 refer to the inlet and exit of the rotor passage respectively [14]. ....	128
Figure 6–19: Circumferentially area averaged spanwise distribution of relative yaw angle (a) and relative Mach number (b) for OP-1 at the rotor inlet. The solid lines show the circumferentially area averaged time resolved results. ....	129
Figure 6–20: Calculated relative yaw angle at the rotor exit for OP-1 according to Eq.(6-7). The dashed lines show the instantaneous maximum and minimum values along the blade span.....	130
Figure 6–21: Energy loss coefficient out of simulations presented by Senoo in [14]. The optimum design case is for an increment of $10^\circ$ in the outlet metal angle relative to the initial quasi-one-dimensional design result. ....	131
Figure 6–22: Calculated instantaneous maximum losses (a) and time averaged losses (b) in the supersonic region for OP-1. Theses plots present the relative increase of the losses compared to the design point as indicated in Figure 6–21. ....	132
Figure 6–23: Calculated time averaged losses for $Ma_2+\Delta Ma$ (a) and $Ma_2-\Delta Ma$ (b) in the supersonic region for OP-1. Theses plots present the relative increase of the losses compared to the design point. ....	133
Figure 6–24: Circumferentially area averaged spanwise distribution of total pressure coefficient (a) and absolute yaw angle (b) with the minimum and maximum values obtained from the time resolved data for OP-1 and OP-4 (part load, $32\% \dot{m}_{OP-1}$ ).....	134
Figure 6–25: Circumferentially area averaged spanwise distribution of dimensionless flow pitch angle for high mass flow (OP-1) and low mass flow (OP-4, $32\% \dot{m}_{OP-1}$ ) operating points. ....	135
Figure 6–26: Circumferentially area averaged spanwise distribution of absolute (a) and relative (b) Mach number with the minimum and maximum values obtained from the time resolved data for high the mass flow (OP-1) and low mass flow (OP-4, $32\% \dot{m}_{OP-1}$ ) operating points. ....	136
Figure 6–27: Time averaged results of droplet rate [#droplet/rev] for (a) OP-3 and (b) OP-2 at L-0 stator exit ( $T_{in,OP-3}=220^\circ C$ & $T_{in,OP-2}=270^\circ C$ ).....	138
Figure 6–28: Time averaged results of Sauter mean droplet diameter [ $\mu m$ ] for (a) OP-3 and (b) OP-2 at L-0 stator exit ( $T_{in,OP-3}=220^\circ C$ & $T_{in,OP-2}=270^\circ C$ ).....	138
Figure 6–29: Time averaged results of droplet mass rate [mg/rev] for (a) OP-3 and (b) OP-2 at L-0 stator exit ( $T_{in,OP-3}=220^\circ C$ & $T_{in,OP-2}=270^\circ C$ ).....	140
Figure 6–30: Sauter mean droplet diameter for OP-2 and OP-3 at L-0 stator exit ( $T_{in,OP-3}=220^\circ C$ & $T_{in,OP-2}=270^\circ C$ ). ....	140

Figure 6–31: Droplet diameter distribution for OP-2 at 75% for four different circumference locations at Pitch: -0.25, -0.5, +0.5 and +0.25 (see Figure 6–29.b). .....	141
Figure 6–32: Circumferential distribution of measured droplet mass rate [mg/sec] at L-0 stator exit for OP-2 at 78% span. ....	142
Figure 6–33: Circumferential distribution of Cps [-] at L-0 stator exit for OP-2 at 78% span. ....	143
Figure 6–34: Circumferential distribution of non dimensional streamwise vorticity [-] at L-0 stator exit for OP-2 at 78% span. ....	144
Figure 6–35: Circumferential distribution of measured droplet mass rate [mg/sec] at L-0 stator exit for OP-2 at 71% span. ....	144
Figure 6–36: Circumferential distribution of Cps [-] at L-0 stator exit for OP-2 at 71% span. ....	145
Figure 6–37: Circumferential distribution of non dimensional streamwise vorticity [-] at L-0 stator exit for OP-2 at 71% span. ....	145

## List of Tables

Table 1: Extended aerodynamic calibration coefficients for FRAP-HTH probe. ....	34
Table 2: FRAP-HTH calibration model accuracy for $Ma=0.7$ and calibration range of $\pm 24^\circ$ in Yaw and $-1^\circ < \text{pitch} < 49^\circ$ in pitch. ....	37
Table 3: Sources of uncertainty (expanded with coverage factor 2) for the flow angles. ....	44
Table 4: Sources of uncertainty (expanded with coverage factor 2) for the total and static pressure. ...	45
Table 5: FRAP-HTH expanded uncertainty (coverage factor 2) calculated for L-0 stator exit for $Ma=0.7$ (see Table 11, OP-1). ....	45
Table 6: Sources of uncertainty (expanded with coverage factor 2) related to the calibration procedure. ....	68
Table 7: Sources of uncertainty (expanded with coverage factor 2) from the measurements. ....	69
Table 8: Operating conditions and geometrical characteristics. ....	79
Table 9: Operating tested conditions. ....	93
Table 10: Spanwise distribution of peak-to-peak fluctuation of $C_{pt,rel}$ as a function of the local mean value for OP-1, OP-2 and OP-3 conditions. ....	99
Table 11: Operating tested conditions. ....	110
Table 12: Peak to peak fluctuations of the main flow field quantities as a function of the mean value for OP-1 for supersonic and subsonic region of the span. ....	115





## List of Publications

Parts of the author's following publications are included in this doctoral thesis.

Bosdas, I., Mansour, M., Kalfas, A. I., Abhari, R. S., and Senoo, S., 2015, "Unsteady Wet Steam Flow Field Measurements in the Last Stage of Low Pressure Steam Turbine," *Journal of Engineering for Gas Turbines and Power*, 138(3), pp. 032601-032601.

Bosdas, I., Mansour, M., Kalfas, A. I., and Abhari, R. S., 2016, "An optical backscatter probe for time resolved droplet measurements in turbomachines," *Measurement Science and Technology*, 27(1), p. 015204.

Bosdas, I., Mansour, M., Kalfas, A., Abhari, R., and Senoo, S., "Unsteady Wet Steam Flow Field and Droplet Measurements at the Last Stage of Low-Pressure Steam Turbine," presented at the IGTC, Tokyo, Japan, 2015.

Bosdas, I., Mansour, M., Kalfas, A., Abhari, R., "Temporal and Spatially Resolved Particle Size and Speed Measurements in Subsonic and Transonic Turbomachines," ISABE Conference 2015, Phoenix Arizona, USA

Bosdas, I., Mansour, M., Kalfas, A. I., and Abhari, R. S., 2015, "A Fast Response Miniature Probe For Wet Steam Flow Field Measurements," *Measurement Science & Technology Journal*

Bosdas, I., Mansour, M., Kalfas, A., Abhari, R., and Senoo, S., 2016 "Unsteady Flow Field and Coarse Droplet Measurements in the Last Stage of a Low Pressure Steam Turbine With Supersonic Airfoils Near the blade Tip," GT2016-57753, IGTI ASME 2016 Seoul, *journal and honors recommendation*

Bosdas, I., Mansour, M., Kalfas, A. I., and Abhari, R. S., "A Miniature Optical Extinction Heated Probe For Fog Droplet Measurements in Steam Turbines," XXIII Biannual Symposium on Measuring Techniques in Turbomachinery Transonic and Supersonic Flow in Cascades and Turbomachines 2016, Stuttgart, Germany



## Curriculum Vitae

### Ilias Bosdas

Born on June 29, 1985 in Athens, Greece.

#### Education

- 2000-2003 Secondary Education, High school of Pallini, Athens, Greece
- 2003-2009 Diploma in Mechanical Engineering, Aristotle University of Thessaloniki, Greece
- 2009-2010 Master in Aircraft Engines (Thermal Power MSc), Cranfield University, UK
- 2010-2016 Swiss Federal Institute of Technology, Zurich (ETHZ), Laboratory for Energy Conversion (LEC)  
Doctoral candidate

#### Experience

- 2006-2008 ICE engine calibration engineer for Formula SAE racing contest, Aristotle Racing Team, Greece
- 2009-2010 Performance engineer, Cranfield University, UK
- 2010-2016 Research assistant, Laboratory for Energy Conversion-ETH Zurich

#### Distinctions/Awards

- 2009 Merit award from Aristotle University of Thessaloniki for constructing the first formula student car of the university and participating successfully in the corresponding international SAE competitions
- 2010 Thermal Power MSc Director's Prize from Cranfield University





